
A

Presented to
the faculty of the School of Engineering and Applied Science
University of Virginia

in partial fulfillment
of the requirements for the degree

by

APPROVAL SHEET

This

is submitted in partial fulfillment of the requirements
for the degree of

Author:

Advisor:

Advisor:

Committee Member:

Committee Member:

Committee Member:

Committee Member:

Committee Member:

Committee Member:

Accepted for the School of Engineering and Applied Science:



Craig H. Benson, School of Engineering and Applied Science

Copyright © by Jack A. Dienes
All Rights Reserved

Statement by Author

This dissertation has been submitted in partial fulfillment of requirements for a doctoral degree at the University of Virginia. Copyright permissions were acquired for all previously published figures.

Brief quotations from this dissertation are allowable without special permission, provided that accurate acknowledgement of source is made. Requests for permission for extended quotation from or reproduction of this manuscript in whole or in part may be granted by the head of the major department, when in their judgement the proposed use of the material is in the interests of scholarship. Permission must be obtained from the author in all other cases.

Acknowledgements

This dissertation is the result of my research and studies at the University of Virginia in pursuit of a Ph.D. in Biomedical Engineering. First and foremost, I would like to acknowledge my advisor, Dr. George Christ, for training me and helping me to navigate this program. I would like to thank Dr. Shawn Russell for his endless patience and guidance as I learned to write code and collect motion capture data. I would like to thank Dr. Silvia Blemker for all of her advice along the way, I would not have made it without that help. I would also like to thank Juliana Passipieri, Ellen Mintz, Emily Dooley, David Remer, and the numerous other members of the Christ Lab and the Russell Lab for their help conducting experiments and collecting/analyzing data. Lastly, I have to thank my family and friends for their unconditional support over the last six years.

The projects described in this dissertation were supported by the DoD/USAMRAA (award number: W81XWH-17-PRORP-ARA), the AR3T Pilot Funding Program, and DoD/USAMRAA (award number: W81XWH-18-2-0036). The contents herein are solely the responsibility of the author and do not represent the official views of the sponsors.

I dedicate this dissertation to my family and friends:

my parents, Kasey and Kara,

my sisters, Grace and Mae,

and to Winona Squires and Devon Zimmerman.

Table of Contents

List of Figures	viii
List of Tables	xi
Nomenclature	xii
Abstract	xv
Chapter 1 – Introduction to Skeletal Muscle Tissue Engineering and Regeneration	
<i>Introduction</i>	1
<i>Hydrogel-based Approaches for VML</i>	4
<i>Scaffold-based Approaches for VML</i>	8
<i>References</i>	13
Chapter 2 – Introduction to Rodent Motion Capture and Gait Analysis	
<i>Introduction</i>	18
<i>Spatiotemporal Parameters</i>	19
<i>Ground Reaction Forces</i>	22
<i>Kinematics</i>	24
<i>Kinetics</i>	28
<i>References</i>	33
Chapter 3 – Hyaluronic Acid-based Hydrogels as Treatment for TA VML Injury	
<i>Abstract</i>	39
<i>Introduction</i>	41
<i>Materials and Methods</i>	44
<i>Results</i>	51
<i>Discussion</i>	63
<i>Conclusion</i>	68
<i>References</i>	70
Chapter 4 – Rodent Gait Biomechanics in Response to TA VML Injury	
<i>Introduction</i>	76
<i>Materials and Methods</i>	78
<i>Results</i>	85
<i>Discussion and Conclusion</i>	89
<i>Future Work</i>	92
<i>References</i>	93
Chapter 5 – Comprehensive Dynamic and Kinematic Analysis of the Rodent Hindlimb Over-Ground Walking	
<i>Abstract</i>	97
<i>Introduction</i>	98
<i>Methods</i>	101
<i>Results</i>	105
<i>Discussion</i>	111
<i>Conclusion</i>	117

<i>References</i>	119
Chapter 6 – Evaluation of Gait Biomechanics in Response to Complex Traumas and Treatment – Tibialis Anterior	
<i>Introduction</i>	124
<i>Materials and Methods</i>	127
<i>Results</i>	137
<i>Discussion</i>	161
<i>Future Work and Conclusion</i>	172
<i>References</i>	174
Chapter 7 – Evaluation of Gait Biomechanics in Response to Complex Traumas – Lateral Gastrocnemius	
<i>Introduction</i>	180
<i>Materials and Methods</i>	183
<i>Results</i>	190
<i>Discussion</i>	205
<i>Future Work and Conclusion</i>	214
<i>References</i>	216
Chapter 8 – Conclusion.....	221

List of Figures

Figure 1-1: Representative images of VML injuries	4
Figure 1-2: Force testing rig and rat orientation for TA testing	8
Figure 1-3: Representative VML injury creation, TEMR construct, and TEMR application.....	10
Figure 2-1: Modeling and reconstruction methods for kinematic analysis.....	25
Figure 3-1: Schematic of experimental design	47
Figure 3-2: Logistic modeling of peroneal nerve-stimulated TA muscle contraction (torque).....	49
Figure 3-3: Baseline torque and body weight measurements	50
Figure 3-4: Comparison of functional metrics observed among different treatment groups at each study timepoint	52
Figure 3-5: Comparison of body weight, functional baseline parameters, and functional recovery observed among different treatment groups at 12-weeks post injury or repair/implantation	54
Figure 3-6: Kinetic analysis of contraction.....	55
Figure 3-7: Representative images of TA muscle tissue morphology and histology in contralateral Control, Non-Repaired, and HyA-treated animals	56
Figure 3-8: Frequency distribution of muscle fiber cross section area (FCSA) in the outer and inner portions of the muscle and centrally located nuclei percentage	60
Figure 3-9: Centrally Located Nuclei	61
Figure 3-10: Capillary density	62
Figure 4-1: Representative surgical defect of 20% by mass volumetric muscle loss injury	80
Figure 4-2: Vicon Nexus 2.8.1 3-D overlay of motion capture markers	82
Figure 4-3: OpenSim rat hindlimb model with reconstructed marker locations	83
Figure 4-4: Force testing results for all VML animals prior to surgery and 2, 4, and 8 weeks post-surgery.....	85
Figure 4-5: Kinematic curves for hip flexion, hip adduction, hip external rotation, knee flexion, and ankle dorsiflexion.....	88
Figure 5-1: Vicon Nexus 2.7.1 3-D overlay of motion capture marker placements.....	102
Figure 5-2: Kinematic (joint angles) and kinetic (joint moments) curves for healthy female Lewis rats	107

Figure 5-3: Ground reaction force (GRF) curves for healthy female Lewis rats.....	109
Figure 5-4: Joint power curves for healthy female Lewis rats.....	110
Figure 6-1: Volumetric muscle loss injury creation and repair	131
Figure 6-2: Sciatic nerve branch site and nerve laceration post-repair.....	132
Figure 6-3: Vicon Nexus 3-D overlay of motion capture marker placements.....	134
Figure 6-4: OpenSim rat hindlimb model with reconstructed marker locations	135
Figure 6-5: Study 1 comparison of body weight, functional baseline parameters, and functional recovery observed among different treatment groups	138
Figure 6-6: Comparison of baseline and 12-week kinematics for healthy control animals	142
Figure 6-7: Kinematic comparisons between the TEMR and NRFe groups vs. baseline for hip flexion, hip adduction, hip internal rotation, knee flexion, and ankle dorsiflexion at all timepoints.....	143
Figure 6-8: Kinetic comparisons between the TEMR and NRFe groups vs. baseline for hip flexion moment, hip adduction moment, hip internal rotation moment, knee flexion moment, and ankle dorsiflexion moment at all timepoints.....	145
Figure 6-9: Study 2 comparison of body weight, functional baseline parameters, and functional recovery observed among different treatment groups	147
Figure 6-10: Kinematic comparisons between NRMa and baseline at all timepoints.....	152
Figure 6-11: Kinematic comparisons between PPN and baseline at all timepoints	153
Figure 6-12: Kinematic comparisons between TAPoly and baseline at all timepoints.....	154
Figure 6-13: Kinetic comparisons between NRMa and baseline at all timepoints.....	158
Figure 6-14: Kinetic comparisons between PPN and baseline at all timepoints	159
Figure 6-15: Kinetic comparisons between TAPoly and baseline at all timepoints	160
Figure 7-1: Lateral gastrocnemius volumetric muscle loss injury creation.....	184
Figure 7-2: Sciatic nerve branch site and nerve laceration post-repair.....	186
Figure 7-3: Vicon Nexus 3-D overlay of motion capture marker placements.....	188
Figure 7-4: OpenSim rat hindlimb model with zeroed angles and reconstructed marker locations.....	189
Figure 7-5: Comparison of body weights and functional recovery observed among different injury groups	191

Figure 7-6: Kinematic comparisons between LGNR and baseline at all timepoints	196
Figure 7-7: Kinematic comparisons between PTN and baseline at all timepoints	197
Figure 7-8: Kinematic comparisons between LGPoly and baseline at all timepoints.....	198
Figure 7-9: Kinetic comparisons between LGNR and baseline at all timepoints.....	202
Figure 7-10: Kinetic comparisons between PTN and baseline at all timepoints	203
Figure 7-11: Kinetic comparisons between LGPoly and baseline at all timepoints	204
Figure 7-12: Additional illustrations of the complexity of the rat hindlimb posterior compartment	213

List of Tables

Table 1-1: Overview of volumetric muscle loss animal studies	2
Table 1-2: Overview of rat hindlimb volumetric muscle loss studies utilizing hydrogel-based treatment approaches	6
Table 1-3: Overview of rat hindlimb volumetric muscle loss studies utilizing scaffold-based treatment approaches	9
Table 2-1: Overview of studies collecting spatiotemporal parameters.....	20
Table 2-2: Overview of studies collecting ground reaction forces	23
Table 2-3: Overview of studies calculating joint kinematics.....	26
Table 2-4: Overview of studies calculating joint kinetics	30
Table 5-1: Compiled spatiotemporal parameters and morphometric measurements for healthy female Lewis rats.....	105
Table 6-1: Compiled spatiotemporal parameters for the Control animals at baseline and the TEMR and NRFe groups at all timepoints.....	140
Table 6-2: Compiled spatiotemporal parameters for the NRMa, PPN, and TAPoly animals at all timepoints	149
Table 6-3: Ranges of motion for Study 2 kinematic parameters (in degrees)	151
Table 6-4: Peak moments for Study 2 kinetic parameters (in Nm/kg)	157
Table 7-1: Compiled spatiotemporal parameters for LGNR, PTN, and LGPoly animals at all timepoints	193
Table 7-2: Ranges of motion for LGNR, PTN, and LGPoly baseline kinematic parameters (in degrees).....	194
Table 7-3: Peak moments for LGNR, PTN, and LGPoly baseline kinetic parameters (in Nm/kg)	201

Nomenclature

ECM	Extracellular matrix
VML	Volumetric muscle loss
HyA	Hyaluronic acid
TA	Tibialis anterior
LG	Lateral gastrocnemius
AcHyA	Acrylated hyaluronic acid
LMN	Laminin
MG	Muscle graft
ASCs	Adipose-derived stem cells
bFGF	Basic fibroblast growth factor
HGF	Hepatocyte growth factor
IGF-1	Insulin-like growth factor 1
KN	Keratin
BAM	Bladder acellular matrix
MPCs	Muscle progenitor cells
MVF	Microvascular fragments
TEMR	Tissue engineered muscle repair
UBM	Urinary bladder matrix
SIS	Small intestine submucosa
MTJ	Musculotendinous junction
OA	Osteoarthritis
GRFs	Ground reaction forces

EDGAR	Experimental dynamic gait arena for rodents
MCL	Medial collateral ligament
LCL	Lateral collateral ligament
MS	Musculoskeletal
MTP	Metatarsophalangeal
TE	Tissue engineering
RM	Regenerative medicine
dECM	Decellularized extracellular matrix
MMP	Metalloproteinase
ADH	Adipic dihydrazide
EDC	1-Ethyl-3-[3-(dimethylamino)propyl] carbodiimide
NaOH	Sodium hydroxide
HCl	Hydrochloric acid
TCEP	Tris(2-carboxyethyl)phosphine
TEOA	Triethanolamine
HOBt	1-Hydroxybenzotriazole
DMSO	Dimethyl sulfoxide
NAS	N-Acryloxysuccinimide
HMWH	High molecular weight heparin
HyAADH	HyA derivative carrying hydrazide groups
DI	Deionized
EDL	Extensor digitorum longus
EHL	Extensor hallucis longus

H&E	Hematoxylin and eosin
SEM	Standard error of mean
ANOVA	Analysis of variance
LSD	Least significant difference
FCSA	Fiber cross sectional area
LASI	Left anterior superior iliac crest
RASI	Right anterior superior iliac crest
spm	Steps per minute
BW	Body weight

Study Group Abbreviations

NR	Female Lewis rats with TA VML injury with no repair performed
HyA	Female Lewis rats with TA VML injury treated with HyA-based hydrogel
Control	Healthy female Lewis rats with no surgical procedures performed
NRFe	Female Lewis rats with TA VML injury and no repair performed
TEMR	Female Lewis rats with TA VML injury treated with the TEMR construct
NRMa	Male Lewis rats with TA VML injury and no repair performed
PPN	Male Lewis rats with a 50% laceration of the right peroneal nerve with repair
TAPoly	Male Lewis rats with TA VML injury and no repair performed in combination with a repaired 50% right peroneal nerve laceration
LGNR	Male Lewis rats with LG VML injury and no repair performed
PTN	Male Lewis rats with a 50% laceration of the right tibial nerve with repair
LGPoly	Male Lewis rats with LG VML injury and no repair performed in combination with a repaired 50% right tibial nerve laceration

Abstract

Research to develop improved methods for regeneration of functional muscle tissue following volumetric muscle loss (VML) injuries remains an active area of preclinical investigation. Defined as a traumatic or surgical loss of skeletal muscle resulting in permanent cosmetic and functional impairments, VML is a common feature of battlefield injuries to service members as well as civilians who experience high-impact trauma. The critical importance of the unmet medical need, and the lack of availability of therapeutics that can restore form and function after VML, continues to drive innovation in this area of military medicine.

Traditionally, metrics for evaluating therapeutics for VML injuries focus on tissue histology, volume reconstitution, and muscle force generation post-treatment. However, studies in humans have repeatedly demonstrated that there is not a direct relationship between improvements in muscle volume or muscle strength and improvements in functional movement ability. In this work, the primary goal was to move beyond these historically relied upon metrics for VML injury/treatment evaluation and advance into sophisticated gait assessment. Overall, the ability to measure changes in 3D gait parameters, such as joint angles (kinematics) and joint moments (kinetics), provides information on how study animals are functionally utilizing muscle and mechanistic insights into strength, motion planning, and control strategies. These mechanisms define the true operational and functional significance of VML injury and VML repair for lower limb trauma—as suboptimal gait restoration will result in additional post-repair physiological and functional deficits.

With this in mind, in order to better quantify the effects of VML injury and repair on movement function we initially developed a model and methodology to measure the 3D kinematics of rat gait during treadmill walking. We investigated the tibialis anterior (TA) and employed our

motion capture approach to evaluate a 20% VML injury. This initial publication identified significant differences between injured and healthy animals at all post-surgical timepoints. These results were especially relevant considering the low gait impact of the TA, as it is solely responsible for ankle dorsiflexion and toe clearance during swing. We then advanced into a more sophisticated motion capture arena to observe over-ground walking and capture concurrent ground reaction force (GRF) data for 3D inverse dynamic calculation. The TA and the 20% VML injury continued to be the model system, but a treatment was added in the form of the Tissue Engineered Muscle Repair (TEMR) cell-seed porcine bladder construct. Differences were again seen across the board in the VML group, with definitive improvements shown in the TEMR treated animals.

In the second half of this dissertation, this initial work was leveraged into the investigation of increasingly severe injury models. These consisted of two separate VML injuries in different animal groups: the traditional injury to the TA, and a new injury to a major gait contributor in the lateral gastrocnemius (LG). As a two-joint muscle in the posterior compartment, and the primary muscle for energy transfer in the lower limb during gait, the functionality of the LG is critical for movement. These injury models were extended to groups of animals receiving partial lacerations of the tibial nerve and peroneal nerve, as well as animals receiving muscle-nerve polytraumas consisting of VML injury combined with laceration to the upstream nerve associated with the injured muscle. It was here that the ultimate value of biomechanical analysis truly shined, providing insight into injury response and compensation patterns that would otherwise be hidden to investigators.

Altogether, this work represents the culmination of an idea to dig deeper into injury compensation and recovery metrics in order to achieve a deeper understanding of the biomechanical impacts of VML injury and repair. In short, the ability to perform kinetic analysis

allows for novel mechanistic insight into the inner workings of muscle compartments in response to traumatic injuries. This analysis will improve the design/evaluation of regenerative therapeutics for VML injuries by identifying the contributions and compensations in the complex muscle compartments that are the target of battlefield relevant injuries. The results of these studies demonstrate that it is possible to extract an incredible amount of information about injury response and recovery using 3D gait analysis, thereby allowing investigators to improve timelines and regenerative technologies to maximize functional returns and limit pathological compensation.

Chapter 1 – Introduction to Skeletal Muscle Tissue Engineering and Regeneration

Introduction

Skeletal muscle makes up the majority of the muscle tissue in the human body^{1,2}, and consists of a complex network of highly innervated and vascularized tissue embedded in an extremely well-organized extracellular matrix (ECM). For normal muscle function and maximum efficiency, it is necessary for all of these components to be present and operating at their full capacity³. However, because skeletal muscle is so abundantly present in our extremities, injuries resulting in muscle damage are incredibly common. In sports specifically, muscle injuries comprise roughly 55% of all injuries incurred⁴⁻⁷. Fortunately, skeletal muscle has a substantial inherent regenerative capacity for self-healing after injury. But despite the fact that the majority of muscular injuries are contusions or strains that heal without intervention, there are a range of congenital conditions or inflicted traumas that can occur and result in such a volume of skeletal muscle loss that it exceeds that natural capacity for recovery⁸ (i.e. compound fractures, high-grade muscle tears, high-impact collision injuries). These injuries and conditions are labeled as volumetric muscle loss (VML) or VML-like injuries, frequently result in permanent cosmetic and functional deficits, and are characterized by the multi-level loss of tissue components (i.e. muscle, nerve, vessel, and ECM).

In general, there are no widely effective treatment options for VML scenarios at this time. Surgical reconstruction methods like muscle flap transfer are frequently ineffective, often leading to incomplete functional recovery and donor site morbidity. There is, however, a significant amount of promising research underway to develop treatments to restore the cosmetic integrity and functional capacity of the affected muscle. To date, the majority of this research has focused on the regenerative potential of hydrogel and scaffold-based biomaterials. As such, the research

performed as part of this dissertation focused on the same areas: a hyaluronic acid (HyA) based hydrogel and a cell seeded porcine bladder-based scaffold for use as treatment for VML injuries. Across the field of VML therapeutic research, there have been a variety of animals and model systems evaluated (see **Table 1-1**). This work has primarily been conducted in the rat hindlimb, but other studies on mice, pigs, dogs, and rabbits can be found in the literature.

Table 1-1: Overview of volumetric muscle loss animal studies

Author	Species	Muscle
Aguilar, et al ¹⁹	Male Lewis rats	Tibialis anterior
Greising, et al ²⁰	Male Lewis rats	Tibialis anterior
Aurora, et al ¹⁸	Male Lewis rats	Gastrocnemius musculotendinous junction (MTJ)
Aurora, et al ¹⁸	Male Lewis rats	Tibialis anterior
Corona, et al ²¹	Male Lewis rats	Tibialis anterior
Corona, et al ²²	Male Lewis rats	Tibialis anterior
Corona, et al ²³	Female Lewis rats	Tibialis anterior
Pollot, et al ²⁴	Male Lewis rats	Tibialis anterior
Goldman, et al ²⁵	Male Lewis rats	Tibialis anterior
De Coppi, et al ²⁶	Female Lewis rats	Core muscles (abdominal wall)
Passipieri, et al ²⁷	Female Lewis rats	Tibialis anterior
Merritt, et al ¹⁶	Male Lewis rats	Gastrocnemius
Pilia, et al ²⁸	Male Lewis rats	Tibialis anterior
Dienes, et al ¹²	Female Lewis rats	Tibialis anterior
Mintz, et al ²⁹	Male Lewis rats	Tibialis anterior
Passipieri, et al ³⁰	Male Lewis rats	Tibialis anterior
Kim, et al ³¹	Fischer 344 rats	Tibialis anterior
Vega-Soto, et al ³²	Female Fischer 344 rats	Tibialis anterior
Merritt, et al ¹⁵	Male Sprague-Dawley rats	Gastrocnemius
Huang, et al ³³	Male Sprague-Dawley rats	Tibialis anterior
Hagiwara, et al ¹⁷	Sprague-Dawley rats	Gastrocnemius

Ju, et al ³⁴	Sprague-Dawley rats	Tibialis anterior
Conconi, et al ³⁵	Male Sprague-Dawley rats	Core muscles (obliquus externus abdominis, obliquus internus abdominis)
Qiu, et al ³⁶	Sprague-Dawley rats	Tibialis anterior
Zhou, et al ³⁷	Female Sprague-Dawley rats	Unspecified back muscle
Natsu, et al ³⁸	Male Sprague-Dawley rats	Tibialis anterior
Greising, et al ³⁹	Male C5BL/6 mice	Gastrocnemius
Sicari, et al ⁹	Female C57BL/6 mice	Quadriceps (tensor fasciae latae, rectus femoris)
Matthias, et al ⁴⁰	NOD.Cg-Prkdc ^{scid} Il2rg ^{tm1Wjl} /SzJ mice	Tibialis anterior
Anderson, et al ⁴¹	Female C57BL/6J mice	Quadriceps (rectus femoris, vastus intermedius, vastus lateralis, vastus medialis)
Anderson, et al ⁴²	Female C57BL/6J mice	Quadriceps (rectus femoris, vastus intermedius, vastus lateralis, vastus medialis)
Nakayama, et al ⁴³	NOD-SCID mice	Tibialis anterior
Grasman, et al ⁴⁴	SHO-SCID mice	Tibialis anterior
Corona, et al ⁴⁵	Nu/nu mice	Latissimus dorsi
Rossi, et al ⁴⁶	C57BL/6J mice	Tibialis anterior
Page, et al ⁴⁷	Female nude SHO-SCID mice	Tibialis anterior
Ma, et al ⁴⁸	C57BL/6J mice	Gastrocnemius
Ma, et al ⁴⁸	SCID mice	Gastrocnemius
Ma, et al ⁴⁸	<i>mdx</i> /SCID mice	Gastrocnemius
Machingal, et al ⁴⁹	Female nu/nu mice	Latissimus dorsi
Kroehne, et al ⁵⁰	C57BL/6 Cr Slc TgN(act-EGFP) OsbC15-001-FJ001 mice crossed with NMRI- <i>nu</i> mice	Tibialis anterior
Corona, et al ⁵¹	Female Yorkshire Cross pigs	Peroneus tertius
Chao, et al ⁵²	Female Yorkshire Cross pigs	Peroneus tertius
Greising, et al ²⁰	Female Yorkshire Cross pigs	Peroneus tertius
Ward, et al ⁵³	Female Yorkshire Cross pigs	Peroneus tertius
Turner, et al ⁵⁴	Female dogs	Quadriceps (vastus lateralis, vastus medialis)
Turner, et al ⁵⁵	Female dogs	Gastrocnemius
Kin, et al ⁵⁶	Male rabbits	Quadriceps (vastus lateralis)

For the purposes of the work presented in this dissertation, the Lewis rat hindlimb was used as the model system. Our early work consisted of modeling VML injuries (see **Figure 1-1**) in the tibialis anterior (TA), and that work was leveraged in the later years to advance to a significantly more complex injury model in the lateral gastrocnemius (LG). The biological relevance of the TA VML injury has been very well characterized⁹⁻¹¹, and the rat TA model of VML is a well-reasoned choice for evaluation because methods for the evaluation of the effect of injury/treatment have been thoroughly established¹⁰⁻¹⁴. The rat LG has been a significantly less studied model for VML injury¹⁵⁻¹⁸, but offers novel opportunities to evaluate the impact of VML injury on a multi-joint muscle in the complex posterior compartment.

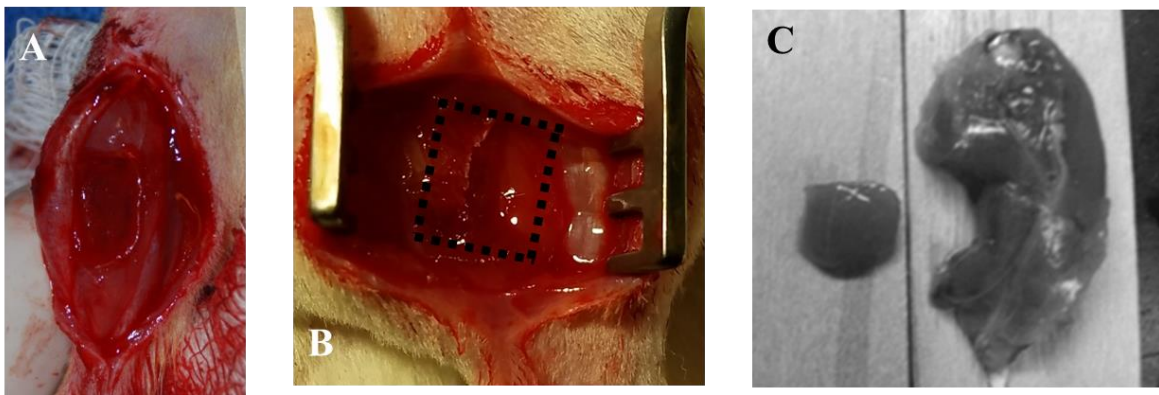


Figure 1-1: Representative images of VML injuries (A) TA VML injury (B-C¹⁵) LG VML injury. Panel C adapted from Merritt et al [2010a] with permission from publisher copyright office (Mary Ann Liebert).

In the following sections, overviews will be presented of the published research evaluating hydrogel-based and scaffold-based technologies for the treatment of VML injuries specific to the rat hindlimb model system.

Hydrogel-based Approaches for VML

Complete recovery from VML or VML-like injuries involves restoration of both form and function to the injured tissue. Beyond remodeling of the muscle, this requires *de novo* innervation and vascularization in the regenerated tissue. Hydrogel-based regenerative technologies offer distinct angiogenic and growth factor recruiting properties that contribute to the recovery of healthy and functional muscle. The acrylated HyA (AcHyA) gel matrix used for the study included in this dissertation (see **Chapter 3**) has previously been shown to promote vascular network formation *in vitro* and *in vivo*, though the angiogenic effects were highly dependent on MMP crosslinker degradation kinetics⁵⁷. In addition to promoting angiogenesis^{58,59}, HyA has also been shown to encourage donor cell integration with the host tissue⁶⁰. A number of studies have also demonstrated that heparin has the ability to sequester and release exogenously added growth factors to ultimately improve wound healing and tissue regeneration⁶¹⁻⁶⁶, so the AcHyA used for our study was complexed with thiolated heparin. Combined, the potential relevance of HyA hydrogels to skeletal muscle regeneration is apparent, and further, these materials have been shown to significantly improve donor survival after transplantation⁶⁷.

As a material overall, HyA based hydrogels have shown varying outcomes^{20,25}, but generally HyA treated groups outperform unrepaired (no repair, NR) groups in muscle isometric force testing (see **Table 1-2**).

Table 1-2: Overview of rat hindlimb volumetric muscle loss studies utilizing hydrogel-based treatment approaches

Author	Species	Muscle	Treatment	Outcome
Greising, et al ²⁰	Male Lewis rats	Tibialis anterior	HyA hydrogel	HyA slightly outperformed NR but significantly underperformed vs. sham in function testing
Goldman, et al ²⁵	Male Lewis rats	Tibialis anterior	HyA hydrogel +/-muscle graft (MG), laminin (LMN)	All groups significantly underperformed as compared to contralateral in function testing, in order: NR, HyA-alone, HyA+LMN, 50% MG+HyA, 50% MG+HyA+LMN; last two were significantly better than NR, HyA-alone, and HyA+LMN groups.
Dienes, et al	Female Lewis rats	Tibialis anterior	HyA hydrogel	HyA outperformed NR animals in functional testing, resulting muscle tissues showed notable cosmetic recovery
Huang, et al ³³	Male Sprague-Dawley rats	Tibialis anterior	Adipose-derived stem cells (ASCs) + collagen hydrogel	Accelerated muscle repair and regeneration, increased transition of M2 macrophages
Hagiwara, et al ¹⁷	Sprague-Dawley rats	Gastrocnemius	Gelatin hydrogel + bFGF	Improvement in implanted myoblast survival rate, myogenesis, and angiogenesis at 4 weeks post-injury
Ju, et al ³⁴	Sprague-Dawley rats	Tibialis anterior	Gelatin hydrogel + HGF, IGF-1, OR bFGF	Increased Pax7+ cells at 2 weeks in the IGF-1 animals, increased number of muscle fibers and centrally located nuclei in all groups
Passipieri, et al ²⁷	Female Lewis rats	Tibialis anterior	Keratin (KN) hydrogel +/- bladder acellular matrix (BAM), IGF-1, bFGF, muscle progenitor cells (MPCs)	NR and BAM performed the same in function testing at 12 weeks, followed by (increasing force): KN, KN+IGF-1, KN+bFGF, KN+IGF-1+bFGF
Qiu, et al ³⁶	Sprague-Dawley rats	Tibialis anterior	Porcine heart ECM +/- MPCs in collagen gel	ECM+MSC far outperformed other treatments in function testing at 8 weeks, ECM and MSC alone outperformed NR but not significantly
Natsu, et al ³⁸	Male Sprague-Dawley rats	Tibialis anterior	Fibrin hydrogel +/- bone marrow-derived MPCs	All groups produced >90% of contralateral force by 12 weeks
Pilia, et al ²⁸	Male Lewis rats	Tibialis anterior	Collagen hydrogel +/- ASCs or microvascular fragments (MVF)	MVF had highest level of vessel density within the defect at 2 weeks, but vessel perfusion was low in all groups

Greising and Goldman showed a reduced functional recovery compared to our own work (**Chapter 3**), but this is likely due to differences in the injury model. Greising utilized a full thickness VML injury and Goldman created a 6mm diameter injury with a punch, leading to the interruption of far more end-to-end muscle fibers in their injuries than what is typical for the divot-type injuries historically created by our group^{12,27,29,68}. We saw a ~20% deficit in our HyA-treated TA muscles by 12 weeks with significant recovery of muscle form using an AcHyA gel complexed with heparin for endogenous growth factor recruitment. Goldman saw a ~45% deficit in their HyA-alone treated group, but saw a ~25% deficit in their HyA+50% minced muscle grafts+laminin-111 treated animals. Lastly, Greising saw a ~35% force deficit in all their study groups, which included NR animals, two different acellular matrix treated groups (small intestine submucosa and urinary bladder matrix, discussed further below), and HyA treated. The lack of any notable differences in the Greising study is suspicious, but is likely due to the extent of the VML injury they created with a full thickness defect.

Beyond these studies, multiple groups have investigated the therapeutic effects of hydrogel-based treatments for VML injuries in the rat hindlimb (see **Table 1-2**), with many of these treatments showing positive results at terminal timepoints. Beyond HyA, groups have investigated gelatin^{17,34}, keratin²⁷, fibrin³⁸, and collagen^{28,33,36} as the basis for their hydrogel matrix. Few of these studies included rigorous force testing, but keratin and fibrin were reported to provide substantial functional recovery. Gelatin and collagen-based hydrogels did not report force testing results but led to increases in other quantifiable areas such as angiogenesis¹⁷, M2 macrophage transition³³, and presence of Pax7+ cells³⁴. Collagen was also reported to increase vessel density in the injury site when complexed with microvascular fragments, but the perfusion through these vessels was very poor²⁸.

As a whole, hydrogel technologies offer a wide array of tunable properties as well as the capability to fill any injury geometry. When complexed with the proper growth factors, it is apparent that the possibilities for the regenerative capacity of hydrogel-based treatments for VML is very high. It is clear, however, that limited studies have occurred in clinically relevant injury models such as the rat hindlimb. In order to validate the capabilities of these technologies, it will be necessary to expand both the volume of preclinical studies evaluating hydrogels as treatment for VML as well as advance the injury models to animals (i.e. pigs) where the VML injuries are size-matched to those that would be seen in humans.

Scaffold-based Approaches for VML

Despite the numerous gel foundations that have been investigated for treatment of VML injury, there is a distinct lack of emphasis on measuring physiologically relevant functional outcomes in the literature. Conveniently, the second form of VML treatment evaluated in this dissertation was the tissue-engineered muscle repair construct (TEMR), and work performed utilizing similar scaffold-based technologies (**Table 1-3**) relies heavily on force testing (**Figure 1-2**) and functional outcomes as a metric for treatment efficacy. While regenerated muscle form and histological analysis of tissues is still of high importance for evaluating these constructs, the inclusion of the force testing data incorporates a significant metric and answers one of the most important questions: does the muscle produce a high enough degree of contractile force after treatment?

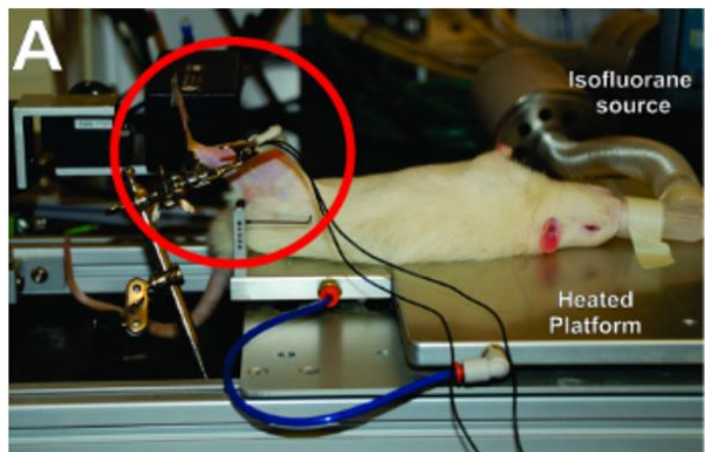


Figure 1-2: Force testing rig and rat orientation for TA testing¹³ (Figure adapted from Mintz et al [2016] with permission from journal copyright office, *JOVE*)

Table 1-3: Overview of rat hindlimb volumetric muscle loss studies utilizing scaffold-based treatment approaches

Author	Species	Muscle	Treatment	Outcome
Aurora, et al ¹⁸	Male Lewis rats	Gastrocnemius MTJ	MatriStem Surgical Matrix PSMX (porcine urinary bladder matrix, UBM)	60% isometric torque deficit at 4-weeks, not mitigated by repair
Aurora, et al ¹⁸	Male Lewis rats	Tibialis anterior	Porcine UBM or autograft	Autograft outperformed UBM, UBM did not outperform no-repair (NR) by 16 weeks
Corona, et al ²²	Male Lewis rats	Tibialis anterior	Syngeneic muscle derived ECM	Treated animals showed a slight functional improvement at 2/4 months, but no difference compared to NR at 6 months
Corona, et al ²³	Female Lewis rats	Tibialis anterior	Tissue engineered muscle repair construct (TEMR) and bladder acellular matrix (BAM)	Some TEMR outperformed BAM at 12 weeks, some underperformed as compared to BAM and NR at same timepoint
Greising, et al ²⁰	Male Lewis rats	Tibialis anterior	Porcine UBM or decellularized small intestine submucosa (SIS)	No difference at 10-weeks between UBM, SIS, or NR animals
Kim, et al ³¹	Fischer 344 rats	Tibialis anterior	Muscle plugs with varying alignment (0, 45, 90 degrees)	Alignment significantly impacts recovery: 0 degrees performed best vs. control (~77%), followed by 45 (64%) and 90 (61%) degrees.
Pollot, et al ²⁴	Male Lewis rats	Tibialis anterior	SIS-ECM	No statistical difference between NR and SIS-ECM animals at 6-weeks
Mintz, et al ²⁹	Male Lewis rats	Tibialis anterior	TEMR	Positive and negative responders to treatment, positive responders exhibited significant functional recovery (~70% of baseline) at 24 weeks
Passipieri, et al ³⁰	Male Lewis rats	Tibialis anterior	TEMR	Substantial tissue regeneration and functional recovery by 12 weeks in treated animals

The TEMR construct^{23,45,49} (**Figure 1-3**, discussed in detail in **Chapter 4**) consists of porcine urinary bladder lamina propria, which is then cell-seeded and mechanically stretched for five days in a custom-designed bioreactor.

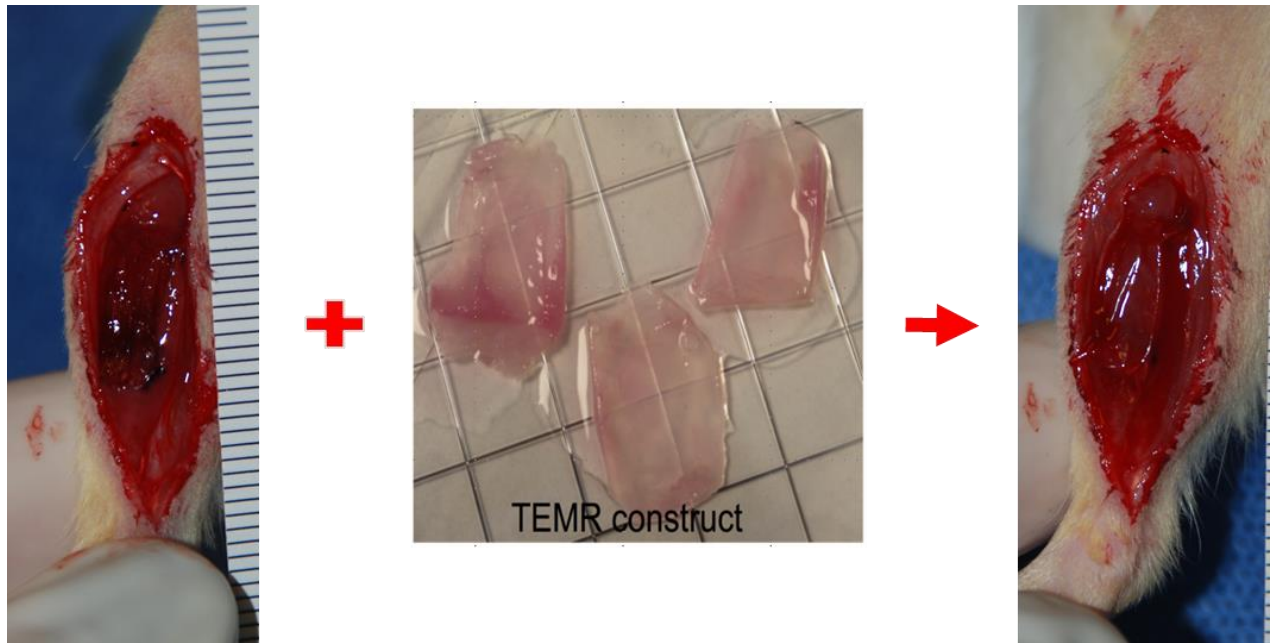


Figure 1-3: Representative VML injury creation, TEMR construct, and TEMR application.

The TEMR treatment, and others utilizing this scaffold-based design, leverages the existing tissue environment at the injury site to recruit endogenous growth factors and provide a structured framework for the adhesion and expansion of developing muscle tissue⁶⁹. As mentioned, the TEMR construct is seeded with cells (muscle progenitor cells, MPCs) but multiple acellular technologies have also been tested. Unfortunately, these acellular treatments have consistently shown little to no ability to improve functional outcomes as compared to untreated animals^{18,20,22,24}. The lack of a cellular component appears to primarily result in fibrosis within the defect site with a notable absence of *de novo* muscle tissue.

The addition of cells (as in the TEMR construct) generally results in a significant improvement in functional outcomes. Though TEMR treated animals have shown a propensity to

divide into positive and negative responders to the treatment^{23,29}, the positive responders have shown significant increases in force production ability as compared to both untreated animals and those treated with acellular matrix. While there is no immediately apparent reason for the split in responses within the treated groups, there is no doubt that in many cases the addition of the cellular component makes a massive difference in the functional recovery. The TEMR is specifically seeded with MPCs isolated from young donor rats, which are then provided with mechanical cues via bioreactor preconditioning to trigger differentiation. These cues result in myoblast fusion and myotube formation on the physical construct prior to implantation in the injury site. The myofibers align in the direction of the mechanical stretching and can then be oriented with the existing muscle fibers in the native tissue. Cell addition is not limited to MPCs though, as bone marrow derived mesenchymal cells have been utilized by multiple groups and have also resulted in favorable functional outcomes^{16,38} for rat VML injuries.

The model system utilized for evaluating scaffold-based treatments for VML injury in the rat hindlimb has primarily been the TA, though one group did investigate the gastrocnemius musculotendinous junction (MTJ)¹⁸. In this dissertation work, we also utilized the TA to investigate the efficacy of the TEMR construct on VML injuries (**Chapter 6**). Additionally, we laid the foundation for future studies into the impact of the TEMR construct on LG VML injuries (**Chapter 7**), as well as muscle-nerve polytrauma injuries in both the TA (**Chapter 6**) and the LG (**Chapter 7**). Though the utility of the TEMR construct to treat TA VML injuries has been well-established, expanding this approach to a far more complex injury in the LG is a significant step for both VML injury models and the range of effectiveness for the TEMR construct. Beyond the fact that the LG is a two-joint muscle (knee and ankle), the injury geometry is vastly different (see **Figure 1-1**). While the TA VML injury resembles a divot scooped from the muscle belly, the LG

injury is through the full thickness of the muscle. This results in fewer points of contact between the TEMR and the muscle, while also removing the ability of the TEMR to lay neatly in the defect site. These differences will undoubtedly make the LG VML injury more difficult to treat, but they also represent a step towards a higher physiological relevance in the injury model due to increased resemblance to blast injuries or other high-impact traumas.

References

1. Huard, J., Li, Y. & Fu, F. H. Muscle injuries and repair: Current trends in research. *Journal of Bone and Joint Surgery - Series A* **84**, 822–832 (2002).
2. Wang, J. *et al.* Engineered skeletal muscles for disease modeling and drug discovery. *Biomaterials* **221**, 119416 (2019).
3. Passipieri, J. A. & Christ, G. J. The Potential of Combination Therapeutics for More Complete Repair of Volumetric Muscle Loss Injuries: The Role of Exogenous Growth Factors and/or Progenitor Cells in Implantable Skeletal Muscle Tissue Engineering Technologies. *Cells. Tissues. Organs* **202**, 202–213 (2016).
4. Beiner, J. M. & Jokl, P. Muscle contusion injuries: current treatment options. *The Journal of the American Academy of Orthopaedic Surgeons* **9**, 227–237 (2001).
5. Garrett, W. J. Muscle strain injuries. *Am J Sport. Med* **24**, 2–8 (1996).
6. Counsel, P. & Breidahl, W. Muscle injuries of the lower leg. *Semin. Musculoskelet. Radiol.* **14**, 162–175 (2010).
7. Järvinen, T. A. H., Järvinen, T. L. N., Kääriäinen, M., Kalimo, H. & Järvinen, M. Muscle Injuries. *Am. J. Sports Med.* **33**, 745–764 (2005).
8. Grogan, B. F. & Hsu, J. R. Volumetric muscle loss. *J. Am. Acad. Orthop. Surg.* **19 Suppl 1**, S35-7 (2011).
9. Sicari, B. M. *et al.* A murine model of volumetric muscle loss and a regenerative medicine approach for tissue replacement. *Tissue Eng. Part A* **18**, 1941–8 (2012).
10. Wu, X., Corona, B. T., Chen, X. & Walters, T. J. A Standardized Rat Model of Volumetric Muscle Loss Injury for the Development of Tissue Engineering Therapies. *Biores. Open Access* **1**, 280–290 (2012).
11. Aurora, A., Garg, K., Corona, B. T. & Walters, T. J. Physical rehabilitation improves muscle function following volumetric muscle loss injury. *BMC Sport. Sci. Med. Rehabil.* **6**, 41 (2014).
12. Dienes, J. A. *et al.* Analysis and Modeling of Rat Gait Biomechanical Deficits in Response to Volumetric Muscle Loss Injury. *Front. Bioeng. Biotechnol.* **7**, 146 (2019).
13. Mintz, E. L., Passipieri, J. A., Lovell, D. Y. & Christ, G. J. Applications of In Vivo Functional Testing of the Rat Tibialis Anterior for Evaluating Tissue Engineered Skeletal Muscle Repair. *J Vis Exp* (2016).
14. Corona, B. T., Rivera, J. C., Owens, J. G., Wenke, J. C. & Rathbone, C. R. Volumetric muscle loss leads to permanent disability following extremity trauma. *J. Rehabil. Res. Dev.* **52**, 785–792 (2015).
15. Merritt, E. K. *et al.* Functional assessment of skeletal muscle regeneration utilizing homologous extracellular matrix as scaffolding. *Tissue Eng. Part A* **16**, 1395–405 (2010).
16. Merritt, E. K. *et al.* Repair of traumatic skeletal muscle injury with bone-marrow-derived

- mesenchymal stem cells seeded on extracellular matrix. *Tissue Eng. Part A* **16**, 2871–81 (2010).
17. Hagiwara, K., Chen, G., Kawazoe, N., Tabata, Y. & Komuro, H. Promotion of muscle regeneration by myoblast transplantation combined with the controlled and sustained release of bFGFcp. *J. Tissue Eng. Regen. Med.* **10**, 325–333 (2016).
 18. Aurora, A., Roe, J. L., Corona, B. T. & Walters, T. J. An acellular biologic scaffold does not regenerate appreciable de novo muscle tissue in rat models of volumetric muscle loss injury. *Biomaterials* **67**, 393–407 (2015).
 19. Aguilar, C. A. *et al.* Multiscale analysis of a regenerative therapy for treatment of volumetric muscle loss injury. *Cell Death Discov.* **4**, 1–11 (2018).
 20. Greising, S. M. *et al.* Unwavering Pathobiology of Volumetric Muscle Loss Injury. *Sci. Rep.* **7**, 1–14 (2017).
 21. Corona, B. T. *et al.* Autologous minced muscle grafts: a tissue engineering therapy for the volumetric loss of skeletal muscle. *Am. J. Physiol. Physiol.* **305**, C761–C775 (2013).
 22. Corona, B. T. *et al.* The promotion of a functional fibrosis in skeletal muscle with volumetric muscle loss injury following the transplantation of muscle-ECM. *Biomaterials* **34**, 3324–3335 (2013).
 23. Corona, B. T., Ward, C. L., Baker, H. B., Walters, T. J. & Christ, G. J. Implantation of In Vitro Tissue Engineered Muscle Repair Constructs and Bladder Acellular Matrices Partially Restore In Vivo Skeletal Muscle Function in a Rat Model of Volumetric Muscle Loss Injury. *Tissue engineering. Part A* **20**, 705–15 (2014).
 24. Pollot, B. E., Goldman, S. M., Wenke, J. C. & Corona, B. T. Decellularized extracellular matrix repair of volumetric muscle loss injury impairs adjacent bone healing in a rat model of complex musculoskeletal trauma. *J. Trauma Acute Care Surg.* **81**, S184–S190 (2016).
 25. Goldman, S. M., Henderson, B. E. P., Walters, T. J. & Corona, B. T. Co-delivery of a laminin-111 supplemented hyaluronic acid based hydrogel with minced muscle graft in the treatment of volumetric muscle loss injury. *PLoS One* **13**, e0191245 (2018).
 26. De Coppi, P. *et al.* Myoblast-acellular skeletal muscle matrix constructs guarantee a long-term repair of experimental full-thickness abdominal wall defects. *Tissue Eng.* **12**, 1929–1936 (2006).
 27. Passipieri, J. A. *et al.* Keratin Hydrogel Enhances In Vivo Skeletal Muscle Function in a Rat Model of Volumetric Muscle Loss. *Tissue Eng. Part A* **23**, 556–571 (2017).
 28. Pilia, M. *et al.* Transplantation and perfusion of microvascular fragments in a rodent model of volumetric muscle loss injury. *Eur. Cells Mater.* **28**, 11–24 (2014).
 29. Mintz, E. L. *et al.* Long-Term Evaluation of Functional Outcomes Following Rat Volumetric Muscle Loss Injury and Repair. *Tissue Eng. Part A* **26**, 140–156 (2020).
 30. Passipieri, J. A. *et al.* In Silico and In Vivo Studies Detect Functional Repair Mechanisms

- in a Volumetric Muscle Loss Injury. *Tissue Eng. Part A* ten.tea.2018.0280 (2019). doi:10.1089/ten.tea.2018.0280
31. Kim, J. *et al.* Graft alignment impacts the regenerative response of skeletal muscle after volumetric muscle loss in a rat model. *Acta Biomater.* **105**, 191–202 (2020).
 32. Vega-Soto, E. E., Rodriguez, B. L., Armstrong, R. E. & Larkin, L. M. A 30% Volumetric Muscle Loss Does Not Result in Sustained Functional Deficits After a 90-Day Recovery in Rats. *Regen. Eng. Transl. Med.* **6**, 62–68 (2020).
 33. Huang, H. *et al.* Preferred M2 Polarization by ASC-Based Hydrogel Accelerated Angiogenesis and Myogenesis in Volumetric Muscle Loss Rats. *Stem Cells Int* **2017**, 2896874 (2017).
 34. Ju, Y. M., Atala, A., Yoo, J. J. & Lee, S. J. In situ regeneration of skeletal muscle tissue through host cell recruitment. *Acta Biomater.* **10**, 4332–4339 (2014).
 35. Conconi, M. T. *et al.* Homologous muscle acellular matrix seeded with autologous myoblasts as a tissue-engineering approach to abdominal wall-defect repair. *Biomaterials* **26**, 2567–2574 (2005).
 36. Qiu, X. *et al.* Mesenchymal stem cells and extracellular matrix scaffold promote muscle regeneration by synergistically regulating macrophage polarization toward the M2 phenotype. *Stem Cell Res. Ther.* **9**, 88 (2018).
 37. Zhou, W. *et al.* Angiogenic gene-modified myoblasts promote vascularization during repair of skeletal muscle defects. *J. Tissue Eng. Regen. Med.* **9**, 1404–1416 (2015).
 38. Natsu, K. *et al.* Allogeneic bone marrow-derived mesenchymal stromal cells promote the regeneration of injured skeletal muscle without differentiation into myofibers. *Tissue Eng.* **10**, 1093–1112 (2004).
 39. Greising, S. M. *et al.* Early rehabilitation for volumetric muscle loss injury augments endogenous regenerative aspects of muscle strength and oxidative capacity. *BMC Musculoskelet. Disord.* **19**, 173 (2018).
 40. Matthias, N. *et al.* Volumetric muscle loss injury repair using in situ fibrin gel cast seeded with muscle-derived stem cells (MDSCs). *Stem Cell Res.* **27**, 65–73 (2018).
 41. Anderson, S. E. *et al.* Determination of a critical size threshold for volumetric muscle loss in the mouse quadriceps. *Tissue Eng. - Part C Methods* **25**, 59–70 (2019).
 42. Anderson, S. E. *et al.* Muscle Stem Cell Niche Dysregulation in Volumetric Muscle Loss Injury. *bioRxiv* 346395 (2018). doi:10.1101/346395
 43. Nakayama, K. H. *et al.* Treatment of volumetric muscle loss in mice using nanofibrillar scaffolds enhances vascular organization and integration. *Commun. Biol.* **2**, 1–16 (2019).
 44. Grasman, J. M., Do, D. M., Page, R. L. & Pins, G. D. Rapid release of growth factors regenerates force output in volumetric muscle loss injuries. *Biomaterials* **72**, 49–60 (2015).
 45. Corona, B. T. *et al.* Further development of a tissue engineered muscle repair construct in

- vitro for enhanced functional recovery following implantation in vivo in a murine model of volumetric muscle loss injury. *Tissue Eng. Part A* **18**, 1213–28 (2012).
46. Rossi, C. A. *et al.* In vivo tissue engineering of functional skeletal muscle by freshly isolated satellite cells embedded in a photopolymerizable hydrogel. *FASEB J.* **25**, 2296–2304 (2011).
 47. Page, R. L. *et al.* Restoration of skeletal muscle defects with adult human cells delivered on fibrin microthreads. *Tissue Eng. Part A* **17**, 2629–40 (2011).
 48. Ma, J., Holden, K., Zhu, J., Pan, H. & Li, Y. The Application of Three-Dimensional Collagen-Scaffolds Seeded with Myoblasts to Repair Skeletal Muscle Defects. *J Biomed Biotechnol* **2011**, 812135 (2011).
 49. Machingal, M. A. *et al.* A Tissue-Engineered Muscle Repair Construct for Functional Restoration of an Irrecoverable Muscle Injury in a Murine Model. *Tissue Eng. Part A* **17**, 2291–2303 (2011).
 50. Kroehne, V. *et al.* Use of a novel collagen matrix with oriented pore structure for muscle cell differentiation in cell culture and in grafts. *J. Cell. Mol. Med.* **12**, 1640–1648 (2008).
 51. Corona, B. T., Rivera, J. C. & Greising, S. M. Inflammatory and Physiological Consequences of Debridement of Fibrous Tissue after Volumetric Muscle Loss Injury. *Clin. Transl. Sci.* **11**, 208–217 (2018).
 52. Chao, T., Burmeister, D. M., Corona, B. T. & Greising, S. M. Oxidative pathophysiology following volumetric muscle loss injury in a porcine model. *J. Appl. Physiol.* **126**, 1541–1549 (2019).
 53. Ward, C. L. *et al.* Autologous minced muscle grafts improve muscle strength in a porcine model of volumetric muscle loss injury. in *Journal of Orthopaedic Trauma* **30**, e396–e403 (Lippincott Williams and Wilkins, 2016).
 54. Turner, N. J., Badylak, J. S., Weber, D. J. & Badylak, S. F. Biologic Scaffold Remodeling in a Dog Model of Complex Musculoskeletal Injury. *J. Surg. Res.* **176**, 490–502 (2012).
 55. Turner, N. J. *et al.* Xenogeneic extracellular matrix as an inductive scaffold for regeneration of a functioning musculotendinous junction. *Tissue Eng. Part A* **16**, 3309–17 (2010).
 56. Kin, S. *et al.* Regeneration of skeletal muscle using in situ tissue engineering on an acellular collagen sponge scaffold in a rabbit model. *ASAIO J.* **53**, 506–513 (2007).
 57. Jha, A. K. *et al.* Matrix metalloproteinase-13 mediated degradation of hyaluronic acid-based matrices orchestrates stem cell engraftment through vascular integration. *Biomaterials* **89**, 136–147 (2016).
 58. Park, D. *et al.* Hyaluronic acid promotes angiogenesis by inducing RHAMM-TGF β receptor interaction via CD44-PKC δ . *Mol. Cells* **33**, 563–574 (2012).
 59. Pardue, E. L., Ibrahim, S. & Ramamurthi, A. Role of hyaluronan in angiogenesis and its utility to angiogenic tissue engineering. *Organogenesis* **4**, 203–14 (2008).

60. Calve, S., Isaac, J., Gumucio, J. P. & Mendias, C. L. Hyaluronic acid, HAS1, and HAS2 are significantly upregulated during muscle hypertrophy. *Am. J. Physiol. Physiol.* **303**, C577–C588 (2012).
61. Sakiyama-Elbert, S. E. & Hubbell, J. A. Development of fibrin derivatives for controlled release of heparin-binding growth factors. *J. Control. Release* **65**, 389–402 (2000).
62. Sakiyama-Elbert, S. E. & Hubbell, J. A. Controlled release of nerve growth factor from a heparin-containing fibrin-based cell ingrowth matrix. *J. Control. Release* **69**, 149–58 (2000).
63. Pike, D. B. *et al.* Heparin-regulated release of growth factors in vitro and angiogenic response in vivo to implanted hyaluronan hydrogels containing VEGF and bFGF. *Biomaterials* **27**, 5242–5251 (2006).
64. Cai, S., Liu, Y., Zheng Shu, X. & Prestwich, G. D. Injectable glycosaminoglycan hydrogels for controlled release of human basic fibroblast growth factor. *Biomaterials* **26**, 6054–6067 (2005).
65. Yang, J. *et al.* Heparin-Binding Epidermal Growth Factor-Like Growth Factor and Mesenchymal Stem Cells Act Synergistically to Prevent Experimental Necrotizing Enterocolitis. *J. Am. Coll. Surg.* **215**, 534–545 (2012).
66. Prokoph, S. *et al.* Sustained delivery of SDF-1 α from heparin-based hydrogels to attract circulating pro-angiogenic cells. *Biomaterials* **33**, 4792–4800 (2012).
67. Jha, A. K. *et al.* Enhanced survival and engraftment of transplanted stem cells using growth factor sequestering hydrogels. *Biomaterials* **47**, 1–12 (2015).
68. Wu, X., Corona, B. T., Chen, X. & Walters, T. J. A standardized rat model of volumetric muscle loss injury for the development of tissue engineering therapies. *Biores. Open Access* **1**, 280–90 (2012).
69. Passipieri, J. A. & Christ, G. J. The potential of combination therapeutics for more complete repair of volumetric muscle loss injuries: The role of exogenous growth factors and/or progenitor cells in implantable skeletal muscle tissue engineering technologies. *Cells Tissues Organs* **202**, 202–213 (2016).

Chapter 2 – Introduction to Rodent Motion Capture and Gait Analysis

Introduction

The rat hindlimb is a highly utilized model system used to study pathologies spanning volumetric muscle loss (VML)¹⁻⁴, nerve injury⁵⁻⁸, ligament injury⁹⁻¹², and osteoarthritis (OA)¹³⁻¹⁵. There is a significant amount of research underway to develop treatments for these pathologies with an emphasis on functional improvements. To date, the methods for evaluating this recovery have primarily focused on the force production ability of the hindlimb and histological analysis. However, studies of human movement have shown that gains in strength do not directly correlate to improvements in functional ability¹⁶⁻²⁰. To rectify this, the work completed for this dissertation resulted in the development of a novel method to comprehensively analyze the full 3D kinetics (joint moments) and 3D kinematics of the rat hindlimb during over-ground walking, providing a clearer picture of the biomechanics required for normal movement function. Our unique ability to accurately measure gait parameters demonstrates a thorough understanding of normal and healthy rodent gait. With this knowledge, it is possible to extend these methods to quantify the relevant functional deficits that result in animals with pathologies as well as the functional effectiveness of the hindlimb after treatment.

The gold standard of motion capture is the combination of recorded GRFs and calculated kinematics to produce kinetic data through the use of an inverse dynamic musculoskeletal model. However, there is a distinct lack of kinetic analysis in the literature for either healthy or pathologic rats despite the emphasis on modeling pathologies in the rat hindlimb. Despite that, multiple groups have acquired biomechanical movement information using spatiotemporal parameters, GRFs, and kinematics on their own. In the following sections, overviews will be presented of the published research covering each of those topic areas.

Spatiotemporal Parameters

Spatiotemporal parameters for evaluating the hindlimb and healthy rat gait have been successfully acquired during both treadmill and over ground walking (see **Table 2-1**). In general, this data is easy to collect and the methodology has been very well characterized. However, spatiotemporal parameters only provide information on the end effect of the foot, not how the motion is actuated. Because there are endless ways to create a given stride length, cadence, etc., this data only provides surface level information.

Spatiotemporal data can be collected using a variety of instruments and methodologies. These include ink pawprint mapping, recorded video, and systems such as DigiGait, CatWalk, TreadScan, and Experimental Dynamic Gait Arena for Rodents (EDGAR)²¹. Ink pawprint mapping is the most basic of these methods, and is primarily used to calculate spatial metrics such as stride length, step width, and toe-out angle. Similarly, high-speed video is best utilized to calculate temporal metrics like stride time, stance/swing time, and time in single vs. double support. More advanced systems are capable of measuring both spatial and temporal parameters, and can collect more sophisticated data such as paw print intensity for low-level calculations of weight bearing. As stated, spatiotemporal parameters are only surface level data, but they can provide initial insight into compensation strategies or movement alterations in response to an injury or improvement due to a treatment.

Table 2-1: Overview of studies collecting spatiotemporal parameters

Author	Species	Pathology	Data Collection Method	Variables
K.D. Allen, et al ²²	Male Lewis rats	OA, MCL transection, medial meniscus transection	High-speed video (200f/s)	Stance time, velocity, stride length, step width, cadence
S.U. Simjee, et al ²³	Female Sprague-Dawley rats	OA	TreadScan	Velocity, stride length, stance time, swing time
P. Coulthard, et al ²⁴	Male Sprague-Dawley rats	Persistent pain via induced paw inflammation	Video (25f/s)	Velocity, stride length, stance time, swing time, single vs. double support
H.E. Kloefkorn, et al ²⁵	Male Lewis rats	OA, MCL transection, medial meniscus transection	High-speed video (250f/s)	Velocity, stance time, swing time, stride time, stride length, step width, single vs. double support
T. Gorska, et al ²⁶	Male Wistar rats	Incomplete thoracic spinal cord lesions	Contact electrodes attached to paws	Cycle duration, velocity, stance time, duty factor
S.W. Bennett, et al ²⁷	Female Long-Evans rats	Peripheral nerve lesion	High-speed video (125f/s)	Velocity, stance percentage
K.A. Clarke, et al ²⁸	Male Wistar rats	OA	Video (25f/s)	Velocity, stride time, stance time, swing time, stride length, single vs. double support
K.D. Allen, et al ²⁹	Male Wister rats	OA	High-speed video (200f/s)	Velocity, stance time, stride length, step width
C.E. Ferland, et al ³⁰	Male Sprague-Dawley rats	OA	CatWalk	Swing time, swing speed, duty cycle ratio
S.C. Fu, et al ³¹	Female Sprague-Dawley rats	OA	CatWalk	Swing duration, limb idleness index
M.H. Hoffmann, et al ³²	Dark Agouti rats	Rheumatoid arthritis (RA)	CatWalk	Stance time, swing time, regularity index
M.K. Boettger, et al ³³	Female Lewis rats	OA	Ink pawprint mapping	Stride length, left-right step distance, guarding score, angle between paws
S. Adaes, et al ³⁴	Male Wistar rats	OA	CatWalk	Paw print intensity (low-quality weight bearing calculation)
K.M. Angeby, et al ³⁵	Male Sprague-Dawley rats	RA	CatWalk	Paw print intensity, guarding index, regularity index
K. Orito, et al ³⁶	Male Sprague-Dawley rats	RA	High-speed video and ink pawprint mapping	Swing time
E.R. Berryman, et al ³⁷	Male and female Crl:CD rats	RA	Digigait	Swing time, stance/swing ratio, braking time, stance time, stance percentage, stride length, stride time, swing percentage, propulsion percentage, paw contact area, stance width

J. Ferreira-Gomes, et al ³⁸	Male Wistar rats	OA	CatWalk	Paw print intensity
G. Ishikawa, et al ³⁹	Male Sprague-Dawley rats	OA	Homemade CatWalk system	Paw contact area, swing speed, paw print intensity
D. Pinho, et al ⁴⁰	Male Wistar Han rats	OA and hypertension	CatWalk	Paw print intensity for load distribution
J. Beckett, et al ⁴¹	Male Wistar rats	OA	Ink pawprint mapping	Stride length, angle between paws
C.S. Bonnet, et al ⁴²	Male Lewis rats	OA	Ink pawprint mapping	Stride length, toe angle, step width
J.A. Dienes, et al ⁴³	Female Lewis rats	TA VML	Vicon 3D motion capture	Cadence, step time, swing percentage
B.Y. Jacobs, et al ⁴⁴	Male Lewis rats, male Long-Evans rats, female Fisher rats	OA, sciatic nerve injury, elbow contracture via LCL transection, spinal cord injury via right lateral hemisection	GAITOR suite and EDGAR walkway	Step width, duty factor, symmetry index, stride length
J.E. Pereira, et al ⁴⁵	Female Wistar rats	None	High-speed video (125f/s)	Velocity, cycle duration, stance time, swing time, stride length
O. Alluin, et al ⁴⁶	Female Wistar rats	Spinal cord clip compression	High-speed video (120f/s)	Cycle duration, stride length, swing time, stance time
C. Garnier, et al ⁴⁷	Male Wistar rats	None	Vicon 3D motion capture	Cycle duration, swing time, stance time, stride length
O. Perrot, et al ⁴⁸	Male Wistar rats	None	Vicon 3D motion capture	Cycle duration, stride length
A. Schmidt, et al ⁴⁹	Female Norway rats	None	High-speed video (1000f/s) and x-ray	Velocity, ground contact time
M.H. Canu, et al ⁵⁰	Male Wistar rats	None	Vicon 3D motion capture	Cycle duration, stance duration, swing duration, stride length
J.A. Dienes et al (Chapter 5)	Female Lewis rats	None	Vicon 3D motion capture	Stride length, stance percentage, velocity, cadence

Ground Reaction Forces

GRFs can be collected in all three planes and provide feedback on weight distribution (Z-axis, vertical), braking/acceleration ability (X-axis, fore-aft, anterior-posterior), and balance (Y-axis, mediolateral). Again, this data has been well characterized and the methodology is straightforward (see **Table 2-2**), with GRFs typically being recorded using embedded load cells or an instrumented system such as TekScan²¹. But GRFs on their own are a whole limb measurement, and they only provide truly informative data when combined with kinematics to calculate moments on a joint by joint basis. In the absence of inverse dynamic analysis, GRFs provide no information on where and how the total limb force is generated. In addition, many of the studies that collect GRF data on rats are collecting only when the animals are immobile to gather information on quadrupedal weight bearing percentages. However, GRF data does allow for some simple inferences to be made, including whether the animal is favoring an injured limb by placing less of a load on it during a gait cycle. This data is particularly informative in extended timepoints after treatment by providing insight on whether the animal is loading the injured limb in a normal way or if some compensation mechanism is in place.

Table 2-2: Overview of studies collecting ground reaction forces

Author	Species	Pathology	Data Collection Method	Variables
K.D. Allen, et al ²²	Male Lewis rats	OA, MCL transection, medial meniscus transection	Instrumented force plate arena	X, Y, Z-direction GRFs
K.A. Clarke, et al ²⁸	Male Wistar rats	OA	Instrumented walkway	Z-direction GRF
M. Roemhildt, et al ⁵¹	Sprague-Dawley rats	OA	Instrumented walkway	X, Y, Z-direction GRFs
A.A. Webb, et al ⁵²	Female Wistar rats	Geriatric gait changes	Instrumented walkway	X, Y, Z-direction GRFs
G.D. Muir, et al ⁵³	Female Long-Evans rats	Corticospinal tract lesions	Instrumented walkway	X, Y, Z-direction GRFs
G.D. Jay, et al ⁵⁴	Male Lewis Rats	ACL transection	TekScan walkway	Z-direction GRF
S.S. Min, et al ⁵⁵	Male Sprague-Dawley rats	OA	Instrumented walkway	Z-direction GRF
L. Skott Gregersen, et al ⁵⁶	Male Sprague-Dawley rats	OA	TekScan walkway	Z-direction GRF
M.H. Rashid, et al ⁵⁷	Male Sprague-Dawley rats	OA	TekScan walkway	Z-direction GRF
C.M. Bagi, et al ⁵⁸	Male Lewis rats	OA	Bioseb dynamic weight bearing system	Z-direction GRF
C.S. Howard, et al ⁵⁹	Female Sprague-Dawley rats	Peripheral nerve laceration	Instrumented walkway	X and Z-direction GRFs
N. Bravenboer, et al ⁶⁰	Female Wistar rats	None, applied loads and changed slopes	Instrumented walkway	X and Z-direction GRFs
G.D. Muir, et al ⁶¹	Female Long-Evans rats	Parkinson's	Instrumented walkway	X, Y, Z-direction GRFs
U. Tasch, et al ⁶²	Male Sprague-Dawley rats	None	Instrumented walkway	Z-direction GRF
E.I. Miklyaeva, et al ⁶³	Female Long-Evans rats	Parkinson's	Instrumented platform	Z-direction GRF
W. Tang, et al ⁶⁴	Male Sprague-Dawley rats	Parkinson's	Instrumented walkway	X, Y, Z-direction GRFs
P.T. Wu, et al ⁶⁵	Male Sprague-Dawley rats	Achilles tendinopathy	Instrumented walkway	X, Y, Z-direction GRFs
E. Andrada, et al ⁶⁶	Male Sprague-Dawley rats	None	Instrumented walkway	X, Y, Z-direction GRFs
E. Andrada, et al ⁶⁷	Male Sprague-Dawley rats	None	Instrumented walkway	X, Y, Z-direction GRFs
J.A. Dienes et al (Chapter 5)	Female Lewis rats	None	Instrumented walkway	X, Y, Z-direction GRFs

Kinematics

Joint kinematics have similarly been acquired by multiple groups (see **Table 2-3**), but there is a lack of agreement in the published data due to methodological differences. A common theme of these studies has been small group sizes or a low volume of collected gait cycles for analysis, both of which could contribute to the wide distribution of sagittal plane kinematics found in the literature. Data collection methods have also been highly variable, with joint center markers ranging from permanent marker dots to true motion capture reflective markers, and many groups using marker digitization rather than established motion tracking cameras and software (**Figure 2-1**). Each of these deviations from the gold standard of human motion capture can compound errors in the kinematic data.

Historically, it has been shown that there can be a significant skin artifact error when calculating the position of the knee depending on the data collection and reconstruction methods⁶⁸. Considering that the knee location impacts the kinematic calculations for the hip, knee, and ankle, it is important to ensure that methods are in place to minimize error when calculating knee marker position. The easiest way to minimize this error is through the use of a validated musculoskeletal model, where the default position of the knee marker can be set and the weight of the knee marker's ability to drive the simulation can be reduced. Further, by using a musculoskeletal model and collecting morphometric measurements of the animals at each timepoint the lengths of the thigh and shank segments can be set and locked before running simulations. However, all of these error reduction methods are useless in the absence of three major methodological steps: collecting motion capture data using a dedicated high-accuracy motion capture system, reconstructing the marker locations using established motion capture software, and running simulations to output kinematic data using a validated and high-quality musculoskeletal model. In the majority of the

kinematic studies in the literature (**Table 2-3**) at least one of these three significant steps are missing, inevitably reducing the value and reliability of the results.

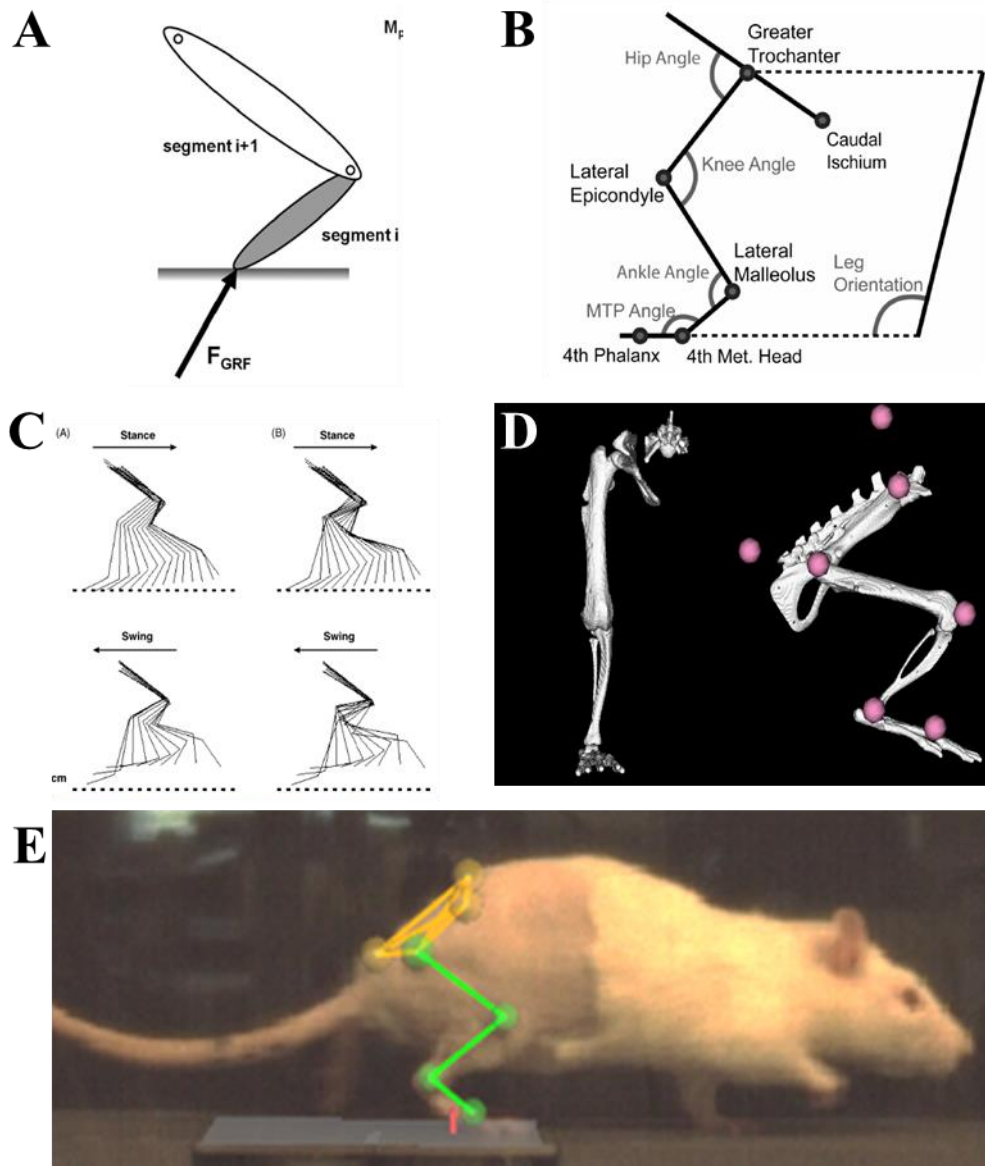


Figure 2-1: Modeling and reconstruction methods for kinematic analysis. (A) Link model for kinematic modeling²⁷ (B) Planar model for kinematic modeling⁶⁸ (C) Marker digitization for kinematic reconstruction⁶⁹ (D) Validated musculoskeletal rat hindlimb model for kinematic modeling (E) Real-time reconstruction of 3D marker positions from Vicon Motion Capture software for kinematic data collection. Figures A-C reproduced with permission from journal copyright offices (A: Bennett et al [2012], *Behav. Brain Res.*, B: Bauman et al [2010], *J. Neurosci. Meth.*, C: Filipe et al [2006], *J. Neurosci. Meth.* All journals published under Elsevier.)

Table 2-3: Overview of studies calculating joint kinematics

Author	Species	n	Pathology	Data Collection Method	Variables	Potential Error Sources
J.E. Pereira, et al ⁴⁵	Female Wistar rats	10	None	High-speed video (125f/s)	Hip, knee, ankle sagittal kinematics	Marker digitization, no validated musculoskeletal (MS) model
S.W. Bennett, et al ²⁷	Female Long-Evans rats	5	Peripheral nerve lesion	High-speed video (125f/s)	Hip, knee, ankle sagittal kinematics	Marker digitization, link model
K.D. Allen, et al ²⁹	Male Wistar rats	24	OA	High-speed video (200f/s)	Toe-out angle	Manual tracing, no validated MS model
J.M. Bauman, et al ⁶⁸	Male Sprague-Dawley rats	6	None	High-speed video (200f/s) and x-ray	Hip, knee, ankle sagittal kinematics	Plane model, marker digitization or joint center triangulation depending on method
O. Alluin, et al ⁴⁶	Female Wistar rats	22	Spinal cord clip compression	High-speed video (120f/s)	Hip, knee, ankle, MTP sagittal kinematics	Treadmill walking, marker digitization, no validated MS model
C. Garnier, et al ⁴⁷	Male Wistar rats	5	None	Vicon 3D motion capture	Hip, knee, ankle, shoulder, elbow sagittal kinematics	No validated MS model
M.H. Canu, et al ⁵⁰	Male Wistar rats	5	None, loaded and unloaded	Vicon 3D motion capture	Knee, ankle, elbow sagittal kinematics	No validated MS model
J.A. Dienes, et al ⁴³	Female Lewis rats	8	TA VML	Vicon 3D motion capture	3D hip kinematics, knee and ankle sagittal kinematics	Treadmill walking
V.M. Filipe, et al ⁶⁹	Female Wistar rats	10	None	High-speed video (125f/s)	Hip, knee, ankle sagittal kinematics	Treadmill walking, marking digitization, no validated MS model, triangulated knee position
A.K. Thota, et al ⁷⁰	Female Long-Evans rats	26	None	Peak Motus motion analysis video system	Shoulder, elbow, hip, knee, ankle sagittal kinematics	Treadmill walking, no validated MS model,
F. Joao, et al ⁷¹	Male Sprague-Dawley rats	7	None	Qualisys 3D motion capture	Knee sagittal kinematics, 3D hip, ankle, MTP kinematics	No validated MS model
P. Gravel, et al ⁷²	Wistar rats	6	None	Video and x-ray fluoroscopy	Hip, knee, ankle, MTP sagittal kinematics	Landmark digitization, no validated MS model

A. Schmidt, et al ⁴⁹	Female Norway rats	2	None	High-speed video (1000f/s) and x-ray	Shoulder, elbow, wrist, hip, knee, ankle, MTP angular excursions	Landmark digitization, no validated MS model
O. Perrot, et al ⁴⁸	Male Wistar rats	10	None	Vicon 3D motion capture	Shoulder, elbow, hip, knee ankle sagittal kinematics	Treadmill walking, no validated MS model
I. Nica, et al ⁷³	Male Sprague-Dawley rats	3	Motor cortex neural injury	Video (30f/s)	Peak forearm extension	No markers, manual landmark identification
G. Balbinot, et al ⁷⁴	Male Sprague-Dawley rats	17	Stroke	Video (60f/s)	Elbow sagittal kinematics, 2D shoulder kinematics	Marker digitization, no validated MS model
J. DiGiovanna, et al ⁷⁵	Female Lewis rats	16	None	Vicon 3D motion capture	Hip, knee, ankle, MTP sagittal kinematics	
A. Nakahata, et al ⁷⁶	Male Wistar rats	18	OA	KinemaTracer 3D motion capture	Knee sagittal kinematics, toe-out angle	No validated MS model
J.A. Dienes, et al (Chapter 5)	Female Lewis rats	20	None	Vicon 3D motion capture	3D hip kinematics, sagittal knee and ankle kinematics	

While a few studies do utilize the gold standard of motion data collection, Vicon 3D motion capture systems, many have simply relied on high speed video. The error propagation potential of using video rather than infrared marker tracking is two-fold: sensitivity in the data collection can be lost without sufficient cameras/angles, and marker positions have to be manually identified and ultimately digitized. When marker positions are digitized rather than automatically triangulated by a series of infrared cameras, error is introduced into the system. On animals as small as rats, even a small misidentification of a joint center can lead to a large change in the kinematic data. Further, using digitization frequently also results in triangulation of the knee location rather than relying on motion capture reconstruction. Most studies also do not utilize a validated musculoskeletal model, instead relying on link models, manual tracing, or manual calculations based on 2D marker positions. The benefits of using a validated model are clear, including the ability to model 3D marker positions and having built-in physiological limitations for movement. Relying on lesser models opens up the possibilities of improbable angle outputs because of both the lack of physiological limits and working only in the 2D space. Even when all the steps taken up to running simulations meet the gold standard, the lack of a physiologically relevant and validated model will always introduce error to the results. Each of these deviations adds some amount of error into the system, and when all of these deviations are combined it is easy to see why there is such an extreme range of kinematic results have been reported for the same joints parameters in the same animals.

Kinetics

Kinetics are regarded as the gold standard of human motion capture and movement analysis, and if these methods are applied to rats it gives researchers the ability to evaluate injuries/pathologies in the hindlimb and treatment efficacy in a new, more effective way. Comprehensive analysis of human walking patterns has frequently been used as a baseline

functional measure of movement quality⁷⁷⁻⁸⁰, and applying those techniques to rats is the logical next step in evaluating the effect of pathologies on the entire hindlimb kinetic chain. By calculating the joint moments during a motion, investigators gain insight into the forces and loads being experienced by the target joints over the duration of the gait cycle. If evaluating an injury, pathologic kinetics can be compared to healthy kinetics to appropriately target treatments that maximize recovery and minimize the threat of developing a secondary pathology.

Whether due to a lack of awareness or an inability to collect accurate motion capture data, most current preclinical rat studies are missing this significant functional metric by neglecting to analyze the effect of pathologies on movement ability. By lacking a comprehensive analysis of the kinematic and kinetic effects of the pathology on rats, these studies are trying to apply a treatment without a full understanding of the functional issues that need to be resolved. Kinetics show us where the forces experienced by the limb during gait are generated, which is significant because animals can actuate the same motions and whole-limb forces by compensating with different muscles at different joints after an injury. Full-scale analysis of 3D kinetics provides a novel ability to discern between motor control changes to accommodate injury and could contribute to further development of technologies to best treat particular pathologies.

Table 2-4: Overview of studies collecting joint kinetics

Author	Species	n	Pathology	Data Collection Method	Variables	Potential Error Sources
S.W. Bennett, et al ²⁷	Female Long-Evans rats	5	Peripheral nerve lesion	High-speed video (125Hz), instrumented walkway	Hip, knee, ankle sagittal kinetics	Marker digitization, link model, did not report GRFs, 2-D kinematics
J.A. Dienes, et al (Chapter 5)	Female Lewis rats	20	None	Vicon 3D motion capture	3D hip kinetics, sagittal knee and ankle kinetics	
E. Andrada, et al ⁶⁶	Male Sprague-Dawley rats	2	None	X-ray fluoroscopy	Hip, knee, ankle sagittal kinetics	Did not report kinematics, only recorded motion data in sagittal plane
E. Andrada, et al ⁶⁷	Male Sprague-Dawley rats	2	None	X-ray fluoroscopy	Hip, knee, ankle sagittal kinetics	Did not report kinematics, only recorded motion data in sagittal plane

To our knowledge, only two other groups have calculated meaningful kinetic data on rats^{27,66,67} (see **Table 2-4**) and they did so on the hip, knee, and ankle. However, they both had a small group size (n=5 and n=2, respectively) and Bennett used a simple planar link model rather than an established musculoskeletal model and software. These studies only examined the kinetics of the sagittal plane and Bennett digitized marker locations rather than utilizing high-speed motion capture to acquire joint centers for kinematic calculations. Andrada utilized x-ray fluoroscopy to measure their joint angles, but they only imaged in one plane and did not report kinematics in their studies. Without great kinematics, it is impossible to calculate accurate and informative kinetic data. One additional group calculated internal kinetics of the femur, but with dubious methodology⁸¹. Rather than collecting concurrent ground reaction forces, they took GRFs from a disparate study and applied them to their in-house model. Any kinetic conclusions made without concurrently collected GRFs should be considered meaningless due to the multitude of minute differences that can occur during the gait cycle.

The primary purpose of the work completed for this dissertation was to develop the necessary data collection/reconstruction methods and a robust understanding for thorough analysis of the rat hindlimb during over ground walking. These advanced motion capture and modeling methods were successfully utilized to capture concurrent joint kinematic and GRF data. We were able to calculate 3D joint kinetic data, which represents a breakthrough in rodent gait analysis. This method can be utilized for any pathology modeled in the rat hindlimb to assess the effect of the pathology on the kinetic chain. Further, the results of kinetic analysis can inform the development of more effective treatments to maximize functional recovery and minimize the adoption of pathologic gait patterns. The work presented here quantifies 3D hindlimb kinetics, 3D hindlimb kinematics, GRFs, and spatiotemporal parameters in large groups of healthy, injured,

and treated rats during over-ground walking, thereby establishing a methodology and standard of comparison for gait analysis for groups utilizing the rat hindlimb model system.

References

1. Passipieri, J. A. *et al.* Keratin Hydrogel Enhances In Vivo Skeletal Muscle Function in a Rat Model of Volumetric Muscle Loss. *Tissue Eng. Part A* **23**, 556–571 (2017).
2. Aurora, A., Garg, K., Corona, B. T. & Walters, T. J. Physical rehabilitation improves muscle function following volumetric muscle loss injury. *BMC Sport. Sci. Med. Rehabil.* **6**, 41 (2014).
3. Corona, B. T., Ward, C. L., Baker, H. B., Walters, T. J. & Christ, G. J. Implantation of In Vitro Tissue Engineered Muscle Repair Constructs and Bladder Acellular Matrices Partially Restore In Vivo Skeletal Muscle Function in a Rat Model of Volumetric Muscle Loss Injury. *Tissue engineering. Part A* **20**, 705–15 (2014).
4. Wu, X., Corona, B. T., Chen, X. & Walters, T. J. A Standardized Rat Model of Volumetric Muscle Loss Injury for the Development of Tissue Engineering Therapies. *Biores. Open Access* **1**, 280–290 (2012).
5. Kemp, S. W. P. *et al.* Functional recovery following peripheral nerve injury in the transgenic Thy1-GFP rat. *J. Peripher. Nerv. Syst.* **18**, 220–231 (2013).
6. Cooney, D. S. *et al.* Mesenchymal Stem Cells Enhance Nerve Regeneration in a Rat Sciatic Nerve Repair and Hindlimb Transplant Model. *Sci. Rep.* **6**, 31306 (2016).
7. Allbright, K. O. *et al.* Delivery of adipose-derived stem cells in poloxamer hydrogel improves peripheral nerve regeneration. *Muscle Nerve* (2018). doi:10.1002/mus.26094
8. Choe, M.-A., Kyung Hwa Kim, K. H., Gyeong Ju An, G. J., Lee, K.-S. & Heitkemper, M. Hindlimb Muscle Atrophy Occurs From Peripheral Nerve Damage in a Rat Neuropathic Pain Model. *Biol. Res. Nurs.* **13**, 44–54 (2011).
9. Komatsu, I., Wang, J. H.-C., Iwasaki, K., Shimizu, T. & Okano, T. The effect of tendon stem/progenitor cell (TSC) sheet on the early tendon healing in a rat Achilles tendon injury model. *Acta Biomater.* **42**, 136–146 (2016).
10. Akamatsu, F. E. *et al.* Experimental model of Achilles tendon injury in rats. *Acta Cir. Bras.* **29**, 417–422 (2014).
11. Black, D. A., Lindley, S., Tucci, M., Lawyer, T. & Benuzzi, H. A New Model for Repair of the Achilles Tendon in the Rat. *J. Investig. Surg.* **24**, 217–221 (2011).
12. Maerz, T. *et al.* Biomechanical Characterization of a Model of Noninvasive, Traumatic Anterior Cruciate Ligament Injury in the Rat. *Ann. Biomed. Eng.* **43**, 2467–2476 (2015).
13. Ramme, A. J., Lendhey, M., Raya, J. G., Kirsch, T. & Kennedy, O. D. A novel rat model for subchondral microdamage in acute knee injury: a potential mechanism in post-traumatic osteoarthritis. *Osteoarthr. Cartil.* **24**, 1776–1785 (2016).
14. Allen, K. D. *et al.* Kinematic and dynamic gait compensations resulting from knee instability in a rat model of osteoarthritis. *Arthritis Res. Ther.* **14**, R78 (2012).
15. Hamilton, C. B. *et al.* Weight-bearing asymmetry and vertical activity differences in a rat model of post-traumatic knee osteoarthritis. *Osteoarthr. Cartil.* **23**, 1178–1185 (2015).

16. Damiano, D. L., Arnold, A. S., Steele, K. M. & Delp, S. L. Can Strength Training Predictably Improve Gait Kinematics? A Pilot Study on the Effects of Hip and Knee Extensor Strengthening on Lower-Extremity Alignment in Cerebral Palsy. *Phys. Ther.* **90**, 269–279 (2010).
17. Damiano, D. L. & Abel, M. F. Functional outcomes of strength training in spastic cerebral palsy. *Arch. Phys. Med. Rehabil.* **79**, 119–125 (1998).
18. Damiano, D. L., Prosser, L. A., Curatalo, L. A. & Alter, K. E. Muscle Plasticity and Ankle Control After Repetitive Use of a Functional Electrical Stimulation Device for Foot Drop in Cerebral Palsy. *Neurorehabil. Neural Repair* **27**, 200–207 (2013).
19. Topp, R., Mikesky, A., Wigglesworth, J., Holt, W. & Edwards, J. E. The effect of a 12-week dynamic resistance strength training program on gait velocity and balance of older adults. *Gerontologist* **33**, 501–6 (1993).
20. Buchner, D. M. *et al.* The effect of strength and endurance training on gait, balance, fall risk, and health services use in community-living older adults. *J. Gerontol. A. Biol. Sci. Med. Sci.* **52**, M218-24 (1997).
21. Lakes, E. H., Allen, K. D. & Pruitt, C. Gait Analysis Methods for Rodent Models of Arthritic Disorders: Reviews and Recommendations. *Osteoarthr. Cartil.* **24**, 1837–1849 (2016).
22. Allen, K. D. *et al.* Kinematic and dynamic gait compensations resulting from knee instability in a rat model of osteoarthritis. doi:10.1186/ar3801
23. Simjee, S. U., Jawed, H., Quadri, J. & Saeed, S. Quantitative gait analysis as a method to assess mechanical hyperalgesia modulated by disease-modifying antirheumatoid drugs in the adjuvant-induced arthritic rat. *Arthritis Res. Ther.* (2007). doi:10.1186/ar2290
24. Coulthard, P., Simjee, S. U. & Pleuvry, B. J. Gait analysis as a correlate of pain induced by carrageenan intraplantar injection. *J. Neurosci. Methods* (2003). doi:10.1016/S0165-0270(03)00154-7
25. Kloefkorn, H. E., Jacobs, B. Y., Loye, A. M. & Allen, K. D. Spatiotemporal gait compensations following medial collateral ligament and medial meniscus injury in the rat: Correlating gait patterns to joint damage. *Arthritis Res. Ther.* (2015). doi:10.1186/s13075-015-0791-2
26. Górska, T., Chojnicka-gittins, B., Majczyn, H. & Zmyslowski, W. Overground Locomotion after Incomplete Spinal Lesions in the Rat: Quantitative Gait Analysis. *J. Neurotrauma* **24**, 1198–1218 (2007).
27. Bennett, S. W., Lanovaz, J. L. & Muir, G. D. The biomechanics of locomotor compensation after peripheral nerve lesion in the rat. *Behav. Brain Res.* **229**, 391–400 (2012).
28. Clarke, K. A., Heitmeyer, S. A., Smith, A. G. & Taiwo, Y. O. Gait analysis in a rat model of osteoarthrosis. *Physiol. Behav.* (1997). doi:10.1016/S0031-9384(97)00022-X
29. Allen, K. D. *et al.* Gait and behavior in an IL1 β -mediated model of rat knee arthritis and

- effects of an IL1 antagonist. *J. Orthop. Res.* (2011). doi:10.1002/jor.21309
30. Ferland, C. E., Laverty, S., Beaudry, F. & Vachon, P. Gait analysis and pain response of two rodent models of osteoarthritis. *Pharmacol. Biochem. Behav.* **97**, 603–610 (2011).
 31. Fu, S. C., Cheuk, Y. C., Hung, L. K. & Chan, K. M. Limb Idleness Index (LII): A novel measurement of pain in a rat model of osteoarthritis. *Osteoarthr. Cartil.* **20**, 1409–1416 (2012).
 32. Hoffmann, M. H. *et al.* Gait changes precede overt arthritis and strongly correlate with symptoms and histopathological events in pristane-induced arthritis. *Arthritis Res. Ther.* **12**, R41 (2010).
 33. Boettger, M. K. *et al.* Gait abnormalities differentially indicate pain or structural joint damage in monoarticular antigen-induced arthritis. *Pain* (2009). doi:10.1016/j.pain.2009.06.006
 34. Adães, S. *et al.* Intra-articular injection of collagenase in the knee of rats as an alternative model to study nociception associated with osteoarthritis. *Arthritis Res. Ther.* **16**, R10 (2014).
 35. Ängeby Möller, K., Kinert, S., Størkson, R. & Berge, O. G. Gait Analysis in Rats with Single Joint Inflammation: Influence of Experimental Factors. *PLoS One* **7**, (2012).
 36. Orito, K. *et al.* A sensitive gait parameter for quantification of arthritis in rats. *J. Pharmacol. Sci.* **103**, 113–116 (2007).
 37. Berryman, E. R., Harris, R. L., Moalli, M. & Bagi, C. M. Digigait™ quantitation of gait dynamics in rat rheumatoid arthritis model. *J. Musculoskelet. Neuronal Interact.* **9**, 89–98 (2009).
 38. Ferreira-Gomes, J., Adães, S. & Castro-Lopes, J. M. Assessment of Movement-Evoked Pain in Osteoarthritis by the Knee-Bend and CatWalk Tests: A Clinically Relevant Study. *J. Pain* **9**, 945–954 (2008).
 39. Ishikawa, G., Nagakura, Y., Takeshita, N. & Shimizu, Y. Efficacy of drugs with different mechanisms of action in relieving spontaneous pain at rest and during movement in a rat model of osteoarthritis. *Eur. J. Pharmacol.* **738**, 111–117 (2014).
 40. Pinho, D. *et al.* Does chronic pain alter the normal interaction between cardiovascular and pain regulatory systems? Pain modulation in the hypertensive-monoarthritic rat. *J. Pain* **12**, 194–204 (2011).
 41. J., B. *et al.* Excessive running induces cartilage degeneration in knee joints and alters gait of rats. *J. Orthop. Res.* **30**, 1604–1610 (2012).
 42. Bonnet, C. S. *et al.* Ampa/kainate glutamate receptors contribute to inflammation, degeneration and pain related behaviour in inflammatory stages of arthritis. *Ann. Rheum. Dis.* **74**, 242–251 (2015).
 43. Dienes, J. A. *et al.* Analysis and Modeling of Rat Gait Biomechanical Deficits in Response to Volumetric Muscle Loss Injury. *Front. Bioeng. Biotechnol.* **7**, 146 (2019).

44. Jacobs, B. Y. *et al.* The Open Source GAITOR Suite for Rodent Gait Analysis. *Sci. Rep.* **8**, 1–14 (2018).
45. Pereira, J. E. *et al.* A comparison analysis of hindlimb kinematics during overground and treadmill locomotion in rats. *Behav. Brain Res.* **172**, 212–218 (2006).
46. Alluin, O. *et al.* Kinematic study of locomotor recovery after spinal cord clip compression injury in rats. *J. Neurotrauma* **28**, 1963–1981 (2011).
47. Garnier, C., Falempin, M. & Ene Canu, M.-H. A 3D analysis of fore- and hindlimb motion during locomotion: Comparison of overground and ladder walking in rats. *Behav. Brain Res.* **186**, 57–65 (2008).
48. Perrot, O., Laroche, D., Pozzo, T. & Marie, C. Kinematics of obstacle clearance in the rat. *Behav. Brain Res.* **224**, 241–249 (2011).
49. Schmidt, A. & Fischer, M. S. The kinematic consequences of locomotion on sloped arboreal substrates in a generalized (*Rattus norvegicus*) and a specialized (*Sciurus vulgaris*) rodent. *J. Exp. Biol.* **214**, 2544–2559 (2011).
50. Canu, M. H. & Garnier, C. A 3D analysis of fore- and hindlimb motion during overground and ladder walking: Comparison of control and unloaded rats. *Exp. Neurol.* **218**, 98–108 (2009).
51. Roemhildt, M. L., Gardner-Morse, M., Rowell, C., Beynnon, B. D. & Badger, G. J. Gait alterations in rats following attachment of a device and application of altered knee loading. *J. Biomech.* **43**, 3227–31 (2010).
52. Webb, A. A., Kerr, B., Neville, T., Ngan, S. & Assem, H. Kinematics and Ground Reaction Force Determination: A Demonstration Quantifying Locomotor Abilities of Young Adult, Middle-aged, and Geriatric Rats. *J. Vis. Exp.* e2138–e2138 (2011). doi:10.3791/2138
53. Muir, G. D. & Whishaw, I. Q. Complete locomotor recovery following corticospinal tract lesions: Measurement of ground reaction forces during overground locomotion in rats. *Behav. Brain Res.* **103**, 45–53 (1999).
54. Jay, G. D. *et al.* Prevention of cartilage degeneration and gait asymmetry by lubricin tribosupplementation in the rat following anterior cruciate ligament transection. *Arthritis Rheum.* **64**, 1162–1171 (2012).
55. Min, S. S. *et al.* A novel method for convenient assessment of arthritic pain in voluntarily walking rats. *Neurosci. Lett.* **308**, 95–98 (2001).
56. Gregersen, L. S., Røslund, T., Arendt-Nielsen, L., Whiteside, G. & Hummel, M. Unrestricted Weight Bearing as a Method for Assessment of Nociceptive Behavior in a Model of Tibiofemoral Osteoarthritis in Rats. *J. Behav. Brain Sci.* **03**, 306–314 (2013).
57. Rashid, M. H., Theberge, Y., Elmes, S. J., Perkins, M. N. & McIntosh, F. Pharmacological validation of early and late phase of rat mono-iodoacetate model using the Tekscan system. *Eur. J. Pain (United Kingdom)* **17**, 210–222 (2013).

58. Bagi, C. M., Zakur, D. E., Berryman, E., Andresen, C. J. & Wilkie, D. Correlation between μ CT imaging, histology and functional capacity of the osteoarthritic knee in the rat model of osteoarthritis. *J. Transl. Med.* **13**, 276 (2015).
59. Howard, C. S., Blakeney, D. C., Medige, J., Moy, O. J. & Peimer, C. A. Functional assessment in the rat by ground reaction forces. *J. Biomech.* **33**, 751–7 (2000).
60. Bravenboer, N., van Rens, B. T. T. M., van Essen, H. W., van Dieën, J. H. & Lips, P. Ground reaction forces during walking with different load and slope combinations in rats. *J. Exp. Orthop.* **4**, 28 (2017).
61. Muir, G. D. & Whishaw, I. Q. Ground reaction forces in locomoting hemi-parkinsonian rats: A definitive test for impairments and compensations. *Exp. Brain Res.* **126**, 307–314 (1999).
62. Tasch, U. *et al.* An instrument that simultaneously measures spatiotemporal gait parameters and ground reaction forces of locomoting rats. in *2008 Proceedings of the 9th Biennial Conference on Engineering Systems Design and Analysis* **2**, 45–49 (American Society of Mechanical Engineers Digital Collection, 2009).
63. Miklyaeva, E. I. *et al.* The ground reaction forces of postural adjustments during skilled reaching in unilateral dopamine-depleted hemiParkinson rats. *Behav. Brain Res.* **88**, 143–152 (1997).
64. Tang, W., Wang, Y. P., Tasch, U., Neerchal, N. & Yarowsky, P. Detection of gait abnormalities in Sprague-Dawley rats after 6-hydroxydopamine injection and the experiment efficient design. in *Proceedings - 2011 1st IEEE International Conference on Healthcare Informatics, Imaging and Systems Biology, HISB 2011* 284–290 (2011). doi:10.1109/HISB.2011.24
65. Wu, P. T. *et al.* Dynamic weight bearing analysis is effective for evaluation of tendinopathy using a customized corridor with multi-directional force sensors in a rat model. *Sci. Rep.* **7**, 1–10 (2017).
66. Andrada, E. *et al.* Biomechanical analyses of rat locomotion during walking and climbing as a base for the design and construction of climbing robots. (2010). doi:10.2495/DN100151
67. Andrada, E. *et al.* From biomechanics of rats' inclined locomotion to a climbing robot. *Int. J. Des. Nat. Ecodynamics* **8**, 191–212 (2013).
68. Bauman, J. M. & Chang, Y.-H. High-speed x-ray video demonstrates significant skin movement errors with standard optical kinematics during rat locomotion. doi:10.1016/j.jneumeth.2009.10.017
69. Filipe, V. M. *et al.* Effect of skin movement on the analysis of hindlimb kinematics during treadmill locomotion in rats. *J. Neurosci. Methods* **153**, 55–61 (2006).
70. Thota, A. K., Watson, S. C., Knapp, E., Thompson, B. & Jung, R. Neuromechanical control of locomotion in the rat. *J. Neurotrauma* **22**, 442–465 (2005).
71. João, F. O. D. S., Amadoa, S., Veloso, A., Armada-da-Silva, P. & Maurício, A. C.

- Anatomical reference frame versus planar analysis: Implications for the kinematics of the rat hindlimb during locomotion. *Rev. Neurosci.* **21**, 469–485 (2010).
72. Gravel, P., Tremblay, M., Leblond, H., Rossignol, S. & de Guise, J. A. A semi-automated software tool to study treadmill locomotion in the rat: From experiment videos to statistical gait analysis. *J. Neurosci. Methods* **190**, 279–288 (2010).
 73. Nica, I., Deprez, M., Nuttin, B. & Aerts, J. M. Automated assessment of endpoint and kinematic features of skilled reaching in rats. *Front. Behav. Neurosci.* **11**, (2018).
 74. Balbinot, G. *et al.* Post-stroke kinematic analysis in rats reveals similar reaching abnormalities as humans. *Sci. Rep.* **8**, 1–13 (2018).
 75. DiGiovanna, J. *et al.* Engagement of the rat hindlimb motor cortex across natural locomotor behaviors. *J. Neurosci.* **36**, 10440–10455 (2016).
 76. Nakahata, A. *et al.* Gait kinematics changes in post traumatic knee osteoarthritis with destabilized medial meniscus in rat. *Osteoarthr. Cartil.* **26**, S390 (2018).
 77. Slater, L. V., Hart, J. M., Kelly, A. R. & Kuenze, C. M. Progressive Changes in Walking Kinematics and Kinetics After Anterior Cruciate Ligament Injury and Reconstruction: A Review and Meta-Analysis. *J. Athl. Train.* 1062-6050.52.6.06 (2017). doi:10.4085/1062-6050.52.6.06
 78. Robbins, S. M. *et al.* Comparison of Gait Characteristics Between Patients With Nontraumatic and Posttraumatic Medial Knee Osteoarthritis. *Arthritis Care Res. (Hoboken)*. **68**, 1215–1223 (2016).
 79. Ferrarin, M. *et al.* Gait pattern classification in children with Charcot-Marie-Tooth disease type 1A. *Gait Posture* **35**, 131–7 (2012).
 80. Ijaz, A. *et al.* Analysis of knee joint kinematics during walking in patients with cerebral palsy through human motion capture and gait model-based measurement. in *2012 IEEE International Conference on Virtual Environments Human-Computer Interfaces and Measurement Systems (VECIMS) Proceedings* 196–199 (IEEE, 2012). doi:10.1109/VECIMS.2012.6273181
 81. Wehner, T. *et al.* Internal forces and moments in the femur of the rat during gait. *J. Biomech.* **43**, 2473–2479 (2010).

Chapter 3 – Hyaluronic Acid-based Hydrogels as Treatment for TA VML Injury

Disclaimer: passages have been quoted verbatim with permission from [Dienes, J., Browne, S., Farjun, B., Passipieri, J.A., Mintz, E.L., Killian, G., Healy, K.E. & Christ, G.J. Semisynthetic Hyaluronic Acid-Based Hydrogel Promotes Recovery of the Injured Tibialis Anterior Skeletal Muscle Form and Function. *ACS Biomater. Sci. Eng.* Published Online 4 March 2021. doi: 10.1021/acsbiomaterials.0c1751]. Copyright 2021 American Chemical Society.

Abstract

Volumetric muscle loss (VML) injuries are characterized by a degree of tissue loss that exceeds the endogenous regenerative capacity of muscle resulting in permanent structural and functional deficits. Such injuries are a consequence of trauma, as well as a host of congenital and acquired diseases and disorders. Despite significant preclinical research with diverse biomaterials, as well as early clinical studies with implantation of decellularized extracellular matrices, there are still significant barriers to more complete restoration of durable form and function following repair of VML injuries. In fact, identification of novel biomaterials with more advantageous regenerative profiles is a critical limitation to the development of improved therapeutics. As a first step in this direction, we evaluated a novel semi-synthetic hyaluronic acid-based (HyA) hydrogel that embodies material features more favorable for robust muscle regeneration. This HyA-based hydrogel is composed of an acrylate-modified HyA (AcHyA) macromer, an AcHyA macromer conjugated with the bsp-RGD(15) peptide sequence to enhance cell adhesion, a high molecular weight heparin (HMWH) to sequester growth factors and a matrix metalloproteinase (MMP)-cleavable cross-linker to allow for cell-dependent remodeling. In a well-established, clinically-relevant rat tibialis anterior VML injury model, we report observations of robust functional recovery, accompanied by volume reconstitution, muscle regeneration and native-like vascularization following implantation of the HyA-based hydrogel at the site of injury. These findings have important implications for the development and clinical application of the improved

biomaterials that will be required for stable and complete functional recovery from diverse VML injuries.

Keywords: Hyaluronic acid, hydrogel system, volumetric muscle loss, regeneration, functional recovery, tibialis anterior

Introduction

Despite the well-documented capability of skeletal muscle to repair, regenerate, and remodel following injury¹⁻⁵, there remain a multitude of diseases, disorders, and traumatic injuries that result in irrecoverable loss of muscle structure and function. For example, volumetric muscle loss (**VML**) injuries are characterized by a degree of composite muscle tissue loss so severe, that it exceeds the native ability of the muscle to repair, thereby resulting in permanent cosmetic and functional deficits to the limbs, neck, or face^{6,7}. These injuries impact both the civilian and military populations, affecting thousands of individuals each year^{8,9}.

Current treatment for VML injury involves surgical muscle transfer, although these procedures are often associated with both poor engraftment and donor site morbidity, as well as incomplete cosmesis and functional recovery¹⁰. Not surprisingly, this unmet medical need has stimulated research efforts to develop new technologies for treatment of VML injuries. Recent attention has focused on development of tissue engineering (**TE**)/regenerative medicine (**RM**) technologies to provide more effective treatment options for large scale muscle injuries. A common approach has been the implantation of decellularized extracellular matrices (**dECM**), both with¹¹⁻¹⁷ and without¹⁸⁻²¹ a cellular component. Several of these approaches have been evaluated in preclinical studies, with results showing that the inclusion of a cellular component generally leads to a greater degree of functional improvement^{11,14,22}. Consistent with these preclinical results, recent clinical studies for treatment of VML injury, solely with implanted dECM scaffolds, have provided evidence for modest functional recovery but with little *de novo* muscle tissue regeneration at the injury site²³⁻²⁵. More recently, bio-printed tissue engineered constructs and their potential applications to treatment of VML injury have been reported in the literature²⁶⁻²⁹. Without question though,

regardless of approach, there is still much room for development of implantable regenerative biomaterials capable of more complete functional recovery following repair of VML injury.

In particular, alternatives to dECM-based implant technologies are already being considered, such as the design and implementation of biological, synthetic or semi-synthetic scaffolds³⁰. In fact, hyaluronic acid (HyA) hydrogels have been studied for a range of therapeutic applications, including as a scaffold for tissue regeneration, cell delivery and drug delivery³⁰⁻³². To this end, we have identified a modular hydrogel technology based on the natural biopolymer hyaluronic acid (HyA). **HyA**-based hydrogels provide an opportunity to develop a highly tunable structural matrix³³⁻³⁵ that is biocompatible, biodegradable, non-immunogenic, easily modified, and furthermore, plays an integral role in encouraging tissue development and repair³⁶. Specifically, we have developed an acrylated HyA (**AcHyA**) hydrogel platform technology wherein it is possible to independently modify a range of key mechanical and biological properties of the hydrogel^{33-35,37-40}. These properties include: 1) the density of peptide sequences for cell attachment via binding to integrin receptors; 2) matrix modulus; 3) cell-mediated degradation kinetics by matrix metalloproteinase (**MMP**)-cleavable crosslinkers; and, perhaps most significantly, 4) sequestration and solid-phase presentation of exogenously added or endogenously synthesized growth factors via conjugation of thiolated heparin to AcHyA within the matrix³³. Previously, we have examined the mechanical properties, mesh size and *in vitro* degradation kinetics of this AcHyA matrix as a function of the AcHyA molecular weight³⁸.

Our AcHyA matrix has previously been shown to promote vascular network formation *in vitro* and *in vivo*, and the angiogenic effects were highly dependent on the presence of the bsp-RGD(15) adhesion ligand³⁵, the degradation kinetics of the MMP crosslinker³⁴, and the presence of high molecular weight heparin³³. In addition to promoting angiogenesis^{41,42}, HyA has been shown to

enhance the migration of muscle progenitors during development⁴³. Furthermore, a number of MMPs have been identified within the milieu of the regenerating muscle, including MMP-2 and MMP-9, both of which cleave the crosslinker within our AcHyA matrix⁴⁴. Numerous studies have also demonstrated that heparin has the ability to sequester and release exogenously added growth factors to ultimately improve wound healing and tissue regeneration⁴⁵⁻⁵⁰. In the context of muscular regeneration, heparin mimetics have demonstrated a capacity of stimulate muscle repair, thought to be through the enhanced bioavailability of endogenously released heparin binding growth factors⁵¹. A range of hydrogels based on HyA have previously been used with applications to VML repair in mind, although it should be noted that in comparison with this study, some of these HyA hydrogels were used/ designed to deliver progenitor cells⁵²⁻⁵⁶. Combined, the potential relevance of HyA hydrogels to skeletal muscle regeneration is apparent, and furthermore, these materials have been shown to significantly improve donor cell survival after transplantation³⁵.

The goal of this study was to evaluate the potential efficacy of our HyA-based, heparin conjugated hydrogel as a potential treatment for VML injury. As described herein, this material displays robust functional regeneration when implanted into the injured muscle site in an established and biologically-relevant rat tibialis anterior (TA) VML injury model. These initial observations have important implications for the field, and moreover, suggest that further development of this technology would have a major impact on improved treatment (functional regeneration/recovery) of VML injuries.

Methods and Materials

Animal Care

This study was conducted in compliance with the Animal Welfare Act, the Implementing Animal Welfare Regulations, and in accordance with the principles of the Guide for the Care and Use of Laboratory Animals. The University of Virginia Animal Care and Use Committee approved all animal procedures. A total of eleven (11) female Lewis rats (Charles River Laboratories) weighing 184.5 ± 12.2 g at 12 weeks of age were pair housed in a vivarium accredited by the American Association for the Accreditation of Laboratory Animal Care, and they were provided with food and water *ad libitum*.

Experimental Design

A total of eleven 12-week old female Lewis rats were used in these studies. All animals received a surgically-created volumetric muscle loss (VML) injury that consisted of removal of approximately 20% of the middle third of the left tibialis anterior muscle, as previously described^{22,57-59}. Animals were randomly divided into two groups: Five (5) VML-injured animals were left untreated (no repair; **NR**), while the remaining six (6) VML-injured animals were immediately treated via implantation of AcHyA hydrogel (**HyA**, treated) (**Figure 3-1**). Function testing occurred prior to surgery to set baselines, and was repeated at 4, 8, and 12 weeks post-surgery. All animals were sacrificed 12-weeks post-VML injury and/or repair.

Materials

Hyaluronic acid (**HyA**, sodium salt, 500 kDa) was purchased from Lifecore Biomedical (Chaska, MN). Adipic dihydrazide (**ADH**), 1-ethyl-3-[3-(dimethylamino)propyl] carbodiimide (**EDC**), sodium hydroxide (**NaOH**), hydrochloric acid (HCl), tris(2-carboxyethyl)phosphine (**TCEP**), triethanolamine-buffer (**TEOA**; 0.3 M, pH 8) and 1-hydroxybenzotriazole (**HOBT**) were

purchased from Aldrich (Milwaukee, WI). Dimethyl sulfoxide (**DMSO**), N-Acryloxysuccinimide (**NAS**) and ethanol were obtained from Fisher Scientific (Waltham, MA). Dialysis membranes (10000 MWCO, SpectraPor Biotech CE) were purchased from Spectrum Laboratories (Rancho Dominguez, CA). High molecular weight heparin (**HMWH**) was obtained from Santa Cruz Biotechnology, Inc (Dallas, Texas). The MMP-degradable crosslinker peptide (CQPQGLAKC), and bsp-RGD(15) adhesion peptide (CGGNGEPRGDTYRAY)⁶⁰⁻⁶² were synthesized by United BioSystem Inc (Herndon, VA).

Synthesis of Acrylated HyA

HyA based hydrogels were synthesized using previously reported methods³³⁻³⁵. Briefly, HyA derivative carrying hydrazide groups (**HyAADH**) was synthesized by addition of 30 molar excess of ADH to HyA in deionized (**DI**) water (100 mL, 3 mg/ml). Solution pH was adjusted to 6.8 using 0.1M NaOH and 0.1M HCl. EDC (3 mmol) and HOBt (3 mmol) were dissolved separately in DMSO/water (1/1 volume ratio, 3 mL) and added to the HyA solution sequentially. The pH was maintained at 6.8 for at least the first 6 h, after which the solution was allowed to react for 24h. After 24 h, the solution was adjusted to pH 7.0 and exhaustively dialyzed against DI water. N-acryloxysuccinimide (700 mg) was subsequently reacted with the HyAADH solution (300mg, 100 mL DI water) to generate acrylate groups on the HyA (**AcHyA**). After 24h, the product was exhaustively dialyzed against DI water and lyophilized. An acrylation efficiency of 25 +/- 3 % was achieved, in line with our previous published studies³⁸.

Generation of AcHyA-bsp-RGD

The AcHyA-RGD derivative was synthesized by reacting CGGNGEPRGDTYRAY (bsp-RGD(15))⁶⁰⁻⁶² (10mg) with AcHyA solution (25mg, 10mL DI water) at room temperature. The peptide was pre-treated with excess TCEP in order to reduce any disulfide bonds that had formed

between thiol groups. The AcHyA-bsp-RGD product was exhaustively dialysed against DI water, followed by lyophilization.

Synthesis of Thiolated Heparin (heparin-SH)

Thiolated-heparin was synthesized according to a previously published method³³. Briefly, heparin (50mg, 10mL DI water) was reacted with an excess of cysteamine in the presence of EDC and HOBt at pH 6.8. After that, a 10-fold molar excess of TCEP was added to reduce the oxidized disulfide groups. This solution was allowed to react for 3 h at pH 7.5 and then adjusted to pH 5.0 by the addition of 1.0 N HCl. The acidified solution was dialyzed against dilute HCl containing 100 mM NaCl, followed by dialysis against dilute HCl and lyophilization.

AcHyA Hydrogel Formation

Hydrogels were formed as previously described^{34,35}. AcHyA (4mg), AcHyA-RGD (6 mg), and heparin-SH (0.03 wt%) were dissolved in 0.3 mL of TEOA buffer, then HyA hydrogels were fabricated by mixing bis-cysteine containing a MMP cleavable peptide (CQPQGLAKC) (3mg, 50 μ L TEOA buffer) with the solution of HyA precursors. Following addition of the crosslinking peptide, gelation occurs in approximately ~5 minutes^{35,38}. The resulting HyA-based hydrogel has a storage modulus (G') of 850 Pa and a bsp-RGD(15) concentration of 380 μ M³⁵.

Creation of VML Injury

VML injuries were surgically created as previously described^{22,59} (**Figure 3-1**). Briefly, a longitudinal incision was made on the lateral portion of the lower left leg. The skin was then cleared from the underlying fascia using blunt separation, and the fascia covering the anterior

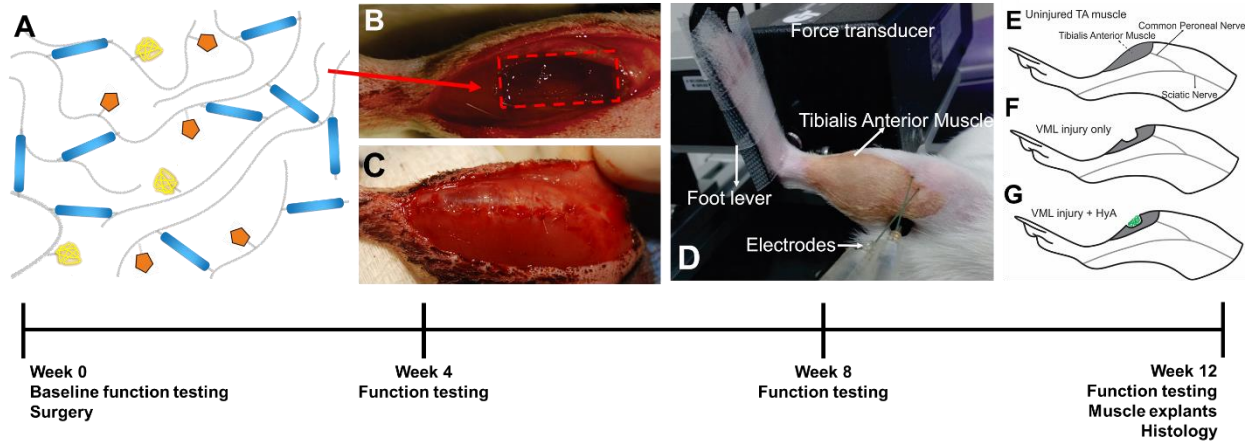


Figure 3-1. Schematic of experimental design. Specifically, (A) HyA-based hydrogel consisting of HyA (gray lines), peptide crosslinker (blue), cell adhesion peptide (RGD, orange), and thiolated heparin (yellow). (B,C) HyA hydrogel is applied directly into the TA VML wound environment (D) functional measurements of torque—dorsiflexion of the foot following stimulation of the common peroneal nerve. (E, F and G) schematic representation of the Uninjured TA muscle, TA VML injury and the application of HyA-based hydrogel.

crural muscles was separated using blunt dissection. The proximal and distal tendons of the Extensor Hallicus Longus (**EHL**) and Extensor Digitorum Longus (**EDL**) muscles were then isolated and ablated. As previously described, the TA muscle corresponds to 0.17% of the gross body weight^{22,59}. The VML injury model was characterized by excision of roughly 20% of the TA muscle weight from the middle third of the muscle. The fascia was closed with 6-0 vicryl sutures and the skin was closed with 5-0 prolene using interrupted sutures. Skin glue was applied over the skin sutures to help prevent the incision from opening. For HyA-treated animals, the hydrogel was injected immediately following closure of the fascia. Once the injection was complete, skin closure continued as normal. The animal remained sedated for 30 minutes to allow the gel to crosslink.

Force Testing

In vivo functional testing was performed as previously described⁶³. Briefly, at 4-, 8- and 12-weeks post-surgery and/or VML repair, rats were anesthetized, and the left hind limb was aseptically prepared. The rat was placed in a supine position on a heated platform and the left knee

was bent to a 90° angle. The leg was secured using a stabilizing rod and the left foot was taped to a footplate. The footplate was attached to the shaft of an Aurora Scientific 305C-LR-FP servomotor, which was controlled using a computer. Sterilized percutaneous needle electrodes were carefully inserted into the skin of the lower left leg for stimulation of the left common peroneal nerve. Electrical stimulus was provided using an Aurora Scientific stimulator with a constant current SIU (Model 701C). Stimulation voltage and needle electrode placement were optimized with a series of 1Hz pulses resulting in twitch contraction. Contractile function of the anterior crural muscles was assessed through measuring the peak isometric tetanic torque determined from maximal response to a series of stimulation frequencies (10-150Hz). Torque at baseline was normalized by the body weight of each animal. Torque at each post-surgical timepoint was normalized by the body weight of each animal on the day of collection and was also normalized as a percent of the baseline for that animal. The normalized torques and torque ratios (% , percent) at each post-surgical timepoint were averaged for analysis. After functional testing, the animals were allowed to recover on the heated platform and were then returned to the vivarium. For terminal time points (12 weeks), animals were euthanized via CO₂ inhalation and cervical dislocation was performed as a secondary.

Logistic Modeling of peroneal nerve stimulated TA muscle contraction (dorsiflexion).

Isolated muscle contraction is frequently accurately modelled as approximating first order kinetics following direct muscle activation. Specifically, approximately 95% of the force generation observed in these studies occurs over a 60ms time frame. At a sampling rate of 2Hz, that allowed us to capture roughly 120 data points. However, force development in the TA muscle during dorsiflexion of the foot exhibits a sigmoidal shape that is not well described by first order kinetics (see **Fig. 3-2** and **Eq. 3-1** below).

$$F(t) = 1 - e^{-kt} \quad \text{Eq. 3-1}$$

Thus, in order to better model the time-dependent nature of contraction described in this report, we have used a normalized four parameter logistic function of the following form:

$$F(t) = (1 - e^{-kt})^{1/\nu} \quad \text{Eq. 3-2}$$

Once again, both the force and the time were normalized such that the range and domain of the function spanned [0,1], with the goal of reducing the parameters necessary for modeling the data. In this setting, the additional parameter ν (nu) is utilized to describe the rapidity with which the maximum activation rate, determined by k , is achieved. This activation rapidity parameter allows the function to model the data with a much greater degree of fidelity, as illustrated in the representative example shown in **Fig. 3-2**. Overall, the sum of squares of residuals of the model against the data were greatly reduced and on the order of $\sim 1E-3$.

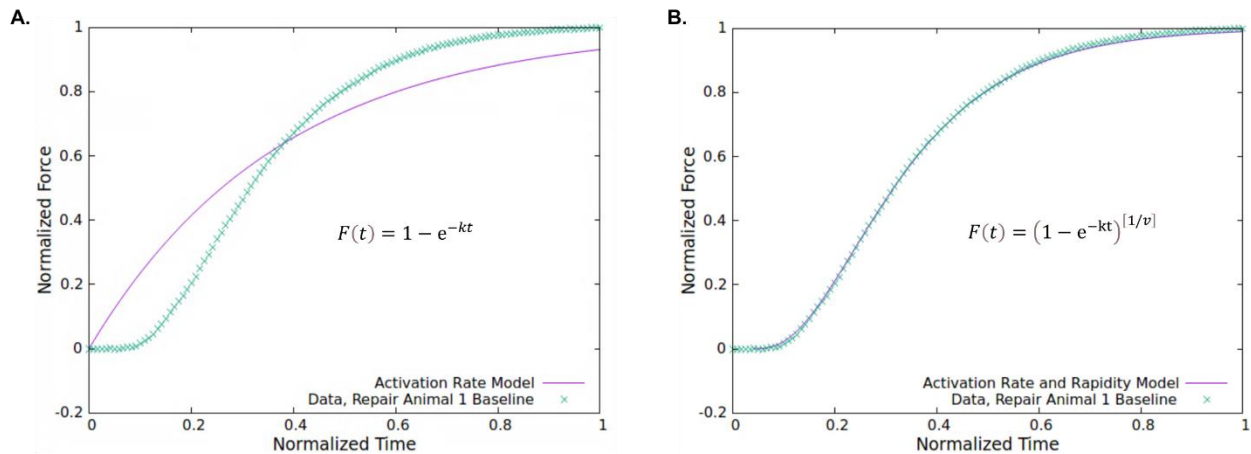


Figure 3-2. Logistic modeling of peroneal nerve-stimulated TA muscle contraction (torque). (A) shows a representative fit of first order kinetics to the raw data for the baseline maximal isometric torque (dorsiflexion) response over a 60ms time frame. Note that first order kinetics overshoots (at early time points), then undershoots (at later time points) the raw data. (B) shows a representative fit of the four parameter logistic equation to the same data set. Note the excellent agreement between the model and the raw data.

Histology and Immunohistochemistry

All samples were fixed in 4% paraformaldehyde, then processed and embedded in paraffin. Serial transverse sections (7 μm) were cut from the paraffin embedded blocks and stained with hematoxylin and eosin (**H&E**) and Masson's trichrome. Cross-sectional areas of ≈ 200 muscle fibers in the outer and inner portions of TA muscle were measured using ImageJ software and examined for the presence of centrally located nuclei, as previously described⁵⁷.

Immunohistochemical staining was performed using rabbit anti-CD31/PECAM1 antibody (NB100-2284, Novus Biological) and stained with a biotinylated goat anti-rabbit IgG (BA-1000, Vector Laboratories Inc.). The sections were next treated with Avidin Biotin Complex Reagent (PK-7100, Vector Laboratories Inc.) and visualized using a NovaRED substrate kit (SK-4800, Vector Laboratories Inc.). Tissue sections without primary antibody were used as negative controls. Images were captured and digitized (DM4000B Leica Upright Microscope, Leica Microsystems). Capillaries were quantified by counting the number of CD31+ cells around individual fibers (at least 100 fibers counted per sample, roughly 1.5mm² of muscle area).

Statistical Analysis

Unless otherwise stated, numerical data are presented as mean \pm standard error of the mean (**SEM**). Morphological (among contralateral control, NR, HyA-treated retrieved TA muscles) and functional data (HyA-treated vs. NR) between groups were analyzed using one-way or two-way analyses of variance (ANOVA), or Student's *t*-test as appropriate and indicated in the figure captions. When a two-way ANOVA was utilized, the two factors were either time and treatment or treatment and fiber size. Upon finding a significant ANOVA, post-hoc comparison testing of parameters of interest was performed using Tukey's post-test at α -level 0.05. For analysis of the

rate constants (k) and the rapidity parameter (nu), we used the 95% Confidence Intervals that define the mean of the baseline measurements for each parameter for all animals.

Results

Creation of VML injury and in vivo functional analysis

None of the animals in the study died during the surgical procedure, no post-implantation mortality occurred, and animals exhibited normal healthy weight gain in all treatment groups over the course of 12 weeks. There was no significant difference in the mean animal body weights (Two-Way ANOVA, $p=0.05$, **Figure 3-3A**) between the groups over the course of the study, nor in the maximal isometric torque generated by the HyA and NR groups at baseline (Unpaired t-Test, $p=0.05$, **Figure 3-3B**). However, because animals gained weight over the course of the study, all statistical comparisons on functional measures were made on data normalized to body weight. **Figure 3-4A-D** shows the isometric torque-frequency response curves for all animals at baseline, as well as 4-, 8- and 12-weeks post injury. As illustrated, post-surgical isometric tetanic dorsiflexion torque testing at 8 and 12 weeks showed a significant increase in the torque generated by the HyA group compared to the NR group (Two-Way ANOVA followed by Sidak's post-hoc test, $p<0.05$).

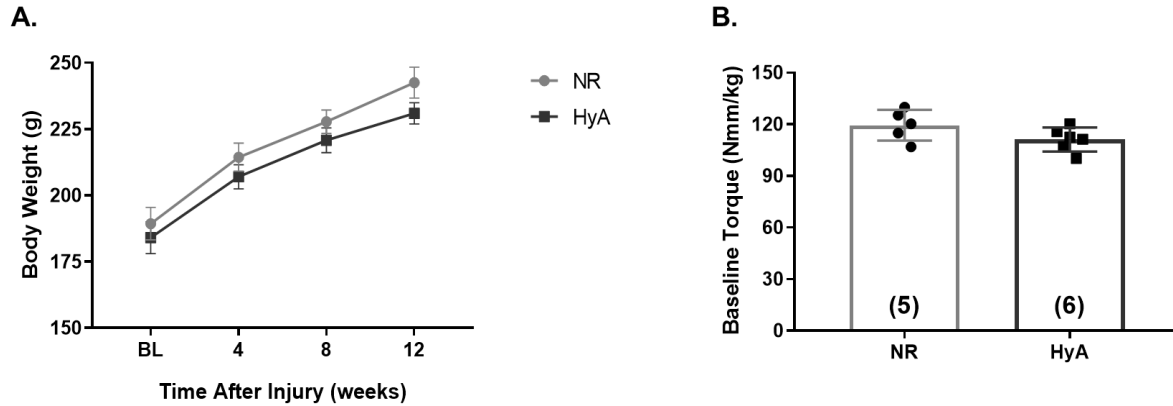


Figure 3-3. Baseline torque and body weight measurements. Body weights of study animals (A) reveal normal healthy weight gain in all treatment groups over the course of 12 weeks and no differences were observed among groups at any time point, according to Two-Way ANOVA, $p > 0.05$. Baseline maximal isometric torque measurements (B) did not significantly differ between the hydrogel treated and untreated groups (unpaired t-Test, $p > 0.05$). Data are presented as Mean \pm SEM. Group size is displayed in parentheses.

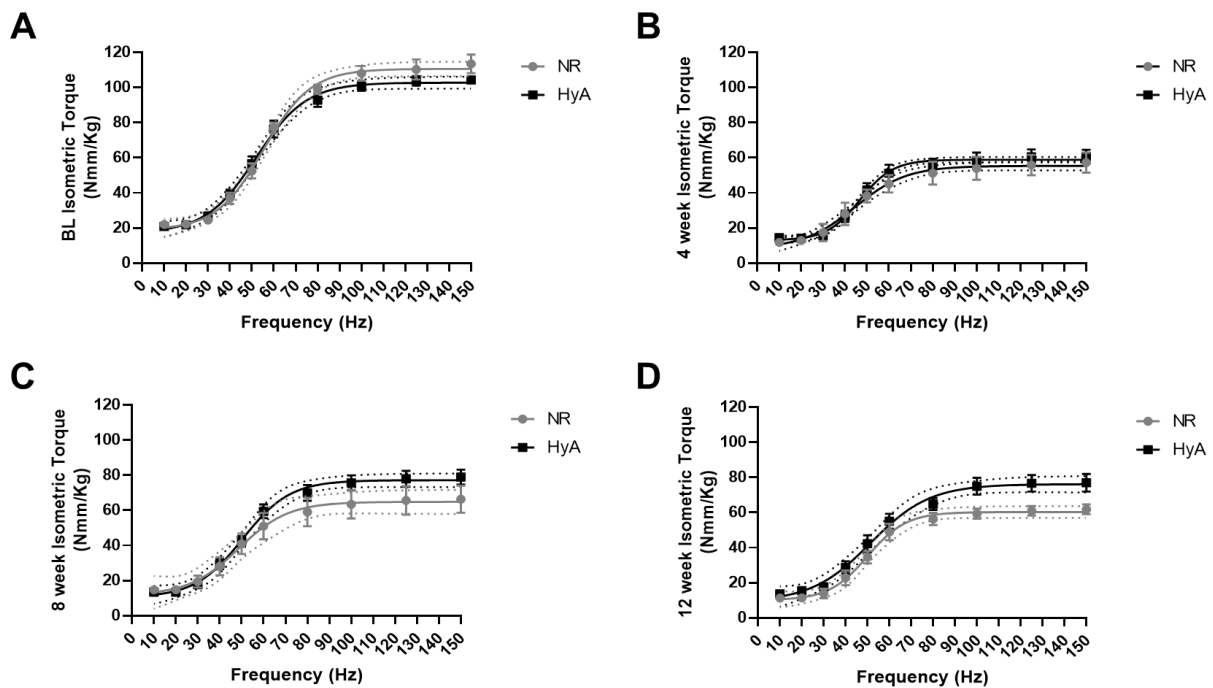


Figure 3-4. Comparison of functional metrics observed among different treatment groups at each study timepoint. Isometric frequency-torque relationship at baseline (A), 4 (B), 8 (C), and 12 weeks post-injury and/or repair/implantation (D). Dotted lines indicate 95% CI of sigmoidal interpolation. Data are presented as Mean \pm SEM.

Figure 3-5A shows the mean maximal isometric torque values (Nmm/kg) normalized to body weight, which were: 61.8 ± 3.4 and 57.9 ± 5.4 at 4 weeks, 79.8 ± 9.1 and 62.0 ± 5.8 at 8 weeks and 81.6 ± 7.5 and 62.6 ± 5.3 at 12 weeks for the HyA and NR groups, respectively. **Figure 3-5B** shows that the mean maximal isometric torques values were also normalized as a percentage of the original baseline response, and these values were: $55.9 \pm 6.1\%$ and $48.7 \pm 6.9\%$ at 4 weeks, $71.9 \pm 8.3\%$ and $52.2 \pm 7.0\%$ at 8 weeks, and $73.4 \pm 5.8\%$ and $52.6 \pm 6.1\%$ at 12 weeks. For both measurements, implantation of HyA was associated with statistically significant increases in mean maximal torque at 8 and 12 weeks post-VML injury. Furthermore, although the average mass of the explanted TA muscles of the HyA-implanted animals was $10.9 \pm 5.6\%$ lower than the contralateral control, it was also $17.5 \pm 0.4\%$ greater than the explanted injured TA muscle of the NR animals (**Figure 3-5C**). There was no evidence of hydrogel remaining in the injury site when the muscles were explanted and weighed at the 12-week timepoint, leaving de novo muscle regeneration as a plausible explanation for the increased TA mass in the HyA-treated group relative to the non-repaired animals.

Kinetic analysis of peroneal nerve-stimulated TA contraction (dorsiflexion)

To provide additional mechanistic insight into the potential impact of VML injury and/or repair on muscle function, we analyzed the contractile response during the rapid rising phase. Of note, approximately 95% on the rise in force (torque) is observed within 60 ms of onset of the contractile response. As noted in the Methods section, and further illustrate in **Figure 3-6A & 3-B**, the data were accurately modeled using a four parameter logistic equation. **Figure 3-6** also provides a graphical depiction, over time, of the calculated values for the rate constant (k) for contraction, as well as the fitting parameter ν (ν)—which describes the rapidity with which the maximum

activation rate, determined by k , is achieved. As shown, both parameters were within the 95% Confidence Interval (CI; determined by the group mean values for all animals at baseline) at all time points, for both treatment groups, in every animal (**Fig. 3-6C-F**).

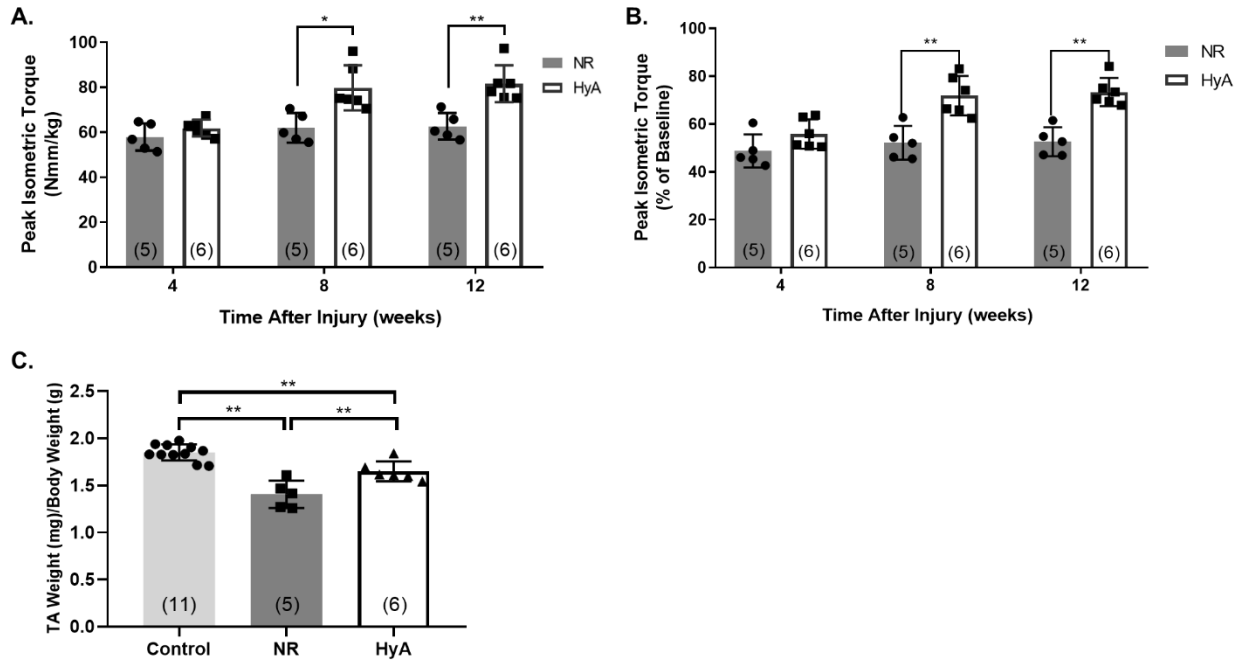


Figure 3-5. Comparison of body weight, functional baseline parameters and functional recovery observed among different treatment groups at 12 weeks post injury or repair/implantation. (A) Peak isometric torque measured at 4, 8 and 12 weeks, showing improved muscle recovery after hydrogel application as early as 8 weeks post implantation. Mean \pm SEM of baseline torque of all animals are shown as the dotted line and shaded region, respectively. (B) Individual responses are also presented as a percentage of the respective initial maximum pre-injury isometric torque response. (C). The TA weight/body weight of untreated and hydrogel-treated VML injuries were significantly lower than control. Notably, TA muscles treated with hydrogel displayed a statistically significant gain of mass comparing to untreated TA muscles, consistent with the observed functional recovery due to the nominally regenerative effect of hydrogel implantation. Data are presented as Mean \pm SEM. Group size is shown in parentheses. *, **, significantly different at $p < 0.05$ and $p < 0.01$, respectively, using Tukey's post-test after performing Two-Way ANOVA in (A, B) and One-Way ANOVA in (C).

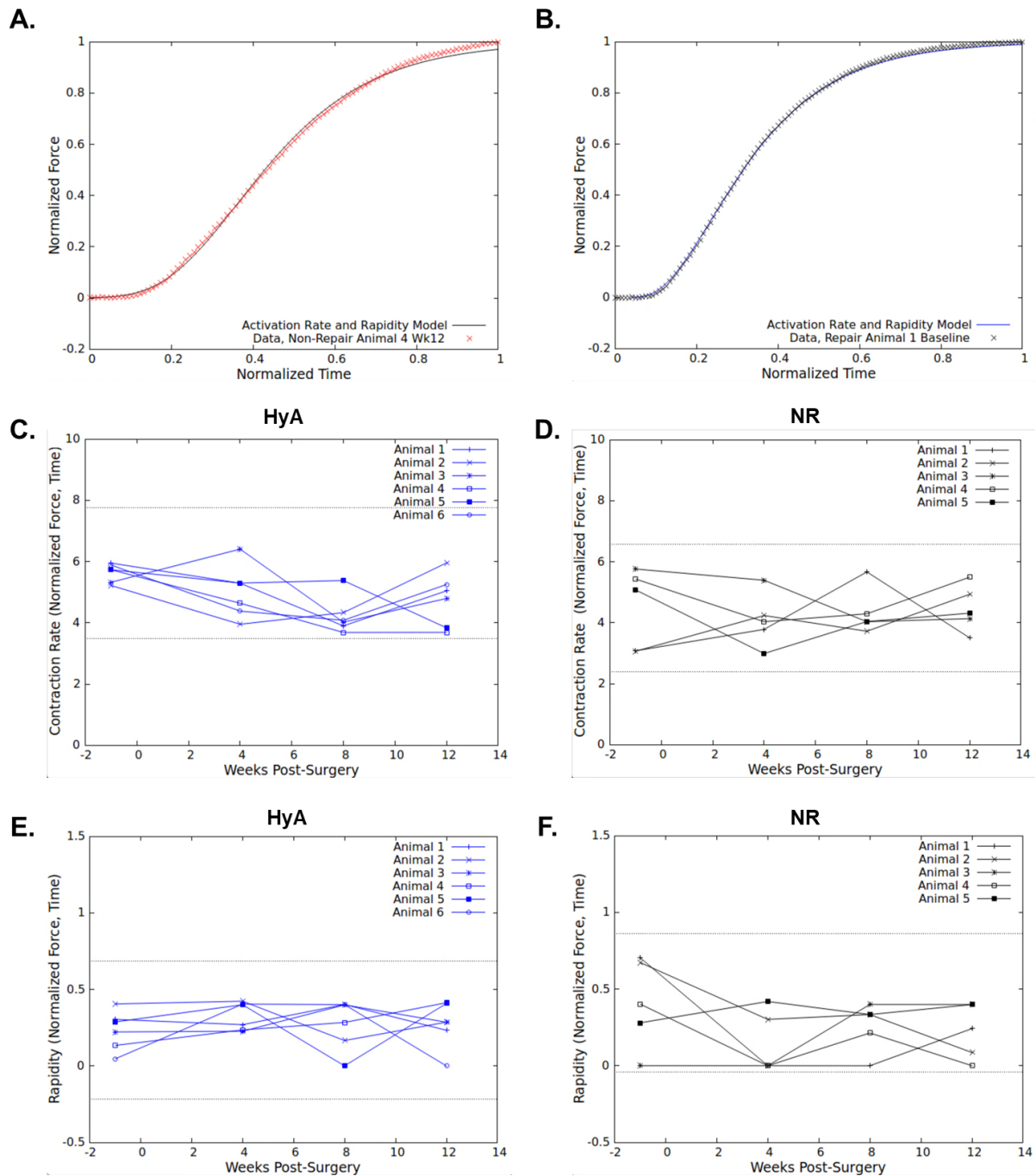


Figure 3-6. Kinetic analysis of contraction. Representative fits of the four-parameter logistic equation (see Eq. 2 in Methods) to the baseline maximal isometric torque (dorsiflexion) response. As illustrated, all raw data were fit to a logistic equation of the form: $F(t) = (1 - e^{-kt})^{[1/v]}$. Data were analyzed both pre-injury and/or treatment (see Methods and Fig. 2 for details), as well as at 4-, 8- & 12-weeks post-injury. Shown in Panels A & B are representative fits of the logistic equation to raw data for representative examples of isometric force contractions in HyA-treated as well as NR animals at 12 weeks. Again, note the excellent agreement between the model and the

raw data. Panels C & D show a graphical depiction of the calculated values of the rate constants (k) derived from fits of the logistic equation to the raw data on all animals in the HyA-repaired and non-repaired animals, respectively, over time. Panels E & F show the corresponding values for the rapidity parameter fitting constant (ν) derived from logistic fits to the same data. Note that all values of k and ν , for all treatment groups and time points, fell within the 95% Confidence Intervals for their corresponding baseline group mean values. These data clearly indicate the equivalence of activation of the TA muscle in the HyA-treated animals relative to their original baseline responses, as well as in comparison to the remaining native tissue following wound healing, but no repair (NR).

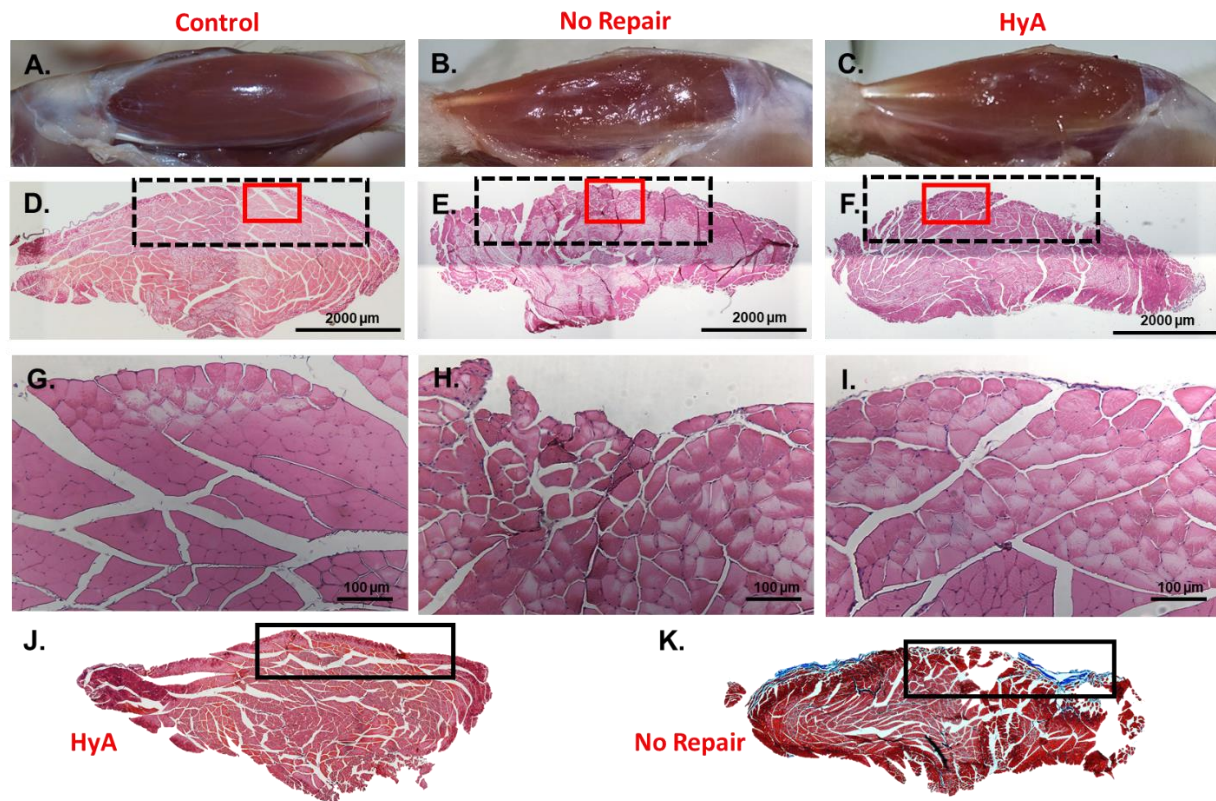


Figure 3-7. Representative images of TA muscle tissue morphology and histology in contralateral Control (Panels A, D, G) Non-Repaired (NR, Panels B, E, H) and HyA-treated (HyA, Panels C, F, I) animals. Panels A-C are images of the gross appearance of the TA muscle at 12 weeks. Panels D-F are H&E stained cross-sectional images through the belly of the TA muscle from retrieved tissues as 12 weeks; where the dashed black box outlines the larger defect region, and the smaller red box corresponds to the magnified region shown in panels G-I. Panels J & K depict Masson's trichrome staining of cross sections from distinct HyA-treated (J) and Non-repaired (NR; K) TA muscles. Note that HyA-treated TA muscles show significant muscle tissue restoration with minimal fibrosis as compared to the TA muscles from NR animals.

TA muscle tissue morphology and histology

Macroscopically, the hydrogel injection was well tolerated by the recipient animals, with no signs of infection, seroma, or rejection. Significant remodeling of the defect site was evident 12 weeks after creation of the VML injury (**Figure 3-7**). More specifically, at 12 weeks post-injury, HyA-treated animals showed significant restoration of gross tissue morphology as compared to the NR group (**Figure 3-7A-C**). This observation is consistent with the fact that in the HyA-treated animals this remodeling was accompanied by a significant increase in TA mass relative to the NR animals (shown previously in **Figure 3-5C**). **Panels D-F** in **Figure 3-7** show representative cross sections through the entire belly of the TA muscle in Control, NR and HyA-treated animals. **Panels G-I** in **Figure 3-7** show higher magnification images from **Panels D-F**, in the indicated regions (small box) within the overall defect region (larger box). Of note, these images were obtained in the first 400 μ m from the surface of the TA, in the center of the muscle belly where the defect was originally created. As illustrated, obvious indentations in the surface of the TA muscle, along the width (**Fig. 3-7, Panels E & H**) and length (**Fig. 3-7, Panel B**) of the muscle, was a common feature in the NR animals when compared to the Control and HyA-treated animals. The Masson's Trichrome staining shown in distinct TA muscles in **Panels J & K** in **Figure 3-7** also emphasize the relative lack of fibrosis in the TA muscle of HyA-treated animals when compared to the TA muscle of the NR animals at 12 weeks post-VML injury.

Muscle fiber cross-sectional area (FCSA) and centrally located nuclei (CLN)

As shown in **Figure 3-8**, in both groups, the overall distribution of **FCSA** values in the TA presented as a non-normal distribution (D'Agostino & Pearson normality test, $p > 0.05$, **Figure 3-8**)—easily visualized as a shoulder to the left and long tail on the right. The median FCSA in the

outer region (Panels A-C) of the TA of the NR animals ($762\pm 131.5\mu\text{m}^2$) was significantly smaller than both the HyA-treated animals ($1055\pm 145.1\mu\text{m}^2$, $p<0.05$) and the contralateral control muscles ($1112\pm 167.8\mu\text{m}^2$, $p<0.05$; One-Way ANOVA with Kruskal-Wallis nonparametric Dunn's post hoc multiple comparisons test). In contrast, the binned values for FCSA were normally distributed. A Two-Way ANOVA (Treatment by FCSA) revealed a highly significant interaction effect ($p<0.0001$), as well as a highly significant effect on FCSA ($p<0.0001$). Post-hoc analysis of pairwise comparisons documented significant differences in the distribution of FCSA binned values in the outer region of the TA when comparing among the NR, HyA-treated and contralateral control animals (Tukey's post-test, $p<0.05$). Specifically, the NR animals showed an abundance of smaller fibers in the $0\text{-}200\mu\text{m}^2$ bin, $201\text{-}400\mu\text{m}^2$ bin, when compared to the corresponding values in either the HyA-treated or control groups. The TA muscle in both the NR and HyA-treated animals displayed a greater proportion of FCSA values in the $401\text{-}600\mu\text{m}^2$ bin. The NR animals showed a smaller proportion of fibers than the control muscles in the $1001\text{-}1200\mu\text{m}^2$, and $1201\text{-}1400\mu\text{m}^2$ bins, while the HyA-treated animals showed a smaller proportion of fibers in the $801\text{-}1000\mu\text{m}^2$ and $1001\text{-}1200\mu\text{m}^2$ bins. However, in the inner region (**Panels D-F, Figure 3-8**) of the TA muscle there was also no significant difference in the median FCSA among the HyA-treated animals, not repaired (**NR**) animals, and the contralateral controls (One-Way ANOVA with Kruskal-Wallis nonparametric Dunn's post hoc multiple comparisons test, $p>0.05$), nor were there any detectable differences in the FCSA distribution among the three treatment groups (Two-Way ANOVA with Tukey's post-test, $p<0.05$). When comparing the percentage of fibers with centrally located nuclei (**CLN**) in the outer region of the TA muscle (**Figure 3-9**), there were significantly more CLN in fibers in the NR and HyA-treated groups when compared to the control muscles

(One-Way ANOVA with Tukey's post-test, $p < 0.05$). However, the percentage of fibers with CLN in the NR and HyA-treated animals were indistinguishable.

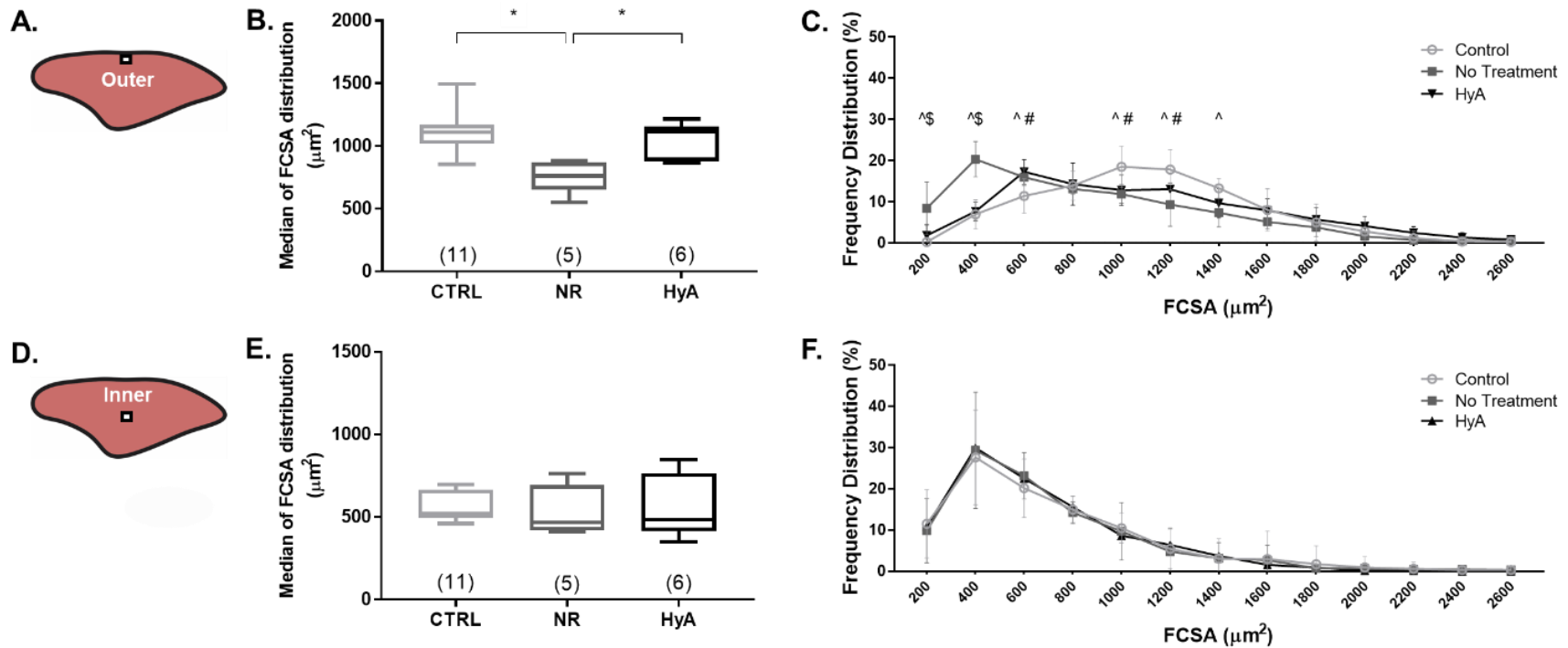


Figure 3-8. Frequency distribution of muscle fiber cross section area (FCSA) in the outer and inner portions of the muscle and centrally located nuclei percentage. Panels A and D provide a schematic depiction of TA muscle cross section, and indicate the relative locations where measurements were made⁴⁷. (B) In upper portion of the TA muscle, the median value of the FCSA distribution was significantly smaller in muscle fibers from untreated TA muscles than the corresponding values in the TA muscles from the contralateral control group and HyA-treated group (Kruskal-Wallis One-Way ANOVA with Dunn's multiple comparisons post hoc test). No statistical difference was observed between control and HyA-treated TA muscles. (C) Distribution of FCSA values in the outer portion of the TA muscle of non-repaired (NR) and HyA-treated muscles, as well as contralateral controls. Note the fiber distribution in the NR group is shifted to the left (smaller fiber sizes), while larger fiber sizes (akin to native skeletal muscle) were observed following HyA treatment. (E) In the inner portion of the TA muscle, no significant differences in the median FCSA values were noted. (F) Accordingly, the distribution of FCSA values in all groups is virtually indistinguishable in the inner portion of the TA muscle of non-repaired (NR), HyA-treated animals, and contralateral controls. (G) Comparison of the percent of centrally located nuclei found in the fibers of the outer portion of the TA muscle. Significant differences were detected by One-Way ANOVA with Tukey's post-test. Of note, in all cases, the overall distribution of FCSA values in the TA presented as a non-normal distribution (D'Agostino & Pearson normality test, $p > 0.05$). Thus, data are presented as Median \pm Min and Max. Group size is displayed in parentheses. For FCSA in panels (C) and (F), ^ indicates that the NR group differs from Control, # indicates that HyA differs from Control, and \$ indicates that HyA differs from NR using Two-Way ANOVA with Tukey's post-test. All significant differences are $p < 0.05$.

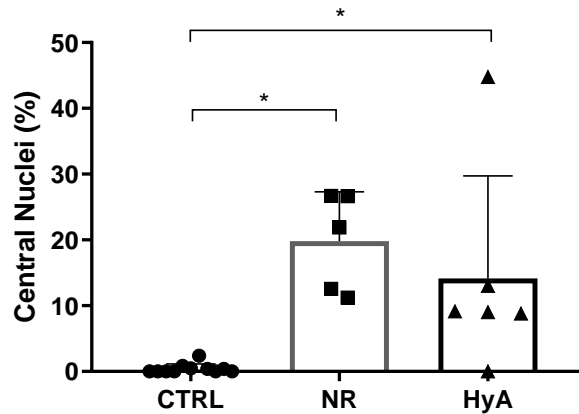


Figure 3-9. Centrally Located Nuclei. Comparison of the percent of centrally located nuclei found in the fibers of the outer portion of the TA muscle. Significant differences were detected by One-Way ANOVA with Tukey’s post-hoc test ($p < 0.05$).

Muscle tissue Vascularization

Vascularization is a critical component of normal skeletal muscle function, and an absolute prerequisite for functional regeneration. As such, we evaluated revascularization of the myofibers in the HyA-implanted defect region as well as the area adjacent to the defect region in the NR animals (where there was little or no new muscle tissue formation). Those were then compared to the vascularization observed in the TA muscle of the contralateral control leg. Specifically, we were interested the number of CD31+ cells surrounding muscle fibers in the injured and implanted region of the TA muscle in the HyA-treated group versus the non-repaired defect and the contralateral control TA—as this was nominally the site of some *de novo* muscle fiber regeneration consistent with mass recovery (demonstrated in **Fig. 3-5C**). As shown in **Figure 3-10**, there were no detectable statistically differences between the number of surrounding capillaries in either of the study groups when compared to each other, nor when compared to the contralateral control TA (4.0 ± 0.6 (HyA) vs. 3.9 ± 0.2 (NR) vs. 3.9 ± 0.4 (Control), 1.5mm^2 analyzed, $p > 0.05$ after *t*-test, **Figure 3-10**).

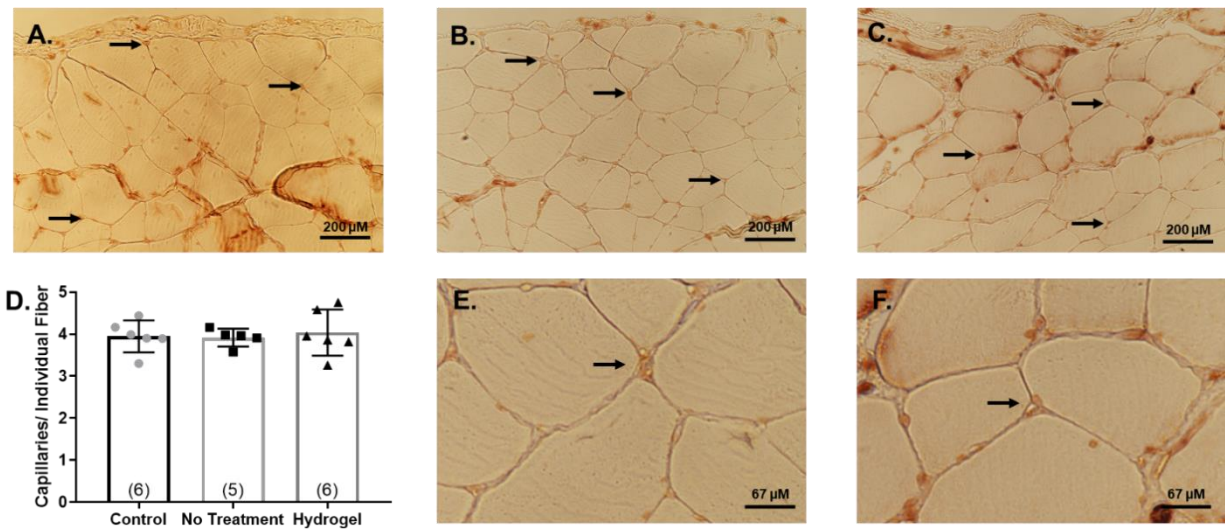


Figure 3-10. Capillary density. The capillary density was assessed by CD31 staining. Panels A, B, and C display representative images of CD31 staining in the outer portion of the TA muscles from contralateral control (A), HyA-treated animals (B), and unrepaired animals (C)—this is the region of the TA that was injured and implanted with HyA (treated) or injured and left untreated. Black arrows depict CD31 positive cells. Panel D illustrates that there was no significant difference ($p > 0.05$) in capillary density, quantified by number of capillaries per individual muscle fiber, was observed between the groups using a Student’s t-test. Panels E and F are magnified portions of panels B and C to better illustrate the CD31+ cells. Data are presented as Mean \pm SEM. Group size is noted in parentheses.

Discussion

While the substantial intrinsic capacity for regeneration of skeletal muscle has been well documented, there remain no commercially available tissue engineered products to leverage this regenerative ability into effective treatments for irreversible muscle damage/loss (i.e. VML). Despite some encouraging results from recent pre-clinical and clinical studies into treatment of VML injury with dECM implantation^{23-25,64-66}, there is still vast room for improvement in regenerative therapeutics. This fact has directly facilitated a rapidly increasing preclinical effort into the development of tissue engineered and regenerative medicine technologies with greater efficacy and a broader range of applications for VML and VML-like injuries.

In pursuit of additional approaches to the treatment of VML injuries, this study evaluated the efficacy and utility of semi-synthetic HyA hydrogels. Our HyA-based hydrogels are biocompatible, biodegradable, non-immunogenic, and can also play an integral role in encouraging tissue development and repair³³ by sequestering endogenously synthesized growth factors through the addition of conjugated heparin³⁵. The overall approach is highlighted in **Figure 3-1**. While this study has not explicitly examined the role played by each individual component within our HyA system (adhesion ligand, MMP-sensitive crosslinker, heparin), previous studies have demonstrated the role each component plays related to muscle regeneration^{33-35,41,42,44,51}.

In short, as illustrated, the baseline measurements, as well as the mean maximal torque in the NR group is consistent with previously published data^{22,57-59}, indicating the reproducibility and applicability of the rodent tibialis anterior (TA) VML injury model (**Figs. 3-3 through 3-5**). If one uses statistically significant increases in maximal isometric torque over the NR group as an indication of functional recovery, then one can conclude that the implantation of HyA hydrogel has a positive impact (**Figs. 3-5A&B**). To put these observations into context, it should be noted

that the TA synergist muscles (Extensor Digitorum Longus (EDL) and Extensor Hallucis Longus (EHL)) were ablated (surgically removed at the time of creation of the surgical VML injury, resulting in a permanent ~20% functional deficit²². As such, after removal of 20-30% of the TA muscle, the total functional deficit is ~50%, of which only 30% is understood to be the theoretical maximal ceiling of recovery over a 12-week evaluation period. Nonetheless, this is not an absolute measure of complete functional recovery, but rather, a physiologically relevant barometer against which we can evaluate the relative degree of functional regeneration over time.

As noted above, the expected theoretical maximum, though not absolute, implies a recovery ceiling of roughly 80% of the preinjury baseline maximal isometric torque response (note that the normalized peak torque response does not change over time in age-matched control animals). In this setting, the NR group exhibited a mean maximal torque response of $52.6 \pm 6.1\%$ whereas the HyA-implanted group exhibited mean values of $71.9 \pm 8.3\%$ and $73.4 \pm 5.8\%$ at both 8 and 12 weeks post-injury and repair. These values represent robust functional recoveries of 89.8% and 91.7% of the 80% expected theoretical maximum possible recovery. This is also the first instance of statistically significant recovery of muscle function observed at 8 weeks post-implantation in this animal model of VML injury, illustrating a substantial leftward shift in the recovery timeline (**Fig. 3-5**).

Qualitative and quantitative morphological and histological analyses also provide important insights into the potential mechanisms responsible for the observed functional recovery in the HyA group. For example, consistent with the robust functional recovery observed, as illustrated by the representative examples and functional data in **Figures 3-4 & 3-5**, the TA muscles treated with our HyA-hydrogels appeared to show significant volume reconstitution. That is, the HyA-treated animals showed significantly greater mass than the NR animals (**Figure 3-5C**), as well as

decreased fibrotic deposition compared to the NR animals in this study (compare panels J & K in **Figure 3-7**). Additionally, we document in **Fig. 3-5C** that the normalized average mass of the retrieved TA muscle from the HyA-treated rats is significantly greater ($\approx 18\%$) than the average mass of the NR. Given the important link between muscle mass and muscle force, this is an important observation that likely accounts for a significant fraction of the force recovery we observed—specifically $\approx 60\%$ of the total 30% force difference in the TA muscle between HyA and NR animals at 12 weeks.

Capillary density in the area of HyA implantation and VML repair (where there should be no tissue as a result of the VML injury (see **Figs. 3-7 & 3-10**)) was statistically indistinguishable from that observed in the native TA muscle tissue in the NR and contralateral control animals. This is consistent with the supposition that vascularization of the repaired/regenerated tissue in the HyA-treated animals was similar to that in the contralateral control and non-repaired animals (where the lack of gain in weight and force in the NR TA muscle indicated that we were primarily surveying remaining native fibers at the interface with the surgically created VML injury). In addition, the median fiber cross sectional area (FCSA) value in the contralateral control and HyA-treated animals were equivalent, and both were greater than that observed in the NR (no repair) TA muscles (**Fig. 3-8**). Moreover, there were twice the number of significant differences in FCSA binned values between the TA muscles of the NR and control (6; see **Fig. 3-8**), than between the binned FCSA values in the TA of the HyA-treated when compared to control (3; see **Fig. 3-8**). Finally, an increase in centrally located nuclei (CLN) was detected in TA muscle fibers of both the NR and HyA-treated animals (**Fig. 3-9**). While the precise mechanism(s) responsible for this finding is not known, it is likely that the former reflects a relatively continuous cycle of tissue damage and repair due to overload injury on the smaller mass/volume of muscle fibers (overload

injury is also consistent with the observed diffuse fibrosis in the NR animals), while the latter is consistent with *de novo* muscle regeneration and repair. Certainly, this matter requires further investigation in future work. Of note, the magnitude of functional recovery observed in these studies also compares favorably with prior work following therapeutic implantation with other technologies^{22,57,58}. Since no donor cells were added, taken together, these findings make it reasonable to conclude that the observed functional recovery was attributable, at least in part, to the observed volume/mass recovery, and thus, related to *de novo* muscle fiber regeneration. Furthermore, our data also support the supposition that the accelerated functional recovery observed at 8 weeks and sustained at 12 weeks may be a reflection of the previously documented enhanced angiogenic potential of the HyA-based matrix^{34,35}, and the proposed subsequent enhanced migration of cells into the matrix during wound healing.

Lastly, we also include a kinetic analysis of the peroneal nerve stimulated contractile responses in our system. In short, our analyses revealed that the activation kinetics for muscle contraction in HyA-treated animals, as reflected by the calculated rate constant (see Methods section for logistic analysis description and **Fig. 3-6**) is indistinguishable from the calculated rate constant of the baseline control measurements, as well as the mean calculated rate constant in the unrepaired animals (NR). Specifically, all three treatment groups achieve more than 95% of their maximal isometric contractile (torque) responses within 60ms of contractile onset. Thus, while the VML injury per se diminishes the magnitude of TA contractile response due to removal of bulk tissue in the NR animals, the activation of the remaining native tissue is unaffected. Similarly, the robust, though not complete, restoration of the magnitude of the TA contractile response following implantation of the HyA-gel is still achieved over the same 60ms time frame as the baseline

response. As such, sound scientific logic suggests that neural activation of the repaired tissue is largely equivalent to that observed for the baseline response (see Methods).

As noted in the Introduction, hyaluronic acid (HyA) hydrogels are widely used for tissue engineering and regenerative medicine applications³⁰⁻³². Of particular relevance to this work, are a few examples of more recent studies that have used HyA-based biomaterials for muscle regeneration/VML-repair⁵²⁻⁵⁶ as they highlight some of the key distinctions from our biomaterial system. For example, while Goldman et al.⁵³ and Rossi et al.⁵⁵ do use an implantable HyA-based hydrogel system in a VML injury, in both cases progenitor cells are co-delivered which is quite different to our cell-free HyA system. Desiderio et al.⁵² demonstrate that a HyA hydrogel can support the differentiation of NG2+ ASCs, although this is demonstrated in a subcutaneous model rather than a VML injury model. Garcia et al. demonstrate the importance of adhesion peptides in the context of HyA biomaterials, identifying the IKVAV sequence as superior to a basic RGDS motif and a Tenascin-C derived peptide with respect to migration, proliferation and gene expression of myoblasts—though this system has yet to be tested in vivo. Furthermore, it should be noted that the bsp-RGD(15) sequence used in this study is superior to the basic RGD sequences⁶¹, as well as IKVAV⁶⁷ (which can be a poor ligand for many cell types⁶⁷). Finally, Narayanan and colleagues⁵⁴ have developed a promising implantable HyA-based biomaterial and provided initial proof of concept for functional recovery in a relatively small mouse quadriceps VML injury model (less than ½ the size of the rat TA VML injury). However, no direct measures of muscle contractile force were reported, and follow-up was limited to 1-month post-injury, limiting interpretation of durability. In addition, there are also key biomaterial differences in their system, most notably the lack of cell adhesion ligands and cell-responsive degradation kinetics. While the extant published preclinical work with HyA-based biomaterials is clearly promising,

further improvements in functional recovery and scale up are still needed, and our biomaterial system is sufficiently distinct from other current approaches, and moreover, highly tunable to provide increased therapeutic efficacy in future studies.

Conclusion

In conclusion, it is clear that we cannot ascribe all of the functional recovery observed in the TA muscles from the HyA-treated animals to *de novo* muscle tissue regeneration *per se*. Nonetheless, the morphological changes (as a 18% increase in muscle mass compared to the NR TA—nominally accounting for $\approx 60\%$ of the 30% force difference between the TA muscles of the HyA-treated and NR animals), and histological observations (the median FCSA value in TA muscles from control and HyA-treated animals were statistically indistinguishable, and there was little or no fibrosis and no detectable hydrogel remaining in the HyA-treated animals) are both consistent with the physiological findings (significantly increased muscle force in HyA-treated relative to NR TA muscles). Thus, taken together, our findings do indicate that the characteristics of the HyA-repaired TA muscle more closely approximate expected key native muscle tissue features, and moreover, result in statistically significant and functionally important improvements muscle contraction. In short, we have shown that our tunable heparin-conjugated HyA hydrogel-based system can successfully promote rapid (8 weeks), significant and sustainable functional recovery in instances of severe and otherwise irrecoverable skeletal muscle damage in an established and biologically relevant rodent model of TA VML injury. Without question, there is still considerable room for therapeutic improvement—in terms of more complete functional recovery of muscle force, mass and structure. The presumptive mode of action is that the HyA hydrogel stabilizes the defect area and promotes a microenvironment that is more favorable for endogenous muscle regeneration and remodeling in the injured region of the TA muscle. These

initial observations bode well for the potential utility of this biomaterial system for improved treatment of VML injury.

Data availability statement

The raw and processed data required to reproduce these findings will be made available via contact with the corresponding author.

Acknowledgements

Thanks to the members of the Laboratory of Regenerative Therapeutics at the University of Virginia for their contributions.

Funding Sources

For UCB: Support for this work was provided by in part by American Heart Association Postdoctoral Fellowship to S.B. (17POST33670003), National Heart Lung and Blood Institute of the NIH R01HL096525 (K.E.H.), the Jan Fandrianto and Selfia Halim Chair (K.E.H.).

For UVA: DoD/USAMRAA, award number: W81XWH-17-PRORP-ARA (Christ, PI; Healy, CO-I)

Conflict of Interest

The authors confirm that there are no known conflicts of interest associated with this publication and there has been no significant financial support for this work that could have influenced its outcome.

References

- 1 Carlson, B. M. Regeneration of the completely excised gastrocnemius muscle in the frog and rat from minced muscle fragments. *Journal of Morphology* **125**, 447-471, doi:10.1002/jmor.1051250405 (1968).
- 2 Carlson, B. M. & Faulkner, J. A. The regeneration of skeletal muscle fibers following injury: a review. *Medicine and science in sports and exercise* **15**, 187-198, doi:10.1249/00005768-198315030-00003 (1983).
- 3 Ciciliot, S. & Schiaffino, S. Regeneration of mammalian skeletal muscle. Basic mechanisms and clinical implications. *Current pharmaceutical design* **16**, 906-914, doi:10.2174/138161210790883453 (2010).
- 4 Warren, G. L. *et al.* Mechanisms of skeletal muscle injury and repair revealed by gene expression studies in mouse models. *The Journal of physiology* **582**, 825-841, doi:10.1113/jphysiol.2007.132373 (2007).
- 5 White, T. P. & Devor, S. T. Skeletal muscle regeneration and plasticity of grafts. *Exercise and sport sciences reviews* **21**, 263-295, doi:10.1249/00003677-199301000-00009 (1993).
- 6 Grogan, B. F. & Hsu, J. R. Volumetric muscle loss. *The Journal of the American Academy of Orthopaedic Surgeons* **19 Suppl 1**, S35-37, doi:10.5435/00124635-201102001-00007 (2011).
- 7 Holcomb, J. B., Stansbury, L. G., Champion, H. R., Wade, C. & Bellamy, R. F. Understanding Combat Casualty Care Statistics. *The Journal of Trauma: Injury, Infection, and Critical Care* **60**, 397-401, doi:10.1097/01.ta.0000203581.75241.f1 (2006).
- 8 Amin, S., Achenbach, S. J., Atkinson, E. J., Khosla, S. & Melton, L. J. Trends in fracture incidence: A population-based study over 20 years. *Journal of Bone and Mineral Research* **29**, 581-589, doi:10.1002/jbmr.2072 (2014).
- 9 Fowler, K. A., Dahlberg, L. L., Haileyesus, T. & Anness, J. L. Firearm injuries in the United States. *Preventive Medicine* **79**, 5-14, doi:10.1016/j.ypmed.2015.06.002 (2015).
- 10 Lin, C.-H., Lin, Y.-T., Yeh, J.-T. & Chen, C.-T. Free Functioning Muscle Transfer for Lower Extremity Posttraumatic Composite Structure and Functional Defect. *Plastic and Reconstructive Surgery* **119**, 2118-2126, doi:10.1097/01.prs.0000260595.85557.41 (2007).
- 11 Corona, B. T. *et al.* Further development of a tissue engineered muscle repair construct in vitro for enhanced functional recovery following implantation in vivo in a murine model of volumetric muscle loss injury. *Tissue engineering. Part A* **18**, 1213-1228, doi:10.1089/ten.TEA.2011.0614 (2012).
- 12 Corona, B. T. *et al.* The promotion of a functional fibrosis in skeletal muscle with volumetric muscle loss injury following the transplantation of muscle-ECM. *Biomaterials* **34**, 3324-3335, doi:10.1016/j.biomaterials.2013.01.061 (2013).

- 13 Criswell, T. L. *et al.* The role of endothelial cells in myofiber differentiation and the vascularization and innervation of bioengineered muscle tissue in vivo. *Biomaterials* **34**, 140-149, doi:10.1016/j.biomaterials.2012.09.045 (2013).
- 14 Machingal, M. A. *et al.* A Tissue-Engineered Muscle Repair Construct for Functional Restoration of an Irrecoverable Muscle Injury in a Murine Model. *Tissue Engineering Part A* **17**, 2291-2303, doi:10.1089/ten.tea.2010.0682 (2011).
- 15 Merritt, E. K. *et al.* Repair of traumatic skeletal muscle injury with bone-marrow-derived mesenchymal stem cells seeded on extracellular matrix. *Tissue engineering. Part A* **16**, 2871-2881, doi:10.1089/ten.TEA.2009.0826 (2010).
- 16 VanDusen, K. W., Syverud, B. C., Williams, M. L., Lee, J. D. & Larkin, L. M. Engineered skeletal muscle units for repair of volumetric muscle loss in the tibialis anterior muscle of a rat. *Tissue engineering. Part A* **20**, 2920-2930, doi:10.1089/ten.TEA.2014.0060 (2014).
- 17 Williams, M. L., Kostrominova, T. Y., Arruda, E. M. & Larkin, L. M. Effect of implantation on engineered skeletal muscle constructs. *Journal of Tissue Engineering and Regenerative Medicine* **7**, 434-442, doi:10.1002/term.537 (2013).
- 18 Merritt, E. K. *et al.* Functional assessment of skeletal muscle regeneration utilizing homologous extracellular matrix as scaffolding. *Tissue Engineering - Part A* **16**, 1395-1405, doi:10.1089/ten.tea.2009.0226 (2010).
- 19 Perniconi, B. *et al.* The pro-myogenic environment provided by whole organ scale acellular scaffolds from skeletal muscle. *Biomaterials* **32**, 7870-7882, doi:10.1016/j.biomaterials.2011.07.016 (2011).
- 20 Sicari, B. M. *et al.* A murine model of volumetric muscle loss and a regenerative medicine approach for tissue replacement. *Tissue Engineering - Part A* **18**, 1941-1948, doi:10.1089/ten.tea.2012.0475 (2012).
- 21 Turner, N. J., Badylak, J. S., Weber, D. J. & Badylak, S. F. Biologic scaffold remodeling in a dog model of complex musculoskeletal injury. *Journal of Surgical Research* **176**, 490-502, doi:10.1016/j.jss.2011.11.1029 (2012).
- 22 Corona, B. T., Ward, C. L., Baker, H. B., Walters, T. J. & Christ, G. J. Implantation of In Vitro Tissue Engineered Muscle Repair Constructs and Bladder Acellular Matrices Partially Restore In Vivo Skeletal Muscle Function in a Rat Model of Volumetric Muscle Loss Injury. *Tissue Engineering - Part A* **20**, 705-715, doi:10.1089/ten.TEA.2012.0761 (2014).
- 23 Han, N. *et al.* Electrodiagnostic Evaluation of Individuals Implanted With Extracellular Matrix for the Treatment of Volumetric Muscle Injury: Case Series. *Physical Therapy* **96**, 540-549, doi:10.2522/ptj.20150133 (2016).
- 24 Mase, V. J. *et al.* Clinical application of an acellular biologic scaffold for surgical repair of a large, traumatic quadriceps femoris muscle defect. *Orthopedics* **33**, 511-511, doi:10.3928/01477447-20100526-24 (2010).

- 25 Sicari, B. M. *et al.* An Acellular Biologic Scaffold Promotes Skeletal Muscle Formation in Mice and Humans with Volumetric Muscle Loss. *Science Translational Medicine* **6**, 234ra258-234ra258, doi:10.1126/scitranslmed.3008085 (2014).
- 26 Ostrovidov, S. *et al.* 3D Bioprinting in Skeletal Muscle Tissue Engineering. *Small* **15**, e1805530, doi:10.1002/sml.201805530 (2019).
- 27 Choi, Y. J. *et al.* A 3D cell printed muscle construct with tissue-derived bioink for the treatment of volumetric muscle loss. *Biomaterials* **206**, 160-169, doi:10.1016/j.biomaterials.2019.03.036 (2019).
- 28 Bour, R. K. *et al.* Bioprinting on sheet-based scaffolds applied to the creation of implantable tissue-engineered constructs with potentially diverse clinical applications: Tissue-Engineered Muscle Repair (TEMR) as a representative testbed. *Connective Tissue Research* **61**, 216-228, doi:10.1080/03008207.2019.1679800 (2020).
- 29 Russell, C. S. *et al.* In Situ Printing of Adhesive Hydrogel Scaffolds for the Treatment of Skeletal Muscle Injuries. *ACS Applied Bio Materials* **3**, 1568-1579, doi:10.1021/acsabm.9b01176 (2020).
- 30 Prestwich, G. D. & Healy, K. E. Why regenerative medicine needs an extracellular matrix. *Expert opinion on biological therapy* **15**, 3-7, doi:10.1517/14712598.2015.975200 (2015).
- 31 Highley, C. B., Prestwich, G. D. & Burdick, J. A. Recent advances in hyaluronic acid hydrogels for biomedical applications. *Curr Opin Biotechnol* **40**, 35-40, doi:10.1016/j.copbio.2016.02.008 (2016).
- 32 Pereira, H. *et al.* Hyaluronic Acid. *Adv Exp Med Biol* **1059**, 137-153, doi:10.1007/978-3-319-76735-2_6 (2018).
- 33 Jha, A. K. *et al.* Molecular weight and concentration of heparin in hyaluronic acid-based matrices modulates growth factor retention kinetics and stem cell fate. *Journal of Controlled Release* **209**, 308-316, doi:10.1016/j.jconrel.2015.04.034 (2015).
- 34 Jha, A. K. *et al.* Matrix metalloproteinase-13 mediated degradation of hyaluronic acid-based matrices orchestrates stem cell engraftment through vascular integration. *Biomaterials* **89**, 136-147, doi:10.1016/j.biomaterials.2016.02.023 (2016).
- 35 Jha, A. K. *et al.* Enhanced survival and engraftment of transplanted stem cells using growth factor sequestering hydrogels. *Biomaterials* **47**, 1-12, doi:10.1016/J.BIOMATERIALS.2014.12.043 (2015).
- 36 Craig, E. A., Parker, P., Austin, A. F., Barnett, J. V. & Camenisch, T. D. Involvement of the MEKK1 signaling pathway in the regulation of epicardial cell behavior by hyaluronan. *Cellular Signalling* **22**, 968-976, doi:10.1016/j.cellsig.2010.02.004 (2010).
- 37 Browne, S. & Healy, K. E. Matrix-assisted cell transplantation for tissue vascularization. *Advanced Drug Delivery Reviews* **146**, 155-169, doi:10.1016/j.addr.2018.12.016 (2019).
- 38 Browne, S., Hossainy, S. & Healy, K. Hyaluronic Acid Macromer Molecular Weight Dictates the Biophysical Properties and in Vitro Cellular Response to Semisynthetic

- Hydrogels. *ACS Biomaterials Science and Engineering*, doi:10.1021/acsbiomaterials.9b01419 (2020).
- 39 Browne, S. *et al.* TGF- β 1/CD105 signaling controls vascular network formation within growth factor sequestering hyaluronic acid hydrogels. *PLOS ONE* **13**, e0194679-e0194679, doi:10.1371/journal.pone.0194679 (2018).
- 40 Natividad-Diaz, S. L. *et al.* A combined hiPSC-derived endothelial cell and in vitro microfluidic platform for assessing biomaterial-based angiogenesis. *Biomaterials* **194**, 73-83, doi:10.1016/j.biomaterials.2018.11.032 (2019).
- 41 Pardue, E. L., Ibrahim, S. & Ramamurthi, A. Role of hyaluronan in angiogenesis and its utility to angiogenic tissue engineering. *Organogenesis* **4**, 203-214, doi:10.4161/org.4.4.6926 (2008).
- 42 Park, D. *et al.* Hyaluronic acid promotes angiogenesis by inducing RHAMM-TGF β receptor interaction via CD44-PKC δ . *Molecules and Cells* **33**, 563-574, doi:10.1007/s10059-012-2294-1 (2012).
- 43 Leng, Y., Abdullah, A., Wendt, M. K. & Calve, S. Hyaluronic acid, CD44 and RHAMM regulate myoblast behavior during embryogenesis. *Matrix Biology* **78-79**, 236-254, doi:10.1016/j.matbio.2018.08.008 (2019).
- 44 Calve, S., Isaac, J., Gumucio, J. P. & Mendias, C. L. Hyaluronic acid, HAS1, and HAS2 are significantly upregulated during muscle hypertrophy. *American Journal of Physiology-Cell Physiology* **303**, C577-C588, doi:10.1152/ajpcell.00057.2012 (2012).
- 45 Cai, S., Liu, Y., Zheng Shu, X. & Prestwich, G. D. Injectable glycosaminoglycan hydrogels for controlled release of human basic fibroblast growth factor. *Biomaterials* **26**, 6054-6067, doi:10.1016/j.biomaterials.2005.03.012 (2005).
- 46 Pike, D. B. *et al.* Heparin-regulated release of growth factors in vitro and angiogenic response in vivo to implanted hyaluronan hydrogels containing VEGF and bFGF. *Biomaterials* **27**, 5242-5251, doi:10.1016/j.biomaterials.2006.05.018 (2006).
- 47 Prokoph, S. *et al.* Sustained delivery of SDF-1 α from heparin-based hydrogels to attract circulating pro-angiogenic cells. *Biomaterials* **33**, 4792-4800, doi:10.1016/j.biomaterials.2012.03.039 (2012).
- 48 Sakiyama-Elbert, S. E. & Hubbell, J. A. Development of fibrin derivatives for controlled release of heparin-binding growth factors. *Journal of controlled release : official journal of the Controlled Release Society* **65**, 389-402, doi:10.1016/s0168-3659(99)00221-7 (2000).
- 49 Sakiyama-Elbert, S. E. & Hubbell, J. A. Controlled release of nerve growth factor from a heparin-containing fibrin-based cell ingrowth matrix. *Journal of controlled release : official journal of the Controlled Release Society* **69**, 149-158, doi:10.1016/s0168-3659(00)00296-0 (2000).
- 50 Yang, J. *et al.* Heparin-Binding Epidermal Growth Factor-Like Growth Factor and Mesenchymal Stem Cells Act Synergistically to Prevent Experimental Necrotizing

- Enterocolitis. *Journal of the American College of Surgeons* **215**, 534-545, doi:10.1016/j.jamcollsurg.2012.05.037 (2012).
- 51 Desgranges, P., Barbaud, C., Caruelle, J.-P., Barritault, D. & Gautron, J. A substituted dextran enhances muscle fiber survival and regeneration in ischemic and denervated rat EDL muscle. *The FASEB Journal* **13**, 761-766, doi:10.1096/fasebj.13.6.761 (1999).
- 52 Desiderio, V. *et al.* Human Ng2+ adipose stem cells loaded in vivo on a new crosslinked hyaluronic acid-Lys scaffold fabricate a skeletal muscle tissue. *Journal of cellular physiology* **228**, 1762-1773, doi:10.1002/jcp.24336 (2013).
- 53 Goldman, S. M., Henderson, B. E. P., Walters, T. J. & Corona, B. T. Co-delivery of a laminin-111 supplemented hyaluronic acid based hydrogel with minced muscle graft in the treatment of volumetric muscle loss injury. *PloS one* **13**, e0191245, doi:10.1371/journal.pone.0191245 (2018).
- 54 Narayanan, N. *et al.* Biomimetic glycosaminoglycan-based scaffolds improve skeletal muscle regeneration in a Murine volumetric muscle loss model. *Bioact Mater* **6**, 1201-1213, doi:10.1016/j.bioactmat.2020.10.012 (2021).
- 55 Rossi, C. A. *et al.* In vivo tissue engineering of functional skeletal muscle by freshly isolated satellite cells embedded in a photopolymerizable hydrogel. *FASEB journal : official publication of the Federation of American Societies for Experimental Biology* **25**, 2296-2304, doi:10.1096/fj.10-174755 (2011).
- 56 Silva Garcia, J. M., Panitch, A. & Calve, S. Functionalization of hyaluronic acid hydrogels with ECM-derived peptides to control myoblast behavior. *Acta biomaterialia* **84**, 169-179, doi:10.1016/j.actbio.2018.11.030 (2019).
- 57 Mintz, E. L. *et al.* Long-Term Evaluation of Functional Outcomes Following Rat Volumetric Muscle Loss Injury and Repair. *Tissue Engineering Part A* **26**, 140-156, doi:10.1089/ten.tea.2019.0126 (2020).
- 58 Passipieri, J. A. *et al.* Keratin Hydrogel Enhances In Vivo Skeletal Muscle Function in a Rat Model of Volumetric Muscle Loss. *Tissue engineering. Part A* **23**, 556-571, doi:10.1089/ten.TEA.2016.0458 (2017).
- 59 Wu, X., Corona, B. T., Chen, X. & Walters, T. J. A Standardized Rat Model of Volumetric Muscle Loss Injury for the Development of Tissue Engineering Therapies. *BioResearch Open Access* **1**, 280-290, doi:10.1089/biores.2012.0271 (2012).
- 60 Harbers, G. M., Gamble, L. J., Irwin, E. F., Castner, D. G. & Healy, K. E. Development and Characterization of a High-Throughput System for Assessing Cell-Surface Receptor-Ligand Engagement. *Langmuir* **18**, 8374-8384, doi:10.1021/LA050396Y (2005).
- 61 Harbers, G. M. & Healy, K. E. The effect of ligand type and density on osteoblast adhesion, proliferation, and matrix mineralization. *Journal of Biomedical Materials Research Part A* **75A**, 855-869, doi:10.1002/jbm.a.30482 (2005).

- 62 Rezania, A. & Healy, K. E. Biomimetic Peptide Surfaces That Regulate Adhesion, Spreading, Cytoskeletal Organization, and Mineralization of the Matrix Deposited by Osteoblast-like Cells. *Biotechnology Progress* **15**, 19-32, doi:10.1021/bp980083b (1999).
- 63 Mintz, E. L., Passipieri, J. A., Lovell, D. Y. & Christ, G. J. Applications of In Vivo Functional Testing of the Rat Tibialis Anterior for Evaluating Tissue Engineered Skeletal Muscle Repair. *J Vis Exp*, doi:10.3791/54487 (2016).
- 64 Turner, N. J. *et al.* Xenogeneic extracellular matrix as an inductive scaffold for regeneration of a functioning musculotendinous junction. *Tissue engineering. Part A* **16**, 3309-3317, doi:10.1089/ten.TEA.2010.0169 (2010).
- 65 Valentin, J. E., Turner, N. J., Gilbert, T. W. & Badylak, S. F. Functional skeletal muscle formation with a biologic scaffold. *Biomaterials* **31**, 7475-7484, doi:10.1016/j.biomaterials.2010.06.039 (2010).
- 66 Wolf, M. T., Daly, K. A., Reing, J. E. & Badylak, S. F. Biologic scaffold composed of skeletal muscle extracellular matrix. *Biomaterials* **33**, 2916-2925, doi:10.1016/j.biomaterials.2011.12.055 (2012).
- 67 Saha, K., Irwin, E. F., Kozhukh, J., Schaffer, D. V. & Healy, K. E. Biomimetic interfacial interpenetrating polymer networks control neural stem cell behavior. *J Biomed Mater Res A* **81**, 240-249, doi:10.1002/jbm.a.30986 (2007).

Chapter 4 – Rodent Gait Biomechanics in Response to TA VML Injury

Disclaimer: passages have been quoted verbatim from [Dienes, J., Hu, X., Slater, C., Jansen, K., Dooley, E., Christ, G.J. & Russell, S.D. Analysis and Modeling of Rat Gait Biomechanical Deficits in Response to Volumetric Muscle Loss Injury. *Frontiers in Bioengineering and Biotechnology*. 7:146. doi: 10.3389/fbioe.2019.00146]. Figures copied with permission (CC BY 4.0).

Introduction

Volumetric muscle loss (VML) is characterized as an injury that exceeds the intrinsic regenerative capacity of skeletal muscle and results in irrecoverable tissue loss and permanent functional impairment¹. VML can be caused by a wide variety of conditions, including disease, surgical procedures, congenital anomalies, and traumatic injury suffered by both civilians and military personnel. Significant preclinical research into therapies for regeneration of the lost muscle volume is underway, with strategies including various combinations of scaffolds, hydrogels, and exercise regimens²⁻¹². These therapies have seen some success in terms of volume reconstitution, tissue remodeling, and recovery of force generation in the injured muscle. To date, improved force generation ability has been considered the most important and physiologically relevant index of muscle repair/regeneration following implantation of regenerative therapeutics. However, complete restoration of contractile function following treatment of VML injury has yet to be achieved, and human studies have demonstrated that increased strength (force generation capacity) does not necessarily result in increased movement function¹³⁻¹⁷. Moreover, the relationship between VML-related force deficits and gait biomechanics is not established in any biologically-relevant preclinical animal model that we are aware of. The goal of this study was to establish a robust and reproducible method to quantify the biomechanical changes in rat gait following a surgically-created VML injury to the tibialis anterior (TA) muscle.

Gait analysis of rat walking was chosen as a study parameter because it is the minimal reproducible functional level that could be reliably evaluated in all animals. Using a combination

of motion capture and advanced musculoskeletal modeling techniques, it is possible to accurately measure the effects of these severe muscle injuries on the 3D joint kinematics of rats and use this information to develop conclusions about the response to injury. Motion analysis has been used on humans for years to characterize musculoskeletal pathologies by quantifying function in terms of joint kinematics^{18,19} and we sought to apply that same methodology to a rat model of VML.

The biological relevance of the TA VML injury has been previously shown²⁰⁻²² and the rat model of VML injury is advantageous because methods have been established for assessment of force generation ability^{2,5,23,24}. In addition, rats have been successfully utilized as models to predict physiological changes in humans for multiple pathologies including cardiovascular disease²⁵, osteoarthritis^{26,27}, spinal cord injury²⁸⁻³¹, and Parkinson's^{32,33}. The osteoarthritic model of rats has been utilized to analyze changes in gait kinematics³⁴ and spatiotemporal parameters²⁶, but the authors did not rigorously evaluate underlying patterns of compensation.

Similarly, rats with spinal cord injury have been subjected to gait analysis via various acquisition techniques. Some studies utilized CatWalk²⁸ to measure stride length, walking speed, and weight bearing but did not provide specific information on joint kinematics. Another study on rat cadavers utilized X-ray³⁵ to track the joint angles during simulated walking, but this is not an accurate method of analyzing movement function. In order to truly understand what is occurring physiologically and biomechanically, it is necessary to have a reproducible and reliable collection method as well as a data set that comprehensively defines the motion at all three joints throughout the entire gait cycle. More recently, advanced motion capture techniques (Vicon) typically reserved for humans have started being applied to rat models³⁶⁻³⁹. However, 3D gait evaluation has not been performed on rats with VML injury to assess the extent of injury and recovery on

movement function, as the focus of current VML treatments is primarily on recovery of force production ability and volume reconstitution^{4,22,40}.

The present study examined the changes in gait kinematics of rats with VML injury walking on a treadmill. Using 3D motion capture, we developed a methodology to quantify visually observed variations in gait biomechanics and reveal the underlying effect of VML injury on joint kinematics and adaptation or recovery over time. We report here, for the first time, quantifiable kinematic gait alterations in all three axes associated with VML-induced force deficits to the TA muscle in an established rat model. These findings have major implications for evaluating and quantifying the efficacy of both regenerative and rehabilitative therapeutics for the treatment of extremity VML injuries. More generalized applications to the improved understanding and treatment of other forms of extremity injuries or disorders are also envisioned.

Methods and Materials

Experimental Outline

Eight 12-week old female Lewis rats were divided into two groups: four animals given 20% by mass volumetric muscle loss (VML) injuries to their right tibialis anterior (TA) with no repair performed (NR) and four healthy (no sham surgery) age match controls (Control). The gait biomechanics of both groups were analyzed using a combination of Vicon Nexus motion capture software and OpenSim modeling. Baseline motion capture and force testing occurred one week prior to surgery, and these measurements were repeated at 2, 4, and 8 weeks post-surgery to track the effect of the injury and subsequent recovery. The resulting kinematic and functional data from

each timepoint was compared to the data collected at baseline to determine any significant differences.

Animal Care

This study was conducted in compliance with the Animal Welfare Act, the Implementing Animal Welfare Regulations, and in accordance with the principles of the Guide for the Care and Use of Laboratory Animals. The University of Virginia Animal Care and Use Committee approved all animal procedures. A total of 8 female Lewis rats (Charles River Laboratories) weighing $180.2 \pm 6.75\text{g}$ at 12 weeks of age were pair housed in a vivarium accredited by the American Association for the Accreditation of Laboratory Animal Care, and they were provided with food and water *ad libitum*.

Anesthesia and Analgesia

All surgical and mechanical testing procedures as well as motion capture marker placement were conducted under anesthesia with continuous inhalation of isoflurane (1.5-2.5%). The depth of anesthesia was monitored by the response of the animal to a slight toe pinch, where the lack of response was considered the surgical plane of anesthesia. Core temperature was maintained using a heated water perfusion system. Rats were administered slow release buprenorphine (0.1mg/kg, subcutaneously) prior to surgery and quick release buprenorphine (0.1mg/kg, subcutaneously) at 36 and 48 hours post-surgery. Animal pain and distress were monitored daily by qualified members of the veterinary staff to determine the need for additional analgesia. No animal required additional analgesia after 48 hours post-surgery.

TA VML Surgery

The surgical procedure for the creation of a VML injury in the rat TA muscle is depicted in **Figure 4-1**. Using aseptic technique, a longitudinal incision was made on the lateral portion of the lower right leg. The skin was then cleared from the underlying fascia using blunt separation, and the fascia covering the anterior crural muscles was separated using blunt dissection. The proximal and distal tendons of the Extensor Hallicus Longus (EHL) and Extensor Digitorum Longus (EDL) muscles were then isolated and ablated. As previously described,^{3,20} the TA muscle corresponds to 0.17% of the gross body weight. The VML injury model was characterized by excision of roughly 20% of the TA muscle weight from the middle third of the muscle belly. The fascia was closed with 6-0 vicryl sutures and the skin was closed with 5-0 prolene using interrupted sutures. Skin glue was applied over the skin sutures to help prevent the incision from opening. No animals required additional surgical attention after the initial procedure.



Figure 4-1: Representative surgical defect of 20% by mass volumetric muscle loss injury (1.0x0.7x0.2cm)

In vivo Force Testing

In vivo force testing was performed as previously described ⁴¹. Briefly, at -1, 2, 4, and 8 weeks relative to the surgery date, rats were anesthetized and the right hind limb was aseptically prepared. The rat was placed in a supine position on a heated platform and the right knee was bent to a 90° angle. The leg was secured using a stabilizing rod and the right foot was taped to a footplate. The footplate was attached to the shaft of an Aurora Scientific 305C-LR-FP servomotor, which was controlled using a computer. Sterilized percutaneous needle electrodes were carefully inserted into the skin of the lower right leg for stimulation of the right common peroneal nerve. Electrical stimulus was provided using an Aurora Scientific stimulator with a constant current SIU (Model 701C). Needle electrode placement was optimized with a series of 1Hz pulses resulting in twitch contraction ⁴¹. Contractile function of the anterior crural muscles was assessed through measuring the peak isometric tetanic torque determined from maximal response to a series of stimulation frequencies (10-200Hz). Torque at baseline was normalized by the body weight of each animal. Torque at each post-surgical timepoint was normalized by the body weight of each animal on the day of collection, then was normalized to a percent of the baseline for that animal. The normalized torques at each post-surgical timepoint were averaged within the group for analysis. After force testing, the animals were allowed to recover on the heated platform and were then returned to the vivarium. For terminal timepoints, animals were euthanized via CO₂ inhalation and cervical dislocation was performed as a secondary measure.

Treadmill and Motion Capture

In the week prior to the baseline motion capture session, rats were placed in the treadmill for two 20-minute acclimation periods. They remained in their cages with no continued training for all post-surgical timepoints. At -1, 2, 4, and 8 weeks relative to the surgery date, rats were

anesthetized and shaved to allow proper placement of the motion capture marker set illustrated in **Figure 4-2**. Reflective markers were placed on the bony landmarks of the left anterior superior iliac crest (LASI), right anterior superior iliac crest (RASI), spine (L6 vertebra), tail (5th caudal vertebra), hip, lateral knee, ankle, and distal end of the fifth metatarsal. Markers were always applied with the rats sedated and in the same body position in order to limit error due to skin movement and maximize repeatability in precise placement of markers on joint centers. Rats were allowed to recover from anesthesia on a heated mat before being placed in the treadmill. Kinematic data was collected using a Vicon 7-camera (T40) setup collecting at 120Hz. Treadmill speed was set to 40cm/s, a velocity safely in the reported range for walking speed in rats ^{42,43}. The intensity of the shock at the rear of the treadmill was set to 0.1mA to encourage the animals to remain on the belt and continue walking. Treadmill sessions lasted roughly 15 minutes per rat. After data collection the animals were returned to the vivarium.

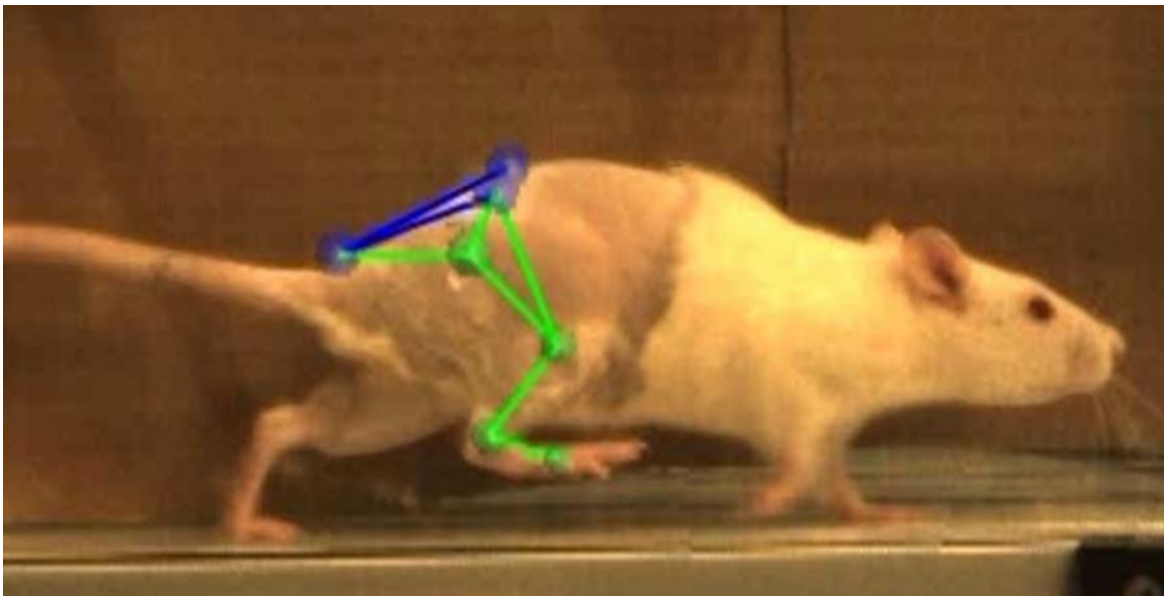


Figure 4-2: Vicon Nexus 2.8.1 3-D overlay of motion capture markers. Markers were placed on the L6 vertebra of the spine (SPINE), caudal-5 vertebra of the tail (TAIL), left and right anterior superior iliac crests (LASI, RASI), hip (HIP), lateral knee (KNEE), ankle (ANKLE), and 5th metatarsal on the toe (TOE).

Gait Modeling and Statistical Analysis

Gait events and marker identification were completed in Nexus and converted to TRC format using a MATLAB script. Inverse kinematic modeling was performed in OpenSim using a modified version of an existing rat hindlimb model³⁹ (**Figure 4-3**). This model consisted of four

segments (pelvis, femur, shank, foot) and had 13 degrees of freedom. The hip and ankle were modeled as ball joints, and the knee was modeled as a hinge joint. Resulting measures included sagittal joint angles of the hip, knee, and ankle as well as frontal and transverse angles of the hip. The model was modified to allow scaling to individual rats and facilitate calculation of joint angles through inverse kinematic simulations. As described in the previous section, the joints were palpated with the rat sedated and markers were placed directly over the joint centers of the hindlimb. This allowed limb segment lengths to be calculated from the motion capture data with

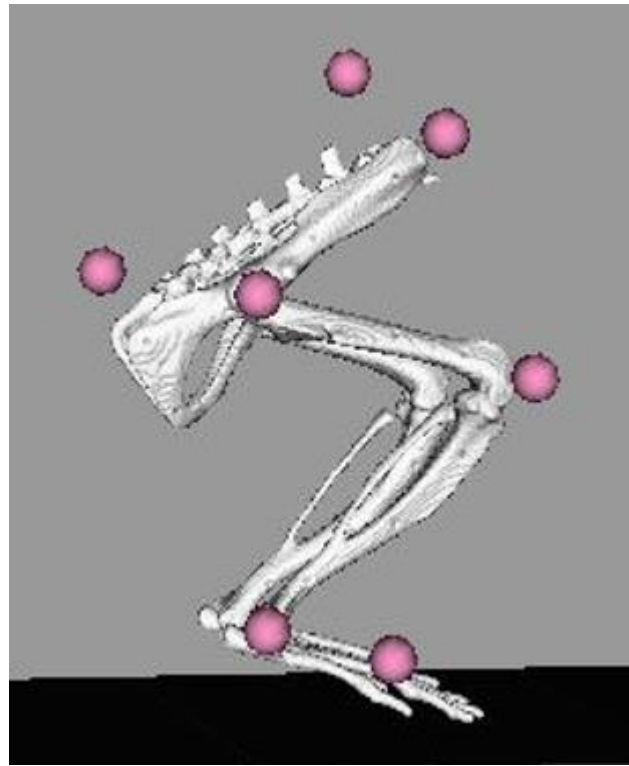


Figure 4-3: OpenSim rat hindlimb model with reconstructed marker locations. Marker locations shown are for the SPINE, TAIL, RASI, HIP, KNEE, ANKLE, and TOE. The model was scaled for each individual rat at each collection timepoint based on the locations of these markers on the animal.

the rat at a known position so the model segments could be scaled appropriately. The knee and ankle were limited to sagittal movement and the limbs segments were modeled as rigid bodies. Together, this facilitated full 3D analysis of kinematics while reducing the number of motion markers. Skin artifact is always an issue in motion capture and working with rats was no exception.

We chose to analyze simple walking as it produced minimal skin to skeletal motion everywhere except for the knee, where this relative motion was still significant. To account for this, the weight/motion contribution of the knee marker was reduced in the sagittal plane, thereby reducing its error contribution to the modeled motion. Sagittal knee angles were calculated using the OpenSim rigid body model and driven by the hip/ankle markers, which tracked the limb motion with higher accuracy. This allowed us to account for the movement of skin over the knee joint in the sagittal plane without losing the motion data. Reported data corresponds to one gait cycle, heel strike to heel strike of the right leg. Heel strike and toe off events were identified through calibrated, synchronized high-speed video that was captured alongside marker data and 3-D overlain with the motion capture marker positions (see **Figure 4-2**). A minimum of three steps per rat at each timepoint were used for statistical analysis, with the exception of one NR rat at the 4-week timepoint where lack of willingness to walk on the treadmill resulted in only two usable trials.

Statistics

Statistical analysis of the force testing data was performed using GraphPad Prism. A one-way ANOVA ($\alpha=0.05$) with multiple comparisons and Fisher's post-test was used to compare each of the post-surgery data sets to the baseline data and to each other. Analysis of the joint kinematic curves was performed using Statistical Parametric Mapping (SPM1) MATLAB code and t-tests. Spatiotemporal parameters were evaluated using paired t-tests ($\alpha=0.05$).

Results

Force testing

Post-surgical force testing at 2, 4, and 8 weeks indicated a significant deficit in isometric tetanic dorsiflexion torque at all three timepoints relative to baseline in the NR group. Average torque as percentage of baseline at Week 2 was $71.51 \pm 5.59\%$ ($p < 0.01$), at Week 4 was $76.48 \pm 5.90\%$ ($p < 0.01$), and at Week 8 was $78.74 \pm 4.85\%$ ($p < 0.01$, **Figure 4-4**). The torques measured at 2, 4, and 8 weeks were not significantly different from each other (W2vW4, $p = 0.48$; W2vW8, $p = 0.19$; W4vW8, $p = 0.90$).

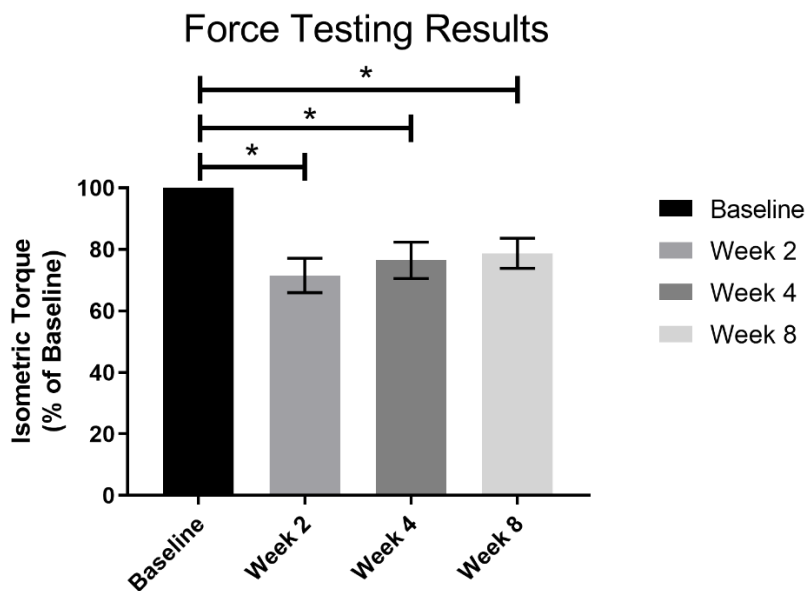


Figure 4-4: Force testing results for all VML animals (n=4) prior to surgery and 2, 4, and 8 weeks post-surgery. There was a significant functional deficit at all post-surgical timepoints as compared to baseline ($p < 0.05$), and no notable recovery as the post-surgical results were not significantly different from each other. Statistics were run as a one-way ANOVA with multiple comparisons and Fisher's LSD post-test.

Spatiotemporal Parameters

Average baseline spatiotemporal parameters are a composite of all rats, and a minimum of three steps per animal were averaged at the 8-week timepoint. Measurements of cadence (steps per minute, spm), step time (seconds), and swing percentage at Week 8 were compared to baseline.

Over the course of the study, cadence significantly increased (172.07 ± 16.77 spm vs. 200.05 ± 30.44 spm, $p < 0.05$), stride time significantly decreased (0.352 ± 0.034 s vs. 0.314 ± 0.059 s, $p < 0.05$), and swing percentage significantly decreased ($45.71 \pm 3.23\%$ vs. $41.82 \pm 2.78\%$, $p < 0.05$).

Joint Kinematics

Average baseline kinematics are a composite of all rats. Compared to baseline data, analysis of joint kinematics of the hip, knee, and ankle at -1, 2, 4, and 8 weeks showed significant differences across the board. (**Figure 4-5**). Observed average ranges of motion for flexion of the hip, knee, and ankle joints were 39.24 ± 6.99 degrees, 52.88 ± 10.21 degrees, and 53.88 ± 10.07 degrees.

At Week 2, primary differences were seen in hip flexion in late stance (decrease, $p < 0.001$), early stance and heel strike hip adduction (decrease, $p < 0.05$), hip external rotation at toe-off (decrease, $p < 0.05$), mid-stance and mid-swing knee flexion (decrease, $p < 0.001$), and ankle flexion throughout stance and through swing (decrease, $p < 0.001$). By Week 4 the trajectories adapted such that primary differences were observed in both early stance and late swing for hip flexion (increase, $p < 0.05$ and $p < 0.01$) and adduction (decrease, $p < 0.05$ and $p < 0.001$), and ankle flexion at toe-off through mid-swing (decrease, $p < 0.05$). At the 8-week timepoint, the differences in hip flexion during late swing (increase, $p < 0.01$) were sustained. Hip adduction exhibited differences across the duration of the gait cycle (decrease, $p < 0.001$) and external rotation showed differences through mid-stance and mid to late swing (increase, $p < 0.001$) showed significant differences across the duration of the gait cycle. Knee flexion showed differences during early stance and late stance through toe-off (decrease, $p < 0.01$ and $p < 0.001$) and ankle flexion showed differences throughout stance and into mid-swing (decrease, $p < 0.001$). Additionally, a delayed phase shift was observed

in all joint angles as the weeks progressed. By Week 8, the delay of hip flexion, hip adduction, hip external rotation, knee flexion, and ankle flexion was 3%, 2%, 3%, 5%, and 4%, respectively.

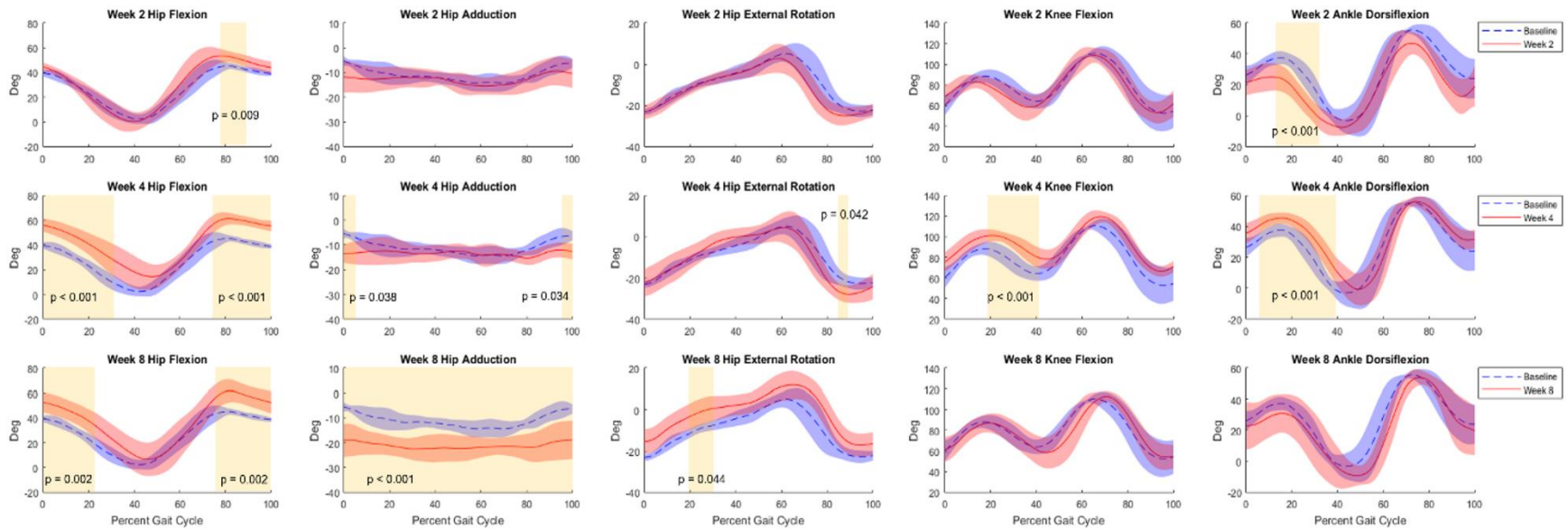


Figure 4-5: Kinematic curves for hip flexion, hip adduction, hip external rotation, knee flexion, and ankle flexion. Graphs shown compare baseline versus 2 weeks (top row), 4 weeks (middle row), and 8 weeks (bottom row) post-surgery. Baseline data (Control+NR, n=8) are shown in blue and post-surgical (NR, n=4) data are shown in red. Regions of significance are shaded yellow with the respective p-value noted. All statistical analyses of kinematics were t-tests performed at an α -level of 0.05.

Discussion and Conclusion

At the outset of this study, we sought to examine a more comprehensive approach to evaluating the effect of volumetric muscle loss injury and recovery on rats by analyzing gait biomechanics rather than simply force generation ability. By collecting motion capture data on rats walking on a treadmill, we were able to delineate clear differences between the gait of healthy animals when compared to injured animals which was quantifiable via kinematic analysis (**Figure 4-5**). Healthy animals without sham surgery were included in this study and evaluated over the 8 weeks partially to ensure that there were no gait changes with age and growth. We found that there were no significant differences in mean or variance between their baseline and 8-week gait patterns. This, along with the demonstrated sensitivity to measure significant differences between healthy and VML injured rats, gives us confidence in the reproducibility of the methods employed in this study. With this in mind, we measured significant differences at all three major joints in the hindlimb and observed clear changes in adaptation in the gait patterns throughout the recovery period. It is possible that some of the kinematic changes could have been due to the surgical procedure, but in the human population there will always be a procedure performed to address the injury so we consider any noise from the surgery to be a part of the injury/recovery process.

As a standard of comparison, we referred to the baseline joint kinematics collected on each of the rats. The range of motion values reported here for flexion of the hip and ankle were similar to previously reported sagittal plane kinematics in healthy rats⁴³. Pereira et al reported average ranges of motion for flexion of the hip and ankle as roughly 45 and 50 degrees, which compare favorably to our observed values of 39.24 and 53.88 degrees.

Even with only eight rats, this method was sensitive enough to reveal significant differences in gait. The observed changes in gait pattern were similar to typical human gait

compensation for foot drop in the forms of vaulting gait and circumduction. Vaulting gait is characterized by excessive hip and knee flexion, as well as pelvic hiking/obliquity. Some evidence of vaulting gait was observed at the 2-week and 4-week timepoints as indicated by increased hip flexion during swing and ankle extension at toe-off. At the later timepoints, a compensatory shift to circumduction was observed. Circumduction is another compensation mechanism for foot drop that is more efficient than vaulting and is characterized by swinging a straight leg around the long axis of the body. This gait pattern was seen at the 8-week timepoint, as evidenced by increased hip abduction and external rotation as well as increased knee and ankle extension at toe-off and during swing.

Though we limited the motion of the knee to the sagittal plane, we do not believe that there would be statistically significant changes in knee varus/valgus in these animals due to a TA VML injury. Further, the range of motion of knee valgus in humans is less than 5 degrees⁴⁴, which is less than the resolution in this study.

As indicated by the force testing results (**Figure 4-4**), the animals were operating at a significant functional deficit at all three post-surgical timepoints. This supports the rightward shift (i.e. more time in stance) in the gait cycle as the weeks progress, as the animal was forced to take more time to develop an impulse to drive the foot forward. The torque values in this study were slightly higher than those for NR animals in previous work⁴, indicating a less severe VML injury but highlighting the sensitivity of the gait analysis presented here. The spatiotemporal results also confirm this functional deficit by showing a significant decrease in swing percentage of the gait cycle. Similarly, analysis of the spatiotemporal parameters showed that cadence increased even though the treadmill velocity remained the same, indicating the animals were trying to increase their stability as compensation for the injury. The gait analysis methods in this study were sensitive

enough to show that compensation patterns were fluid throughout the 8-week observation period. The animals were utilizing circumduction as a compensation mechanism at the 8-week timepoint, however their gait patterns had not yet reached a steady state. While we believe the observed circumduction reflects the final learned or permanent gait pattern resulting in the most efficient mechanism of movement for the given VML injury, we are not able to make such a conclusion. Future studies should employ increased group sizes to improve statistical power and follow the evolution of the rat gait patterns to 16 or 24 weeks to confirm the gait patterns seen at 8 weeks were durable. Extending the final data collection timepoints out further and expanding the group sizes would likely reveal more differences and could provide beneficial information in quantifying the time it takes to reach a kinematic plateau.

In spite of the small group sizes of this pilot study, the developed method for the analysis of rat locomotion resulted in a small variance between unique rats and unique visits for healthy controls and a high sensitivity to small differences between healthy and VML rats, demonstrating its value as an evaluative tool. We were able to accurately calculate the kinematics of the hip, knee, and ankle over complete gait cycles and compare the post-injury kinematics to healthy baseline data. This evaluation method allowed us to detect significant small differences in stance and swing at all three joints throughout the data collection period due to VML in the injured population. Based on these results, we can conclude that the differences observed after injury can be attributed to vaulting gait and circumduction as compensation for drop foot. We believe our method of quantifying functional ability should be considered ahead of the current industry standard of *in vivo* force testing for a variety of reasons, most notably that it quantifies functional recovery on a basis of movement function rather than just force generation ability. By allowing us to determine the variance of kinematic variables and the limitations of a treadmill-based motion

capture arena, this study has established a groundwork for future studies into protocol refinement, joint kinetics, and comparisons of efficacy of regenerative therapeutics as treatment for VML and more significant injuries.

Future Work

This data is a promising start, but it could be improved in a few ways. We believe that using these same motion capture techniques on animals walking over-ground rather than on a treadmill would result in joint kinematics that are more reflective of natural gait patterns. While the shock was a necessary condition to motivate the animals and keep them on the belt, it also created a panic in the animals and led to markedly different walking styles for a brief period afterwards. In addition, the measurement of ground reaction forces via an instrumented walkway would allow us to calculate joint moments in all three planes. The inclusion of force plates, along with the collection of contralateral limb kinematics, would provide a more insightful data set and develop data which would give us an opportunity to evaluate the efficacy of various rehabilitative and regenerative strategies on a deeper functional level.

References

1. Grogan, B. F. & Hsu, J. R. Volumetric muscle loss. *J. Am. Acad. Orthop. Surg.* **19 Suppl 1**, S35-7 (2011).
2. Wu, X., Corona, B. T., Chen, X. & Walters, T. J. A standardized rat model of volumetric muscle loss injury for the development of tissue engineering therapies. *Biores. Open Access* **1**, 280–90 (2012).
3. Corona, B. T., Ward, C. L., Baker, H. B., Walters, T. J. & Christ, G. J. Implantation of *In Vitro* Tissue Engineered Muscle Repair Constructs and Bladder Acellular Matrices Partially Restore *In Vivo* Skeletal Muscle Function in a Rat Model of Volumetric Muscle Loss Injury. *Tissue Eng. Part A* 131219054609007 (2013). doi:10.1089/ten.tea.2012.0761
4. Passipieri, J. A. *et al.* Keratin Hydrogel Enhances *In Vivo* Skeletal Muscle Function in a Rat Model of Volumetric Muscle Loss. *Tissue Eng. Part A* **23**, 556–571 (2017).
5. Corona, B. T., Rivera, J. C., Owens, J. G., Wenke, J. C. & Rathbone, C. R. Volumetric muscle loss leads to permanent disability following extremity trauma. *J. Rehabil. Res. Dev.* **52**, 785–792 (2015).
6. Corona, B. T., Henderson, B. E. P., Ward, C. L. & Greising, S. M. Contribution of minced muscle graft progenitor cells to muscle fiber formation after volumetric muscle loss injury in wild-type and immune deficient mice. *Physiol. Rep.* **5**, (2017).
7. Cittadella Vigodarzere, G. & Mantero, S. Skeletal muscle tissue engineering: strategies for volumetric constructs. *Front. Physiol.* **5**, 362 (2014).
8. Grasman, J. M., Zayas, M. J., Page, R. L. & Pins, G. D. Biomimetic scaffolds for regeneration of volumetric muscle loss in skeletal muscle injuries. *Acta Biomater.* **25**, 2–15 (2015).
9. Mackenzie, T. C., Porada, C. D., Hughes Peranteau, W. & Christ, G. J. Engineering muscle tissue for the fetus: getting ready for a strong life. *Front. Pharmacol.* **6**, (2015).
10. Dziki, J. *et al.* An acellular biologic scaffold treatment for volumetric muscle loss: results of a 13-patient cohort study. *npj Regen. Med.* **1**, 16008 (2016).
11. Passipieri, J. A. & Christ, G. J. The Potential of Combination Therapeutics for More Complete Repair of Volumetric Muscle Loss Injuries: The Role of Exogenous Growth Factors and/or Progenitor Cells in Implantable Skeletal Muscle Tissue Engineering Technologies. *Cells. Tissues. Organs* **202**, 202–213 (2016).
12. Ma, J. *et al.* Exploratory study on the effect of osteoactivin on muscle regeneration in a rat volumetric muscle loss model. *PLoS One* **12**, e0175853 (2017).
13. Damiano, D. L., Arnold, A. S., Steele, K. M. & Delp, S. L. Can strength training predictably improve gait kinematics? A pilot study on the effects of hip and knee extensor strengthening on lower-extremity alignment in cerebral palsy. *Phys. Ther.* **90**, 269–79 (2010).

14. Damiano, D. L. & Abel, M. F. Functional outcomes of strength training in spastic cerebral palsy. *Arch. Phys. Med. Rehabil.* **79**, 119–25 (1998).
15. Damiano, D. L., Prosser, L. A., Curatalo, L. A. & Alter, K. E. Muscle Plasticity and Ankle Control After Repetitive Use of a Functional Electrical Stimulation Device for Foot Drop in Cerebral Palsy. *Neurorehabil. Neural Repair* **27**, 200–207 (2013).
16. Topp, R., Mikesky, A., Wigglesworth, J., Holt, W. & Edwards, J. E. The effect of a 12-week dynamic resistance strength training program on gait velocity and balance of older adults. *Gerontologist* **33**, 501–6 (1993).
17. Buchner, D. M. *et al.* The effect of strength and endurance training on gait, balance, fall risk, and health services use in community-living older adults. *J. Gerontol. A. Biol. Sci. Med. Sci.* **52**, M218-24 (1997).
18. An, K. N. & Chao, E. Y. Kinematic analysis of human movement. *Ann. Biomed. Eng.* **12**, 585–97 (1984).
19. Astephen, J. L., Deluzio, K. J., Caldwell, G. E. & Dunbar, M. J. Biomechanical changes at the hip, knee, and ankle joints during gait are associated with knee osteoarthritis severity. *J. Orthop. Res.* **26**, 332–341 (2008).
20. Wu, X., Corona, B. T., Chen, X. & Walters, T. J. A Standardized Rat Model of Volumetric Muscle Loss Injury for the Development of Tissue Engineering Therapies. *Biores. Open Access* **1**, 280–290 (2012).
21. Sicari, B. M. *et al.* A murine model of volumetric muscle loss and a regenerative medicine approach for tissue replacement. *Tissue Eng. Part A* **18**, 1941–8 (2012).
22. Aurora, A., Garg, K., Corona, B. T. & Walters, T. J. Physical rehabilitation improves muscle function following volumetric muscle loss injury. *BMC Sport. Sci. Med. Rehabil.* **6**, 41 (2014).
23. Aurora, A., Garg, K., Corona, B. T. & Walters, T. J. Physical rehabilitation improves muscle function following volumetric muscle loss injury. *BMC Sport. Sci. Med. Rehabil.* **6**, 41 (2014).
24. Mintz, E. L., Passipieri, J. A., Lovell, D. Y. & Christ, G. J. Applications of In Vivo Functional Testing of the Rat Tibialis Anterior for Evaluating Tissue Engineered Skeletal Muscle Repair. *J. Vis. Exp.* (2016). doi:10.3791/54487
25. Iannaccone, P. M. & Jacob, H. J. Rats! *Dis. Model. Mech.* **2**, 206–10 (2009).
26. Ängeby Möller, K., Kinert, S., Størkson, R. & Berge, O. G. Gait Analysis in Rats with Single Joint Inflammation: Influence of Experimental Factors. *PLoS One* **7**, (2012).
27. Clarke, K. A., Heitmeyer, S. A., Smith, A. G. & Taiwo, Y. O. Gait Analysis in a Rat Model of Osteoarthritis. *Physiol. Behav.* **62**, 951–954 (1997).
28. Datto, J. P. *et al.* Use of the CatWalk Gait Device to Assess Differences in Locomotion between Genders in Rats Inherently and following Spinal Cord Injury. *Dataset Pap. Sci.* **2016**, 1–11 (2016).

29. Canu, M.-H. & Garnier, C. A 3D analysis of fore- and hindlimb motion during overground and ladder walking: Comparison of control and unloaded rats. *Exp. Neurol.* **218**, 98–108 (2009).
30. Perrot, O., Laroche, D., Pozzo, T., Marie, C. & Destee, A. Quantitative Assessment of Stereotyped and Challenged Locomotion after Lesion of the Striatum: A 3D Kinematic Study in Rats. *PLoS One* **4**, e7616 (2009).
31. Johnson, W. L., Jindrich, D. L., Roy, R. R. & Edgerton, V. R. Quantitative metrics of spinal cord injury recovery in the rat using motion capture, electromyography and ground reaction force measurement. *J. Neurosci. Methods* **206**, 65–72 (2012).
32. Deumens, R., Blokland, A. & Prickaerts, J. Modeling Parkinson's Disease in Rats: An Evaluation of 6-OHDA Lesions of the Nigrostriatal Pathway. *Exp. Neurol.* **175**, 303–317 (2002).
33. Duty, S. & Jenner, P. Animal models of Parkinson's disease: a source of novel treatments and clues to the cause of the disease. *Br. J. Pharmacol.* **164**, 1357–91 (2011).
34. Roemhildt, M. L., Gardner-Morse, M., Rowell, C., Beynnon, B. D. & Badger, G. J. Gait alterations in rats following attachment of a device and application of altered knee loading. *J. Biomech.* **43**, 3227–31 (2010).
35. Wehner, T. *et al.* Internal forces and moments in the femur of the rat during gait. *J. Biomech.* **43**, 2473–2479 (2010).
36. Webb, A. A., Kerr, B., Neville, T., Ngan, S. & Assem, H. Kinematics and Ground Reaction Force Determination: A Demonstration Quantifying Locomotor Abilities of Young Adult, Middle-aged, and Geriatric Rats. *J. Vis. Exp.* e2138–e2138 (2011). doi:10.3791/2138
37. Eftaxiopoulou, T., Macdonald, W., Britzman, D. & Bull, A. M. J. Gait compensations in rats after a temporary nerve palsy quantified using temporo-spatial and kinematic parameters. *J. Neurosci. Methods* **232**, 16–23 (2014).
38. Karakostas, T., Hsiang, S., Boger, H., Middaugh, L. & Granholm, A.-C. Three-dimensional rodent motion analysis and neurodegenerative disorders. *J. Neurosci. Methods* **231**, 31–7 (2014).
39. Johnson, W. L., Jindrich, D. L., Roy, R. R. & Reggie Edgerton, V. A three-dimensional model of the rat hindlimb: musculoskeletal geometry and muscle moment arms. *J. Biomech.* **41**, 610–9 (2008).
40. Corona, B. T. *et al.* Autologous minced muscle grafts: a tissue engineering therapy for the volumetric loss of skeletal muscle. *Am. J. Physiol. Physiol.* **305**, C761–C775 (2013).
41. Mintz, E. L., Passipieri, J. A., Lovell, D. Y. & Christ, G. J. Applications of In Vivo Functional Testing of the Rat Tibialis Anterior for Evaluating Tissue Engineered Skeletal Muscle Repair. *J Vis Exp* (2016).
42. Clarke, K. A. Swing Time Changes Contribute to Stride Time Adjustment in the Walking Rat. *Physiol. Behav.* **50**, 1261–1262 (1991).

43. Pereira, J. E. *et al.* A comparison analysis of hindlimb kinematics during overground and treadmill locomotion in rats. *Behav. Brain Res.* **172**, 212–218 (2006).
44. Cherian, J. J. *et al.* Mechanical, Anatomical, and Kinematic Axis in TKA: Concepts and Practical Applications. *Curr. Rev. Musculoskelet. Med.* **7**, 89–95 (2014).

Chapter 5 – Comprehensive Dynamic and Kinematic Analysis of the Rodent Hindlimb Over-Ground Walking

Disclaimer: some passages have been quoted verbatim from [Dienes, J., Hicks, B., Slater, C., Jansen, K., Christ, G.J. & Russell, S.D. Comprehensive Dynamic and Kinematic Analysis of the Rodent Hindlimb during Over Ground Walking. In prep for submission to *Scientific Reports*.]. Due to ongoing refinement of data analysis, some figures and numerical values may change slightly in final publication but the overall conclusions are expected to remain consistent.

Abstract

The rat hindlimb is a frequently utilized pre-clinical model system to evaluate injuries and pathologies impacting the hindlimbs. These studies have demonstrated the translational potential of this model but have typically focused on the force generating capacity of target muscles as the primary evaluative outcome. Historically, human studies investigating extremity injuries/pathologies have utilized biomechanical analysis to better understand the impact of injury and extent of recovery. In this study, we expand that full biomechanical workup to a rat model in order to characterize the spatiotemporal parameters, ground reaction forces, 3-D joint kinematics, 3-D joint kinetics, and energetics of gait in healthy rats. We report data on each of these metrics that meets or exceeds the standards set by the current literature and are the first to report on all these metrics in a single set of animals. The methodology and findings presented in this study have significant implications for the development and clinical application of the improved regenerative therapeutics and rehabilitative therapies required for durable and complete functional recovery from extremity traumas and pathologies.

Introduction

The rat hindlimb is a frequently utilized model system for studying diverse conditions/pathologies spanning volumetric muscle loss¹⁻⁴, nerve injury⁵⁻⁸, ligament injury⁹⁻¹², and osteoarthritis¹³⁻¹⁵. These studies have been very effective in demonstrating the translational potential of regenerative therapeutics, changing our approach to pre-clinical research from evaluating only the local impact of an injury or treatment to evaluating the entire systemic response. This has opened the door to numerous future studies in the scope of regenerative rehabilitation to better understand and predict the outcomes of pathologies modeled in the rat hindlimb.

Muscle moments (kinetics) are the driving force behind movement patterns, but to date kinetics have not been reliably calculated and researchers have primarily relied on spatiotemporal parameters^{13,14,16-21}, ground reaction forces (GRFs)^{14,22-28}, or 1-D kinematics (joint angles)^{17,29-33} to quantify gait changes. Spatiotemporal parameters and GRFs have well characterized methodologies, are easy data to obtain, and have both been collected on rats during over-ground walking. These methods are the most sensitive to detecting changes in rat walking mechanics and weight distribution, and have been shown to provide insight into compensation mechanisms due to spinal and knee injuries. Joint kinematics have also been investigated extensively, but there is a lack of congruence in the literature due to vast methodological differences. These include small group sizes, low volumes of analyzed gait cycles, and highly variable data collection and reconstruction protocols, each of which can contribute to the range of outcomes observed in the kinematic literature. But despite the broad differences in the literature, kinematics have been used on a case-by-case basis to evaluate changes in joint motion due to arthritis, spinal injury, or varied walking conditions. These are incredibly useful evaluative methods, and in this study, we added all these previously utilized metrics to our own developed method for calculating 3-D joint-by-

joint kinetics. Because of the overall utility of spatiotemporal parameters and GRFs, we have made a point to report them within our normative database.

3-D kinetics have long been the gold standard of human motion capture and movement analysis, and if these methods are effectively applied to rats then pathological effects and treatment efficacy can be more extensively evaluated. Kinetics offer insight into neuromuscular recruitment strategies and joint loading that no other analysis can provide. Kinetics are the gold standard for human motion analysis for that reason, they allow you to see how the muscles and joints in a system are working to actuate a motion and put a number on the forces being experienced at each of the joints. They also provide insight into joint loading, compensation patterns, joint power, and efficiency of motion that would otherwise be undetectable. This is specifically important for pre-clinical volumetric muscle loss (VML) rat studies, where maximum isometric torque has been the primary evaluative metric but does not necessarily result in improved functional outcomes³⁴⁻³⁸. With the volume of pre-clinical studies being performed on the rat hindlimb to assess muscle, nerve, tendon, and joint injuries, kinetic insight into the extent of injury and the road to recovery would be instrumental in fine-tuning rehabilitative and regenerative therapies.

The primary objective of this study was to develop the necessary modeling methods, as well as a robust database for thorough analysis of the rat hindlimb during normal over-ground walking. We successfully implemented these advanced motion capture and modeling techniques to capture concurrent marker and GRF data. We were then able to calculate 3D joint kinetic data, which represents a breakthrough in rodent gait analysis. This thorough kinetic analysis can inform the development of more effective treatments to maximize functional recovery and minimize the adoption of compensatory gait patterns by providing detailed insight into the true mechanisms responsible for diminished function following various injuries and pathologies.

In this regard, we have developed a comprehensive method to analyze the full 3D kinetics and 3D kinematics of the rat hindlimb during over ground walking to provide a clearer picture of the biomechanics required for normal movement function. Our unique ability to measure gait parameters, as demonstrated in this study, facilitates a more thorough understanding of normal and healthy rodent gait. With this methodology and developed kinetic database in hand, it is possible to extend these protocols to quantify relevant functional deficits in rat models, as well as the functional effectiveness of therapeutic interventions on movement quality. Further, the normative database presented herein provides valuable data for comparison for any study making use of rat models for full biomechanical analysis (spatiotemporal parameters, GRFs, kinematics, kinetics, and energetics) of pathologies modeled in the hindlimb.

Methods

Experimental Outline

A total of 20 female Lewis rats (Charles River Laboratories) weighing 182.1 ± 6.1 g at 12 weeks of age were tasked with walking down a 2.7m instrumented walkway. Motion data was collected and analyzed using a combination of Vicon Nexus motion capture software and OpenSim musculoskeletal modeling. Concurrent GRF data was acquired from these trials using ATI sensors. Trials were excluded if the rats stopped in the middle of the collection volume, turned around, accelerated beyond a lateral sequence walk ($17\text{cm/s} < \text{walking velocity} < 48\text{cm/s}$ ³⁹). Spatiotemporal parameters were acquired from marker positions calculated by Vicon Nexus. Kinetics were calculated by performing inverse dynamics to combine the joint angle and GRF data in the OpenSim model^{40,41}. Spatiotemporal parameters, joint kinematics, GRFs, joint moments, and joint powers were compiled and averaged to create a normative database for rodent gait. Data presented represents a minimum of 3 averaged steps/rat for kinematic and spatiotemporal calculations and a minimum of two averaged foot strikes recorded on the force plates per rat for kinetic calculations.

Animal Care

This study was conducted in compliance with the Animal Welfare Act, the Implementing Animal Welfare Regulations, and in accordance with the principles of the Guide for the Care and Use of Laboratory Animals. The University of Virginia Animal Care and Use Committee approved all animal procedures. Animals were pair housed in a vivarium accredited by the American Association for the Accreditation of Laboratory Animal Care, and they were provided with food and water *ad libitum*.

Acquisition of Motion Data and Ground Reaction Forces

Rats were anesthetized prior to motion capture and shaved to allow proper placement of the motion capture marker set⁴⁰ illustrated in **Figure 5-1**. 3mm and 5mm reflective markers were placed on the bony landmarks of the left anterior superior iliac crest (LASI), right anterior superior iliac crest (RASI), spine (L6 vertebra), tail (5th caudal vertebra), hip, lateral knee, ankle, and distal end of the fifth metatarsal. Rats were allowed to recover from anesthesia on a heated mat before being placed in the instrumented walkway. Marker data was collected using a 7-camera setup (Vicon, Oxford Metrics, Oxfordshire, ENG) collecting at 200Hz and GRF data was collected at 1000Hz. After data collection the animals were returned to the vivarium.

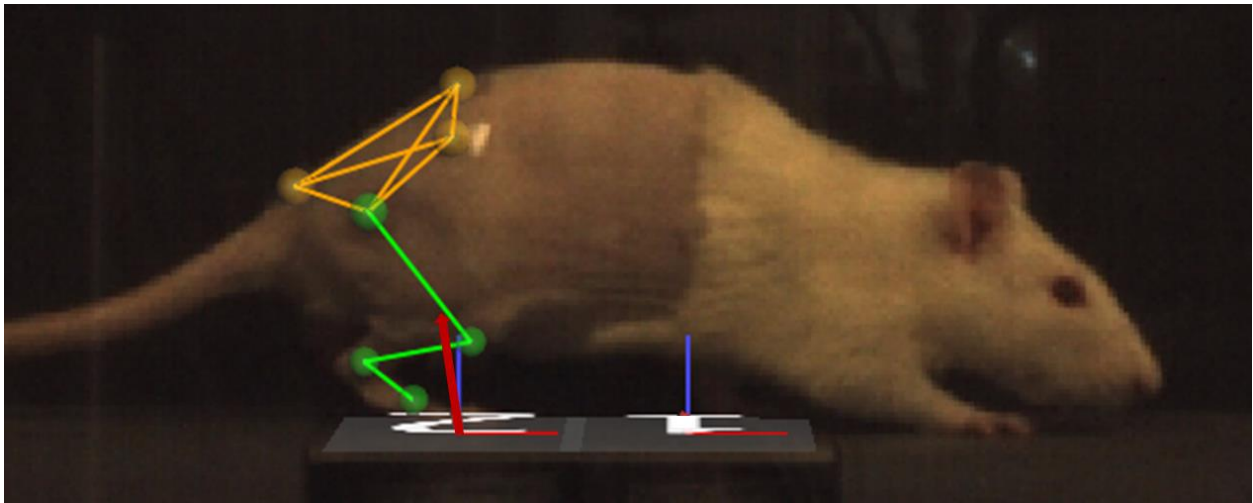


Figure 5-1: Vicon Nexus 2.7.1 3-D overlay of motion capture marker placements. 3mm markers were applied to the lateral knee, ankle, and fifth metatarsal (TOE) of the female Lewis rats. 5mm markers were applied to the spine, hip, right anterior superior iliac crest (RASI), and the tail. Motion capture data was collected at 200hz and ground reaction force (GRF) data was collected at 1000hz. Data was reconstructed using Vicon Nexus 2.7.1 resulting in overlays of joint positions and GRF vector projections as shown above.

Limb Morphometrics and MoI/CoM Calculations

We have previously developed a kinematic model for the rat hindlimb⁴⁰, but in order to calculate accurate kinetic data, it is necessary to have both GRF data and inertial data of the rat limbs. To determine inertial parameters, rat limb morphometrics were compiled from the fresh cadavers of 17 female Lewis rats. For each segment of the hindlimb (thigh, shank, foot), lengths (joint center to joint center), and masses were measured, normalized by body weight, and averaged (n=34 limbs) to obtain morphometric data. We then scaled the normalized data geometrically to extrapolate values for animals of different body weights. This data was used to inform accurate weights for each limb segment within the OpenSim model prior to scaling of the model to each individual rat. Centers of mass (CoM) and moments of inertia (MoI) were determined by performing laser surface scans of the left and right hindlimbs of a representative sample of 5 female Lewis rats. The scans were meshed, smoothed, and reconstructed using Meshmixer software (Autodesk, USA). Reconstructed limbs were then converted to solids and segmented into thigh, shank, and foot sections using Fusion 360 software. Segment masses were extrapolated based on the body weight of the scanned animal and equations determined from the rat limb morphometric database. Once these parameters were established, CoM and 3-D MoI data for each limb segment was calculated by Fusion 360 (Autodesk, USA). CoM and MoI values were normalized to body weight and limb length then averaged so they could be applied to animals over a range of sizes and ages. These inertial measurements were added to the OpenSim model prior to performing inverse kinematics and inverse dynamics.

Inverse Kinematics

Gait events and marker identification was completed in Nexus (Vicon, Oxford Metrics, Oxfordshire, ENG) and marker position data was lowpass filtered at 15Hz (two-way Butterworth).

Inverse kinematic modeling was performed in OpenSim using a validated rat hindlimb kinematic model^{40,41}. Calculated CoM and MoI data for the limb segments of each rat was programmed into the kinematic model prior to modeling any walkway trials. This model consisted of four segments (pelvis, femur, tibia, foot) and each joint was modeled as free, ball, revolute, and revolute, respectively. This facilitated full 3D analysis of hip and pelvis kinematics and kinetics while reducing the number of motion markers required.

Inverse Dynamics

Kinetics were calculated using inverse dynamics by pairing 3D GRF data with concurrently captured motion data using a validated rat hindlimb kinematic model in OpenSim⁴¹. Calculated CoM and MoI data for the limb segments of each rat was programmed into the kinematic model prior to modeling any walkway trials. Marker data and measured GRFs were extracted from Nexus for each trial. Marker data was lowpass filtered at 15Hz and GRFs were lowpass filtered at 100Hz (two-way Butterworth). This data was then imported into OpenSim and models were run using the inverse dynamics solver, resulting in 3D joint moments at the hip and sagittal plane joint moments at the knee and ankle. Kinetics for each rat, at each timepoint, were normalized by body mass. Utilizing the joint moments and the sagittal plane joint kinematic data, power absorption/dissipation at each joint was calculated over the whole stride equation 1.

$$P = M\omega \quad \text{Eq. 5-1}$$

Where P is joint power, M is joint moment, and ω is joint angular velocity.

Results

We successfully collected morphometric, spatiotemporal, kinematic, and 3D ground reaction force data on 21 12-week old female Lewis rats. We then used that data to calculate joint angles, joint moments, and joint powers for the same population. The joint angles, joint moments, and power data are reported over a full gait cycle, heel strike to heel strike of the right leg.

Spatiotemporal Parameters and Morphometrics

Morphometric data for segment lengths as well as spatiotemporal parameters for stride length, velocity, cadence, and stance percentage are shown in **Table 5-1**.

Parameter	Value
Stride Length (mm)	122.4 ± 4.8
Velocity (cm/sec)	30.3 ± 3.4
Cadence (steps/min)	294.2 ± 30.7
Stance Percentage (%)	63.9 ± 3.6
Thigh Segment Length (mm)	31.5 ± 2.7
Shank Segment Length (mm)	32.3 ± 2.2
Foot Segment Length (mm)	35.9 ± 2.2

Table 5-1: Spatiotemporal parameters and morphometric measurements for healthy female Lewis rats

Kinematics

Kinematic trajectories of each joint are reported in **Figure 5-2**. The ranges of motion for hip flexion, adduction, and rotation were 46.4 ± 6.7 , 8.4 ± 2.5 , and 32.7 ± 4.6 degrees. The average maximum flexion of the hip was 44.9 ± 6.4 degrees. The ranges of motion for knee and ankle flexion were 45.9 ± 8.3 and 32.3 ± 9.6 degrees. Average maximum flexions for the knee and ankle were 140.6 ± 5.4 and 31.5 ± 4.2 degrees.

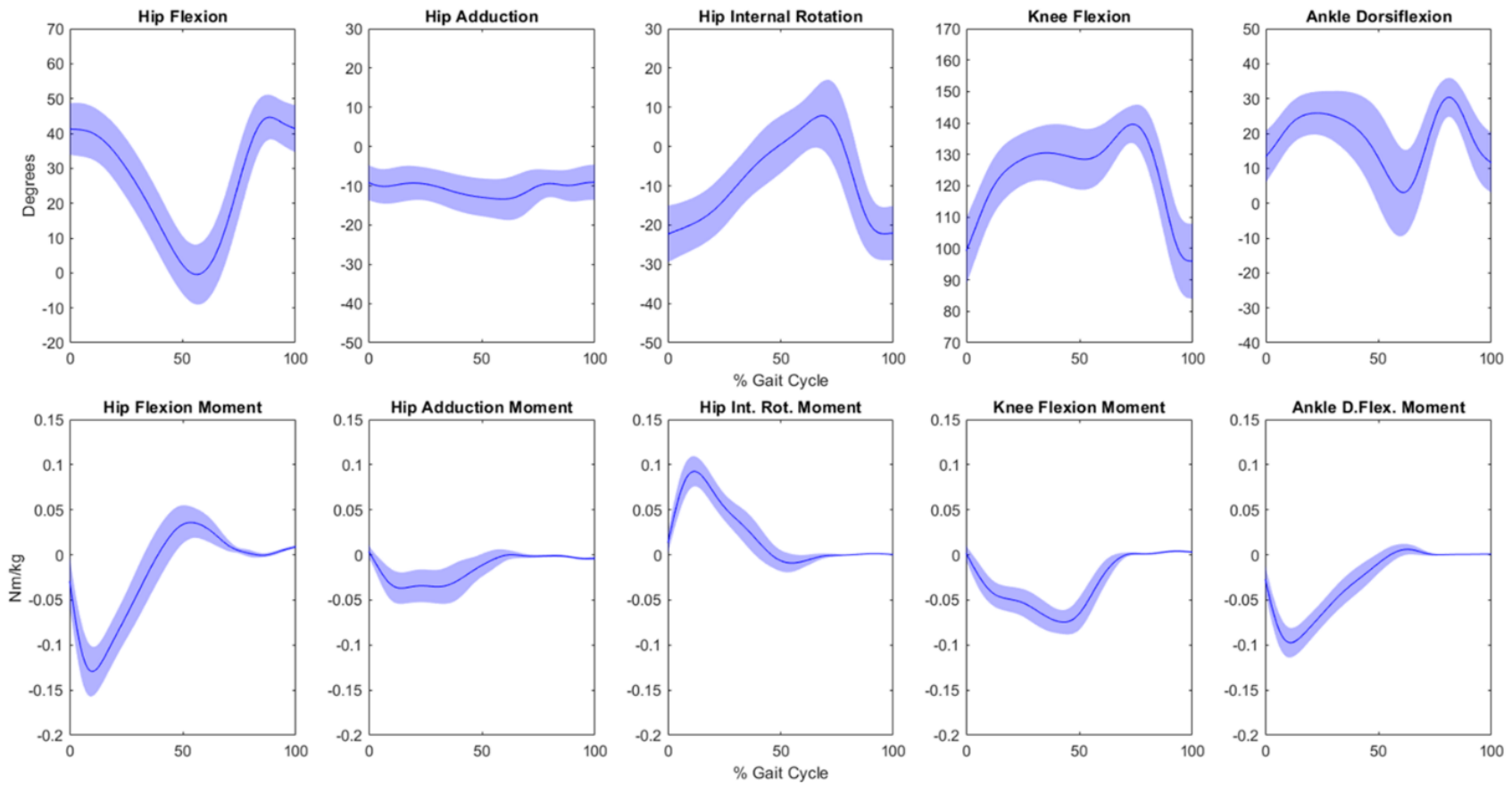


Figure 5-2. Kinematic (joint angles, top row) and kinetic (joint moments, bottom row) curves for healthy female Lewis rats. Curves are shown as mean \pm 1STD for hip flexion angle/moment, hip adduction angle/moment, hip internal rotation angle/moment, knee flexion angle/moment, and ankle dorsiflexion angle/moment.

Ground Reaction Forces

GRFs measured from the load cells are shown in **Figure 5-3**. The average peak anterior and posterior forces were -1.298 ± 0.697 N/kg and 0.499 ± 0.384 N/kg. The average peak medial and lateral forces were 0.047 ± 0.077 N/kg and -1.092 ± 0.319 N/kg. The average peak vertical force was 6.628 ± 0.758 N/kg.

Joint Moments and Power

Joint moments calculated from concurrently recorded joint kinematics and GRFs are shown in **Figure 5-2**. The average peak flexion and extension moments about the hip were 0.043 ± 0.016 and -0.133 ± 0.028 Nm/kg. The average peak adduction and abduction moments about the hip were 0.006 ± 0.006 and -0.043 ± 0.020 Nm/kg. The average peak internal rotation moment about the hip was 0.095 ± 0.017 Nm/kg. The average peak extension moment about the knee was -0.078 ± 0.013 Nm/kg. The average peak flexion and extension moments about the ankle were 0.008 ± 0.005 and -0.099 ± 0.026 Nm/kg. Power was calculated from joint moments and angular momentum data extracted from kinematics, and the results are shown in **Figure 5-4**. Average peak generation and absorption power for the hip was 0.314 ± 0.128 W/kg and -0.223 ± 0.115 W/kg. Average peak generation and absorption power for the knee was 0.193 ± 0.186 W/kg and -0.301 ± 0.136 W/kg. Average peak generation and absorption power for the ankle was 0.108 ± 0.067 W/kg and -0.426 ± 0.202 W/kg.

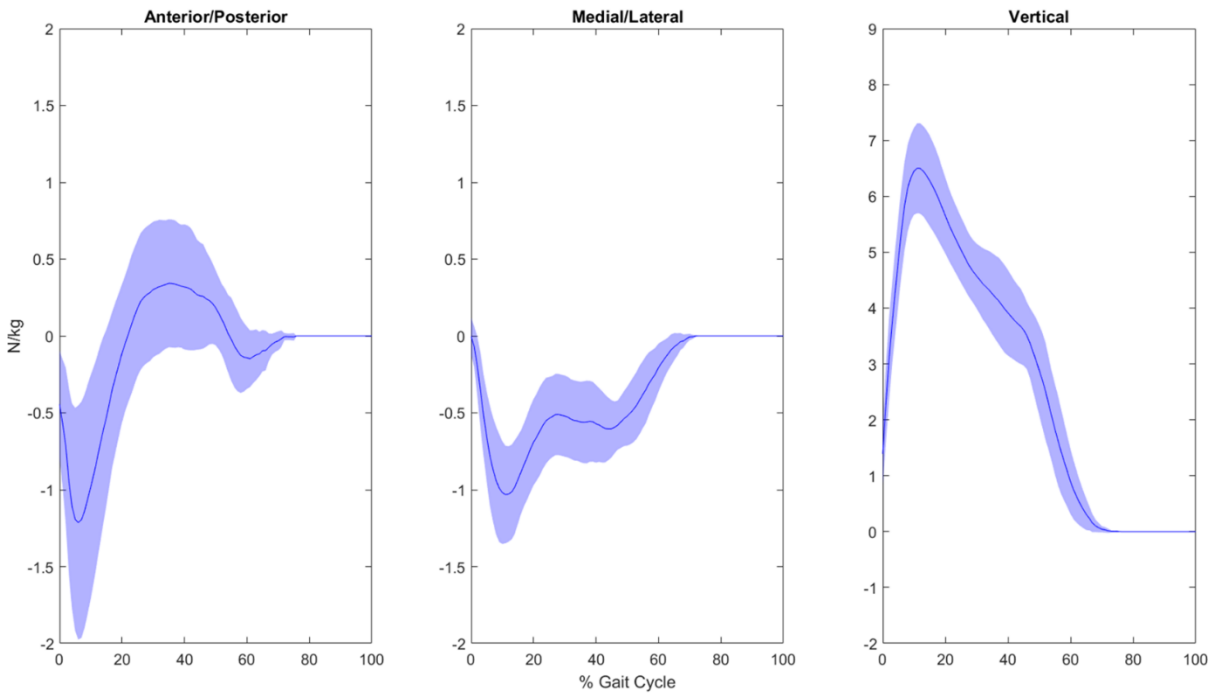


Figure 5-3. Ground reaction force (GRF) curves for healthy female Lewis rats. Curves are shown as mean \pm 1STD for all three axes (x, y, z). The X-axis is represented by the anterior/posterior forces, the Y-axis is represented by the medial/lateral forces, and the Z-axis is represented by the vertical forces. Data was compiled from load-cell footstrikes from 20 female Lewis rats.

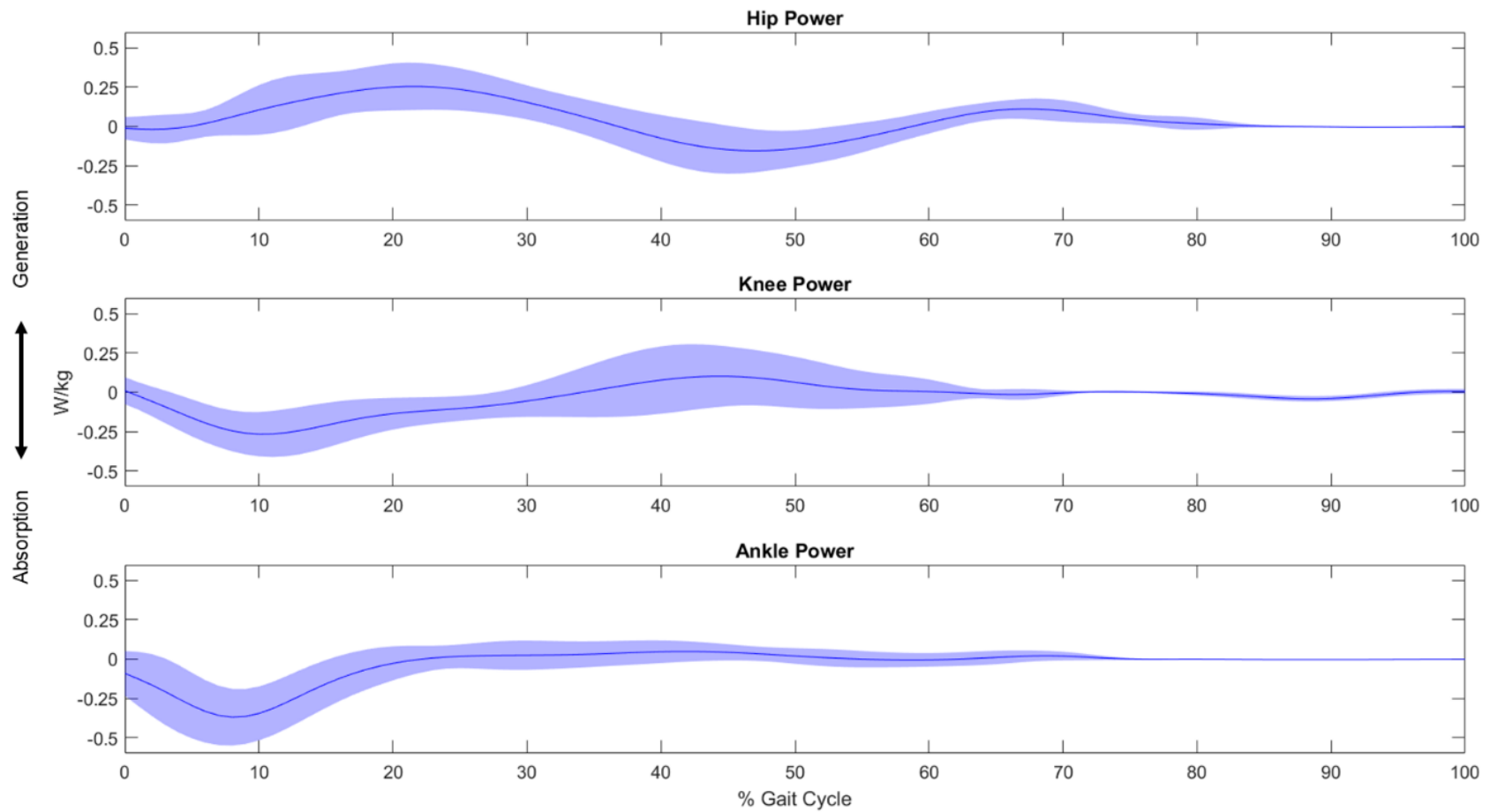


Figure 5-4. Joint power curves for healthy female Lewis rats. Curves are shown as mean \pm 1STD for all three joints (hip, knee, ankle) for 20 healthy female Lewis rats. All power plots represent the sagittal plane (i.e. flexion/extension) in W/kg.

Discussion

The methods and data developed in this work expand the scope of pre-clinical rat studies to evaluate any pathology modeled in the rat hindlimb with an extreme level of biomechanical and physiological detail. This study is the first to report 3D kinematics and 3D kinetics from concurrently recorded motion capture marker and GRF data. This study also compiled data from more animals than previous kinematic or kinetic studies (20 vs. an average of 11^{17,19,21,29-33,40,42-50}) to generate a more comprehensive dataset. While we have previously shown that measurable kinematic differences exist before and after rats are given VML injuries, the methods developed here will allow us to evaluate the 3-D kinetic implications of these injuries. Among others, these include changes in motor control, neuromuscular recruitment patterns, and compensation strategies in response to an injury or pathology. Further, the efficacy of regenerative therapeutics for treatment of injury can and will be more extensively evaluated beyond tissue morphology and isometric force generation. As mentioned, these methods allow for analysis of the impact of injury and treatment on both a joint-by-joint and systemic basis, providing a complete picture of the response to injury and the recovery timeline.

Though kinematics and kinetics were the primary outcomes of this study, spatiotemporal parameters remain important metrics. Spatiotemporal data includes parameters such as stride length, velocity, cadence, and time in swing, stance, and double vs. single support, all of which have been successfully calculated for both treadmill and over-ground walking^{13,14,16-21,25,31,51-57}. This data is important to evaluate because it is the most sensitive to changes in gait mechanics, despite providing little insight to the mechanisms driving the change. From the list above, walking speed and step length are the best identifiers of gait abnormalities, but they offer little insight to underlying cause. Our recorded values (shown in **Table 5-1**) are similar to previously reported

values for rat walking, demonstrating that the rats in this study were moving at a reasonable self-selected pace. Specifically, the average walking speed of $30.3 \pm 3.4 \text{ cm/s}$ falls well within the range of previously published literature values for healthy walking of $22\text{-}71 \text{ cm/s}$ ^{16,17,19,21,25,55-57}. In addition, the mean stance percentage of $63.9 \pm 3.6\%$ compares favorably to a range of $60\text{-}73.9\%$ ^{17,18,54,57}, as well as mean stride length of $122.4 \pm 4.8 \text{ mm}$, when compared to a reported range of $82.5\text{-}150 \text{ mm}$ ^{16,17,20,21,53,54,57}.

GRFs (**Figure 5-3**) provide insight on the amount of body support, the impacts of injury, and balance during ground contact in the stance phase of the gait cycle. They also identify where and when the rats absorb and generate propulsive force during heel strike and toe-off, as well as how stable the rats are during the contralateral swing phase as indicated by the lateral forces. GRFs for normal locomotion have been obtained for healthy rats^{14,22-28}, but previous studies collecting GRF data have varied in the velocity of their control animals ($30\text{-}85 \text{ cm/s}$ ^{14,23,28}) indicating that some of these animals were likely not walking. The data presented here was collected on animals with an average moving velocity of 30.3 cm/s , within the threshold for a lateral sequence walk ($<48 \text{ cm/s}$ ³⁹), thereby providing a basis for GRFs during normal walking. On average, the vertical GRFs in this study represent 67.5% of body weight and falls in the range of previously reported vertical GRF data ($65\text{-}87\%$ of BW ²²⁻²⁸). These vertical forces are highest in early stance and then steadily decrease, which is different than what is typically seen in humans. The anterior-posterior GRFs represent braking/acceleration forces and pass just above and below the zero-level (braking 13.2% vs $4\text{-}15\%$ of BW ^{22-24,27,28}, acceleration 5.1% vs $2\text{-}16\%$ of BW ^{22-24,27,28}). Similar to humans, these forces show that the rats decelerate in early stance and accelerate in late stance. The medial-lateral GRFs pass below the zero-level as the rat lands on the outside of their foot at heel strike and rolls off the second phalange at toe-off (medial 0.47% vs $0\text{-}3\%$, lateral 11.2% vs $5\text{-}8\%$ ^{22-24,28}).

The fact that the medial-lateral GRF is always pushing back towards center is likely exaggerated by the wide step width of rats relative to what is typically seen in human subjects. The high number of foot strikes obtained in this study, low variance, and similarity to published data show the presented values are representative of normal over ground walking at self-selected pace for healthy rats. However, as noted earlier GRFs are a whole limb measurement. It is only when combined with kinematics that GRFs provide truly informative data through the calculation of joint-by-joint moments. In the absence of this advanced analysis, GRFs provide no information on where and how the total limb force is generated.

Joint kinematics have been examined extensively in rat models^{17,29-33} to evaluate changes in joint motion due to muscle, nerve, or joint injuries. 3-D kinematics provide significant data for gait evaluation because they easily characterize classic compensation patterns (such as circumduction or vaulting) while also having enough precision to identify smaller changes in the motion of the hip, knee, or ankle that could have longer-term osteoarthritic effects. Kinematics also provide the foundation for kinetic and energetic analysis by providing information on the angular acceleration and angular velocity of the limb segments. But as previously mentioned, there is a lack of congruence in the kinematic literature due to vast methodological differences. Previously reported values for sagittal plane kinematics vary significantly in their raw angles, primarily due to limited motion capture techniques and higher variance methods for the modeling of marker positions. Specifically, many groups using marker digitization rather than established motion tracking cameras and software, used permanent ink dots rather than reflective markers to track joint locations, or only utilized 2-D motion capture to evaluate solely the sagittal plane.

Further, there are frequent differences in model definitions in the kinematic literature, such as neutral joint angle definitions. Some groups define the neutral angle as 0° and others define

neutral as 90°, leading to a disconnect in how data is reported. To address the latter point, we defined our neutral position consistent with existing protocols for human movement analysis⁵⁸. Similarly, another limitation of kinematic analysis in rodents has been the inaccuracy of modeling the motion of the knee due to the extreme amount of skin artifact. Bauman et al (2009)²⁹ used 2-D X-ray fluoroscopy to show that there are broad differences in the kinematics of the knee when using skin-derived, triangulated, and bone-derived angle measurements. The data presented here compares favorably to the shape and motion of bone-derived knee kinematics reported by Bauman²⁹ relative to their own skin-derived kinematics. We only observed two differences when comparing the two datasets. The first difference was a slight offset in our hip flexion angle due to the aforementioned differences in neutral angle definition (we used the sacroiliac crest and they used the caudal ischium). Second, there is a discrepancy in the knee angle at mid-stance that could be attributed to the difference in collecting 3-D versus 2-D motion data. We observed significant out of plane movement of the knee joint center which would not be accounted for when using single plane fluoroscopy (**Figure 5-2**).

As mentioned, joint kinetics are the gold standard for the evaluation of human biomechanics. They provide information on the internal forces being experienced on a joint-by-joint basis that cannot be captured with any other evaluative method. This information is significant because the same angular joint motion can be produced using drastically different muscle activation patterns, and many times those alternative patterns are the driving cause of long-term comorbid joint conditions. Kinetics also reveal the working relationship between joints, as a deviation at one joint in a system nearly always results in a deviation at another joint, many times hidden in the contralateral limb. Further, the ability to do kinetic analysis of gait informs everything from the etiology of a disease to treatment decisions, treatment outcomes, and the

ultimate health of the entire system. Recovery from a musculoskeletal or neural injury is more than just the local recovery from the immediate issue, it is a systemic undertaking that requires a systemic evaluation in order to assess the true extent of recovery.

Three studies have previously attempted to characterize rat gait kinetics, conducted by Bennett et al (2012)³¹ and Andrada et al (2010; 2013)^{25,26}. They performed these studies on 5 animals and 2 animals, respectively, and calculated joint moments for the hip, knee, and ankle in only the sagittal plane. The curve shapes of the kinetic analysis presented here align well with the pre-surgery moments presented by Bennett³¹ (2012) and the shapes of the kinetic curves of the hip and ankle compare well to both sets of data presented by Andrada^{25,26} (2010; 2013), with our peak values falling within the range of their reported values. There is some disparity in the shape of the knee torque graphs, but because Andrada^{25,26} (2010; 2013) did not publish their kinematic curves it is also difficult to pinpoint the exact source of these differences. However, they did publish their recognition that imaging in 2D would impact their sagittal plane angles. By design, imperfect knee angles would lead to incorrect knee moments. In this study, the reported methods and data permitted calculation of joint moments in all three planes at the hip (flexion/extension, ab/adduction, internal/external rotation). Because of the combination of consistent 3D kinematic curves and low variance GRFs in this study, the calculated kinetic results in all three planes are reliable and provide a solid benchmark for 3D rat gait analysis moving forward.

Joint power analysis is an under-researched area with respect to rodent gait studies, but the relative shapes of our power plots for the hip, knee, and ankle (**Figure 5-4**) compare favorably to the three other published datasets in Bennett et al (2012)³¹ and Andrada et al (2010; 2013)^{25,26}. However, the values reported by Bennett³¹ for normalized power are extremely high (peaks greater than 60W/kg). This may be due to a failure to convert from degrees/second to radians/second for

angular momentum values, because both their kinematic and kinetic curves present reasonable data. For comparison, Bennett³¹ (2012) reports a peak hip power of ~60W/kg, but this value is significantly higher than peak values reported for humans (~1.8W/kg⁵⁹), horses (~6W/kg⁶⁰), or rats in the Andrada^{25,26} (2010, 2013) studies (0.08-1.2W/kg^{25,26}). There is a clear discrepancy between Bennett's reported values and the field, but the values presented by Andrada^{25,26} (2010; 2013) fall far more within the reasonable expected range for peak joint power of walking rats. Based on that data, our power curves fall within the range presented by Andrada^{25,26} (2010, 2013) and are on the proper scale of the expected hip, knee, and ankle joint powers during healthy, normal walking for Lewis rats.

Because the rat hindlimb is utilized as a model system for the treatment and evaluation of so many pathologies, this method of comprehensive gait evaluation should be of broad utility to the field. The data presented in this paper is the first to characterize kinetics in all three planes, providing comprehensive insight into the biomechanics of rat walking on a joint-by-joint basis. In addition, kinematic analysis in this study was conducted on a larger cohort (20 vs. an average of 11^{17,19,21,29-33,40,42-50}) and included more kinetic data on both an animal basis and foot-strike basis than previous studies in the field. As such, this work extends the analytic methods available to investigators to study the rat hindlimb in beyond more widely used measurements such muscle force production to include insight into internal forces and movement compensation patterns. Similarities of rat gait to the human crouch gait benchmark should provide additional translational value to these investigations for improved understanding, evaluation, and treatment in humans. \

Conclusion

We are particularly excited about the potential applications of this approach to provide improved solutions for treatment of extremity trauma. High impact trauma such as volumetric muscle loss and/or peripheral nerve injury to the extremities impacts thousands of wounded warriors and civilians each year. Frequently, especially in complex compartments with multiple muscles and innervation patterns, the biomechanical effects of these injuries and the route to recovery can be difficult to precisely identify. The addition of 3D kinetic analysis provides an important new tool to gain greater insight into the “black box” of potential mechanisms responsible for the functional deficits observed in these complex injuries, as well as any compensatory neuromuscular responses/adaptations. In theory, implementing this new evaluative tool into the armamentarium of methods available should accelerate development of more effective treatments for functional restoration of extremity trauma, and ultimately significantly increase the quality of life for impacted individuals.

Acknowledgements

This work was supported in part by the AR³T Pilot Funding Program. Additional thanks to the members of the Motion Analysis and Motor Performance Laboratory and the Laboratory of Regenerative Therapeutics at the University of Virginia for their contributions.

Author Contributions

JD performed the experiments, analyzed data, and wrote/edited the manuscript. BH analyzed the data, wrote the underlying code to process the data, and created/ran the models. CS helped run models and write code. KJ helped perform the experiments. GJC and SDR were the co-PIs on the study, planned and helped perform the experiments, and helped to write and edit the manuscript.

Additional Information

The authors have no competing interests to disclose.

References

1. Passipieri, J. A. *et al.* Keratin Hydrogel Enhances In Vivo Skeletal Muscle Function in a Rat Model of Volumetric Muscle Loss. *Tissue Eng. Part A* **23**, 556–571 (2017).
2. Aurora, A., Garg, K., Corona, B. T. & Walters, T. J. Physical rehabilitation improves muscle function following volumetric muscle loss injury. *BMC Sport. Sci. Med. Rehabil.* **6**, 41 (2014).
3. Corona, B. T., Ward, C. L., Baker, H. B., Walters, T. J. & Christ, G. J. Implantation of In Vitro Tissue Engineered Muscle Repair Constructs and Bladder Acellular Matrices Partially Restore In Vivo Skeletal Muscle Function in a Rat Model of Volumetric Muscle Loss Injury. *Tissue engineering. Part A* vol. 20 705–15 <http://www.ncbi.nlm.nih.gov/pubmed/24066899> (2014).
4. Wu, X., Corona, B. T., Chen, X. & Walters, T. J. A Standardized Rat Model of Volumetric Muscle Loss Injury for the Development of Tissue Engineering Therapies. *Biores. Open Access* **1**, 280–290 (2012).
5. Kemp, S. W. P. *et al.* Functional recovery following peripheral nerve injury in the transgenic Thy1-GFP rat. *J. Peripher. Nerv. Syst.* **18**, 220–231 (2013).
6. Cooney, D. S. *et al.* Mesenchymal Stem Cells Enhance Nerve Regeneration in a Rat Sciatic Nerve Repair and Hindlimb Transplant Model. *Sci. Rep.* **6**, 31306 (2016).
7. Allbright, K. O. *et al.* Delivery of adipose-derived stem cells in poloxamer hydrogel improves peripheral nerve regeneration. *Muscle Nerve* (2018) doi:10.1002/mus.26094.
8. Choe, M.-A., Kyung Hwa Kim, K. H., Gyeong Ju An, G. J., Lee, K.-S. & Heitkemper, M. Hindlimb Muscle Atrophy Occurs From Peripheral Nerve Damage in a Rat Neuropathic Pain Model. *Biol. Res. Nurs.* **13**, 44–54 (2011).
9. Komatsu, I., Wang, J. H.-C., Iwasaki, K., Shimizu, T. & Okano, T. The effect of tendon stem/progenitor cell (TSC) sheet on the early tendon healing in a rat Achilles tendon injury model. *Acta Biomater.* **42**, 136–146 (2016).
10. Akamatsu, F. E. *et al.* Experimental model of Achilles tendon injury in rats. *Acta Cir. Bras.* **29**, 417–422 (2014).
11. Black, D. A., Lindley, S., Tucci, M., Lawyer, T. & Bughuzzi, H. A New Model for Repair of the Achilles Tendon in the Rat. *J. Investig. Surg.* **24**, 217–221 (2011).
12. Maerz, T. *et al.* Biomechanical Characterization of a Model of Noninvasive, Traumatic Anterior Cruciate Ligament Injury in the Rat. *Ann. Biomed. Eng.* **43**, 2467–2476 (2015).
13. Lakes, E. H., Allen, K. D. & Pruitt, C. Gait Analysis Methods for Rodent Models of Arthritic Disorders: Reviews and Recommendations. *Osteoarthr. Cartil.* **24**, 1837–1849 (2016).
14. Allen, K. D. *et al.* Kinematic and dynamic gait compensations resulting from knee instability in a rat model of osteoarthritis. doi:10.1186/ar3801.
15. Hamilton, C. B. *et al.* Weight-bearing asymmetry and vertical activity differences in a rat

- model of post-traumatic knee osteoarthritis. *Osteoarthr. Cartil.* (2015) doi:10.1016/j.joca.2015.03.001.
16. Simjee, S. U., Jawed, H., Quadri, J. & Saeed, S. Quantitative gait analysis as a method to assess mechanical hyperalgesia modulated by disease-modifying antirheumatoid drugs in the adjuvant-induced arthritic rat. *Arthritis Res. Ther.* (2007) doi:10.1186/ar2290.
 17. Pereira, J. E. *et al.* A comparison analysis of hindlimb kinematics during overground and treadmill locomotion in rats. *Behav. Brain Res.* **172**, 212–218 (2006).
 18. Berryman, E. R., Harris, R. L., Moalli, M. & Bagi, C. M. Digigait™ quantitation of gait dynamics in rat rheumatoid arthritis model. *J. Musculoskelet. Neuronal Interact.* **9**, 89–98 (2009).
 19. Schmidt, A. & Fischer, M. S. The kinematic consequences of locomotion on sloped arboreal substrates in a generalized (*Rattus norvegicus*) and a specialized (*Sciurus vulgaris*) rodent. *J. Exp. Biol.* **214**, 2544–2559 (2011).
 20. Bonnet, C. S. *et al.* Ampa/kainate glutamate receptors contribute to inflammation, degeneration and pain related behaviour in inflammatory stages of arthritis. *Ann. Rheum. Dis.* **74**, 242–251 (2015).
 21. Allen, K. D. *et al.* Gait and behavior in an IL1 β -mediated model of rat knee arthritis and effects of an IL1 antagonist. *J. Orthop. Res.* (2011) doi:10.1002/jor.21309.
 22. Webb, A. A., Kerr, B., Neville, T., Ngan, S. & Assem, H. Kinematics and Ground Reaction Force Determination: A Demonstration Quantifying Locomotor Abilities of Young Adult, Middle-aged, and Geriatric Rats. *J. Vis. Exp.* e2138–e2138 (2011) doi:10.3791/2138.
 23. Muir, G. D. & Wishaw, I. Q. Ground reaction forces in locomoting hemi-parkinsonian rats: A definitive test for impairments and compensations. *Exp. Brain Res.* **126**, 307–314 (1999).
 24. Roemhildt, M., Gardner-Morse, M., Rowell, C., Beynnon, B. & Badger, G. Gait alterations in rats following attachment of a device and application of altered knee loading. (2010) doi:10.1016/j.jbiomech.2010.07.036.
 25. Andrada, E. *et al.* From biomechanics of rats' inclined locomotion to a climbing robot. *Int. J. Des. Nat. Ecodynamics* **8**, 191–212 (2013).
 26. Andrada, E. *et al.* Biomechanical analyses of rat locomotion during walking and climbing as a base for the design and construction of climbing robots. (2010) doi:10.2495/DN100151.
 27. Howard, C. S., Blakeney, D. C., Medige, J., Moy, O. J. & Peimer, C. A. Functional assessment in the rat by ground reaction forces. *J. Biomech.* **33**, 751–7 (2000).
 28. Muir, G. D. & Wishaw, I. Q. Complete locomotor recovery following corticospinal tract lesions: Measurement of ground reaction forces during overground locomotion in rats. *Behav. Brain Res.* **103**, 45–53 (1999).

29. Bauman, J. M. & Chang, Y.-H. High-speed x-ray video demonstrates significant skin movement errors with standard optical kinematics during rat locomotion. doi:10.1016/j.jneumeth.2009.10.017.
30. Alluin, O. *et al.* Kinematic study of locomotor recovery after spinal cord clip compression injury in rats. *J. Neurotrauma* **28**, 1963–1981 (2011).
31. Bennett, S. W., Lanovaz, J. L. & Muir, G. D. The biomechanics of locomotor compensation after peripheral nerve lesion in the rat. *Behav. Brain Res.* **229**, 391–400 (2012).
32. Garnier, C., Falempin, M. & Ene Canu, M.-H. A 3D analysis of fore- and hindlimb motion during locomotion: Comparison of overground and ladder walking in rats. *Behav. Brain Res.* **186**, 57–65 (2008).
33. Canu, M. H. & Garnier, C. A 3D analysis of fore- and hindlimb motion during overground and ladder walking: Comparison of control and unloaded rats. *Exp. Neurol.* **218**, 98–108 (2009).
34. Damiano, D. L., Arnold, A. S., Steele, K. M. & Delp, S. L. Can Strength Training Predictably Improve Gait Kinematics? A Pilot Study on the Effects of Hip and Knee Extensor Strengthening on Lower-Extremity Alignment in Cerebral Palsy. *Phys. Ther.* **90**, 269–279 (2010).
35. Damiano, D. L. & Abel, M. F. Functional outcomes of strength training in spastic cerebral palsy. *Arch. Phys. Med. Rehabil.* **79**, 119–125 (1998).
36. Damiano, D. L., Prosser, L. A., Curatalo, L. A. & Alter, K. E. Muscle Plasticity and Ankle Control After Repetitive Use of a Functional Electrical Stimulation Device for Foot Drop in Cerebral Palsy. *Neurorehabil. Neural Repair* **27**, 200–207 (2013).
37. Topp, R., Mikesky, A., Wigglesworth, J., Holt, W. & Edwards, J. E. The effect of a 12-week dynamic resistance strength training program on gait velocity and balance of older adults. *Gerontologist* **33**, 501–6 (1993).
38. Buchner, D. M. *et al.* The effect of strength and endurance training on gait, balance, fall risk, and health services use in community-living older adults. *J. Gerontol. A. Biol. Sci. Med. Sci.* **52**, M218-24 (1997).
39. Gillis, G. B. & Biewener, A. A. Hindlimb muscle function in relation to speed and gait: in vivo patterns of strain and activation in a hip and knee extensor of the rat (*Rattus norvegicus*) - PubMed. *J Exp Biol* **204**, 2717–2731 (2001).
40. Dienes, J. A. *et al.* Analysis and Modeling of Rat Gait Biomechanical Deficits in Response to Volumetric Muscle Loss Injury. *Front. Bioeng. Biotechnol.* **7**, 146 (2019).
41. Johnson, W. L., Jindrich, D. L., Roy, R. R. & Reggie Edgerton, V. A three-dimensional model of the rat hindlimb: musculoskeletal geometry and muscle moment arms. *J. Biomech.* **41**, 610–9 (2008).
42. Thota, A. K., Watson, S. C., Knapp, E., Thompson, B. & Jung, R. Neuromechanical control of locomotion in the rat. *J. Neurotrauma* **22**, 442–465 (2005).

43. João, F. O. D. S., Amadoa, S., Veloso, A., Armada-da-Silva, P. & Maurício, A. C. Anatomical reference frame versus planar analysis: Implications for the kinematics of the rat hindlimb during locomotion. *Rev. Neurosci.* **21**, 469–485 (2010).
44. Gravel, P., Tremblay, M., Leblond, H., Rossignol, S. & de Guise, J. A. A semi-automated software tool to study treadmill locomotion in the rat: From experiment videos to statistical gait analysis. *J. Neurosci. Methods* **190**, 279–288 (2010).
45. Perrot, O., Laroche, D., Pozzo, T. & Marie, C. Kinematics of obstacle clearance in the rat. *Behav. Brain Res.* **224**, 241–249 (2011).
46. Nica, I., Deprez, M., Nuttin, B. & Aerts, J. M. Automated assessment of endpoint and kinematic features of skilled reaching in rats. *Front. Behav. Neurosci.* **11**, (2018).
47. Balbinot, G. *et al.* Post-stroke kinematic analysis in rats reveals similar reaching abnormalities as humans. *Sci. Rep.* **8**, 1–13 (2018).
48. DiGiovanna, J. *et al.* Engagement of the rat hindlimb motor cortex across natural locomotor behaviors. *J. Neurosci.* **36**, 10440–10455 (2016).
49. Nakahata, A. *et al.* Gait kinematics changes in post traumatic knee osteoarthritis with destabilized medial meniscus in rat. *Osteoarthr. Cartil.* **26**, S390 (2018).
50. Filipe, V. M. *et al.* Effect of skin movement on the analysis of hindlimb kinematics during treadmill locomotion in rats. *J. Neurosci. Methods* **153**, 55–61 (2006).
51. Ferland, C. E., Laverty, S., Beaudry, F. & Vachon, P. Gait analysis and pain response of two rodent models of osteoarthritis. *Pharmacol. Biochem. Behav.* **97**, 603–610 (2011).
52. Fu, S. C., Cheuk, Y. C., Hung, L. K. & Chan, K. M. Limb Idleness Index (LII): A novel measurement of pain in a rat model of osteoarthritis. *Osteoarthr. Cartil.* **20**, 1409–1416 (2012).
53. Boettger, M. K. *et al.* Gait abnormalities differentially indicate pain or structural joint damage in monoarticular antigen-induced arthritis. *Pain* **145**, 142–150 (2009).
54. Clarke, K. A., Heitmeyer, S. A., Smith, A. G. & Taiwo, Y. O. Gait analysis in a rat model of osteoarthrosis. *Physiol. Behav.* (1997) doi:10.1016/S0031-9384(97)00022-X.
55. Górska, T., Chojnicka-gittins, B., Majczyn, H. & Zmyslowski, W. Overground Locomotion after Incomplete Spinal Lesions in the Rat: Quantitative Gait Analysis. *J. Neurotrauma* **24**, 1198–1218 (2007).
56. Kloefkorn, H. E., Jacobs, B. Y., Loye, A. M. & Allen, K. D. Spatiotemporal gait compensations following medial collateral ligament and medial meniscus injury in the rat: Correlating gait patterns to joint damage. *Arthritis Res. Ther.* (2015) doi:10.1186/s13075-015-0791-2.
57. Coulthard, P., Simjee, S. U. & Pleuvry, B. J. Gait analysis as a correlate of pain induced by carrageenan intraplantar injection. *J. Neurosci. Methods* (2003) doi:10.1016/S0165-0270(03)00154-7.
58. Wu, G. (Ed.) . Standards Documents. *International Society of Biomechanics*.

<https://isbweb.org/about-us/29-standards-documents?layout>.

59. Farris, D. J. & Sawicki, G. S. The mechanics and energetics of human walking and running: A joint level perspective. *J. R. Soc. Interface* (2012) doi:10.1098/rsif.2011.0182.
60. Dutto, D. J., Hoyt, D. F., Clayton, H. M., Cogger, E. A. & Wickler, S. J. Joint work and power for both the forelimb and hindlimb during trotting in the horse. *J. Exp. Biol.* **209**, 3990–3999 (2006).

Chapter 6 – Evaluation of Gait Biomechanics in Response to Complex Traumas and Treatment – Tibialis Anterior

Disclaimer: Due to ongoing refinement of data analysis, some figures and numerical values may change slightly in final publication but the overall conclusions are expected to remain consistent.

Introduction

As extensively covered in previous chapters, despite the well-documented ability of skeletal muscle to repair, regenerate, and remodel after injury¹⁻⁵, a vast number of diseases, disorders, and traumas that result in an irrecoverable loss of muscle function remain. Included among these traumatic injuries is volumetric muscle loss (VML)⁶. VML injuries are characterized by such a significant degree of muscle tissue loss that it exceeds the native ability of the muscle to recover, resulting in permanent cosmetic and functional deficits⁷ to the limbs, neck, or face. These injuries impact both the civilian and military populations, affecting thousands of individuals each year. It should be noted, however, that large scale VML injuries do not occur without the coincidence of damage to peripheral nerve structures. With that in mind, the second set of studies presented in this chapter shifted focus away from isolated VML injuries to isolated peripheral nerve trauma and combined muscle-nerve polytraumas. These injuries align with what would most commonly be seen in injuries incurred by armed services personnel in the line of duty and civilians who experience a high-impact trauma.

Peripheral nerve injuries result in the partial or total loss of motor, sensory, and autonomic signals conveyed by the lacerated nerves to the denervated segments of the body⁸. Further, while the potential for regeneration of injured nerve is dependent on the severity of the damage, regeneration is extremely poor if large segments of nerve trunks are lost, even when there is no disruption of the connective tissue macrostructure. Even in the best-case scenarios, peripheral

nerves only grow at a rate of 1-3mm/day^{9,10} and the downstream muscles are subject to increasingly extreme atrophy as more time passes before a signal is restored.

Current options for regenerative therapeutics for treatment of VML injury have shown a limited ability to produce the desired functional and cosmetic recovery, and are associated with donor site morbidities¹¹. This fact has shifted attention to tissue engineering (TE) technologies that provide more effective treatment options for large scale muscle injuries. A common TE approach has been the implantation of decellularized extracellular matrices (ECM), both with¹²⁻¹⁸ and without¹⁹⁻²² cellular components (see **Chapter 1**). Several of these approaches have been evaluated in preclinical studies, with results showing that the implantation of a cell-seeded ECM matrix generally leads to a significant functional improvement^{12,15,23-25}. However, it is also important to acknowledge that current approaches for the repair of VML injury involve implantation of regenerative technologies at the injury site irrespective of the co-occurrence or severity of accompanying nerve injury. This is a significant point due to atrophy concerns stemming from the lack of downstream signaling from the injured nerve. Without the appropriate endogenous neural cues, the myotubes/myofibers of an implanted TEMR construct could also atrophy or become apoptotic²⁶, thereby reducing the effectiveness of the treatment. An explicit goal of the work presented in this dissertation is to better understand the appropriate time course for treatment of VML injury given the impact of functional nerve regeneration on treatment efficacy.

Historically, multiple VML^{13,16,31-40,19,41,42,23-25,27-30} and peripheral nerve injury⁴³⁻⁴⁷ studies have utilized rats as the model system, but results are typically focused on volume reconstitution and recovery of force generation. In humans, analysis of walking patterns (gait) is frequently used as a baseline functional measure of movement quality⁴⁸⁻⁵¹. However, studies of human movement

have shown that gains in strength do not necessarily result in improvements in movement function⁵²⁻⁵⁶. To address this, we have developed a method to quantify changes in gait for rats with tibialis anterior (TA) VML injuries and treatments using methods similar to those used for human gait analysis. These techniques revealed gait changes both in response to injury and during recovery. The ability to measure changes in rat gait parameters gives information on how the animal is functionally utilizing damaged or regenerated muscle tissue, providing insight on strength, motion planning, and neuromuscular motor control strategies.

While other groups have utilized motion capture to study rat gait⁵⁷⁻⁶¹ (see **Chapter 2**), few have attempted to evaluate peripheral nerve injury and only one has attempted to acquire over-ground gait information on rats with VML injuries⁶². However, these groups did not utilize high accuracy motion capture or modeling techniques in their data collection or kinematic calculations, instead opting for manual post-hoc tracing of paw and limb locations for angle calculations.

With regard to the current studies, we are the first group to successfully capture three-plane kinematic and kinetic data, the first to use gait analysis to evaluate the biomechanical impact of a muscle-nerve polytrauma injury, and most significantly, the first to evaluate the efficacy of an ECM-based treatment of VML injury in the form of the Tissue Engineered Muscle Repair (TEMR) therapeutic. Using a combination of VICON motion capture, advanced musculoskeletal modeling techniques in OpenSim, and concurrently captured ground reaction forces (GRFs), we were able to detect significant differences in joint angles and joint moments post-VML injury in both the treated and untreated groups, and track changes in movement quality over time. This enhanced understanding of rat function post-VML injury and repair will help to expedite the development and refinement of regenerative therapeutics and rehabilitation strategies for humans. With

improved treatment methodologies, the ultimate goal is to improve long term quality of life for VML patients and accelerate the return to action for military personnel.

Materials and Methods

Experimental Outline

Twenty-four healthy 12-week old female Lewis rats were observed walking on a custom-built walkway and had their gait analyzed using a combination of Vicon Nexus motion capture software and OpenSim modeling. After baseline collection on all animals, 8 animals were designated to a healthy control group (Control), 8 were given a 20% by mass VML injury to the right tibialis anterior (TA) with no repair performed (NRFe, injured), and 8 were given the injury and immediately treated with an implanted Tissue Engineered Muscle Repair (TEMR) construct.

In a second study, twenty-four healthy 12-week old male Lewis rats were observed walking on a custom-built walkway and had their gait analyzed using the same methodology. After baseline collection on all animals, 8 were given a 20% by mass VML injury with no repair performed to the right TA (NRMa), 8 were given only a partial peroneal nerve laceration with repair (no VML injury, PPN), and 8 were given the partial peroneal nerve laceration in combination with the unrepaired VML injury (TAPoly).

Motion capture was repeated at 4, 8, and 12 weeks after surgery. Kinematic and GRF data was acquired from the trials through motion capture. Individual gait cycles were compiled and averaged to create kinematic and kinetic curves for each animal, which were averaged within each group and timepoint for statistical analysis. Force testing was also performed on the animals at -1, 4, 8, and 12 weeks relative to the surgery date to identify the deficit created by the surgery and track any recovery of force generation ability.

Animal Care

This study was conducted in compliance with the Animal Welfare Act, the Implementing Animal Welfare Regulations, and in accordance with the principles of the Guide for the Care and Use of Laboratory Animals. The University of Virginia Animal Care and Use Committee approved all animal procedures. A total of 24 female Lewis rats (Charles River Laboratories) weighing 180.0 ± 7.67 g at 12 weeks of age and a total of 24 male Lewis rats (Charles River Laboratories) weighing 283.4 ± 23.8 g at 12 weeks of age were pair housed in a vivarium accredited by the American Association for the Accreditation of Laboratory Animal Care, and they were provided with food and water *ad libitum*.

Isolation of Muscle Progenitor Cells (MPCs)

Tibialis anterior and soleus muscles from 4 week old female Lewis rats were harvested for primary cell culture using previously described methods^{12,15,23,33}. Briefly, skeletal muscle cells were digested in 0.2% collagenase (Gibco) solution prepared in low glucose Delbecco's modified Eagle medium (DMEM; Gibco) for 2 hours at 37°C. Diced muscle tissue was plated onto culture dishes coated with Matrigel (BD Biosciences) in myogenic medium containing DMEM high glucose with 20% fetal bovine serum (FBS; Gemini), 10% horse serum (Gibco), 1% chicken embryo extract (Life Science), and 1% antibiotic/antimycotic (AA; Gibco). Cells were passaged at ~75% confluence, cultured in DMEM low glucose supplemented with 15% FBS and 1% AA, and used for seeding at the second passage.

Bladder Acellular Matrix (BAM) Preparation

BAM scaffolds were prepared from porcine urinary bladder as previously described^{23,33}. Briefly, bladders obtained from City Packing Company (Burlington, NC) were washed and

trimmed to obtain the lamina propria, which was then placed in 0.05% trypsin (Gibco) for 1 hour at 37°C. The bladder was then transferred to DMEM solution supplemented with 10% FBS and 1% AA and kept overnight at 4°C. The prepared bladders were then washed in a solution containing 1% triton-X (Sigma-Aldrich) and 0.1% ammonium hydroxide (Fisher Scientific) in de-ionized water for 4 days at 4°C. Finally, the bladders were washed in de-ionized water for 3 days at 4°C. The decellularized scaffold was further dissected to obtain a scaffold of 0.2-0.4mm thickness. The prepared acellular matrix was cut into strips of 3x2cm and placed on a silicon mold. Scaffolds and molds were then placed in culture dishes, lyophilized, and sterilized by ethylene oxide.

TEMR Preparation

The TEMR construct was prepared as previously described^{12,15,23}. Briefly, sterilized scaffolds were seeded with 5.4 million cells on one side, and 24h later the scaffold and mold were flipped and 5.4 million cells were seeded on the alternate side. After 3 days in seeding media, a media change was performed to immerse the scaffolds in differentiation media (DMEM F12, 2% horse serum, 1% AA) for an additional 7 days. After ten days in static culture, the cell-seeded scaffolds were placed in a bioreactor system as previously described. The bioreactor allowed for cyclic stretching of the TEMR scaffolds to ~10% strain three times per minute for the first 5 minutes of every hour over a 5-day period. The TEMR scaffolds were immersed in seeding media for the duration of their time in the bioreactor, and the bioreactor was placed in an incubator that was continuously aerated with 95% air-5% carbon dioxide at 37°C.

Creation of VML Injury

VML injuries were surgically created as previously described^{23,33,63}. Briefly, a longitudinal incision was made on the lateral portion of the lower right leg. The skin was then cleared from the underlying fascia using blunt separation, and the fascia covering the anterior crural muscles was separated using blunt dissection. The proximal and distal tendons of the Extensor Hallicus Longus (EHL) and Extensor Digitorum Longus (EDL) muscles were then isolated and ablated. As previously described, the TA muscle corresponds to 0.17% of the gross body weight^{23,33,63}. The VML injury model was characterized by excision of roughly 20% of the TA muscle weight from the middle third of the muscle (**Figure 6-1A**). In the TEMR animals, the construct was sutured into the defect site immediately upon creation of the injury (**Figure 6-1B**). The fascia was closed with 6-0 vicryl sutures and the skin was closed with 5-0 prolene using interrupted sutures. Skin glue was applied over the skin sutures to help prevent the incision from opening.

Creation of Peroneal Nerve Injury and Polytrauma

The partial laceration of the peroneal nerve was created by opening an incision parallel to the femur on the right leg. Through this incision, a second incision was created to cut through the biceps femoris muscle and access the branching site of the sciatic nerve. At this location, the sciatic nerve branches into three smaller nerves (**Figure 6-2A**): tibial (the largest), peroneal, and sural (the smallest). Through a surgical microscope, the peroneal nerve was identified and specialized instruments were utilized to create a ~50% laceration of the nerve as distally as close to the knee as possible. The nerve ends were then sutured together using 10-0 silk microsuture (**Figure 6-2B**). The biceps femoris was then sutured closed using 6-0 vicryl, followed by the skin using 5-0

prolene. Skin glue was applied over the skin sutures to help prevent the incision from opening. To create the polytrauma injuries, the VML injury creation protocol was followed immediately after the completion of the peroneal nerve surgery.

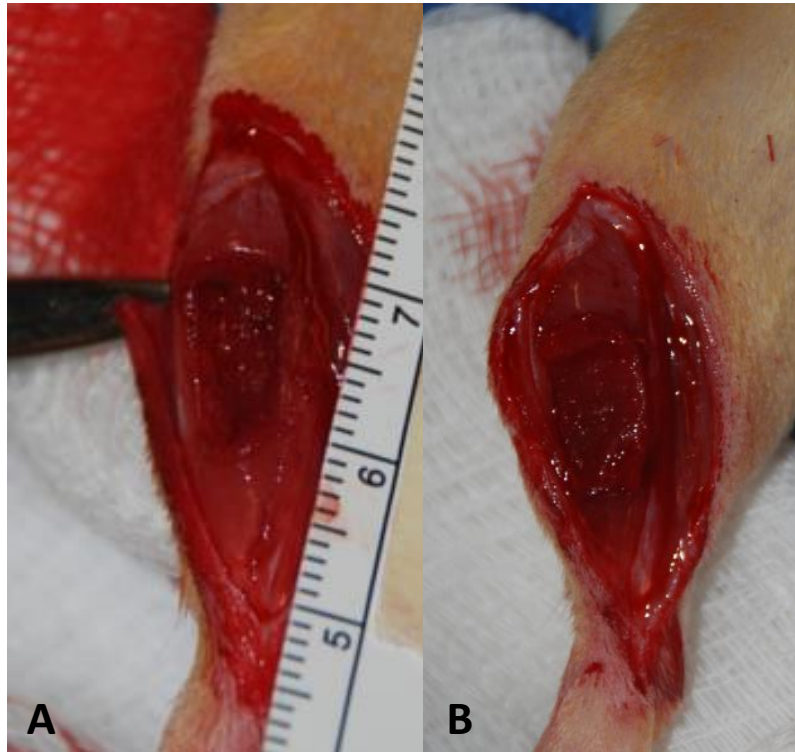


Figure 6-1: Volumetric muscle loss injury creation and repair. (A) Representative surgical defect created to mimic 20% by mass volumetric muscle loss injury (1.0x0.7x0.2cm) (B) Same defect as (A) with the Tissue Engineered Muscle Repair (TEMR) construct sutured into the defect site.

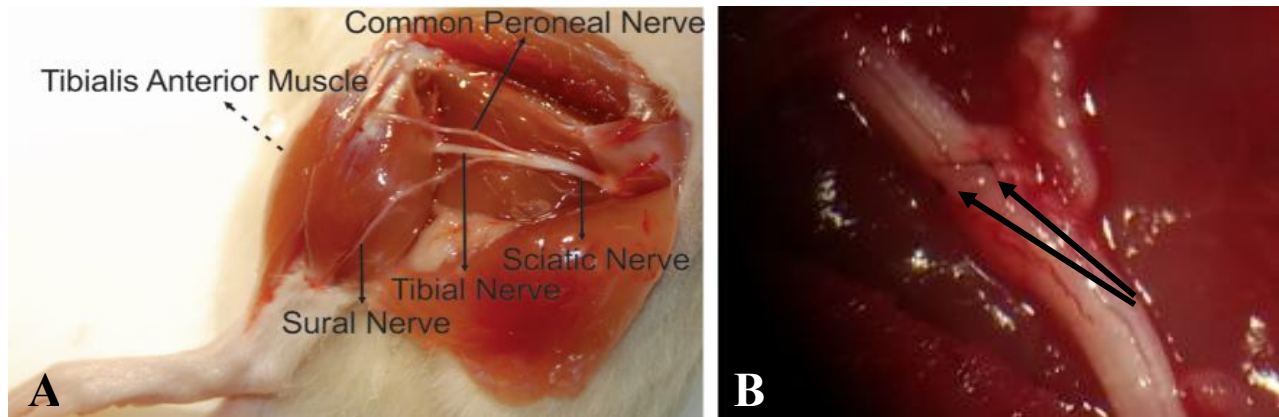


Figure 6-2: Sciatic nerve branch site and nerve laceration post-repair (A) Dissected rat limb exposing the nerves of the hindlimb and the branch point of the sciatic nerve into the tibial, peroneal, and sural nerves (B) Arrows indicating the locations of microsutures used to reattach portions of a nerve that was partially lacerated to create a recoverable nerve injury.

Force Testing for VML Animals

At -1, 4, 8, and 12 weeks relative to the surgery date, rats were anesthetized and the right hind limb was aseptically prepared for *in vivo* force testing^{33,64}. The rat was placed in a supine position on a heated platform and the right knee was bent to a 90° angle. The leg was secured using a stabilizing rod and the right foot was taped to a footplate. The footplate was attached to the shaft of an Aurora Scientific 305C-LR-FP servomotor, which was controlled using a computer. Sterilized percutaneous needle electrodes were carefully inserted into the skin of the lower right leg for stimulation of the right common peroneal nerve. Electrical stimulus was provided using an Aurora Scientific stimulator with a constant current SIU (Model 701C). Stimulation voltage and needle electrode placement were optimized with a series of 1Hz pulses resulting in twitch contraction. Contractile force of the anterior crural muscles was assessed through measuring the peak isometric tetanic torque determined from maximal response to a series of stimulation frequencies (10-200Hz). Torque at baseline was normalized by the body weight of each animal. Torque at each post-surgical timepoint was normalized by the body weight of each animal on the

day of collection, then was normalized to a percent of the baseline for that animal. The normalized torques at each post-surgical timepoint were averaged for analysis. After force testing, the animals were allowed to recover on the heated platform and were then returned to the vivarium. For terminal time points, animals were euthanized via CO₂ inhalation and cervical dislocation was performed as a secondary measure.

Force Testing for Peroneal Nerve and Polytrauma Animals

Terminal force testing on animals with nerve injuries was conducted using a nerve cuff around the peroneal or sciatic nerve. The nerve was accessed by making the same set of incisions as during the injury creation surgery. In ideal scenarios, the cuff was placed around the peroneal nerve proximal to the laceration. However, if the nerve was too difficult to access then the sciatic nerve was cuffed. If the sciatic method was chosen, the tibial and sural nerves were severed from the sciatic nerve so electrical stimulation only traveled down the peroneal nerve. Once the cuff was secured, the same stimulation protocol and analysis procedures as described in the previous section were followed. Animals were euthanized via CO₂ inhalation and cervical dislocation was performed as a secondary measure upon completion of this protocol.

Motion Capture

At -1, 4, 8, and 12 weeks relative to the surgery date, rats were anesthetized and shaved to allow proper placement of the motion capture marker set illustrated in **Figure 6-3**. Reflective markers were placed on the bony landmarks of the left anterior superior iliac crest (LASI), right anterior superior iliac crest (RASIS), spine (L6 vertebra), tail (5th caudal vertebra), hip, lateral knee, ankle, and distal end of the fifth metatarsal. Kinematic data on the female animals was collected

using a Vicon 7-camera (T40) setup collecting at 200Hz. Kinematic data on the male animals was collected using a Vicon 5-camera (Vue) setup collecting at 200Hz. The animals were placed at one end of the walkway and allowed to walk to the opposite end at a self-selected pace. This process was repeated until a minimum of five acceptable trials with clean footstrikes were obtained, with acceptable being defined as a consistent walk through the entirety of the collection volume with no abnormalities (i.e. starting/stopping, jumping, running, marker/camera dropout). After data collection the animals were returned to the vivarium.

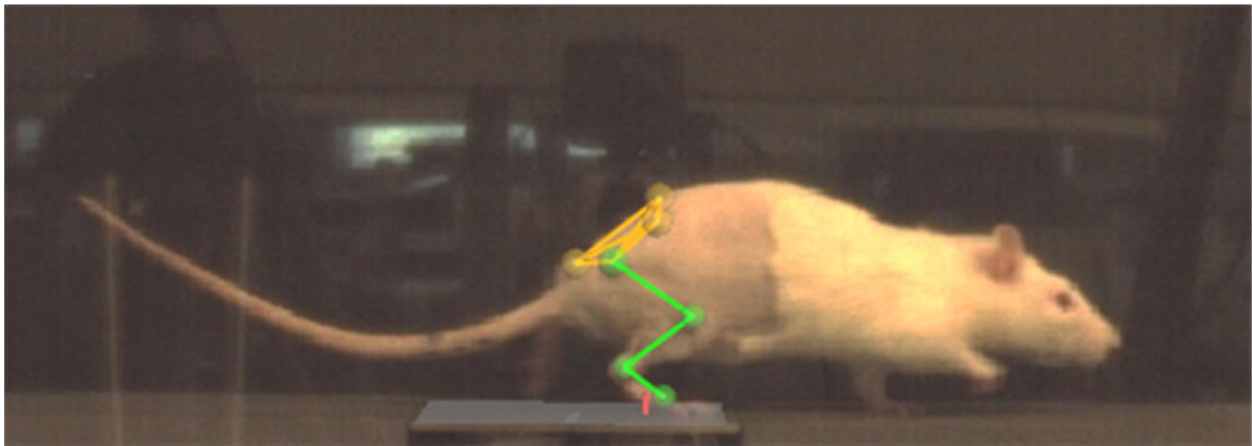


Figure 6-3. Vicon Nexus 3-D overlay of motion capture marker placements.

Inverse Kinematics

Inverse kinematics were calculated as previously described (**Chapter 4, Chapter 5**). Briefly, gait event and marker identification was completed in Nexus and data were filtered at 50Hz. Inverse kinematic modeling was performed in OpenSim using a modified version of an existing rat hindlimb model (**Figure 6-4**). This model consisted of four segments (hip, femur, tibia, foot) and each joint was modeled as first order. The hip and ankle were modeled as ball joints, and the knee was modeled as a hinge joint. Modifications were limited to adjusting the default location of the knee and spine markers on the model to more closely reflect the anatomical placement of

markers on the Lewis rats in this study, and the knee was simplified to a zeroth order hinge joint to accommodate scaling. The model was scaled to each rat before inverse kinematics were performed. When scaling, the weight of the knee marker was set to 1/10 of the other markers to account for the movement of the skin artifact over the knee joint during the trials. Reported data corresponded to one gait cycle, heel strike to heel strike of the right leg. Steps more than three standard deviations from the mean at any point in the gait cycle were excluded from the study.

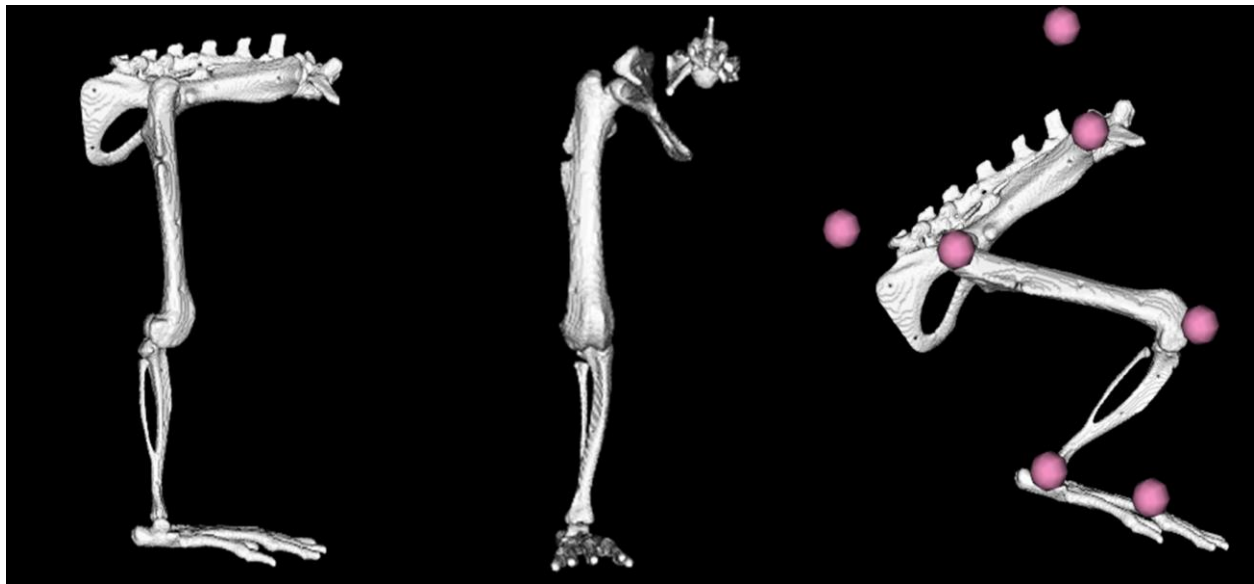


Figure 6-4. OpenSim rat hindlimb model with reconstructed marker locations. (A) Zeroed angles for hip, knee, and ankle flexion. (B) Zeroed angles for hip internal rotation and adduction. (C) Reconstructed marker locations for the SPINE, TAIL, RASI, HIP, KNEE, ANKLE, and TOE. The model was scaled for each individual animal at each collection time point based on the locations of these markers.

Inverse Dynamics

Inverse dynamics were performed by pairing GRF data with concurrently captured motion data in OpenSim (see **Chapter 5**). Briefly, kinematics were modeled for the entire trial as described in the previous section. Ground reaction forces and moments about the load cell were extracted from Nexus allowing for calculation of pressure centers. The gait cycle of interest was isolated by zeroing the GRFs prior to heel strike and after toe-off. Limb moments of inertia (MOI)

and centers of mass (COM) were determined as previously described (Normative Gait) and fed into the OpenSim model. The isolated GRF data then was loaded into OpenSim as a point force and applied to the foot, resulting in flexion, adduction, and internal rotation moments about the hip, a flexion moment about the knee, and a flexion moment about the ankle. Reported data corresponds to one gait cycle, heel strike to heel strike. Joint moments more than three standard deviations from the mean were excluded from the study.

Statistics

Numerical data are presented as mean \pm standard error of the mean (SEM). Needle electrode force data between the two female groups (NRFe, TEMR) and the three male groups (NRMa, PPN, TAPoly) were analyzed using one- and two-way analyses of variance (ANOVA) as indicated in the figure caption. Upon finding a significant ANOVA, post-hoc comparison testing of parameters of interest was performed using Fisher's least significant difference (LSD) test at α -level 0.05. These statistical analyses were conducted using GraphPad Prism 8.0 (La Jolla, CA). The statistical significance of spatiotemporal parameters and nerve cuff force data was also determined in GraphPad Prism using one-way ANOVA. Last, analysis of the joint kinematic and kinetic curves was performed using SPM-1 Matlab code (Study 1), GraphPad Prism (Study 2), and multiple t-tests ($\alpha=0.05$).

Results

Study 1

Creation of VML injury and force testing

One of the 16 female animals that received surgery contracted an infection from frequent reopening of the surgical site. This animal was euthanized and removed from the study. Beyond this, no animals in the study died during the surgical procedure and no additional post-implantation mortality occurred. There were no significant differences between the mean animal body weights (**Figure 6-5A**) between the groups over the course of the study or the torque generated by the any of the groups at baseline (**Figure 6-5B**). However, because animals in all groups gained weight over the course of the study, statistical comparisons on force measures were made on data normalized to body weight. Post-surgical isometric tetanic dorsiflexion torque testing at 8 and 12 weeks showed a significant increase in the torque generated by the TEMR group compared to the NRFe group (two-way ANOVA, $p < 0.05$). The average maximum torques as a percentage of baseline measured for the TEMR and NRFe groups were $61.5 \pm 7.2\%$ and $57.9 \pm 6.9\%$ at 4 weeks, $75.5 \pm 2.3\%$ and $62.5 \pm 5.6\%$ at 8 weeks, and $77.9 \pm 2.6\%$ and $64.8 \pm 4.8\%$ at 12 weeks (**Figure 6-5C**).

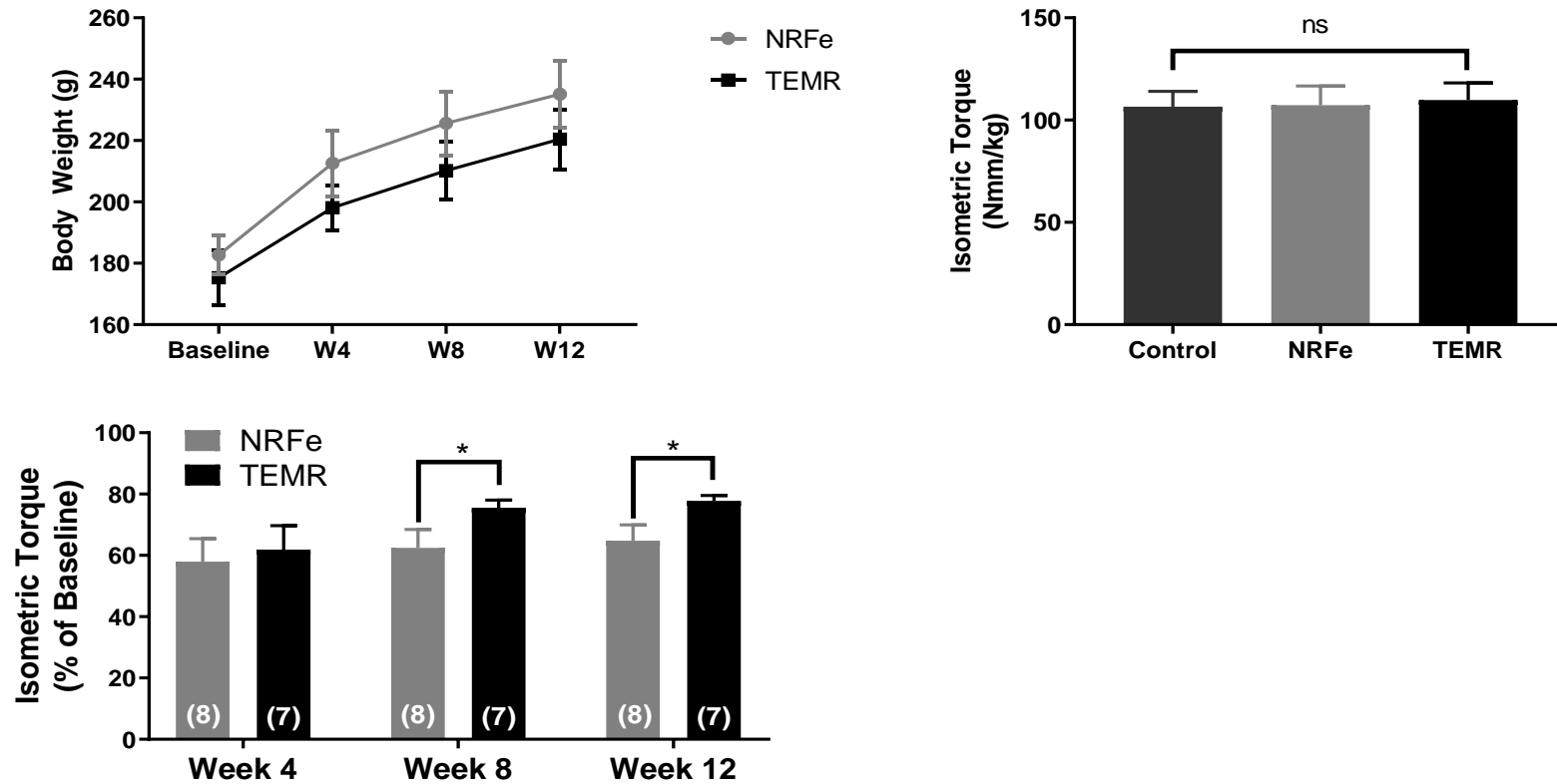


Figure 6-5. Study 1 comparison of body weight, functional baseline parameters, and functional recovery observed among different treatment groups (A) Body weights of study animals reveal normal healthy weight gain in all treatment groups over the course of 12 weeks. (B) Graphical comparison illustrating the equivalence of the mean baseline contraction force resulting from peroneal nerve stimulation and measured with footplate force transducer in all treatment groups. (C) Peak isometric torque measured at 4, 8 and 12 weeks, showing improved muscle recovery after TEMR application as early as 8 weeks post implantation. Individual responses are presented as a percentage of the respective individual mean of the initial maximum pre-injury isometric torque response. * significantly different at $p < 0.05$ level using t-tests (B) or Sidak post-hoc after performing Two-Way ANOVA in (C).

Spatiotemporal Parameters

For the initial study, a minimum of 3 steps per animal were averaged at the baseline, 4, 8, and 12-week timepoints for the injured groups (NRFe and TEMR). Measurements of stance percentage, stride length (mm), and velocity (cm/s) at all timepoints within each group were compared to baseline (**Table 6-1**). There were no significant differences between the baseline measurements for any of the female groups (Control, NRFe, TEMR). For the NRFe animals, stance percentage, and walking velocity significantly decreased between baseline and Week 4. Additionally, stride length significantly increased between baseline and Weeks 8. For the TEMR animals, significant decreases compared to baseline were seen in stride length (Week 4) and velocity (Week 4). Relative to each other, the TEMR animals walked at a significantly higher velocity relative to the NRFe animals at Week 4, but otherwise the two groups showed no differences.

Table 6-1: Compiled spatiotemporal results for the Control animals at Baseline and the TEMR and NRFe groups at all timepoints. Significant differences between each group compared to its own Baseline are indicated with a star (*), and differences between TEMR and NR as compared to each other at each timepoint are indicated with a caret (^) (t-tests, p<0.05).

Rat Group	Timepoint	Stance Percentage	Stride Length (mm)	Velocity (cm/s)
Control	Baseline	61.6±1.7%	130.4±5.6	34.8±6.1
NRFe	Baseline	62.9±2.6%	127.3±14.3	32.4±6.6
	Week 4	60.0±5.9%*	125.0±20.8	25.1±7.5*
	Week 8	61.4±2.3%	135.8±10.8*	33.7±5.9
	Week 12	61.4±2.7%	133.6±6.8	32.7±2.3
TEMR	Baseline	61.6±2.9%	130.7±7.4	33.9±4.1
	Week 4	62.0±2.2%	123.0±10.2*	29.4±3.2*^
	Week 8	61.2±2.5%	129.8±4.0	31.2±4.6
	Week 12	61.0±2.2%	131.0±6.6	32.4±3.3

Joint Kinematics

Average baseline kinematics are a composite of all rats. Repeatability of the motion capture data collection and reconstruction protocol was determined by comparing Baseline and Week 12 kinematics for the Control animals only (**Figure 6-6**). The results of this analysis showed no significant differences in the data, providing justification for comparison of the gait parameters of the injured/treated animals at post-surgical timepoints to baseline measurements.

For the first study, observed average ranges of motion for flexion of the hip, knee, and ankle joints in the baseline measurements were 48.1 ± 8.0 degrees, 48.6 ± 7.6 degrees, and 48.9 ± 4.7 degrees. When compared to baseline the NRFe animals showed clear differences ($p < 0.05$) at all three timepoints (**Figure 6-7**, red). Hip flexion showed significant decreases during stance at Week 8 and during the entire gait cycle at Week 12. Hip adduction decreased throughout the gait cycle at Week 4 and from heel strike to mid-stance at Week 8. Hip internal rotation increased during swing at Week 4 and decreased in early stance, mid-stance to toe-off, and late swing at Week 12. Knee flexion increased during swing at Week 4, decreased from late stance through toe-off at Week 8, and decreased from late stance through mid-swing at Week 12. Ankle dorsiflexion only showed one difference, a decrease around toe-off at Week 12.

The TEMR animals showed differences ($p < 0.05$) at all three timepoints when compared to the baseline, but at a far lower magnitude (**Figure 6-7**, blue). There was a significant reduction in hip flexion from mid to late stance at Week 4, a decrease in hip adduction at initial heel strike and late swing into secondary heel strike at Week 8, and a decrease in hip internal rotation during mid-stance at Week 8. Lastly, knee flexion decreased slightly in late stance at Week 4 and ankle dorsiflexion increased very slightly in late stance at Week 12.

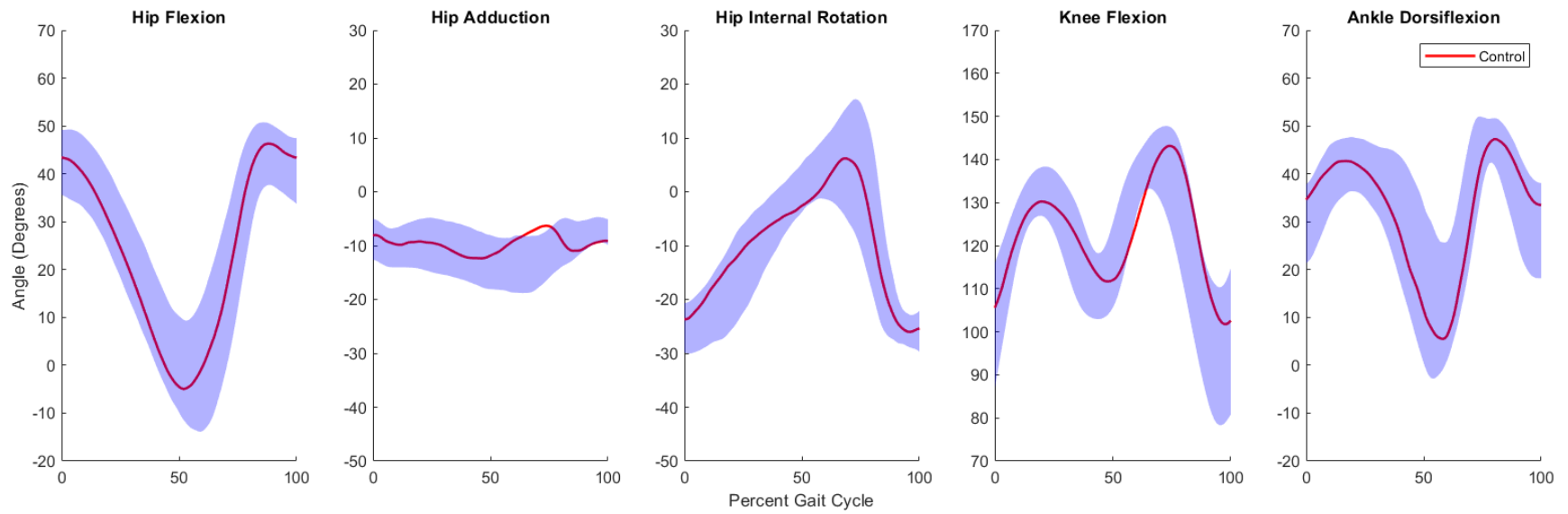


Figure 6-6: Comparison of baseline and Week 12 kinematics for healthy animals

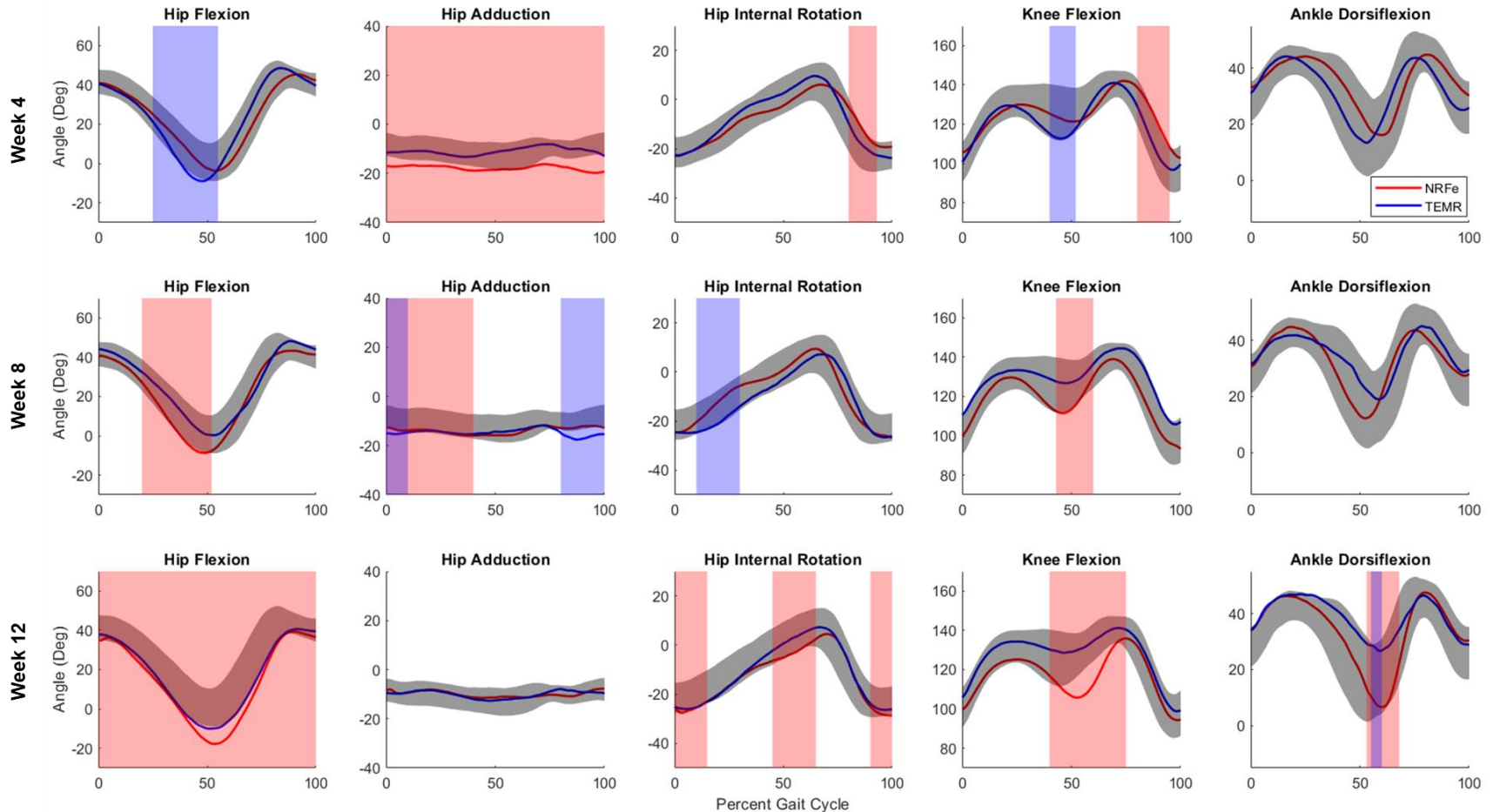


Figure 6-7. Kinematic comparisons between the TEMR and NRFe groups for hip flexion, hip adduction, hip internal rotation, knee flexion, and ankle dorsiflexion at all time points. The Baseline kinematic curves are shown as black clouds, the TEMR curves are shown in blue, and the NRFe curves are shown in red. Week 4 kinematics are in the top row, Week 8 in the middle, and Week 12 at the bottom. Areas of significant difference between the TEMR and Baseline curves are shown as blue shaded regions and between the NRFe and Baseline curves are shown as red shaded regions. (SPM1, multiple t-tests, $p < 0.05$).

Joint Moments

Average baseline kinetics for Study 1 are a composite of all rats. A minimum of 2 footstrikes per rat per timepoint were averaged for analysis. For the first study, the average baseline peak flexion and extension torques about the hip were 0.068 ± 0.039 and -0.087 ± 0.030 N*m/kg. The average peak adduction and internal rotation torques about the hip were 0.004 ± 0.008 and 0.077 ± 0.024 N*m/kg. The average peak extension moment about the knee was -0.094 ± 0.024 N*m/kg. The average peak flexion and extension moments about the ankle were 0.016 ± 0.010 and -0.084 ± 0.023 N*m/kg.

Again, the NRFe animals showed kinetic differences ($p < 0.05$) at all three timepoints as compared to the baseline (**Figure 6-8**, red). Hip flexion torque increased during early stance at Week 8, hip adduction torque decreased during early stance at Week 4 and increased during early stance at Week 12, and hip internal rotation torque decreased from early through late stance at Week 4. Knee flexion torque decreased in early stance at all timepoints, and ankle dorsiflexion torque decreased at toe-off at Week 12.

Finally, the TEMR animals also showed differences ($p < 0.05$) when compared to baseline at all timepoints. Hip flexion torque increased in early stance at Week 4. Hip adduction torque increased in early stance at Week 8 and Week 12, and hip internal rotation torque decreased during early through mid-stance at Week 4 and Week 8. Knee flexion torque decreased in early stance at Week 8 and Week 12, and ankle dorsiflexion torque increased in early stance at Week 8 and Week 12.

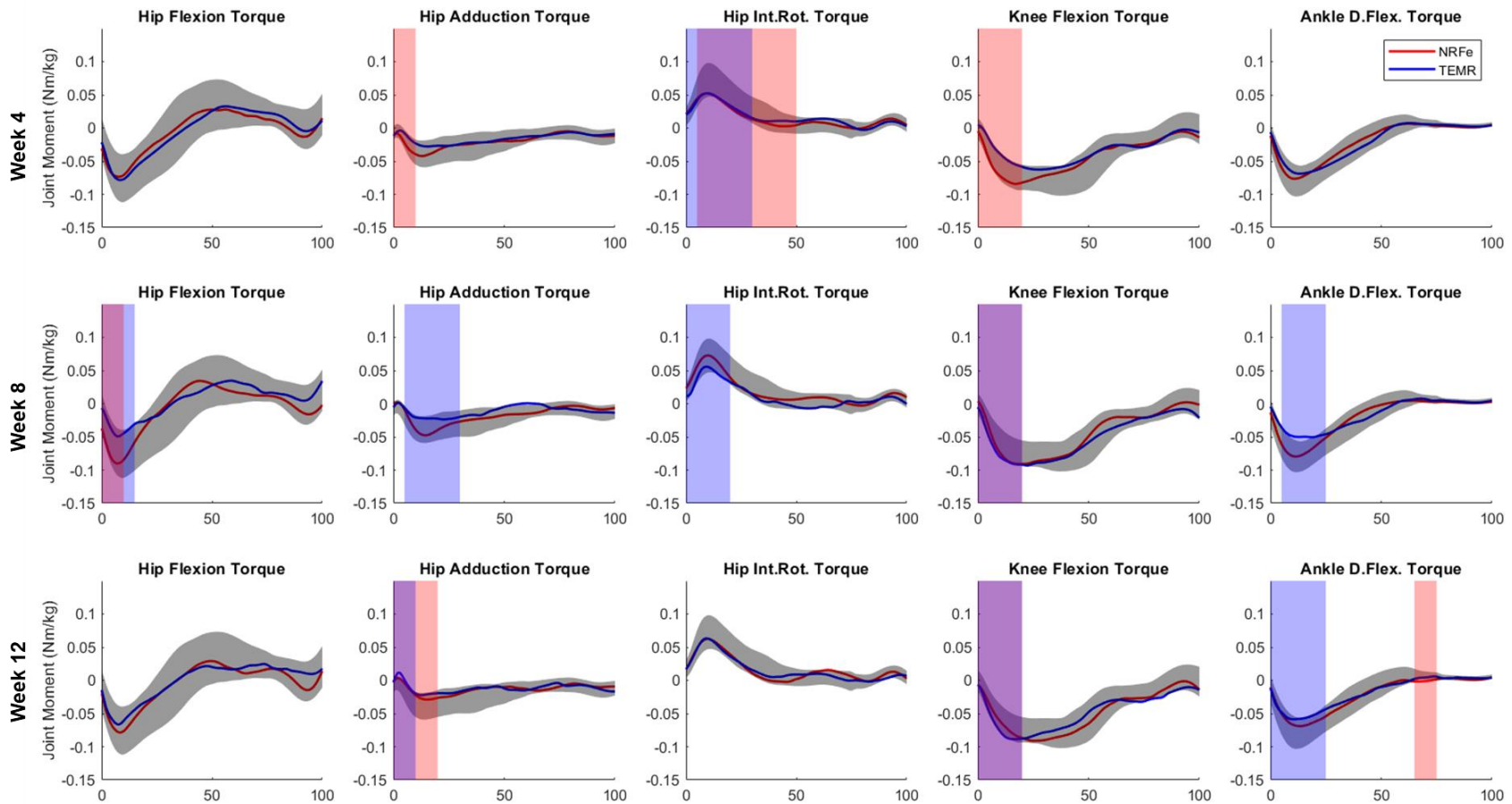


Figure 6-8: Kinetic comparisons between the TEMR and NRFe groups as compared to Baseline for hip flexion moment, hip adduction moment, hip internal rotation moment, knee flexion moment, and ankle dorsiflexion moment at all timepoints. The Baseline kinetic curves are shown as a black cloud, the TEMR curves are shown in blue, and the NRFe curves are shown in red. Week 4 kinetics are in the top row, Week 8 in the middle, and Week 12 at the bottom. Areas of significant difference between the TEMR and Baseline curves are shown as blue shaded regions and between the NRFe and Baseline curves are shown as red shaded regions. (SPM1, multiple t-tests, $p < 0.05$).

Study 2

Creation of VML injury and force testing

No animals in the study died during the surgical procedure and no post-implantation mortality occurred. There was no significant difference between the mean animal body weights (**Figure 6-9A**) between the groups over the course of the study or the torque generated by the any of the groups at baseline (**Figure 6-9B**). However, because animals in all groups gained weight over the course of the study, statistical comparisons on force measures were made on data normalized to body weight.

Post-surgical isometric tetanic dorsiflexion torque testing at 4 and 8 weeks showed a significant deficit between the TAPoly group compared to both the NRMa and PPN groups, but no significant difference between NRMa and PPN. The 12-week timepoint showed a significant deficit for the TAPoly group compared to both the NRMa and PPN groups, and a significant increase in torque for the PPN group as compared to NRMa (two-way ANOVA, $p < 0.05$). The significant deficit between the TAPoly group and the PPN group at 12-weeks was confirmed by nerve cuff testing (t-test, $p < 0.05$). The average maximum torques as a percentage of baseline measured through electrode stimulation for the groups at 4, 8, and 12 weeks were as follows: $27.3 \pm 17.2\%$, $37.1 \pm 17.6\%$, and 39.6 ± 15.6 for TAPoly; $57.8 \pm 3.7\%$, $63.4 \pm 5.2\%$, and $63.2 \pm 4.6\%$ for NRMa; and $59.4 \pm 18.4\%$, $75.0 \pm 14.9\%$, and $83.8 \pm 14.7\%$ for PPN (**Figure 6-9C**). The average maximum torques as a percentage of baseline measured through nerve cuff stimulation at Week 12 for the TAPoly and PPN groups were $46.9 \pm 12.3\%$ and $81.0 \pm 12.5\%$ (**Figure 6-9C**).

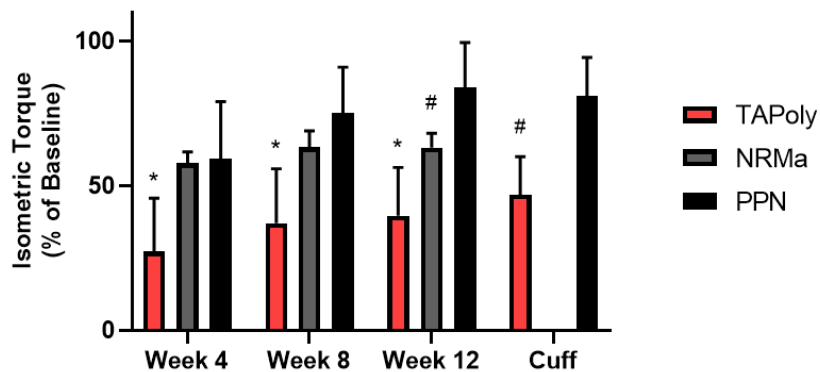
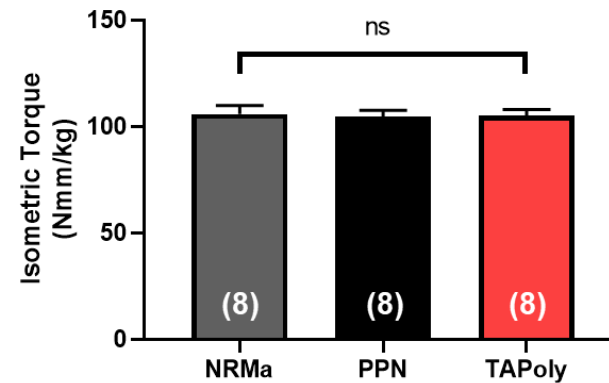
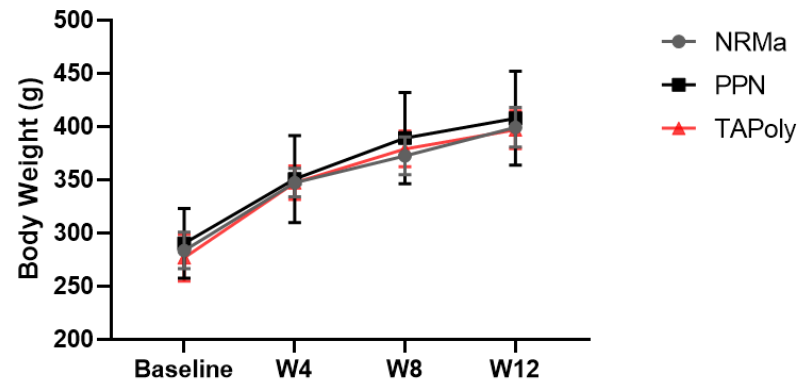


Figure 6-9: Study 2 comparison of body weight, functional baseline parameters, and functional recovery observed among different treatment groups. (A) Body weights of study animals reveal normal healthy weight gain in all treatment groups over the course of 12 weeks. (B) Graphical comparison illustrating the equivalence of the mean baseline contraction force resulting from peroneal nerve stimulation and measured with footplate force transducer in all treatment groups. (C) Peak isometric torque measured at 4, 8 and 12 weeks, showing improved muscle recovery after TEMR application as early as 8 weeks post implantation. Individual responses are presented as a percentage of the respective individual mean of the initial maximum pre-injury isometric torque response. * significantly different from PPN and NRMa, # significantly different from PPN at $p < 0.05$ level using t-tests (B) or Sidak post-hoc after performing Two-Way ANOVA in (C).

Spatiotemporal Parameters

For the second study, a minimum of 3 steps per animal per timepoint were analyzed for all groups (NRMa, PPN, TAPoly). Measurements of stride length (mm), velocity (cm/s), and stance percentage at all timepoints within each group were compared to the baseline measurements for that group (**Table 6-2**). There were no significant differences between the baseline measurements for any of the groups. For the NRMa animals, stride length significantly increased compared to baseline at 8 weeks and 12 weeks. For the TAPoly animals, stance percentage significantly decreased at 8 weeks compared to baseline. There were no significant differences detected in the data for the PPN animals.

Table 6-2: Compiled spatiotemporal results for the NRMa, PPN, and TAPoly animals at all timepoints. Significant differences between each group compared to its own Baseline are indicated with a star (*) (p<0.05, t-tests).

Rat Group	Timepoint	Stance Percentage	Stride Length (mm)	Velocity (cm/s)
NRMa	Baseline	67.3±5.0%	136.2±24.4	29.9±7.4
	Week 4	64.6±8.2%	150.5±15.1	35.2±7.5
	Week 8	63.0±4.0%	160.5±11.5*	35.7±6.8
	Week 12	64.2±3.8%	160.4±12.5*	35.0±6.4
PPN	Baseline	68.5±3.6%	128.5±11.2	26.6±2.3
	Week 4	69.5±3.5%	135.8±18.7	27.4±6.0
	Week 8	66.7±5.7%	141.8±13.9	30.0±8.1
	Week 12	66.8±4.3%	143.7±19.1	31.2±7.0
TAPoly	Baseline	70.2±4.2%	131.0±11.8	27.1±5.8
	Week 4	68.3±5.3%	127.9±18.4	27.0±8.2
	Week 8	65.1±5.6%*	143.2±17.7	32.4±8.7
	Week 12	67.1±5.5%	141.3±17.5	28.4±8.4

Joint Kinematics

For the second study, average ranges of motion for the kinematic parameters of the hip, knee, and ankle joints in the baseline measurements for each group can be seen in **Table 6-3**. The shapes and ranges of motion of these parameters compared favorably to literature values (see **Chapter 5**).

When compared to their baseline measurements, the NRMa animals showed clear differences ($p < 0.05$) at all three timepoints (**Figure 6-10**, blue). Hip flexion showed significant increases during swing at Week 4 and Week 8. Hip adduction increased during swing at Week 4. Hip internal rotation showed significant differences during swing at Week 8 and showed a trend towards increasing at toe-off at all three timepoints. Knee flexion showed decreased in early stance, late stance, and late swing at Week 4 and Week 8. Knee flexion also decreased near toe-off at Week 12. Ankle dorsiflexion decreased during late swing/toe-off at all timepoints and decreased in late swing at Week 4.

The PPN animals also showed significant differences ($p < 0.05$) at all three timepoints as compared to their baseline measurements (**Figure 6-11**, green). Hip flexion increased in mid-stance at Week 4 and Week 8, increased in late swing at Week 8, and decreased in late swing at Week 12. Hip adduction increased during mid-swing at all timepoints and decreased in early stance and near heel-strike at Week 12. Hip internal rotation increased during late stance and early swing at Week 4 and Week 8, and also decreased in early stance at Week 8 and Week 12. Knee flexion increased during the majority of stance at all timepoints and increased during mid-swing at all timepoints. There were no significant differences in ankle dorsiflexion, but there was a trend towards increased dorsiflexion during stance at Week 4.

Last, the TAPoly animals were demonstrating significantly different ($p < 0.05$) movement patterns at all timepoints as compared to their baseline measurements (**Figure 6-12**, red). Hip flexion increased from mid-stance to mid-swing at Week 4, and from toe-off through mid-swing at Week 8 and Week 12. Hip adduction decreased in early stance at Week 4 and Week 12, increased in mid-stance at Week 4 and Week 8, and decreased at heel-strike in Week 12. Hip internal rotation increased in early swing at Week 4 and showed decreases in early stance and late swing/heel-strike at Week 8. Knee flexion increased in late stance/toe-off at all timepoints. Ankle dorsiflexion increased during mid-swing at all timepoints and decreased in late stance at Week 12.

Table 6-3: Ranges of motion for Study 2 kinematic parameters (in degrees)

Group		NRMa	PPN	TAPoly	Normative Database
Hip	Flexion	44.9±6.5	42.3±2.6	44.9±6.4	46.4±6.7
	Adduction	12.0±4.3	8.3±1.2	11.0±3.1	8.4±2.5
	Rotation	39.0±10.6	36.2±4.4	36.9±3.9	32.7±4.6
Knee	Flexion	37.2±7.0	37.1±5.1	35.9±2.5	45.9±8.3
Ankle	Flexion	38.8±9.1	38.5±7.3	38.9±8.6	32.3±9.6

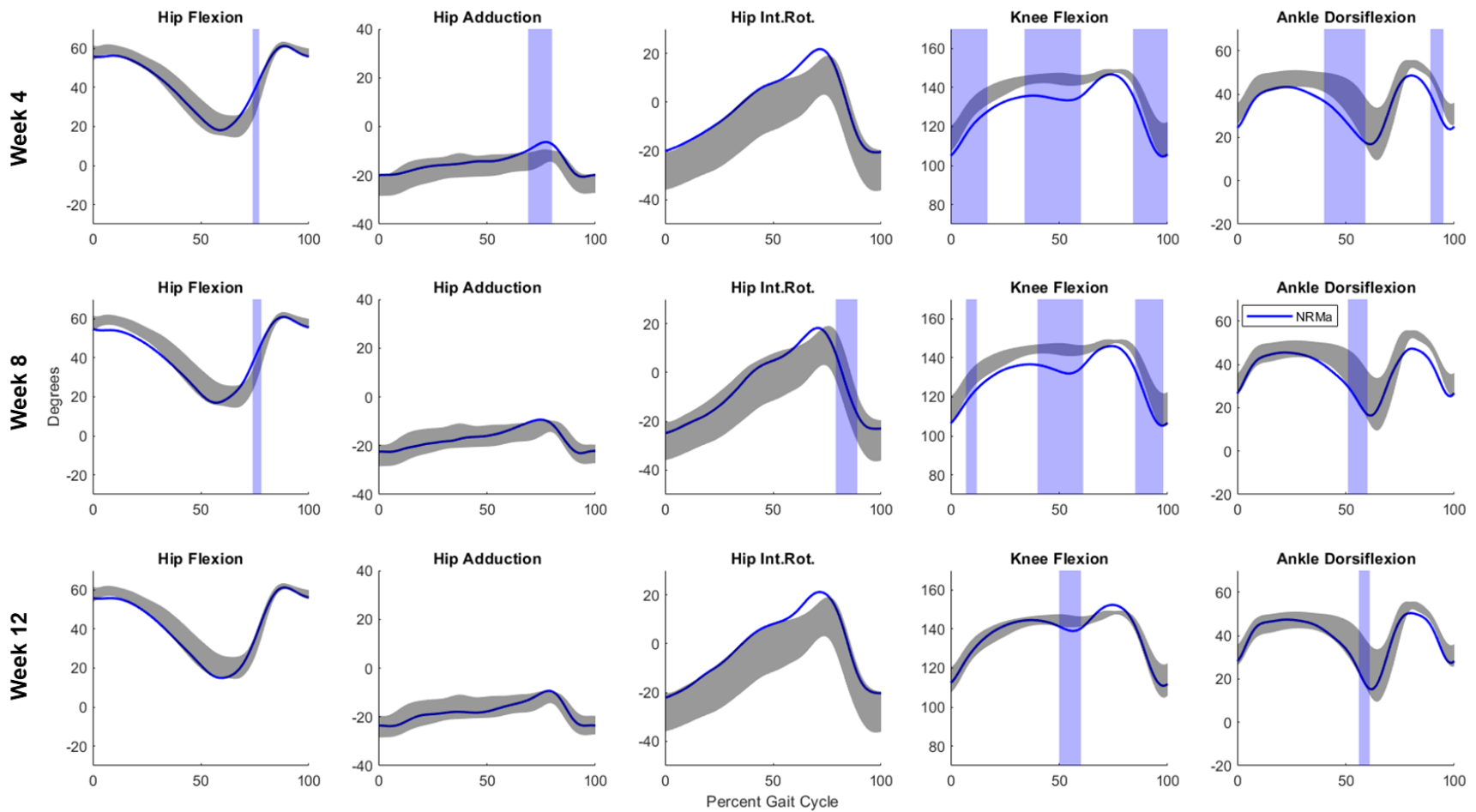


Figure 6-10: Kinematic comparisons between NRMa and baseline at all timepoints. The NRMa baseline kinematic curves are shown as black clouds and the NRMa post-surgical curves are shown in blue. Week 4 kinematics are in the top row, Week 8 in the middle, and Week 12 at the bottom. Areas of significant difference between the post-surgical and baseline curves are shown as blue shaded regions (GraphPad Prism, 2-way ANOVA w/ multiple comparisons and Fisher's least significant difference (LSD) test, $p < 0.05$).

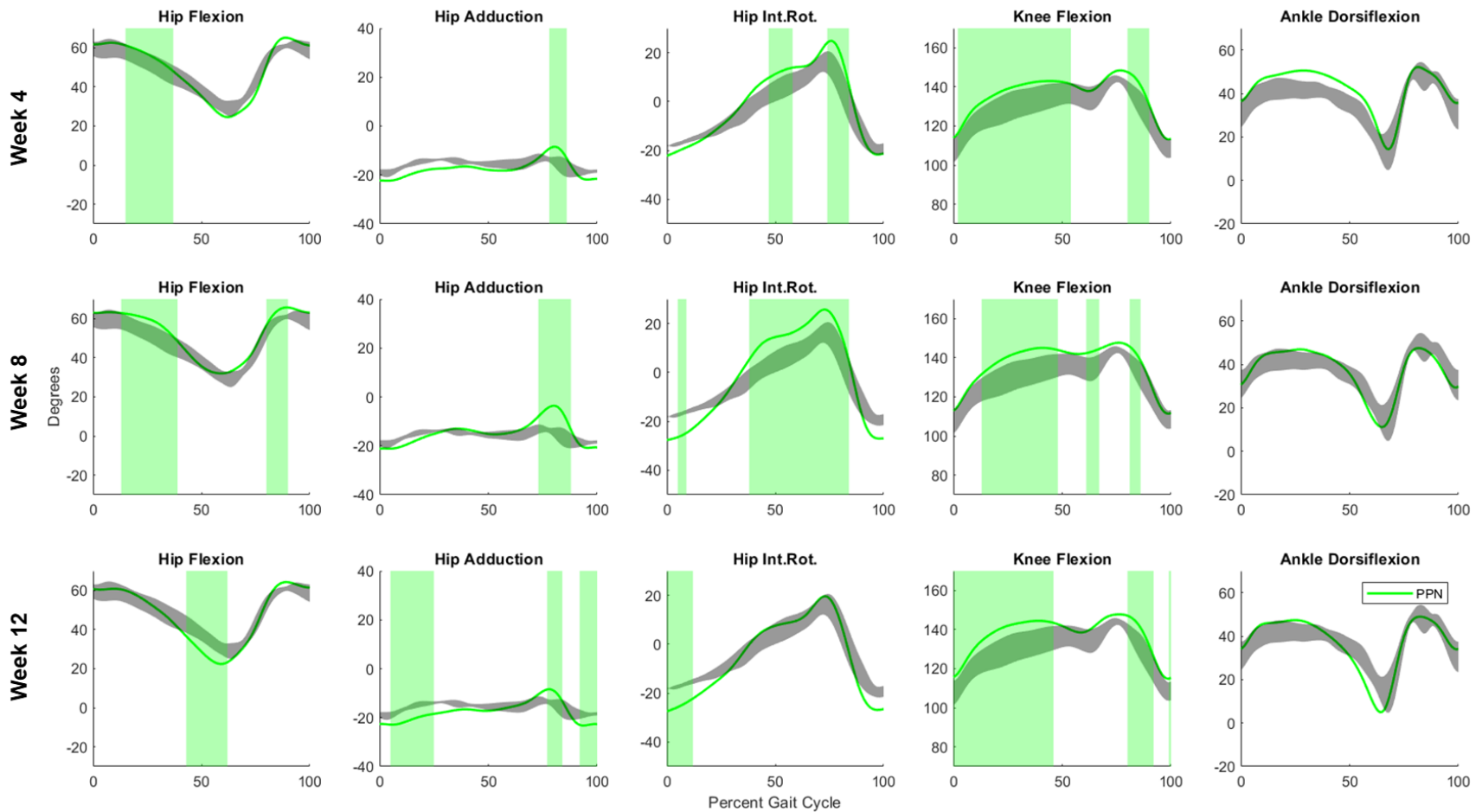


Figure 6-11: Kinematic comparisons between PPN and baseline at all timepoints. The PPN baseline kinematic curves are shown as black clouds and the PPN post-surgical curves are shown in green. Week 4 kinematics are in the top row, Week 8 in the middle, and Week 12 at the bottom. Areas of significant difference between the post-surgical and baseline curves are shown as green shaded regions (GraphPad Prism, 2-way ANOVA w/ multiple comparisons and Fisher’s least significant difference (LSD) test, $p < 0.05$).

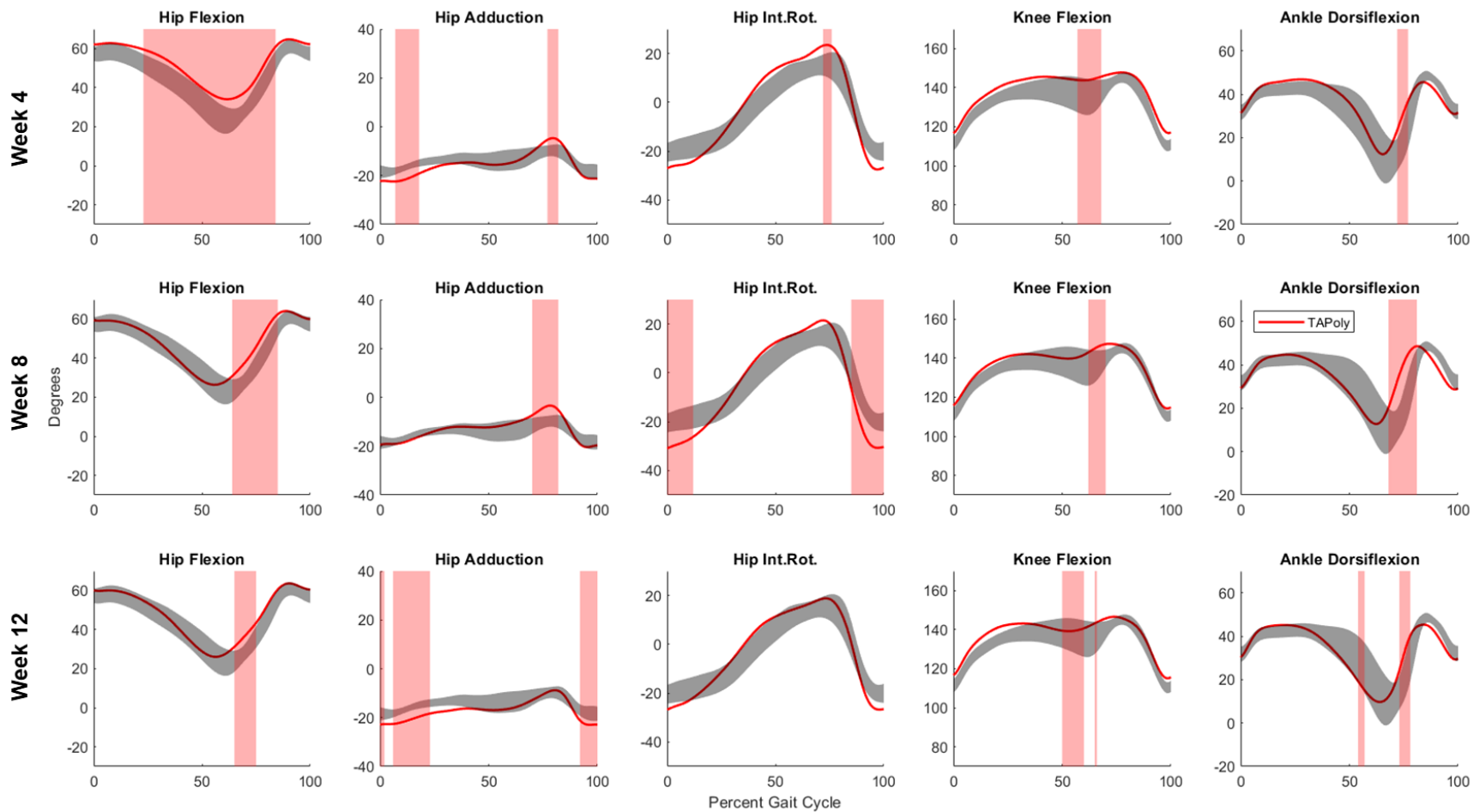


Figure 6-12: Kinematic comparisons between TAPoly and baseline at all timepoints. The TAPoly baseline kinematic curves are shown as black clouds and the TAPoly post-surgical curves are shown in red. Week 4 kinematics are in the top row, Week 8 in the middle, and Week 12 at the bottom. Areas of significant difference between the post-surgical and baseline curves are shown as red shaded regions (GraphPad Prism, 2-way ANOVA w/ multiple comparisons and Fisher's least significant difference (LSD) test, $p < 0.05$).

Joint Kinetics

For the second study, average peak moments for the kinetic parameters of the hip, knee, and ankle joints in the baseline measurements for each group can be seen in **Table 6-4**. These peak moments compared favorably to literature values (see **Chapter 5**).

When compared to their baseline measurements, the NRMa animals showed significant differences ($p < 0.05$) in their kinetic parameters at all timepoints (**Figure 6-13**, blue). Hip flexion torque increased in early stance and mid-to-late stance at all timepoints. Hip adduction torque increased from early to late stance at Week 8. Hip internal rotation torque decreased in early stance at Week 4 and Week 8 and decreased in mid-stance at Week 12. Knee extension torque increased from early to late stance at Week 8 and Week 12. Ankle dorsiflexion torque decreased in early stance at Week 8 and Week 12 and increased in late stance at Week 8.

The PPN animals also showed significant differences ($p < 0.05$) at all three timepoints as compared to their baseline kinetic parameters (**Figure 6-14**, green). Hip flexion torque decreased in early stance at all timepoints. Hip adduction torque increased in early stance at Week 8 and Week 12. Hip internal rotation torque increased in early stance at all timepoints. Knee extension torque decreased in early stance and late stance/toe-off at all timepoints and increased during mid-stance at Week 12. Ankle dorsiflexion torque increased during mid-stance at Week 4 but showed no significant differences at the other timepoints.

Finally, the TAPoly animals were demonstrating significantly different ($p < 0.05$) joint moments at all timepoints as compared to their baseline kinetic values (**Figure 6-15**, red). Hip flexion torque decreased in early stance at Week 8 and Week 12, decreased from early stance through mid-stance at Week 4, and increased in mid-to-late stance at Week 12. Hip adduction torque increased in early stance and mid-to-late stance at Week 8 and Week 12. Hip internal

rotation torque increased in early stance at Week 4 and Week 12 and decreased during mid-to-late stance at Week 8 and Week 12. Knee extension torque increased from early to mid-stance at Week 8 and Week 12 and decreased in late stance at Week 8. Ankle dorsiflexion torque increased in late stance at Week 8 and decreased in early stance at Week 12.

Table 6-4: Peak moments for Study 2 kinetic parameters in N*m/kg

Group		NRMa	PPN	TAPoly	Normative Database
Hip	Flexion Moment	0.033±0.012	0.040±0.013	0.023±0.010	0.043±0.016
	Extension Moment	-0.183±0.037	-0.122±0.036	-0.131±0.032	-0.133±0.028
	Adduction Moment	0.019±0.021	0.017±0.009	0.020±0.011	0.006±0.006
	Int. Rotation Moment	0.151±0.029	0.086±0.020	0.088±0.020	0.095±0.017
Knee	Extension Moment	-0.109±0.015	-0.102±0.015	-0.095±0.010	-0.078±0.013
Ankle	Flexion Moment	0.004±0.002	0.008±0.004	0.003±0.002	0.008±0.005
	Extension Moment	-0.099±0.018	-0.102±0.020	-0.102±0.027	-0.099±0.026

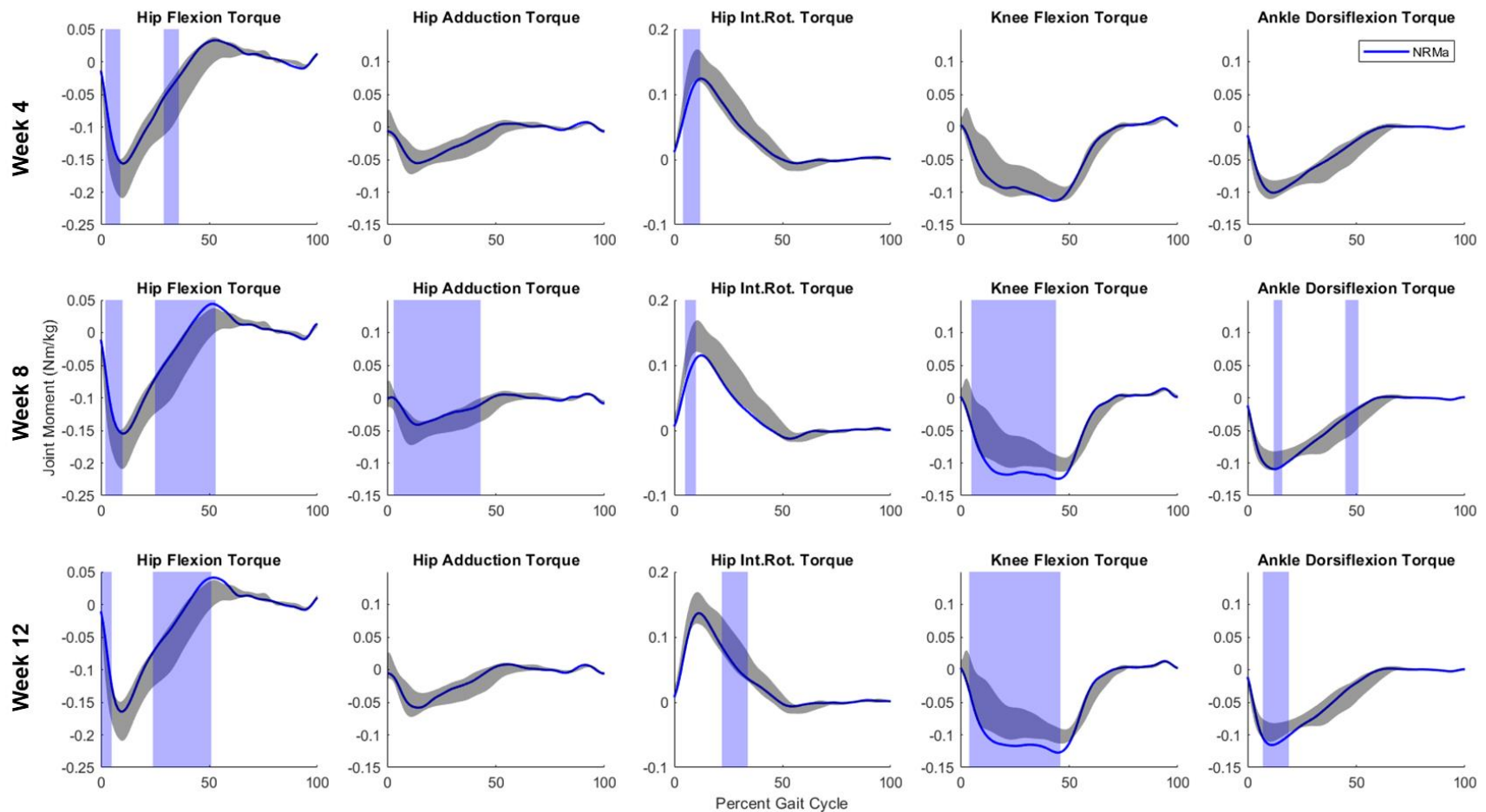


Figure 6-13: Kinetic comparisons between NRMa and baseline at all timepoints. The NRMa baseline kinetic curves are shown as black clouds and the NRMa post-surgical curves are shown in blue. Week 4 kinetics are in the top row, Week 8 in the middle, and Week 12 at the bottom. Areas of significant difference between the post-surgical and baseline curves are shown as blue shaded regions (GraphPad Prism, 2-way ANOVA w/ multiple comparisons and Fisher's least significant difference (LSD) test, $p < 0.05$).

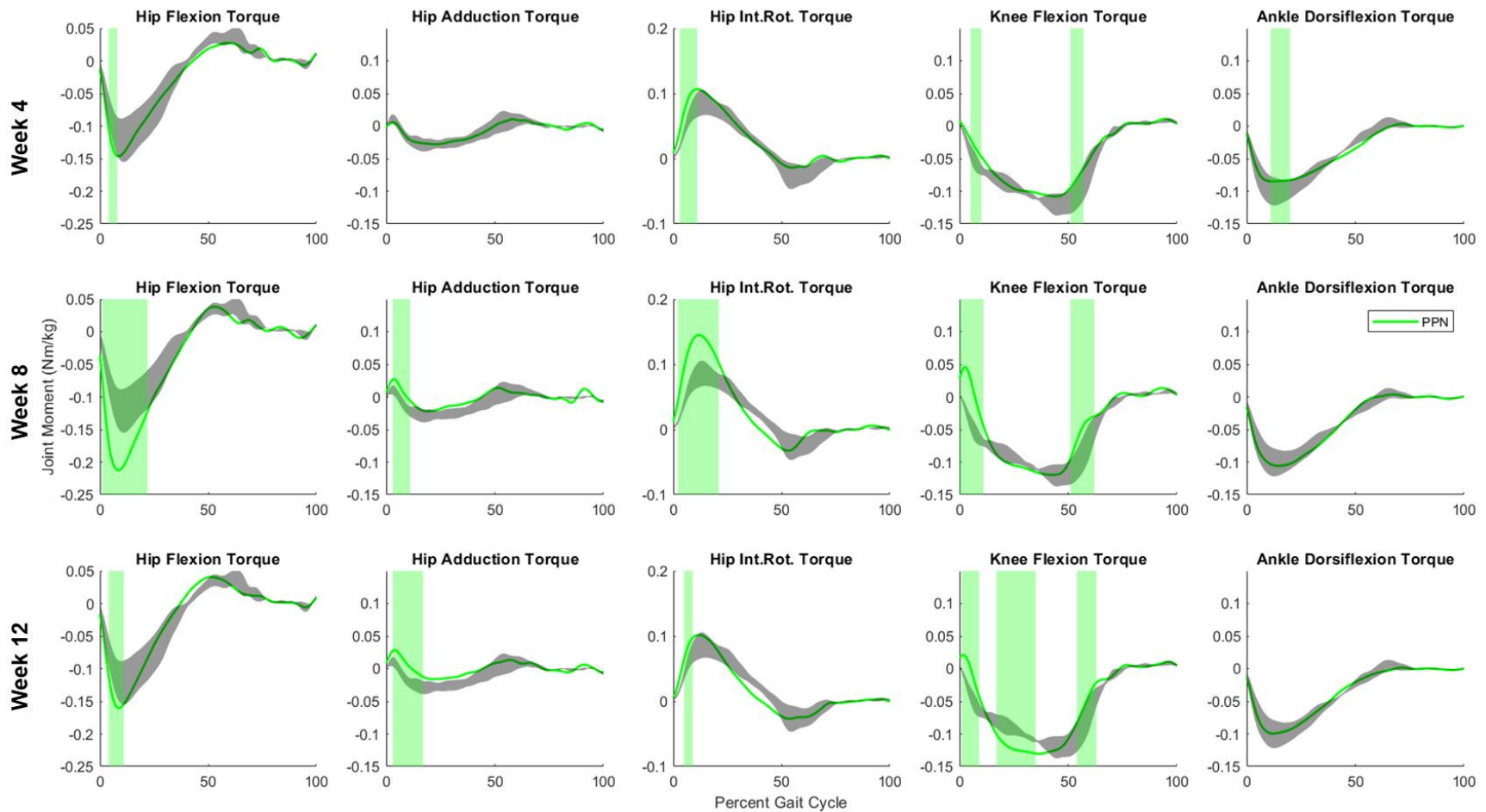


Figure 6-14: Kinetic comparisons between PPN and baseline at all timepoints. The PPN baseline kinetic curves are shown as black clouds and the PPN post-surgical curves are shown in green. Week 4 kinetics are in the top row, Week 8 in the middle, and Week 12 at the bottom. Areas of significant difference between the post-surgical and baseline curves are shown as green shaded regions (GraphPad Prism, 2-way ANOVA w/ multiple comparisons and Fisher's least significant difference (LSD) test, $p < 0.05$).

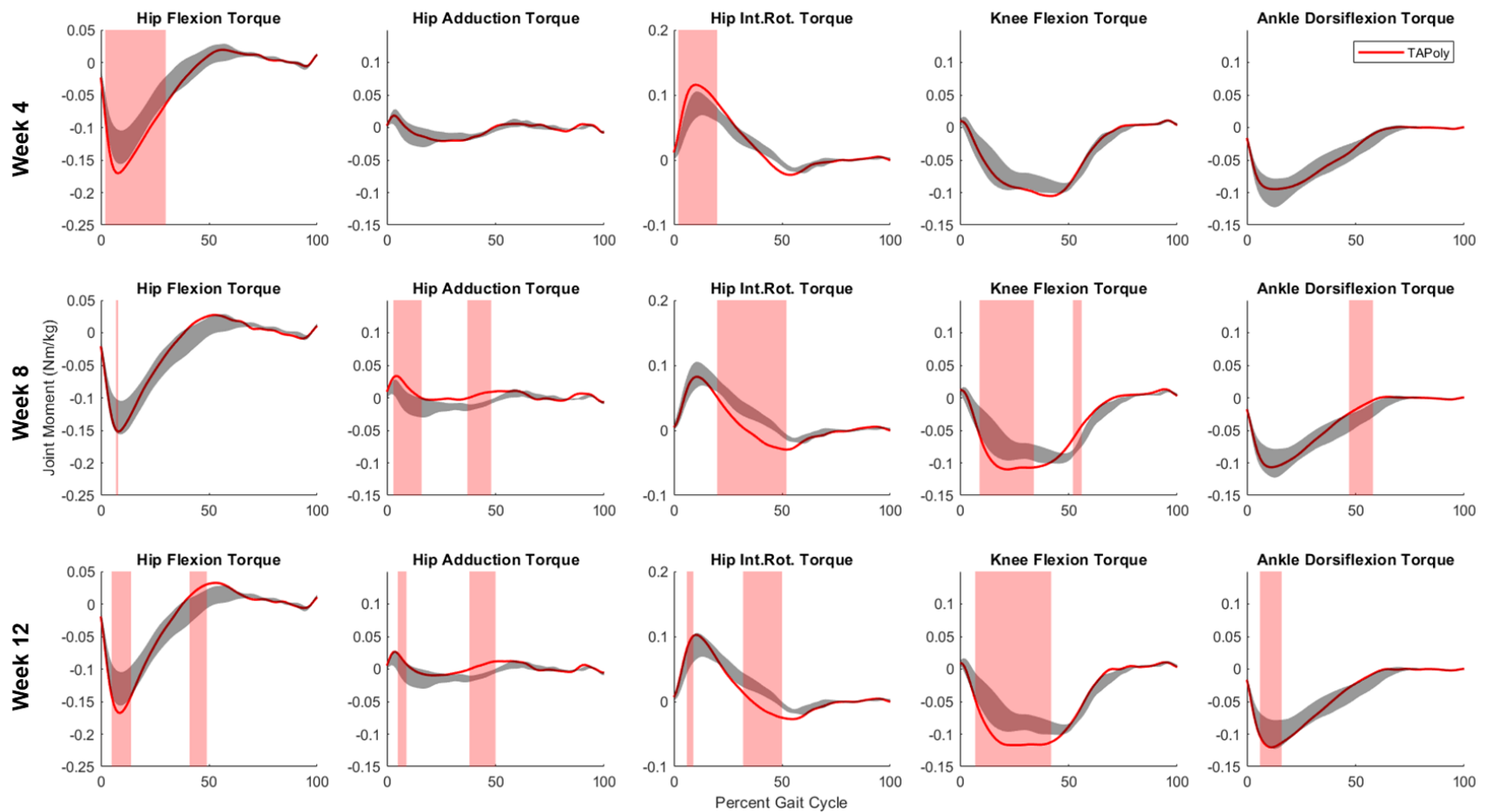


Figure 6-15: Kinetic comparisons between TAPoly and baseline at all timepoints. The TAPoly baseline kinetic curves are shown as black clouds and the TAPoly post-surgical curves are shown in red. Week 4 kinetics are in the top row, Week 8 in the middle, and Week 12 at the bottom. Areas of significant difference between the post-surgical and baseline curves are shown as red shaded regions (GraphPad Prism, 2-way ANOVA w/ multiple comparisons and Fisher's least significant difference (LSD) test, $p < 0.05$).

Discussion

Study 1

While the substantial inherent capacity for regeneration of skeletal muscle has been well documented, there remain no effective commercially available tissue engineered options to leverage regenerative ability into treatments for VML injuries. Despite encouraging results from recent preclinical studies into treatment of VML injury with ECM scaffold implantation^{22,65-68}, there remains vast room for improvement in regenerative therapeutics. This fact has directly resulted in a rapidly increasing clinical effort into the development of tissue engineered and regenerative medicine-based technologies with greater efficacy and a broader range of applications for VML injuries.

In pursuit of additional approaches for the treatment of VML injuries, the first study evaluated the efficacy and utility of the Tissue Engineered Muscle Repair (TEMR) construct. This construct represents the state of the art technology for cell-seeded ECM scaffolds, and has already been shown to result in increased force generation ability when applied to VML injuries in previous studies^{12,15,23}. As shown in **Figure 6-5C**, these previous force generation results were confirmed in this study. The no-repair (NRFe) group exhibited a mean maximal torque response of 64.8% as compared to baseline, whereas the TEMR group exhibited maximal values of 75.5% and 77.8% and Week 8 and Week 12, respectively. Because the EDL and EHL synergist muscles are ablated during surgery, it is only expected that the animals have the potential to recover 80% of their baseline force production. Therefore, the Week 8 and Week 12 values for the TEMR group represent 94.4% and 97.2% of the maximum expected recovery. However, because of the numerous published studies on the disconnect between force generation and true functional recovery in human patients, the primary objective of this initial study was to utilize motion capture

and advanced musculoskeletal modeling techniques to assess the effect of the TEMR construct on quality of movement and recovery of motion control by analyzing joint kinematics and joint moments.

Kinematics

The motion capture method utilized in this study proved sensitive enough to reveal significant differences in the gait parameters of the NRFe and TEMR groups in all three planes and at all three post-surgical timepoints when compared to Baseline. Most notably, despite the many significant differences between NRFe/Baseline kinematics at Week 12, the only differences observed between the TEMR group and baseline measurements at Week 12 were at the ankle and in hip adduction at toe-off. However, the ankle was an expected difference based on the surgical procedure used to create the VML injury. Because the tibialis anterior primarily acts as an ankle dorsiflexor and the EDL and EHL synergist muscles were ablated during surgery, the ability to ambulate the ankle in a normal way was expected to take the longest to return.

To validate the calculated values for joint kinematics, the baseline data collected on the rats prior to VML injury creation was referenced. The range of motion values reported here for flexion of the hip, knee, and ankle were similar to previously reported sagittal plane kinematics in healthy rats^{43,57,58,69-71}. Literature values for average ranges of motion for flexion of the hip (30-55 degrees^{43,57,58,69,70}), knee (35-60 degrees^{43,57,58,69-71}), and ankle (30-60 degrees^{43,57,58,69-71}) compare favorably to the values observed in this study of 48.1 ± 8.0 degrees, 48.6 ± 7.9 degrees, and 42.6 ± 9.6 degrees.

Looking at the NRFe kinematics on their own, a compensation pattern resembling vaulting gait in humans can be observed at Week 4. This is indicated by increased knee flexion during the

swing phase of the gait cycle. Week 8 represents a transitional period, but as the animals moved into the 12-week time point there was a compensatory switch towards circumduction. This was revealed through increased hip extension, increased hip external rotation, increased knee extension, and excessive ankle plantarflexion during toe-off and swing. These observations are significant because vaulting and circumduction are two of the compensation patterns utilized by humans when dealing with drop foot, a pathology caused by weakness in the ankle dorsiflexors such as the TA, our target muscle for VML injury in this study.

The TEMR animals demonstrated significantly reduced kinematic compensation due to the VML injury as compared to the NRFe group. By Week 12, the differences were limited to a single small region at the ankle. The lack of significant differences between TEMR/Baseline at Week 12 indicates that the TEMR group had made strides in recovery towards healthy kinematics while the NRFe group showed no such progress. It is important to recognize that the TEMR animals are still not walking in a way that precisely mirrors healthy animals at Week 12, but their gait patterns are coming very close to falling within the confidence bands for normal movement.

Kinetics

The healthy baseline calculations for joint kinetics of the animals in this initial study were utilized as part of the creation of the normative curves discussed in **Chapter 5**, and information can be found in that chapter for how that data was validated.

Contrary to expectations, the joint moments of the NRFe group did not show serious differences at the ankle. Due to the nature of the VML injury, it was theorized that the most significant deviations from normal movement patterns would be seen in ankle dorsiflexion torque. But instead, differences were primarily seen at the hip/knee, and the observed differences were not

particularly large. This shows adaptation to their chosen compensation pattern, which makes them more efficient at their motion and leads to the absence of excessive joint moments as compared to baseline. However, efficiency utilizing a compensatory gait pattern is not the same as healthy movement, and the vast deviations from baseline seen in the NRFe kinematics illustrate that these animals would be vulnerable to secondary joint and muscle pathologies down the line.

The TEMR kinetics show more of the expected differences at the ankle at the later time points, plus two additional differences at Week 12 in the form of increased hip adduction torque and decrease hip flexion torque at initial heel strike. Again, these kinetic results do not mirror what we see in healthy animals, but they show that the TEMR animals are getting closer to utilizing healthy neuromuscular motor control mechanisms because they are not large-scale deviations from the normal range.

Study 2

In recognition that severe VML injuries do not occur in the absence of peripheral nerve injury, the second study presented in this chapter expanded this work into male Lewis rats and to re-evaluated unrepaired VML injuries, repaired partial peroneal nerve lacerations, and polytraumas consisting of both the muscle and nerve injury in the same animals. Peripheral nerve injuries are notoriously difficult to heal^{9,10,43-47}, and inducing them in combination with TA VML injuries was the most severe trauma investigated to date utilizing either traditional force measurements or comprehensive gait analysis. With this in mind, the primary goal of this second study was to develop an understanding of the effects of peripheral nerve injuries individually and in polytrauma scenarios on recovery timeframes and movement function.

Force Testing

Compared to previous studies completed by our group, the NRMa animals fell within the expected range for maximum isometric torque for TA VML injuries without repair. This study showed a maximum recovery of ~63% of the force produced relative to baseline for the NRMa animals, compared to 53% (**Chapter 3**), 65% (Study 1 in this chapter), 70%²³, and 72%³³.

For the PPN animals, the work proposed in the grant for this study defined that one of our objectives was to create a recoverable nerve injury. A full laceration with immediate repair was the first injury investigated, but this proved to result in very little recovery of muscle force production ability. When the model was adjusted to a 50% laceration with immediate repair, the improvement in functional strength was massive (**Figure 6-9C**). By Week 8 and Week 12, the PPN animals were producing 75% and 84% of the bodyweight normalized force that they were producing at baseline. As previously mentioned, because the EDL and EHL synergist muscles are ablated during surgery it is only expected that the animals have the potential to recover 80% of their baseline force production. Therefore, the Week 8 and Week 12 values for the PPN group represent 93.8% and 104.8% of the maximum expected recovery. Based on those results, it was determined that the partial peroneal nerve laceration was indeed a fully recoverable nerve injury and the surplus in force was due to hypertrophy and strengthening of the TA after recovery from the nerve injury. Further, the PPN animals generated significantly more force than the NRMa animals at Week 12, and significantly outperformed the TAPoly animals at all timepoints.

The TAPoly animals incurred an injury that was a combination of TA VML and a partial laceration of the peroneal nerve. Because of this, it was expected that the force testing results would show a massive deficit when compared to baseline and when compared to the other animals. When the force testing data was analyzed, the deficits were as severe as expected. The TAPoly animals showed a maximum recovery of 40% (46% when stimulated with the nerve cuff) of the

bodyweight normalized force they produced at baseline. This was truly a catastrophic injury, there was very little muscle remaining at the injury site by Week 8 due to the combination of muscle loss via VML injury and the associated atrophy from the peroneal nerve injury. Even with four more weeks of recovery and a very slight increase in force production, there was little to no volume reconstitution between Week 8 and Week 12 for the TAPoly animals.

Kinematics

While significant effort was spent identifying the specific compensation patterns being utilized by the study groups in Study 1, that was not the explicit purpose of Study 2. The second goal of this study was to simply identify how drastic the gait differences are that result from these injuries in order to inform a third, future study into regenerative therapeutics for muscle-nerve polytrauma. With that in mind, this discussion will focus on trends and differences between the injuries and the groups rather than attempting to diagnose specific pathological compensation patterns in the NRMa, PPN, and TAPoly animals.

As discussed earlier, the average literature ranges of motion for the hip (30-55 degrees^{43,57,58,69,70}), knee (35-60 degrees^{43,57,58,69-71}), and ankle (30-60 degrees^{43,57,58,69-71}) compare well to the ranges of motion calculated for healthy animals in **Chapter 4** (~48, 48, 43 degrees). In this second study, the calculated ranges of motion for the hip, knee, and ankle for the each of the three groups were roughly: 45, 37, and 39 degrees for NRMa; 42, 37, and 39 degrees for PPN; and 45, 36, and 39 degrees for TAPoly. Compared to the literature and the data calculated in **Chapter 4**, these values fall reasonably within the range that would be expected for healthy animals.

Just as in Study 1, the motion capture approach utilized here was sensitive enough to detect differences in all groups at all timepoints as compared to the group's own baseline data. Looking

at the NRMa kinematics (**Figure 6-10**), there are significant increases in knee extension and ankle plantarflexion at Week 4, indicating some level of circumduction at compensation for the TA VML injury. These results sustain through Week 8 but mostly alleviate by Week 12. There are trends towards increased hip extension and increased hip internal rotation at Week 12, but very few areas of statistically significant differences. This was the first study completed using this motion capture methodology on male Lewis rats, as only females had been previously evaluated. In the study of those female rats, there were substantially more differences in movement patterns at Week 12 in the unrepaired TA VML animals. Historically, have been some studies on humans and mice indicating that testosterone can have a regenerative effect on skeletal muscle⁷²⁻⁷⁴. Based on this, there is the potential that other muscles in the hindlimb experienced hypertrophy in the absence of the TA contribution after injury and that increased strength facilitated a return to more normal movement patterns. This theory is investigated further in the discussion of the kinetic results.

The PPN group showed many more differences in their gait kinematics (**Figure 6-11**) as compared to NRMa. This was especially apparent at Week 12, which was surprising considering the force recovery that was shown by the PPN animals. Beginning at Week 4, the PPN animals exhibited increased hip flexion, hip internal rotation, increased knee flexion, and increased ankle dorsiflexion. Most of these differences occurred during stance, which indicates that the animals were crouched down on the injured limb and the limb was folding under the load. These results sustained through Week 8, then there was a bit of a compensatory switch in Week 12. The animals demonstrated increased hip extension, hip abduction, hip external rotation, and knee flexion during stance. This indicates the while the knee was flexed, the leg itself was being set outside the normal location under the body. The PPN animals clearly had the force production ability necessary to move in a normal way, but since they gained roughly 10% in force production between Week 8

and Week 12 it is reasonable to assume that the functional motion is lagging behind the functional ability. Though this is not a particularly satisfying conclusion, it is logical when you consider the months of physical rehabilitation that humans have to undergo after injury even while their strength steadily increases back to pre-injury levels.

The TAPoly kinematics (**Figure 6-12**) do not show the extreme number of significant differences that would be expected considering their massive force production deficits, but they do show more differences than the NRMa animals and many trends towards pathological movement patterns. At Week 4 there was a general increase in hip flexion across the gait cycle, as well as increases in hip adduction, hip internal rotation, knee flexion, and ankle dorsiflexion in early swing. However, these kinematic results do not tell the whole story. At this timepoint, the animals were very hesitant to put weight on the injured leg and were instead keeping their foot almost “holstered” and tucked up high into the body, likely due to the extreme effects of the polytrauma injury. At Week 8 the majority of the differences were in swing, as the animals presented with increased hip flexion, hip adduction, hip external rotation, knee flexion, and ankle dorsiflexion. This again illustrates that the animals were holstering the foot during the swing phase of the gait cycle. By Week 12, the differences seen at Week 8 had reduced in severity but were still generally present. On the whole, this demonstrates that while 12 weeks is sufficient time for the evaluation of recovery from unrepaired TA VML injuries and repaired partial peroneal nerve lacerations, it does not appear to be a long enough timeframe for evaluating injuries as severe as these polytraumas.

Kinetics

The kinetic values calculated at baseline for each of the three groups compared well to the peak moments calculated for healthy animals in **Chapter 5** (see **Table 6-4**). In this study, the average peak hip flexion, hip extension, hip adduction, hip internal rotation, knee flexion, ankle flexion, and ankle extension moments were all reasonably within the normal range.

Looking at NRMa kinetics (**Figure 6-13**), Week 4 showed very few significant differences compared to baseline. However, Week 8 showed increases over large percentages of stance in hip flexion torque, hip adduction torque, and knee flexion torque. There were also small increases in hip external rotation torque and ankle extension torque. With the exception of the increase to hip adduction torque, these significant differences sustained through Week 12. When considered in combination with the relatively few kinematic differences observed in the NRMa animals at Week 12, these kinetic results lend support to the idea that there is increased strengthening in other muscles in the hindlimb to shift the body and drive the motion through the stance phase of the gait cycle. The reduction in ankle dorsiflexion torque speaks to the fact that the TA is weakened as a result of the surgery. Because of this, the kinetic results demonstrate that the animals relying heavier on the hip and knee to drive their motion through stance.

The PPN group showed a reduced area of significant kinetic differences versus baseline (**Figure 6-14**) as compared to the NRMa animals, but similarly drove their motion more through the hip and knee at Week 12. Interestingly though, there were no significant differences (or even trends towards differences) in the moment about the ankle at Week 8 or Week 12. This would indicate that the ankle was operating normally, which is supported by the recovery of dorsiflexion strength that was measured through the force testing. The residual differences seen in the moments about the hip and knee at Week 12 are largely reduced compared to the differences at the same points at Week 8. As previously discussed, there is a lag between developing functional strength

and reincorporating that strength into normal movement patterns, so based on the trends in the measured parameters for the PPN animals it is reasonable to expect that they would return to normal gait pattern ranges if the experimental timepoints were slightly extended.

The TAPoly kinetics (**Figure 6-15**) exhibited many of the same significant differences as what were observed with the NRMa group, but at a higher severity at the Week 12 timepoint. The TAPoly animals also do not appear to show any improvement in their kinetics between the Week 8 and Week 12 timepoint, and both timepoints show an increased degree of differences as compared to Week 4. Similar to the NRMa animals, Week 12 for TAPoly shows increases in both hip flexion torque and hip extension torque, increases in hip adduction torque, increases in both hip internal rotation torque and external rotation torque, an increase in knee extension torque, and an increase in ankle extension torque. As stated in the analysis of the NRMa animals, the ankle difference is expected due to the nature of the injury. However, compared to the differences seen in the Week 12 data for NRMa, many of the gaps between the kinetic curves for TAPoly and the baseline measurements are much larger. Due to the severity of the polytrauma injury it is difficult to attribute the observed differences to any one thing, but it is clear that the polytrauma impacts far more than just the TA and ankle dorsiflexion. With such a high degree of strength and muscle volume loss, this injury had widespread effects that were led to systematic changes in movement function and activation patterns.

In both of these studies, it is important to reinforce the point that we were able to identify differences throughout all phases of the gait cycle. This is significant because the TA muscle is primarily active during the early swing phase to dorsiflex the ankle and provide ground clearance for the toe. This contrasts with the stance phase, where the TA is only minorly activated to control foot position. Despite this, we saw substantial differences in both gait kinematics and kinetics

during all phases of the gait cycle from heel strike and stance through toe-off and swing. The presence of stance phase gait alteration indicates that the animals were loading differently during stance in order to compensate for the lack of TA contribution during swing. This needed to occur for the animals to execute a successful swing phase, though successful in this case is defined as the completion of a step and does not refer to step quality. Overall, the fact that we were able to detect these differences and infer these conclusions speaks to the sensitivity of 3-D motion capture gait analysis. This analytical method offers broad utility for evaluating the nuanced gait changes and compounding compensatory effects that occur throughout the gait cycle in response to an injury to a muscle that is a relatively minor gait contributor.

Future Work and Conclusions

While an absolute restoration of functional movement was not fully achieved in Study 1, the results still represent an important step forward due to the increased ability to evaluate the efficacy of regenerative therapeutics. Additionally, in future studies it is expected that timepoints will be extended to determine if these trends of recovery, or lack thereof, are durable. In Study 2, important strides were made towards understanding the effects of nerve injuries and muscle-nerve polytraumas on movement function. As mentioned, this sets the stage for a future third study into the development and evaluation of regenerative therapeutics to treat these complex and highly clinically relevant injuries. Last, combining all of our motion capture and reconstruction strategies to acquire bilateral kinematics and kinetics would allow for assessment of the effect of injuries and treatments on the contralateral limb in the hopes of revealing any other compensatory mechanisms.

In summary, Study 1 demonstrated for the first time that cell-seeded ECM scaffolds can successfully promote a significant recovery of functional ability in instances of severe skeletal muscle damage in an established and biologically relevant rodent model of VML injury. The TEMR construct resulted in both recovery of force generation ability and functional movement, such that there were no significant differences between the joint kinematics of the TEMR group and their baseline at a 12-week post-surgical timepoint other than at the directly impacted joint. Although further studies are clearly warranted to more fully understand the mechanisms responsible for recovery and compensatory shifts, these observations have important implications for the future of regenerative therapeutics for VML injury. High-accuracy motion capture provides an additional set of metrics for testing the efficacy of regenerative therapeutics, and by these metrics the TEMR construct has demonstrated its capability and utility as a treatment for VML injury that could vastly extend the range of current clinical applications.

Study 2 demonstrated that it is possible to create a fully recoverable peroneal nerve injury from a 50% laceration, and the animals are clearly trending towards recovery even though there is a lag in the physiological application of the recovered muscle force production ability. Further, Study 2 illustrated the incredible systemic impact of muscle-nerve polytrauma injuries. Despite combining a fully recoverable nerve injury with a TA VML injury that has a known and measurable impact, the result of both injuries in tandem was an additional ~20% force deficit and nearly complete loss of muscle volume. While undoubtedly important information, this study has demonstrated the difficulties ahead in trying to treat more complex injuries with regenerative therapeutics.

Lastly, it is important to note the possibility of differences that arise due to the gender of the rats evaluated in these two studies. Due to inherent geometric differences, it would not be surprising to discover inertial differences between the female Lewis rats evaluated in the **Chapter 5** normative database and Study 1 and the male Lewis rats evaluated in Study 2. Further, in terms of recovery from the muscular injuries with the help of the TEMR construct, the impact of testosterone or menstrual cycles on regeneration cannot be discounted. Both these factors warrant further investigation in future studies.

References

1. Carlson, B. M. & Faulkner, J. A. The regeneration of skeletal muscle fibers following injury: a review. *Med. Sci. Sports Exerc.* **15**, 187–98 (1983).
2. Carlson, B. M. Regeneration of the completely excised gastrocnemius muscle in the frog and rat from minced muscle fragments. *J. Morphol.* **125**, 447–471 (1968).
3. Ciciliot, S. & Schiaffino, S. Regeneration of mammalian skeletal muscle. Basic mechanisms and clinical implications. *Curr. Pharm. Des.* **16**, 906–14 (2010).
4. Warren, G. L. *et al.* Mechanisms of skeletal muscle injury and repair revealed by gene expression studies in mouse models. *J. Physiol.* **582**, 825–41 (2007).
5. White, T. P. & Devor, S. T. Skeletal muscle regeneration and plasticity of grafts. *Exerc. Sport Sci. Rev.* **21**, 263–95 (1993).
6. Grogan, B. F. & Hsu, J. R. Volumetric muscle loss. *J. Am. Acad. Orthop. Surg.* **19 Suppl 1**, S35-7 (2011).
7. Holcomb, J. B., Stansbury, L. G., Champion, H. R., Wade, C. & Bellamy, R. F. Understanding Combat Casualty Care Statistics. *J. Trauma Inj. Infect. Crit. Care* **60**, 397–401 (2006).
8. Menorca, R. M. G., Fussell, T. S. & Elfar, J. C. Nerve physiology: mechanisms of injury and recovery. *Hand Clin.* **29**, 317–30 (2013).
9. Höke, A. A (heat) shock to the system promotes peripheral nerve regeneration. *J. Clin. Invest.* **121**, 4231–4 (2011).
10. Grinsell, D. & Keating, C. P. Peripheral nerve reconstruction after injury: a review of clinical and experimental therapies. *Biomed Res. Int.* **2014**, 698256 (2014).
11. Lin, C.-H., Lin, Y.-T., Yeh, J.-T. & Chen, C.-T. Free Functioning Muscle Transfer for Lower Extremity Posttraumatic Composite Structure and Functional Defect. *Plast. Reconstr. Surg.* **119**, 2118–2126 (2007).
12. Corona, B. T. *et al.* Further development of a tissue engineered muscle repair construct in vitro for enhanced functional recovery following implantation in vivo in a murine model of volumetric muscle loss injury. *Tissue Eng. Part A* **18**, 1213–28 (2012).
13. Corona, B. T. *et al.* The promotion of a functional fibrosis in skeletal muscle with volumetric muscle loss injury following the transplantation of muscle-ECM. *Biomaterials* **34**, 3324–3335 (2013).
14. Criswell, T. L. *et al.* The role of endothelial cells in myofiber differentiation and the vascularization and innervation of bioengineered muscle tissue in vivo. *Biomaterials* **34**, 140–149 (2013).
15. Machingal, M. A. *et al.* A Tissue-Engineered Muscle Repair Construct for Functional Restoration of an Irrecoverable Muscle Injury in a Murine Model. *Tissue Eng. Part A* **17**, 2291–2303 (2011).

16. Merritt, E. K. *et al.* Repair of traumatic skeletal muscle injury with bone-marrow-derived mesenchymal stem cells seeded on extracellular matrix. *Tissue Eng. Part A* **16**, 2871–81 (2010).
17. VanDusen, K. W., Syverud, B. C., Williams, M. L., Lee, J. D. & Larkin, L. M. Engineered skeletal muscle units for repair of volumetric muscle loss in the tibialis anterior muscle of a rat. *Tissue Eng. Part A* **20**, 2920–30 (2014).
18. Williams, M. L., Kostrominova, T. Y., Arruda, E. M. & Larkin, L. M. Effect of implantation on engineered skeletal muscle constructs. *J. Tissue Eng. Regen. Med.* **7**, 434–442 (2013).
19. Merritt, E. K. *et al.* Functional assessment of skeletal muscle regeneration utilizing homologous extracellular matrix as scaffolding. *Tissue Eng. Part A* **16**, 1395–405 (2010).
20. Perniconi, B. *et al.* The pro-myogenic environment provided by whole organ scale acellular scaffolds from skeletal muscle. *Biomaterials* **32**, 7870–7882 (2011).
21. Sicari, B. M. *et al.* A murine model of volumetric muscle loss and a regenerative medicine approach for tissue replacement. *Tissue Eng. Part A* **18**, 1941–8 (2012).
22. Turner, N. J., Badylak, J. S., Weber, D. J. & Badylak, S. F. Biologic Scaffold Remodeling in a Dog Model of Complex Musculoskeletal Injury. *J. Surg. Res.* **176**, 490–502 (2012).
23. Corona, B. T., Ward, C. L., Baker, H. B., Walters, T. J. & Christ, G. J. Implantation of In Vitro Tissue Engineered Muscle Repair Constructs and Bladder Acellular Matrices Partially Restore In Vivo Skeletal Muscle Function in a Rat Model of Volumetric Muscle Loss Injury. *Tissue engineering. Part A* **20**, 705–15 (2014).
24. Passipieri, J. A. *et al.* In Silico and In Vivo Studies Detect Functional Repair Mechanisms in a Volumetric Muscle Loss Injury. *Tissue Eng. Part A* ten.tea.2018.0280 (2019). doi:10.1089/ten.tea.2018.0280
25. Mintz, E. L. *et al.* Long-Term Evaluation of Functional Outcomes Following Rat Volumetric Muscle Loss Injury and Repair. *Tissue Eng. Part A* **26**, 140–156 (2020).
26. Langer, H. T. *et al.* Muscle Atrophy Due to Nerve Damage Is Accompanied by Elevated Myofibrillar Protein Synthesis Rates. *Front. Physiol.* **9**, (2018).
27. Aguilar, C. A. *et al.* Multiscale analysis of a regenerative therapy for treatment of volumetric muscle loss injury. *Cell Death Discov.* **4**, 1–11 (2018).
28. Greising, S. M. *et al.* Unwavering Pathobiology of Volumetric Muscle Loss Injury. *Sci. Rep.* **7**, 1–14 (2017).
29. Aurora, A., Roe, J. L., Corona, B. T. & Walters, T. J. An acellular biologic scaffold does not regenerate appreciable de novo muscle tissue in rat models of volumetric muscle loss injury. *Biomaterials* **67**, 393–407 (2015).
30. Corona, B. T. *et al.* Autologous minced muscle grafts: a tissue engineering therapy for the volumetric loss of skeletal muscle. *Am. J. Physiol. Physiol.* **305**, C761–C775 (2013).
31. Pollot, B. E., Goldman, S. M., Wenke, J. C. & Corona, B. T. Decellularized extracellular

- matrix repair of volumetric muscle loss injury impairs adjacent bone healing in a rat model of complex musculoskeletal trauma. *J. Trauma Acute Care Surg.* **81**, S184–S190 (2016).
32. Goldman, S. M., Henderson, B. E. P., Walters, T. J. & Corona, B. T. Co-delivery of a laminin-111 supplemented hyaluronic acid based hydrogel with minced muscle graft in the treatment of volumetric muscle loss injury. *PLoS One* **13**, e0191245 (2018).
 33. Passipieri, J. A. *et al.* Keratin Hydrogel Enhances In Vivo Skeletal Muscle Function in a Rat Model of Volumetric Muscle Loss. *Tissue Eng. Part A* **23**, 556–571 (2017).
 34. Pilia, M. *et al.* Transplantation and perfusion of microvascular fragments in a rodent model of volumetric muscle loss injury. *Eur. Cells Mater.* **28**, 11–24 (2014).
 35. Kim, J. *et al.* Graft alignment impacts the regenerative response of skeletal muscle after volumetric muscle loss in a rat model. *Acta Biomater.* **105**, 191–202 (2020).
 36. Vega-Soto, E. E., Rodriguez, B. L., Armstrong, R. E. & Larkin, L. M. A 30% Volumetric Muscle Loss Does Not Result in Sustained Functional Deficits After a 90-Day Recovery in Rats. *Regen. Eng. Transl. Med.* **6**, 62–68 (2020).
 37. Huang, H. *et al.* Preferred M2 Polarization by ASC-Based Hydrogel Accelerated Angiogenesis and Myogenesis in Volumetric Muscle Loss Rats. *Stem Cells Int* **2017**, 2896874 (2017).
 38. Hagiwara, K., Chen, G., Kawazoe, N., Tabata, Y. & Komuro, H. Promotion of muscle regeneration by myoblast transplantation combined with the controlled and sustained release of bFGFcp. *J. Tissue Eng. Regen. Med.* **10**, 325–333 (2016).
 39. Qiu, X. *et al.* Mesenchymal stem cells and extracellular matrix scaffold promote muscle regeneration by synergistically regulating macrophage polarization toward the M2 phenotype. *Stem Cell Res. Ther.* **9**, 88 (2018).
 40. Ju, Y. M., Atala, A., Yoo, J. J. & Lee, S. J. In situ regeneration of skeletal muscle tissue through host cell recruitment. *Acta Biomater.* **10**, 4332–4339 (2014).
 41. Natsu, K. *et al.* Allogeneic bone marrow-derived mesenchymal stromal cells promote the regeneration of injured skeletal muscle without differentiation into myofibers. *Tissue Eng.* **10**, 1093–1112 (2004).
 42. Dienes, J. A. *et al.* Analysis and Modeling of Rat Gait Biomechanical Deficits in Response to Volumetric Muscle Loss Injury. *Front. Bioeng. Biotechnol.* **7**, 146 (2019).
 43. Bennett, S. W., Lanovaz, J. L. & Muir, G. D. The biomechanics of locomotor compensation after peripheral nerve lesion in the rat. *Behav. Brain Res.* **229**, 391–400 (2012).
 44. Jacobs, B. Y. *et al.* The Open Source GAITOR Suite for Rodent Gait Analysis. *Sci. Rep.* **8**, 1–14 (2018).
 45. Howard, C. S., Blakeney, D. C., Medige, J., Moy, O. J. & Peimer, C. A. Functional assessment in the rat by ground reaction forces. *J. Biomech.* **33**, 751–7 (2000).

46. Schilling, B. K. *et al.* Adipose-derived stem cells delay muscle atrophy after peripheral nerve injury in the rodent model. *Muscle and Nerve* **59**, 603–610 (2019).
47. Passipieri, J. A. *et al.* Adipose Stem Cells Enhance Nerve Regeneration and Muscle Function in a Peroneal Nerve Ablation Model. *Tissue Eng. Part A* (2019). doi:10.1089/ten.TEA.2018.0244
48. Slater, L. V., Hart, J. M., Kelly, A. R. & Kuenze, C. M. Progressive Changes in Walking Kinematics and Kinetics After Anterior Cruciate Ligament Injury and Reconstruction: A Review and Meta-Analysis. *J. Athl. Train.* 1062-6050.52.6.06 (2017). doi:10.4085/1062-6050.52.6.06
49. Robbins, S. M. *et al.* Comparison of Gait Characteristics Between Patients With Nontraumatic and Posttraumatic Medial Knee Osteoarthritis. *Arthritis Care Res. (Hoboken)*. **68**, 1215–1223 (2016).
50. Ferrarin, M. *et al.* Gait pattern classification in children with Charcot-Marie-Tooth disease type 1A. *Gait Posture* **35**, 131–7 (2012).
51. Ijaz, A. *et al.* Analysis of knee joint kinematics during walking in patients with cerebral palsy through human motion capture and gait model-based measurement. in *2012 IEEE International Conference on Virtual Environments Human-Computer Interfaces and Measurement Systems (VECIMS) Proceedings* 196–199 (IEEE, 2012). doi:10.1109/VECIMS.2012.6273181
52. Topp, R., Mikesky, A., Wigglesworth, J., Holt, W. & Edwards, J. E. The effect of a 12-week dynamic resistance strength training program on gait velocity and balance of older adults. *Gerontologist* **33**, 501–6 (1993).
53. Damiano, D. L., Arnold, A. S., Steele, K. M. & Delp, S. L. Can strength training predictably improve gait kinematics? A pilot study on the effects of hip and knee extensor strengthening on lower-extremity alignment in cerebral palsy. *Phys. Ther.* **90**, 269–79 (2010).
54. Damiano, D. L. & Abel, M. F. Functional outcomes of strength training in spastic cerebral palsy. *Arch. Phys. Med. Rehabil.* **79**, 119–25 (1998).
55. Damiano, D. L., Prosser, L. A., Curatalo, L. A. & Alter, K. E. Muscle Plasticity and Ankle Control After Repetitive Use of a Functional Electrical Stimulation Device for Foot Drop in Cerebral Palsy. *Neurorehabil. Neural Repair* **27**, 200–207 (2013).
56. Buchner, D. M. *et al.* The effect of strength and endurance training on gait, balance, fall risk, and health services use in community-living older adults. *J. Gerontol. A. Biol. Sci. Med. Sci.* **52**, M218-24 (1997).
57. Bauman, J. M. & Chang, Y.-H. High-speed x-ray video demonstrates significant skin movement errors with standard optical kinematics during rat locomotion. doi:10.1016/j.jneumeth.2009.10.017
58. Garnier, C., Falempin, M. & Ene Canu, M.-H. A 3D analysis of fore-and hindlimb motion during locomotion: Comparison of overground and ladder walking in rats. *Behav. Brain Res.* **186**, 57–65 (2008).

59. Canu, M.-H. & Garnier, C. A 3D analysis of fore- and hindlimb motion during overground and ladder walking: Comparison of control and unloaded rats. *Exp. Neurol.* **218**, 98–108 (2009).
60. Roemhildt, M. L., Gardner-Morse, M., Rowell, C., Beynon, B. D. & Badger, G. J. Gait alterations in rats following attachment of a device and application of altered knee loading. *J. Biomech.* **43**, 3227–31 (2010).
61. Allen, K. D. *et al.* Kinematic and dynamic gait compensations resulting from knee instability in a rat model of osteoarthritis. *Arthritis Res. Ther.* **14**, R78 (2012).
62. McClure, M. J. *et al.* Decellularized Muscle Supports New Muscle Fibers and Improves Function Following Volumetric Injury. *Tissue Eng. Part A* (2018). doi:10.1089/ten.TEA.2017.0386
63. Wu, X., Corona, B. T., Chen, X. & Walters, T. J. A standardized rat model of volumetric muscle loss injury for the development of tissue engineering therapies. *Biores. Open Access* **1**, 280–90 (2012).
64. Mintz, E. L., Passipieri, J. A., Lovell, D. Y. & Christ, G. J. Applications of In Vivo Functional Testing of the Rat Tibialis Anterior for Evaluating Tissue Engineered Skeletal Muscle Repair. *J Vis Exp* (2016).
65. Sicari, B. M. *et al.* An Acellular Biologic Scaffold Promotes Skeletal Muscle Formation in Mice and Humans with Volumetric Muscle Loss. *Sci. Transl. Med.* **6**, 234ra58-234ra58 (2014).
66. Turner, N. J. *et al.* Xenogeneic extracellular matrix as an inductive scaffold for regeneration of a functioning musculotendinous junction. *Tissue Eng. Part A* **16**, 3309–17 (2010).
67. Valentin, J. E., Turner, N. J., Gilbert, T. W. & Badylak, S. F. Functional skeletal muscle formation with a biologic scaffold. *Biomaterials* **31**, 7475–7484 (2010).
68. Wolf, M. T., Daly, K. A., Reing, J. E. & Badylak, S. F. Biologic scaffold composed of skeletal muscle extracellular matrix. *Biomaterials* **33**, 2916–2925 (2012).
69. Alluin, O. *et al.* Kinematic study of locomotor recovery after spinal cord clip compression injury in rats. *J. Neurotrauma* **28**, 1963–1981 (2011).
70. Pereira, J. E. *et al.* A comparison analysis of hindlimb kinematics during overground and treadmill locomotion in rats. *Behav. Brain Res.* **172**, 212–218 (2006).
71. Canu, M. H. & Garnier, C. A 3D analysis of fore- and hindlimb motion during overground and ladder walking: Comparison of control and unloaded rats. *Exp. Neurol.* **218**, 98–108 (2009).
72. Serra, C. *et al.* Testosterone Improves the Regeneration of Old and Young Mouse Skeletal Muscle. *J Gerontol A Biol Sci Med Sci* **68**, 17–26 (2013).
73. Sinha-Hikim, I., Cornford, M., Gaytan, H., Lee, M. L. & Bhasin, S. Effects of Testosterone Supplementation on Skeletal Muscle Fiber Hypertrophy and Satellite Cells in

- Community-Dwelling Older Men. *J. Clin. Endocrinol. Metab.* **91**, 3024–3033 (2006).
74. Herbst, K. L. & Bhasin, S. Testosterone action on skeletal muscle. *Current Opinion in Clinical Nutrition and Metabolic Care* **7**, 271–277 (2004).

Chapter 7 – Evaluation of Gait Biomechanics in Response to Complex Traumas – Lateral Gastrocnemius

Disclaimer: Due to ongoing refinement of data analysis, some figures and numerical values may change slightly in final publication but the overall conclusions are expected to remain consistent.

Introduction

As extensively covered in previous chapters of this dissertation, despite the well-documented ability of skeletal muscle to repair, regenerate, and remodel after injury¹⁻⁵, a vast number of diseases, disorders, and traumas that result in an irrecoverable loss of muscle function remain. Included among these traumatic injuries is volumetric muscle loss (VML)⁶. VML injuries are characterized by such a significant degree of muscle tissue loss that they exceed the inherent ability of the muscle to recover, resulting in permanent cosmetic and functional deficits⁷ to the limbs, neck, or face. These injuries impact both the civilian and military populations, affecting thousands of individuals each year.

Historically, preclinical rat hindlimb models of VML injury have focused on the tibialis anterior (TA), a small muscle in the anterior compartment of the lower hindlimb that is solely responsible for ankle dorsiflexion. The effects of VML injury to the TA have been well characterized in terms of both force production⁸⁻¹⁴ and biomechanical deficits¹⁵, making it a perfect target for proof of concept and basic treatment studies. However, in terms of clinical relevance for the severe and high impact traumas that are typically associated with VML injury, the TA is limited because of its relative lack of physiological responsibility. As demonstrated in the previous chapters, we have extensively characterized the effects of VML injury to the TA, and in this chapter we leveraged that work to investigate VML injuries to a significantly more complex muscle and system by injuring the lateral gastrocnemius (LG).

The LG is a two-joint muscle, acting on the knee and ankle. It connects to the foot through the Achilles tendon and is the primary muscle for energy transfer during movement in the lower hindlimb. Additionally, because rats ambulate using a crouch gait pattern (see **Chapter 5**) the LG is under a higher constant tension during the gait cycle as compared to bipedal walking. One group has previously investigated VML injuries to the LG^{16,17}, and their injury creation and evaluation methodologies provided the framework for the procedures performed in this study. The effects of incurring a 20% VML injury to the LG are easy to identify, as multiple joints would feel the impact and that impact would be spread throughout the gait cycle. This is in contrast to the TA, which is primarily active during the swing phase of gait. Further, the posterior compartment containing the LG is far more complex than the anterior compartment of the TA. The TA synergist muscles can be ablated at the time of VML injury creation, focusing all recovery on the TA. In the posterior compartment there are significantly more muscles than cannot be removed, which complicates the isolation of the LG for identifying the true effect of injury and could potentially limit the extent of recovery.

Additionally, it should be noted that significant VML injuries do not occur without the coincidence of peripheral nerve damage. With that in mind, the study presented in this chapter evaluated peripheral nerve trauma and muscle-nerve polytrauma in addition to traditional isolated VML injuries. These injuries align with what would most commonly be seen in injuries incurred by armed services personnel in the line of duty and civilians who experience a high-impact trauma. Peripheral nerve injuries result in the partial or total loss of motor, sensory, and autonomic signals conveyed by the lacerated nerves to the denervated segments of the body¹⁸. The potential for regeneration of injured nerve is largely dependent on the severity of the damage, but recovery is extremely poor if large segments of nerve trunks are lost. Even when there is no disruption of the

connective tissue macrostructure, this trend of poor recovery sustains. Further, peripheral nerves only grow at a rate of 1-3mm/day^{19,20} in the best case scenarios and the downstream muscles are subject to increasingly extreme atrophy as time passes before a signal is restored.

Historically, results of the extensive VML^{8,9,12,14,16,17,21-36} and peripheral nerve injury³⁷⁻⁴¹ studies in rats have focused on volume reconstitution and recovery of force generation. In humans, analysis of walking patterns (gait) is frequently used as a baseline functional measure of movement quality⁴²⁻⁴⁵. However, studies of human movement have shown that gains in strength do not necessarily result in improvements in movement function⁴⁶⁻⁵⁰. To address this, we have developed a method to quantify changes in gait for rats with hindlimb injuries using methods similar to human gait analysis. These techniques reveal gait changes both in response to muscle and nerve injuries and during recovery. The ability to measure changes in rat gait parameters gives information on how the animal is functionally utilizing damaged or regenerated muscle tissue, providing insight on strength, motion planning, and neuromuscular motor control strategies.

While other groups have utilized motion capture to study rat gait⁵¹⁻⁵⁵ (see **Chapter 2**), few have attempted to evaluate peripheral nerve injury, only one has attempted to acquire over ground gait information on rats with VML injuries⁵⁶, and none have investigated the LG. With regard to the current studies, we are the first to investigate polytrauma injuries to the LG and the posterior compartment, and the first to investigate the biomechanical impacts of LG injuries of any kind. Using a combination of VICON motion capture, advanced musculoskeletal modeling techniques, and concurrently captured ground reaction forces (GRFs), we were able to detect significant differences in joint angles and joint moments post-injury and track changes in movement quality over time in all groups. This enhanced understanding of rat function post-LG VML injury will help to expedite the development and refinement of regenerative therapeutics and rehabilitation

strategies these injuries to complex muscular compartments, and facilitate the ability of researchers to identify the true effects of injury to multi-joint muscles.

Methods and Materials

Experimental Outline

Twenty-four healthy 12-week old male Lewis rats were observed walking on a custom-built walkway and had their gait analyzed using the same methodology. After baseline collection on all animals, 8 were given a 20% by mass VML injury with no repair performed to the right LG (LGNR), 8 were given only a partial tibial nerve laceration with repair (no VML injury, PTN), and 8 were given the partial tibial nerve laceration in combination with the unrepaired VML injury (LGPoly).

Motion capture was repeated at 4, 8, and 12 weeks after surgery. Kinematic and GRF data was acquired from the trials through motion capture. Individual gait cycles were compiled and averaged to create kinematic and kinetic curves for each animal, which were averaged within each group and timepoint for statistical analysis. Nerve cuff force testing was also performed on the animals at 12 weeks relative to the surgery date to identify the deficit created by the injuries and any recovery of force generation ability.

Animal Care

This study was conducted in compliance with the Animal Welfare Act, the Implementing Animal Welfare Regulations, and in accordance with the principles of the Guide for the Care and Use of Laboratory Animals. The University of Virginia Animal Care and Use Committee approved all animal procedures. A total of 24 male Lewis rats (Charles River Laboratories) weighing

280.7±24.5g at 12 weeks of age were pair housed in a vivarium accredited by the American Association for the Accreditation of Laboratory Animal Care, and they were provided with food and water *ad libitum*.

Creation of VML Injury

As very few studies have been conducted on LGAS VML injuries, the methodology of Merritt et al⁵⁷ was used as a guideline for creating these injuries. A longitudinal incision was made parallel to the tibia on the outside of the lower right leg. The skin was then cleared from the underlying fascia using blunt separation. A second incision was made through the biceps femoris to expose the lateral gastrocnemius. The muscles within the posterior compartment were also separated using blunt separation. Once exposed, the midpoint of the LG between the knee and ankle was identified. Preliminary evaluation of LG weights from sacrificed animals from other studies showed that the LG muscle corresponds to roughly 0.25% of the gross body weight of Lewis rats. A rectangular chunk of muscle was excised beginning at the lateral edge, measuring

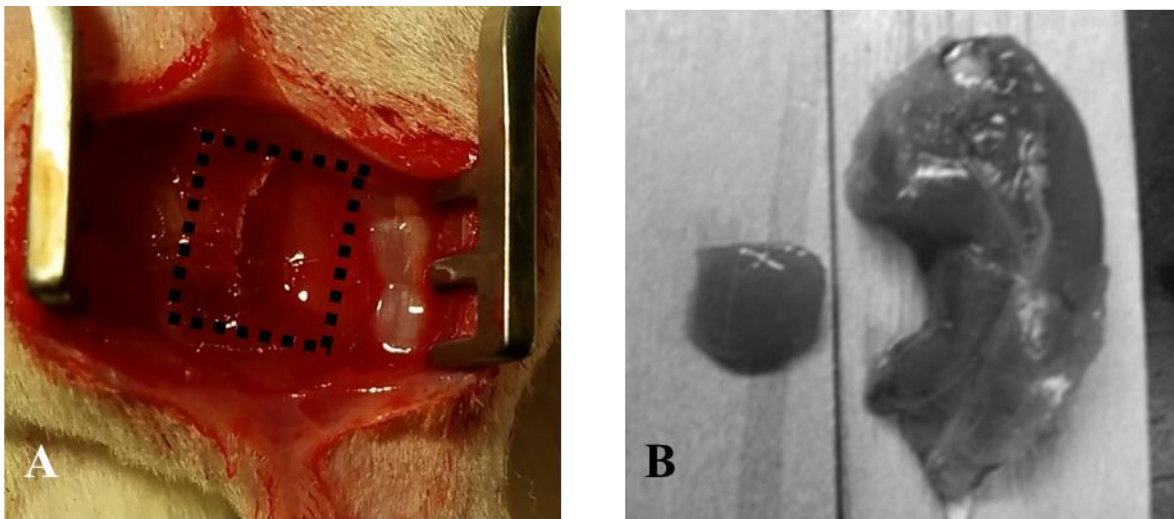


Figure 7-1: Lateral gastrocnemius volumetric muscle loss injury creation. (A) Representative surgical defect created to mimic 20% by mass volumetric muscle loss injury (1.0x0.7x0.2cm) (B) Explanted whole gastrocnemius with 20% VML injury to the lateral head (Merritt, et al [2010a]^{16,17}, figure copied with permission from Mary Ann Liebert)

roughly 1.0(L) x 0.6(W) cm and corresponding to ~20% of the total LG weight (**Figure 7-1**). The fascia was closed with 6-0 vicryl sutures and the skin was closed with 5-0 prolene using interrupted sutures. Skin glue was applied over the skin sutures to help prevent the incision from opening.

Creation of Tibial Nerve Injury and Polytrauma

The partial laceration of the tibial nerve was created by opening an incision parallel to the femur on the right leg. Through this incision, a second incision was created to cut through the biceps femoris muscle and access the branching site of the sciatic nerve. At this location, the sciatic nerve branches into three smaller nerves (**Figure 7-2A**): tibial (the largest), peroneal, and sural (the smallest). Through a surgical microscope, the tibial nerve was identified and specialized instruments were utilized to create a ~50% laceration of the nerve as distally as close to the knee as possible. The nerve ends were then sutured together using 10-0 silk microsuture (**Figure 7-2B**). The biceps femoris was then sutured closed using 6-0 vicryl, followed by the skin using 5-0 prolene. Skin glue was applied over the skin sutures to help prevent the incision from opening. To create the polytrauma injuries, the VML injury creation protocol was followed immediately after the completion of the peroneal nerve surgery.

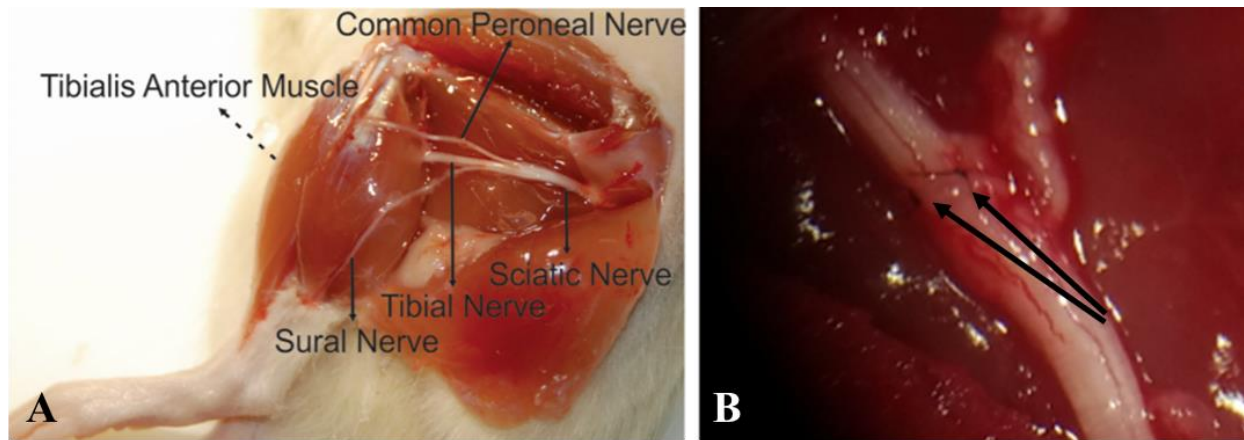


Figure 7-2: Sciatic nerve branch site and nerve laceration post-repair (A) Dissected rat limb exposing the nerves of the hindlimb and the branch point of the sciatic nerve into the tibial, peroneal, and sural nerves (B) Arrows indicating the locations of microsutures used to reattach portions of the nerve that was partially lacerated to create a recoverable nerve injury.

Force Testing

Force testing of the LG is a terminal procedure and only occurs at the 12-week post-surgical timepoint. This protocol began by making an L-shaped incision beginning at the hip, following the femur to the knee, and then following the tibia to the ankle. The skin was cleared away to reveal the entirety of the biceps femoris. The L-shaped incision was then be repeated through the biceps femoris, with care taken not to lacerate the target nerve, LG, or too many major blood vessels. Once the tibial nerve was isolated and cuffed, the peroneal and sural nerves were severed to ensure that the electrical stimulus only traveled down the tibial nerve. Next, the calcaneus bone was cut from the foot with the Achilles tendon remaining attached. Silk suture was be used to tie a small length of string from the calcaneus to attach to the force testing rig. The soleus and plantaris muscles were then cleared from the LGAS, revealing the underside of the muscle. The medial branch of the tibial nerve was severed to ensure that only our target muscle, the LG, is stimulated for contraction. The muscle was then ready for testing and was connected to the force testing rig with a chain hooked to the calcaneus/suture loop. Once attached, electrical stimulus was provided

using an Aurora Scientific stimulator with a constant current SIU (Model 701C). Muscle length was optimized with a series of 1Hz pulses resulting in twitch contraction. Contractile force of the LG was assessed through measuring the peak isometric tetanic torque determined from maximal response to a series of stimulation frequencies (10-200Hz). Torque was normalized by the body weight of each animal on the day of collection. This procedure will be performed on both legs of each animal and the maximum forces produced by the injured vs. healthy LGAS muscles were averaged and compared for analysis. Animals were euthanized via CO₂ inhalation and cervical dislocation was performed as a secondary measure upon completion of this protocol.

Motion Capture

At -1, 4, 8, and 12 weeks relative to the surgery date, rats were anesthetized and shaved to allow proper placement of the motion capture marker set illustrated in **Figure 7-3**. Reflective markers were placed on the bony landmarks of the left anterior superior iliac crest (LASI), right anterior superior iliac crest (RASIS), spine (L6 vertebra), tail (5th caudal vertebra), hip, lateral knee, ankle, and distal end of the fifth metatarsal. Kinematic data on the animals was collected using a Vicon 5-camera (Vue) setup collecting at 200Hz. The animals were placed at one end of the walkway and allowed to walk to the opposite end at a self-selected pace. This process was repeated until a minimum of five acceptable trials with clean footstrikes were obtained, with acceptable being defined as a consistent walk through the entirety of the collection volume with no abnormalities (i.e. starting/stopping, jumping, running, marker/camera dropout). After data collection the animals were returned to the vivarium.

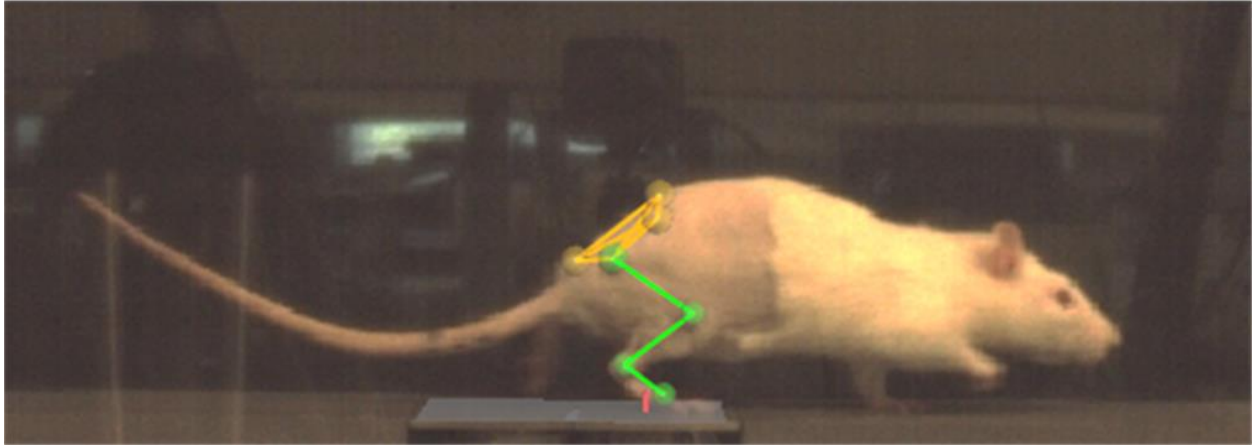


Figure 7-3. Vicon Nexus 3-D overlay of motion capture marker placements.

Inverse Kinematics

Gait event and marker identification was completed in Nexus and data were filtered at 50Hz (**Chapters 4-6**). Inverse kinematic modeling was performed in OpenSim using a rat hindlimb musculoskeletal model (**Figure 7-4**). This model consisted of four segments (hip, femur, tibia, foot) and each joint was modeled as first order. The hip and ankle were modeled as ball joints, and the knee was modeled as a hinge joint. Modifications were limited to adjusting the default location of the knee and spine markers on the model to more closely reflect the anatomical placement of markers on the Lewis rats in this study, and the knee was simplified to a zeroth order hinge joint to accommodate scaling. The model was scaled to each rat before inverse kinematics were performed. When scaling, the weight of the knee marker was set to 1/10 of the other markers to account for the movement of the skin artifact over the knee joint during the trials. Reported data corresponded to one gait cycle, heel strike to heel strike of the right leg. Steps more than three standard deviations from the mean at any point in the gait cycle were excluded from the study.

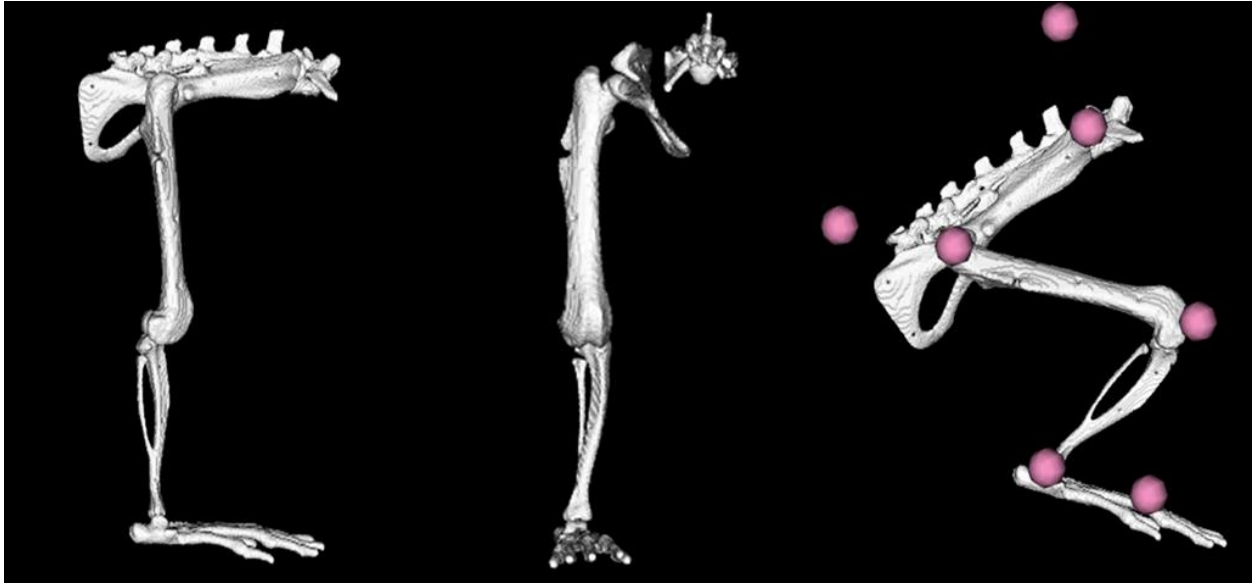


Figure 7-4. OpenSim rat hindlimb model with zeroed angles and reconstructed marker locations. (A) Zeroed angles for hip, knee, and ankle flexion. (B) Zeroed angles for hip internal rotation and adduction. (C) Reconstructed marker locations for the SPINE, TAIL, RASI, HIP, KNEE, ANKLE, and TOE. The model was scaled for each individual animal at each collection time point based on the locations of these markers.

Inverse Dynamics

Kinematics were modeled for the entire trial as described in the previous section and in **Chapters 4-6**. Ground reaction forces and moments about the load cell were extracted from Nexus allowing for calculation of pressure centers. The gait cycle of interest was isolated by zeroing the GRFs prior to heel strike and after toe-off. Limb moments of inertia (MOI) and centers of mass (COM) were determined as previously described (**Chapter 5**) and fed into the OpenSim model. The isolated GRF data then was loaded into OpenSim as a point force and applied to the foot, resulting in flexion, adduction, and internal rotation moments about the hip, a flexion moment about the knee, and a flexion moment about the ankle. Reported data corresponds to one gait cycle, heel strike to heel strike. Joint moments more than three standard deviations from the mean were excluded from the study.

Statistics

Numerical data are presented as mean \pm standard error of the mean (SEM). The statistical significance of spatiotemporal parameters and nerve cuff force data was determined in GraphPad Prism 8.0 (La Jolla, CA) using multiple t-tests, paired t-tests, and the Holm-Sidak post-hoc test. Analysis of the joint kinematic and kinetic curves GraphPad Prism (Study 2), and multiple t-tests ($\alpha=0.05$).

Results

Creation of VML injury and force testing

None of the 24 animals that received surgery died during the surgical procedure or suffered any kind of post-surgical mortality. There were no significant differences between the mean animal body weights between any of the groups over the course of the study (**Figure 7-5A**). However, because animals in all groups gained weight over the course of the study, statistical comparisons on forces measures were made on data normalized to body weight. Post-surgical isometric torque testing at 12 weeks showed a significant deficit in the torque generated by all three groups in their injured muscles as compared to their contralateral control muscles (paired t-tests, $p<0.05$). The average maximum torques of the contralateral controls and injured muscles for each group were (in N/kg): 18.5 \pm 3.6 and 12.2 \pm 3.2 for the LGNR animals (**Figure 7-5B**), 20.9 \pm 2.4 and 13.8 \pm 3.2 for the PTN animals (**Figure 7-5C**), and 21.7 \pm 2.7 and 13.2 \pm 3.0 for the LGPoly animals (**Figure 7-5D**). As percentages of the contralateral forces, the injured muscles measured as 65.3 \pm 8.9% for LGNR, 67.1 \pm 18.2% for PTN, and 60.8 \pm 12.9% for LGPoly.

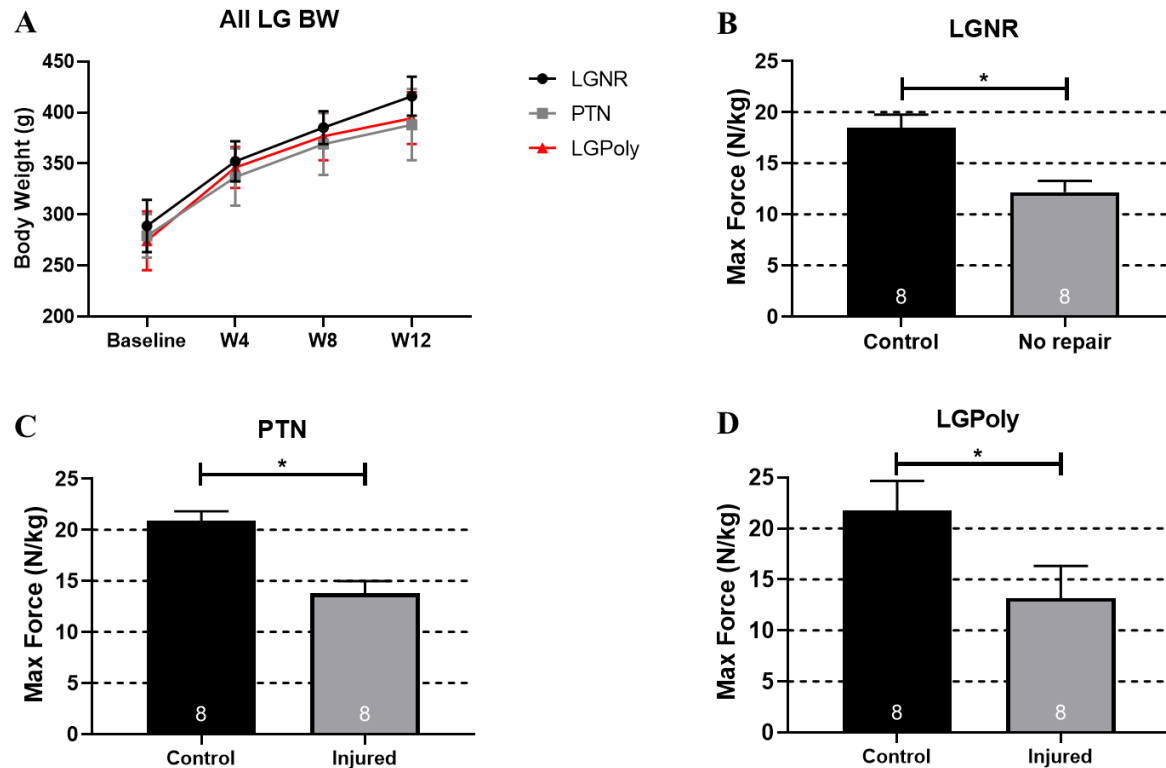


Figure 7-5: Comparison of body weights and functional recovery observed among different injury groups. (A) Comparison of animal body weights in each group at each study timepoint. (B) LGNR maximal force testing data, comparison between contralateral control muscles (left) and experimental injured muscle (right) for each animal. (C) PTN maximal force testing data, comparison between contralateral control muscles (left) and experimental injured muscle (right) for each animal. (D) LGPoly maximal force testing data, comparison between contralateral control muscles (left) and experimental injured muscle (right) for each animal. (GraphPad Prism, paired t-tests, * indicates significant difference with $p < 0.05$)

Spatiotemporal Parameters

A minimum of 3 steps per animal were averaged at the baseline, 4, 8, and 12-week timepoints for all groups (LGNR, PTN, LGPoly). All animals were randomized prior to baseline data collection and whole groups of animals were never tested on the same day. Measurements of stride length (mm), walking velocity (cm/s), and stance percentage at all timepoints within each group were compared to the group's own baseline measurements (**Table 7-1**). When comparing baseline measurements between groups, the PTN animals had a significantly higher stance percentage (vs. LGNR), shorter stride length (vs. LGNR), and slower velocity (vs. LGNR and LGPoly). The PTN animals significantly decreased their stance percentage and increased their stride length at all post-surgical timepoints. The PTN animals also significantly increased their walking velocity at 4 and 8-weeks. The LGPoly animals showed only one significant difference as compared to their baseline, an increased in stride length at Week 12.

Table 7-1: Compiled spatiotemporal results for the LGNR, PTN, and LGPoly animals at all timepoints. Significant differences between each group compared to its own Baseline are indicated with a star (*) ($p < 0.05$, t-tests).

Rat Group	Timepoint	Stance Percentage	Stride Length (mm)	Velocity (cm/s)
LGNR	Baseline	64.9±5.4%	145.5±14.0	36.9±7.1
	Week 4	67.2±5.4%	151.3±13.7	31.5±6.6
	Week 8	65.6±5.2%	160.1±13.1	33.9±7.7
	Week 12	68.0±3.9%	151.8±17.6	29.4±7.1
PTN	Baseline	71.8±4.2%	127.9±15.7	24.7±5.5
	Week 4	64.8±6.0%*	142.4±20.6*	33.9±11.2*
	Week 8	64.9±5.9%*	147.4±15.6*	33.6±8.7*
	Week 12	68.2±5.8%	145.6±17.2*	29.6±8.6
LGPoly	Baseline	68.5±5.9%	132.2±18.6	31.0±10.0
	Week 4	65.1±7.0%	135.8±17.9	32.9±10.4
	Week 8	65.8±7.2%	141.6±22.5	33.8±13.5
	Week 12	65.7±5.3%	151.6±17.5*	34.3±9.2

Joint Kinematics

A minimum of three steps per rat per timepoint were averaged for analysis. Observed ranges of motion for the kinematic parameters of the hip, knee, and ankle in the baseline measurements for each group can be seen in **Table 7-2**. The shapes and ranges of motion of these parameters compare favorably to literature values (see **Chapter 5/6**).

Table 7-2: Ranges of motion for LGNR, PTN, and LGPoly kinematic parameters (in degrees)

Group		LGNR	PTN	LGPoly	Normative Database
Hip	Flexion	46.2±7.0	37.9±6.3	38.0±6.4	46.4±6.7
	Adduction	15.1±3.6	12.7±3.3	10.4±4.0	8.4±2.5
	Rotation	40.5±8.1	42.3±7.3	39.6±7.8	32.7±4.6
Knee	Flexion	33.1±3.5	36.3±4.9	35.3±6.2	45.9±8.3
Ankle	Flexion	36.2±9.0	35.8±8.6	33.2±8.2	32.3±9.6

When compared to their baseline measurements, the LGNR animals showed clear differences ($p < 0.05$) at all three timepoints (**Figure 7-6**, blue). Hip flexion significantly decreased throughout stance at all timepoints. Hip adduction decreased during early to mid-stance at all timepoints, and also decreased during late swing at Week 8 and Week 12. Hip external rotation increased in late swing through toe-off at Week 4, from mid-swing through toe-off at Week 8, and from early swing through toe-off at Week 12. Knee extension increased throughout stance and from mid-swing through heel strike at all timepoints. Last, ankle dorsiflexion decreased at toe-off into swing at all three timepoints. Across the board, the LGNR animals did not appear to show any significant improvement in kinematics throughout the observation period.

The PTN animals also showed significant differences ($p < 0.05$) at all three timepoints as compared to their baseline measurements (**Figure 7-7**, green). Hip extension increased during mid to late stance and during mid-swing at all three timepoints. Hip adduction decreased during mid-stance at Week 4 and Week 8. Hip internal rotation increased during mid-stance at Week 4 and Week 8, and slightly increased just after toe-off at Week 4. Knee extension increased during late stance at all three timepoints, and increased in early and late stance at Week 12. Ankle dorsiflexion increased during mid-stance at Week 4, and increased at toe-off at all three timepoints though most prominently at Week 4. It is important to note that the differences at Week 12 were not as severe as those observed at the earlier timepoints.

Last, the LGPoly animals were demonstrating significantly different ($p < 0.05$) movement patterns at all timepoints as compared to their baseline measurements (**Figure 7-8**, red). Hip extension increased during mid-stance at all timepoints, and hip flexion increased during midswing at Week 4 and Week 8. There were no significant differences in hip adduction. Hip external rotation increased during mid-swing at all timepoints. Knee extension increased in mid to late stance at all timepoints, and increased in late swing at Week 4. Ankle dorsiflexion significantly increased from mid-stance to mid-swing at Week 4 and from toe-off through mid-swing at Week 8. As in the PTN group, the kinematic differences seen at Week 12 for the LGPoly animals were not as drastic as in the earlier timepoints.

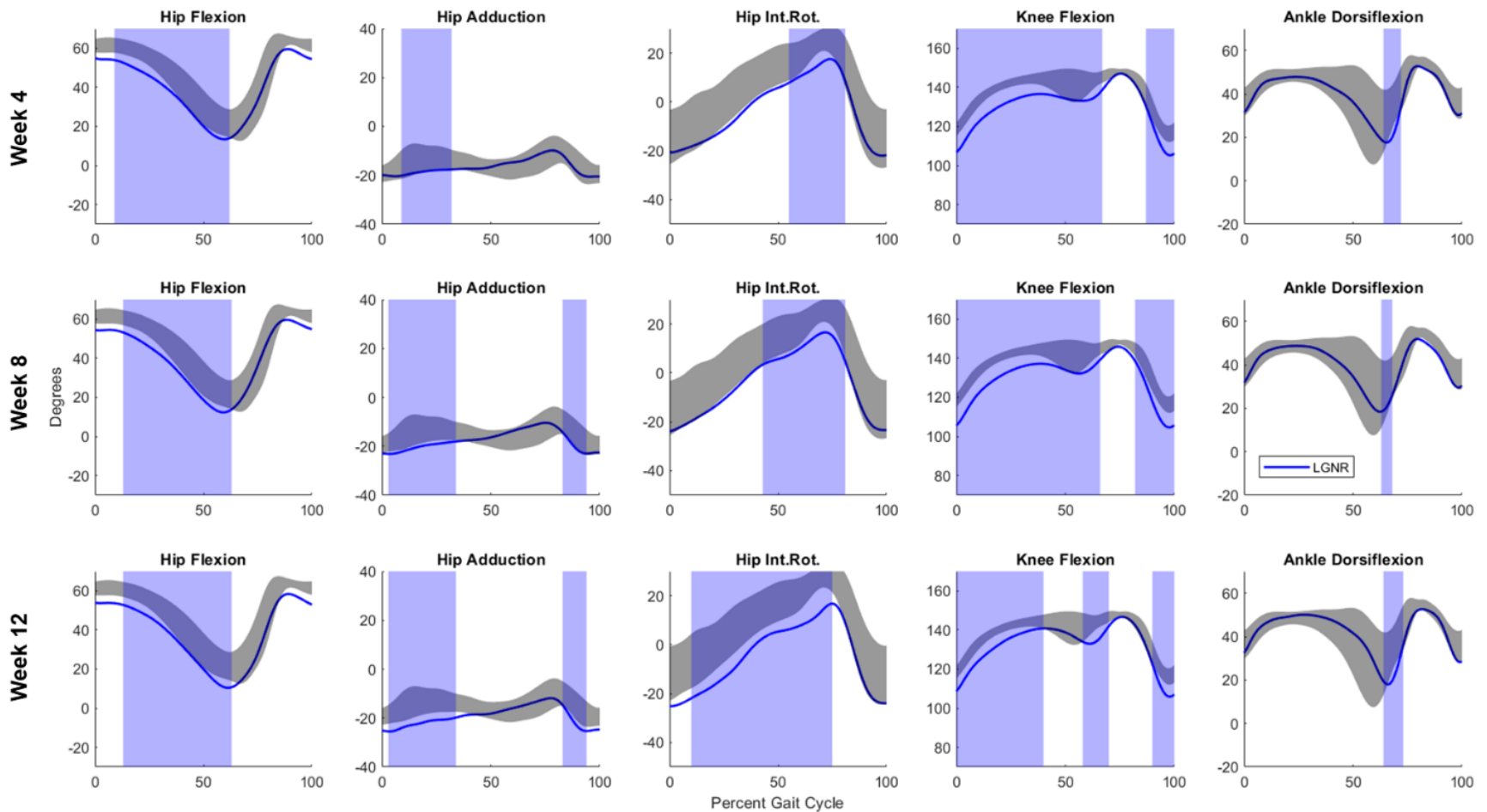


Figure 7-6: Kinematic comparisons between LGNR and baseline at all timepoints. The LGNR baseline kinematic curves are shown as black clouds and the LGNR post-surgical curves are shown in blue. Week 4 kinematics are in the top row, Week 8 in the middle, and Week 12 at the bottom. Areas of significant difference between the post-surgical and baseline curves are shown as blue shaded regions (GraphPad Prism, 2-way ANOVA w/ multiple comparisons and Fisher's least significant difference (LSD) test, $p < 0.05$).

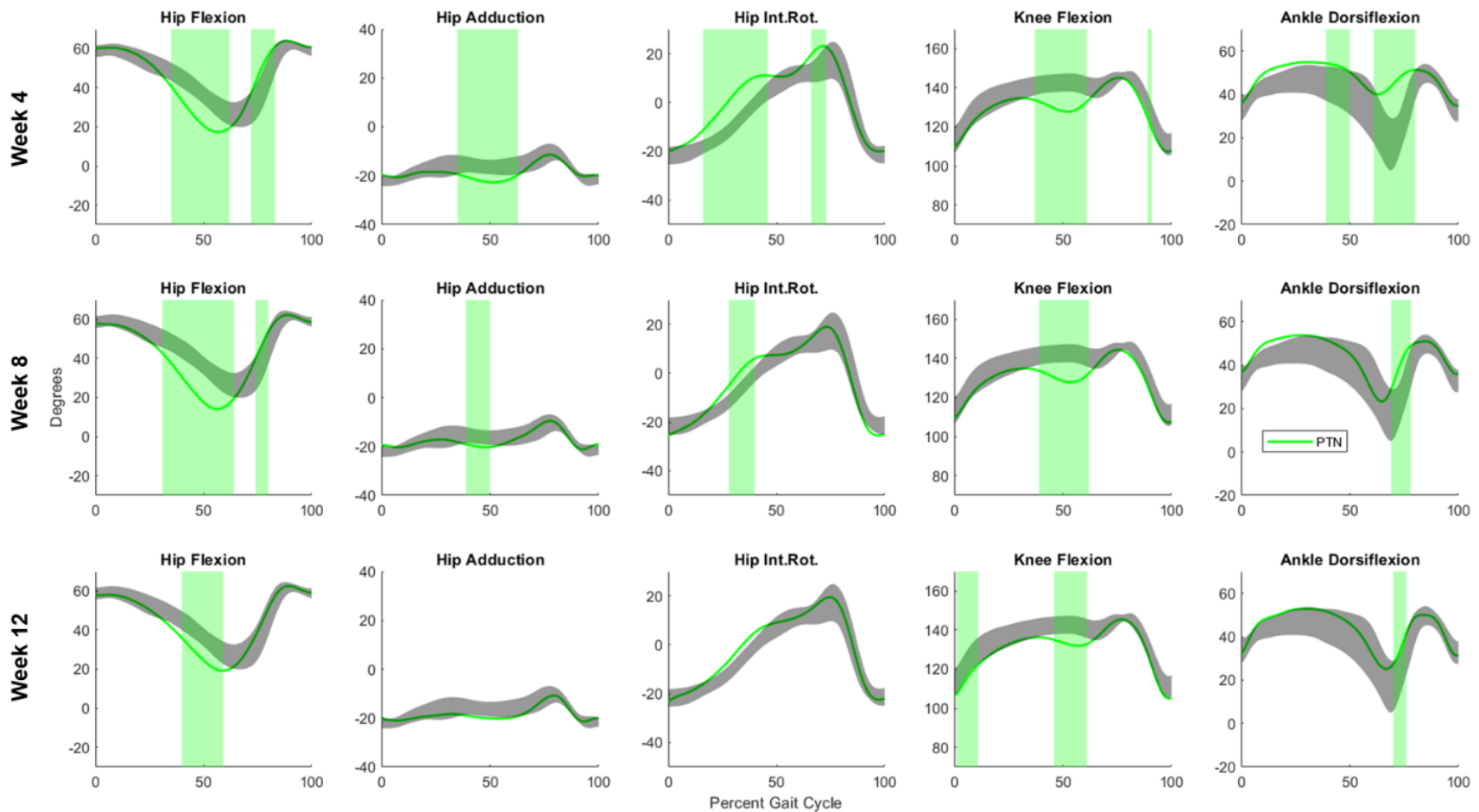


Figure 7-7: Kinematic comparisons between PTN and baseline at all timepoints. The PTN baseline kinematic curves are shown as black clouds and the PTN post-surgical curves are shown in green. Week 4 kinematics are in the top row, Week 8 in the middle, and Week 12 at the bottom. Areas of significant difference between the post-surgical and baseline curves are shown as green shaded regions (GraphPad Prism, 2-way ANOVA w/ multiple comparisons and Fisher's least significant difference (LSD) test, $p < 0.05$).

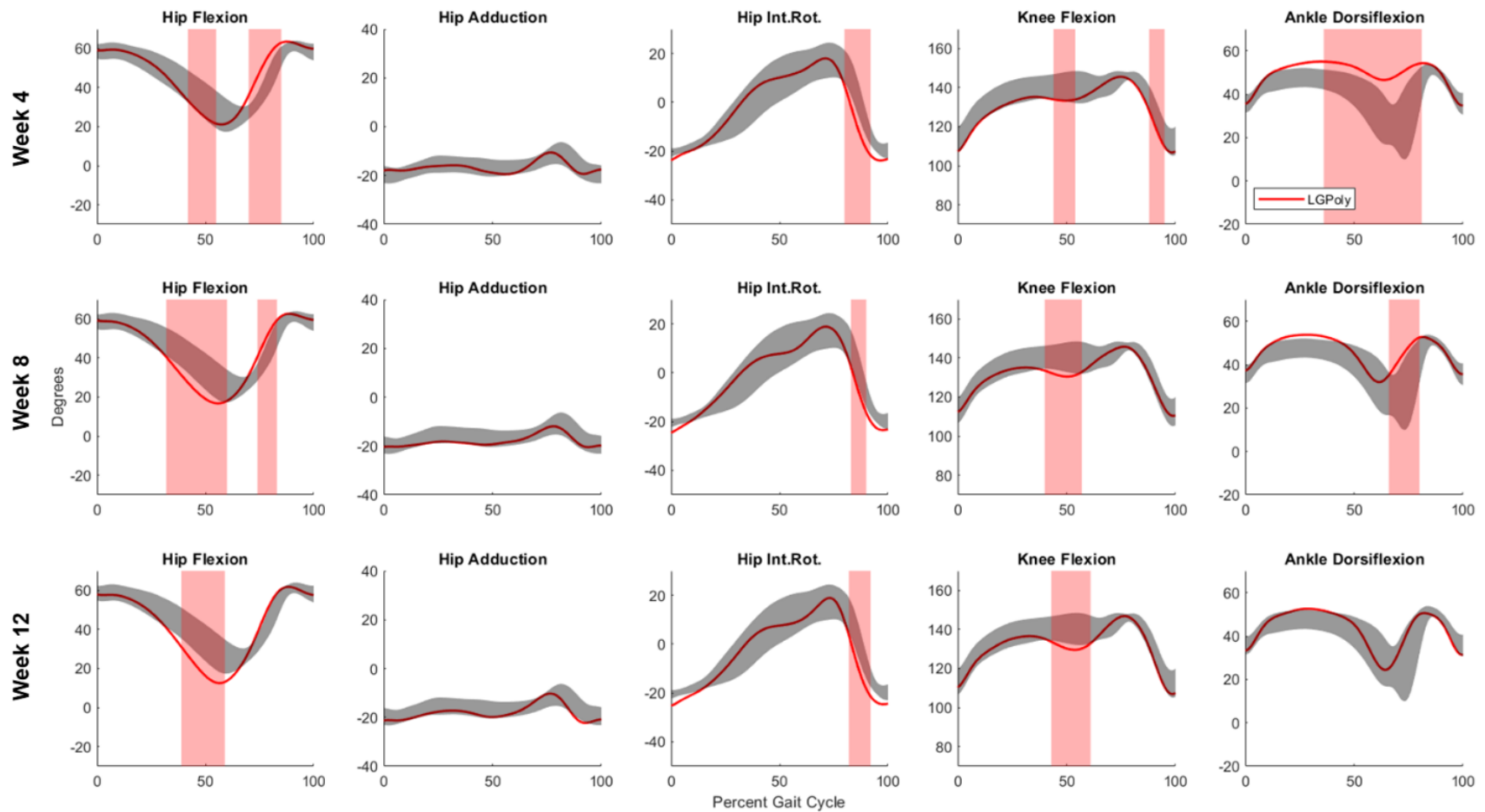


Figure 7-8: Kinematic comparisons between LGPoly and baseline at all timepoints. The LGPoly baseline kinematic curves are shown as black clouds and the LGPoly post-surgical curves are shown in red. Week 4 kinematics are in the top row, Week 8 in the middle, and Week 12 at the bottom. Areas of significant difference between the post-surgical and baseline curves are shown as red shaded regions (GraphPad Prism, 2-way ANOVA w/ multiple comparisons and Fisher’s least significant difference (LSD) test, $p < 0.05$).

Joint Moments

A minimum of two footstrikes per rat per timepoint were averaged for kinetic analysis. Observed average peak moments for the kinetic parameters of the hip, knee, and ankle joints in the baseline measurements for each group can be seen in **Table 7-3**. These peak moments compared favorably to literature values (see **Chapter 5**).

When compared to their baseline measurements, the LGNR animals showed significant differences ($p < 0.05$) at all timepoints (**Figure 7-9**, blue). Hip flexion torque slightly increased in late stance at Week 4 and also increased over a broader range of mid to late stance at Week 8 and Week 12. Hip adduction torque increased slightly at Week 8 and more significantly from early to mid-stance at Week 12. Hip external rotation torque increased in late stance at Week 12, but showed no significant differences at the other timepoints. Knee extension torque increased at all timepoints, but only very slightly in early stance at Week 4 versus far more impactful increased through nearly the entirety of stance at Week 8 and Week 12. Last, ankle dorsiflexion torque increased slightly in late stance at Week 4 and Week 8. In general, the differences seen at Week 12 were more severe than those seen at Week 4 or Week 8.

The PTN animals also showed significant differences ($p < 0.05$) at all three timepoints as compared to baseline (**Figure 7-10**, green). Hip flexion torque increased from early through late stance at all three timepoints. Hip adduction torque also increased at all three timepoints from mid-stance to toe-off. Hip external rotation torque increased from early through late stance at all three timepoints as well. Knee extension torque increased from early through mid-stance and flexion torque increased from late stance through toe-off, again at all three timepoints. Last, ankle dorsiflexion torque increased from heel strike through mid-stance at Week 4 and briefly prior to

toe-off at Week 8. The majority of the differences seen at all timepoints were substantial deviations from baseline and no significant improvement was observed.

Finally, the LGPoly animals demonstrated significant ($p < 0.05$) and consistently severe differences in their kinetic parameters at all three timepoints as compared to baseline (**Figure 7-11**, red). Hip flexion torque increased from early to late stance at Week 4 and Week 8, and from mid to late stance at Week 12. Hip adduction torque increased from mid to late stance at Week 4 and Week 8, and from early stance through toe-off at Week 12. Hip external rotation torque increased from early to late stance at Week 4 and Week 8, and from mid to late stance at Week 12. Knee extension torque increased from early to mid-stance and flexion torque increased from late stance through toe-off at all timepoints. Ankle dorsiflexion torque increased from early through mid-stance at Week 4, in early stance alone at Week 8, and briefly in early stance then again from late stance through toe-off at Week 12. Again, the majority of the observed differences were large deviations from baseline and no significant improvement was seen.

Table 7-3: Peak moments for LGNR, PTN, and LGPoly kinetic parameters (in N*m/kg)

Group		LGNR	PTN	LGPoly	Normative Database
Hip	Flexion Moment	0.031±0.013	0.025±0.009	0.027±0.008	0.043±0.016
	Extension Moment	-0.159±0.045	-0.151±0.027	-0.133±0.024	-0.133±0.028
	Adduction Moment	0.010±0.004	0.015±0.011	0.016±0.004	0.006±0.006
	Int. Rotation Moment	0.122±0.032	0.106±0.028	0.087±0.015	0.095±0.017
Knee	Extension Moment	-0.115±0.015	-0.106±0.010	-0.094±0.014	-0.078±0.013
Ankle	Flexion Moment	0.003±0.001	0.003±0.002	0.003±0.003	0.008±0.005
	Extension Moment	-0.114±0.024	-0.094±0.010	-0.097±0.015	-0.099±0.026

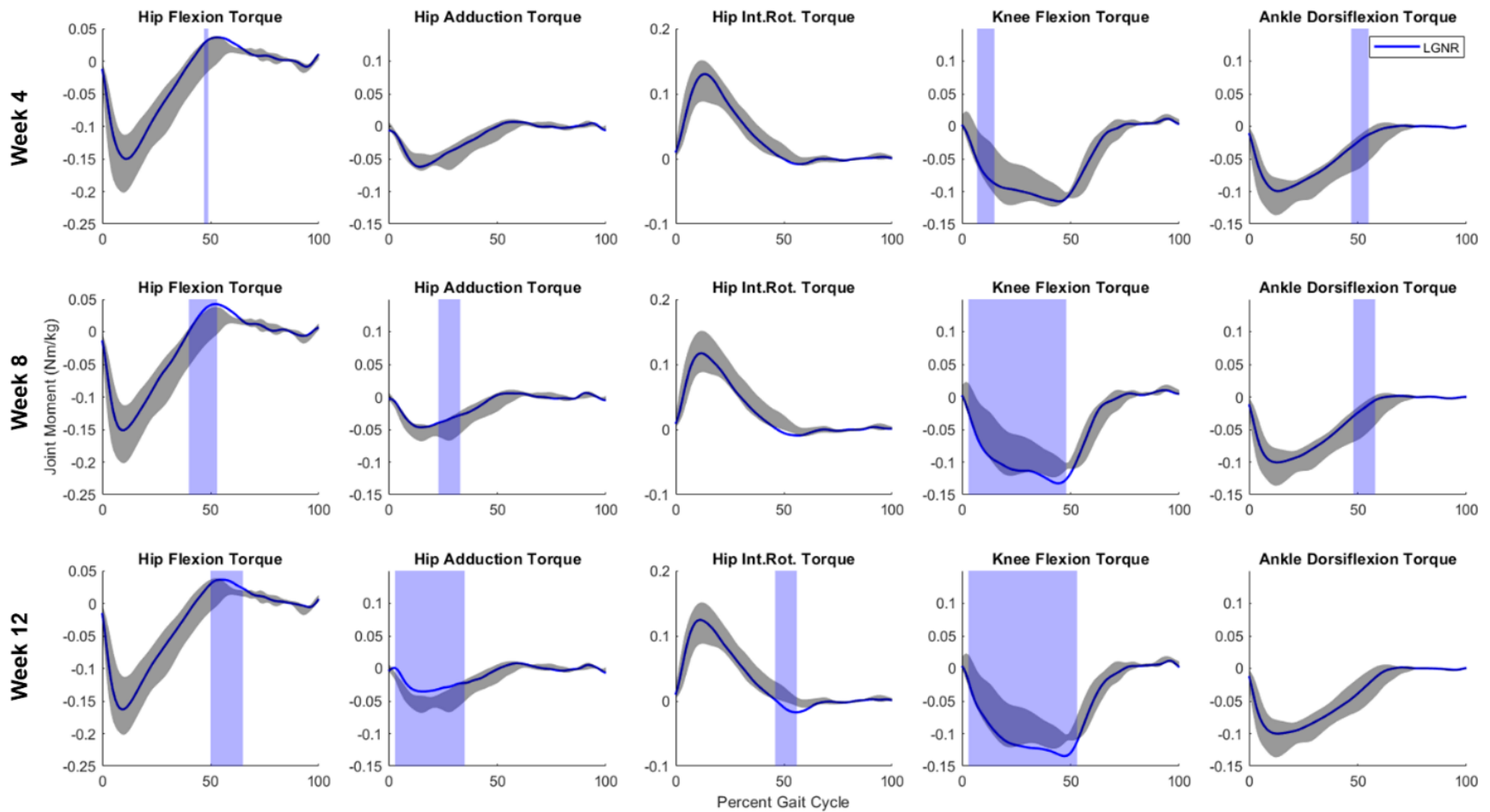


Figure 7-9: Kinetic comparisons between LGNR and baseline at all timepoints. The LGNR baseline kinetic curves are shown as black clouds and the LGNR post-surgical curves are shown in blue. Week 4 kinetics are in the top row, Week 8 in the middle, and Week 12 at the bottom. Areas of significant difference between the post-surgical and baseline curves are shown as blue shaded regions (GraphPad Prism, 2-way ANOVA w/ multiple comparisons and Fisher's least significant difference (LSD) test, $p < 0.05$).

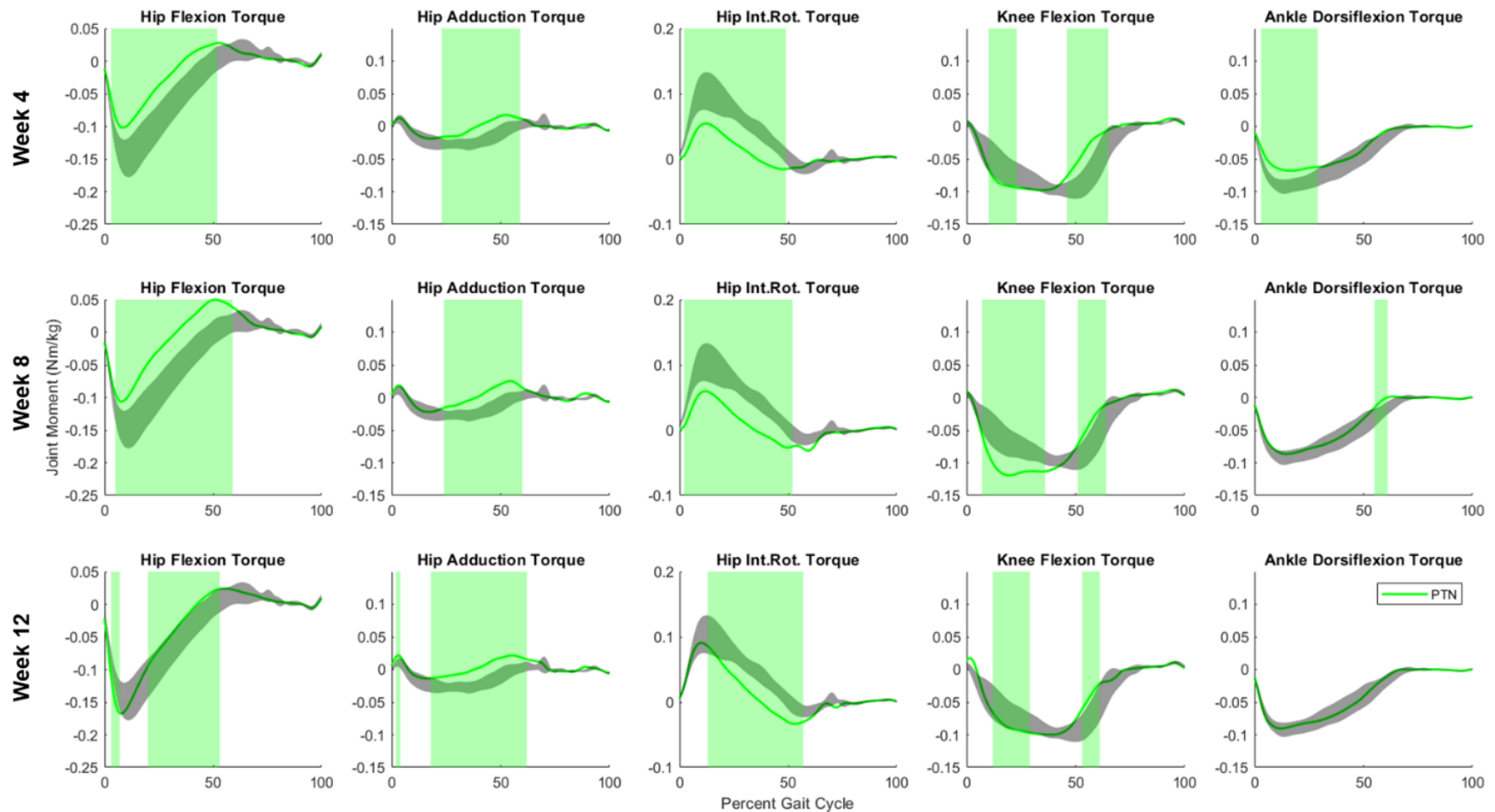


Figure 7-10: Kinetic comparisons between PTN and baseline at all timepoints. The PTN baseline kinetic curves are shown as black clouds and the PTN post-surgical curves are shown in green. Week 4 kinetics are in the top row, Week 8 in the middle, and Week 12 at the bottom. Areas of significant difference between the post-surgical and baseline curves are shown as green shaded regions (GraphPad Prism, 2-way ANOVA w/ multiple comparisons and Fisher's least significant difference (LSD) test, $p < 0.05$).

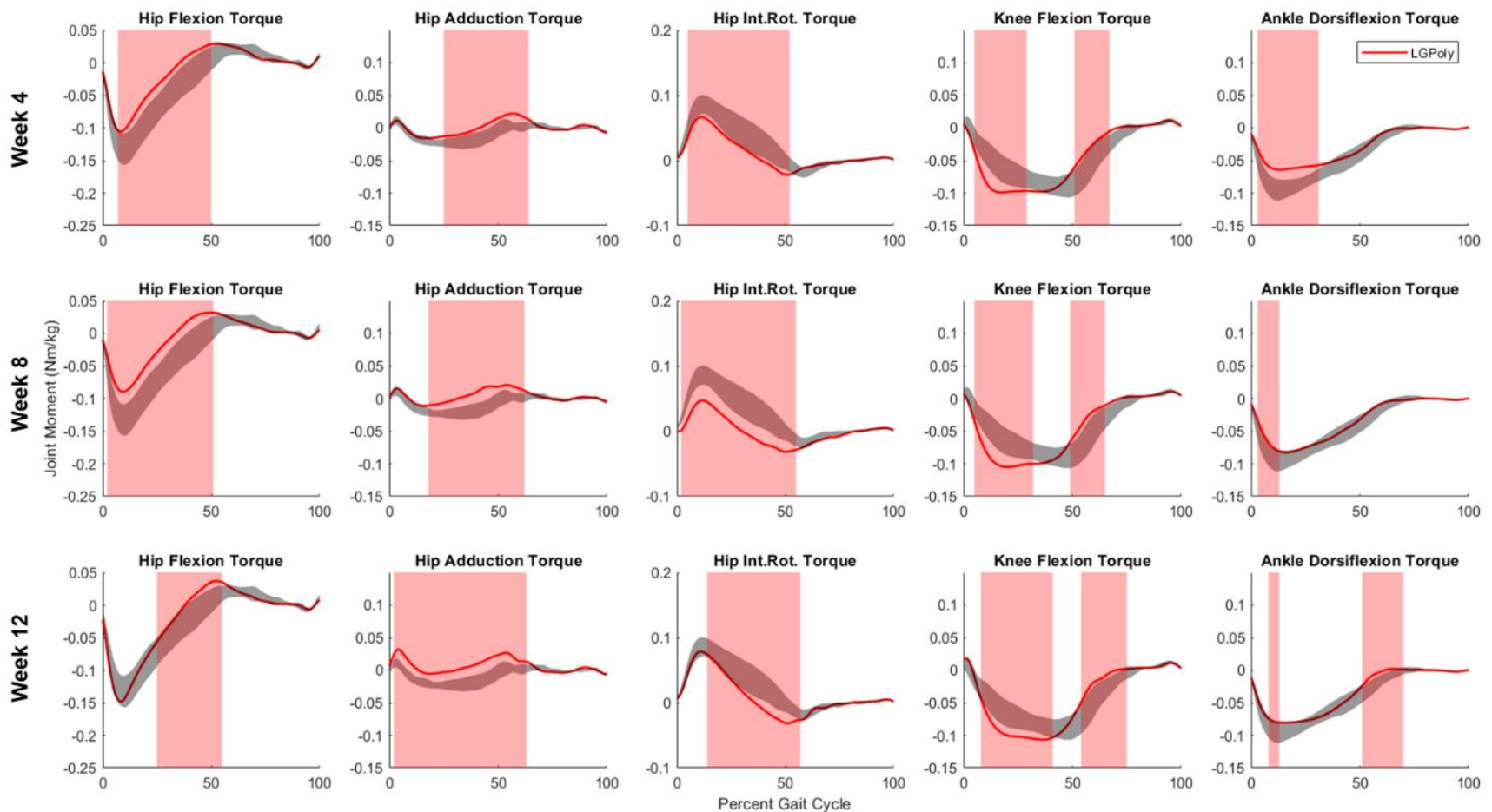


Figure 7-11: Kinetic comparisons between LGPoly and baseline at all timepoints. The LGPoly baseline kinetic curves are shown as black clouds and the LGPoly post-surgical curves are shown in red. Week 4 kinetics are in the top row, Week 8 in the middle, and Week 12 at the bottom. Areas of significant difference between the post-surgical and baseline curves are shown as red shaded regions (GraphPad Prism, 2-way ANOVA w/ multiple comparisons and Fisher's least significant difference (LSD) test, $p < 0.05$).

Discussion

As discussed in **Chapter 6**, severe VML injuries to the extremities do not occur without the co-occurrence of peripheral nerve injury. With that in mind, we previously investigated the biomechanical and force production effects of a laceration of the peroneal nerve alone and in combination with a TA VML injury. The methodology for creating nerve and polytrauma injuries learned through that study were then leveraged into this current study, where we expanded our injury models to the tibial nerve and the lateral gastrocnemius (LG). In contrast to the TA, the LG carries a significantly heavier burden throughout the gait cycle. The TA is solely responsible for ankle dorsiflexion and clearing the toe during the swing phase of gait, whereas the LG acts on both the ankle and the knee. This makes the LG a two joint muscle that is constantly bearing load, and makes it the primary muscle for energy transfer in the lower limb during movement. In theory, injuring a muscle that carries such a high level of responsibility during gait should result in clear and measurable differences in both kinematic and kinetic parameters throughout the gait cycle. Further, when combined with a partial laceration of the tibial nerve, the differences should be even more profound. The difficulty in recovering from peripheral nerve injuries is well documented^{19,20,37-41}, so the creation of a tibial nerve injury in combination with a 20% full-thickness VML injury was expected to result in massive, systemic gait alterations.

To investigate the effects of these injuries on the three study groups (LG VML alone [LGNR], partial tibial nerve laceration alone [PTN], and LG VML+tibial nerve laceration [LGPoly]), the first evaluative metric was muscle force production. There are very few studies that have evaluated VML injury in the LG or made any attempts at collecting force production information on the LG alone (rather than the entirety of the gastrocnemius), but Merritt et al¹⁶ reported the force production of the healthy LG at roughly 22N/kg. The contralateral controls

muscles for the three groups in this study measured $18.5 \pm 3.6 \text{N/kg}$ for LGNR, $20.9 \pm 2.4 \text{N/kg}$ for PTN, and $21.7 \pm 2.7 \text{N/kg}$ for LGPoly, which all compared well with the literature value. The LGNR injured muscle exhibited a mean maximal force of $12.2 \pm 3.2 \text{N/kg}$ at 12 weeks post-injury, which represents roughly 65% of the contralateral force. Merritt saw roughly 74% force production compared to the contralateral limb in their unrepaired VML animals, but historical data from the Christ Lab TA VML work (Corona et al²¹, Passipieri et al⁸, **Chapter 6**). demonstrates the estimated force deficit resulting from a 20% VML injury should be on the order of 30-40%. Because these animals were all tested using the same equipment and protocols as those previous studies, the ~35% deficit observed from the LG VML injury falls in line with the expected injury impact.

The PTN animals were only inflicted with a partial laceration of the tibial nerve, which was immediately repaired after creation. This injury was given to the peroneal nerve in **Chapter 6**, and force testing of the experimental TA at 12 weeks demonstrated full recovery of muscle force production ability. However, in this case the PTN experimental LG muscles only produced $13.8 \pm 3.2 \text{N/kg}$ at 12 weeks, which corresponds to roughly 67% of the contralateral force. The LG was untouched during the surgical procedure, meaning it was left entirely intact for the duration of the study period. Despite this, there was a significant deficit in force production ability when the expectation was full recovery.

In the same vein, the force production results of the LGPoly group at 12 weeks were also surprising. These animals produced $13.2 \pm 3.0 \text{N/kg}$ for roughly 61% of their contralateral force, which is a non-significant difference as compared to the LGNR and PTN animals. This result was unexpected for multiple reasons. First, the combination of the LG VML and the nerve laceration should have caused a more significant force deficit than either of those injuries alone. Second, after knowing that the PTN animals were more functionally hindered than expected, there was

even more reason for the LGPoly animals to have a massive deficit. Last, the TA-peroneal nerve polytrauma animals from **Chapter 6** showed a greater than 60% force deficit as compared to baseline, a 25% difference as compared to the unrepaired TA VML animals, and a 45% difference as compared to the peroneal nerve laceration animals. There were multiple ideas being floated to explain the results for both the LGPoly and PTN animals, but it was only after completion of kinematic and kinetic analysis that one theory truly took hold.

Kinematics

As discussed in **Chapter 5** and **Chapter 6**, literature values for average ranges of motion for flexion of the hip (30-55 degrees^{37,51,52,58,59}), knee (35-60 degrees^{37,51,52,58-60}), and ankle (30-60 degrees^{37,51,52,58-60}) compared well to the sagittal plane ranges of motion calculated for healthy animals in **Chapter 4** (~49, 44, 37 degrees). In this current study, the average calculated ranges of motion for the hip, knee, and ankle for each of the three groups at baseline were roughly: 46, 33, and 36 degrees for LGNR; 38, 36, and 36 degrees for PTN, and 38, 35, and 33 degrees for LGPoly. Compared to the literature and the data calculated in **Chapter 5**, these values fell reasonably within the range that would be expected for healthy animals.

Just as in **Chapter 6**, the motion capture approach utilized here was sensitive enough to detect differences in all groups at all timepoints as compared to the group's own baseline data. Looking at the LGNR kinematics (**Figure 7-6**), there are significant increases in hip extension during stance, hip external rotation through much of the gait cycle, and knee extension throughout the gait cycle at Week 4 and Week 8. This is indicative of the animal placing a reduced load on the injured limb at those timepoints, which makes sense when the injured muscle is considered. The LG connects directly to the Achilles tendon, which transfers the necessary energy from the

foot to drive the leg and start the swing phase. If the animal recognizes that they do not have the ability to drive motion using the injured leg, they put less of a load onto that leg – similar to a limp in humans after a fresh injury. By Week 12, these differences observed at the earlier timepoints have not changed, giving no indication that the animal is exhibiting any kinematic improvements from their injury. These animals had a ~35% force deficit in the injured leg at this point, and that deficit appears to be considerably influencing their ability to return to normal movement patterns.

The PTN group also showed significant differences at all three timepoints (**Figure 7-7**), though not the same full gait cycle differences that were observed in the LGNR animals. These animals exhibited increased hip extension in mid-stance at all timepoints. Hip abduction increased during mid to late stance at Week 4 and Week 8, and hip internal rotation increased during mid-stance (Week 4 and Week 8) and around toe-off (Week 4). Similar to hip extension, knee extension increased in late stance at all timepoints. Last, ankle dorsiflexion increased during mid-stance (Week 4) and around toe-off (all timepoints). Interestingly though, most of the differences present at Week 4 and Week 8 are either substantially reduced or entirely alleviated by Week 12. Despite the fact that the PTN animals are exhibiting significant compensations at the early timepoints, the Week 12 data demonstrates that the animals are progressing out of compensatory joint motions and are trending back towards normal movement patterns. In theory, this would be reflective of recovery from the partial tibial nerve injury and would be a similar result to that seen in **Chapter 6** with the partial peroneal nerve injury, despite the PTN animals maintaining a ~33% force production deficit.

The LGPoly animals showed a relative lack of differences as compared to the other two groups (**Figure 7-8**), especially considering the extent of injury. At all three timepoints, the LGPoly animals showed an increase in hip extension during mid to late stance and an increase in

hip flexion during mid-swing. There was also an increase in hip external rotation at all three timepoints during mid-swing. Knee extension increased from late stance through toe-off, again at all three timepoints. Ankle dorsiflexion increased substantially from mid-stance through mid-swing at Week 4 and from toe-off through mid-swing at Week 8. When accounting for the severity of the polytrauma these LGPoly animals were given, there are far fewer differences than in either of the other injured groups. And in a similar pattern as the PTN animals, the Week 12 curves for the LGPoly group showed improvement despite the animals carrying a massive force production deficit in their injured limb.

Kinetics

Given the contradictory results of the force measurements and the kinematics for the LGPoly and PTN animals, our distinct ability to evaluate joint moments took on new significance. Calculating the internal forces experienced by these animals shed light on the load distribution and activation patterns of the muscles and joints within the hindlimb. In situations such as this, where the force production data implies that there should be massive functional compensations but the kinematic data shows extremely limited deviations from normal movement patterns, kinetic analysis unlocks the black box of the internal machinations of the hindlimb.

The kinetic values calculated at baseline for each of the three groups compared well to the peak moments calculated for healthy animals in **Chapter 5** (see **Table 7-3**). In this study, the average peak hip flexion, hip extension, hip adduction, hip internal rotation, knee flexion, ankle flexion, and ankle extension moments were all reasonably within the normal range.

Looking at the LGNR kinetics (**Figure 7-9**), there were significant differences detected at all three post-surgical timepoints. Week 4 showed only very slight differences compared to the

other timepoints, with small increases in hip flexion torque and ankle dorsiflexion torque in late stance and a small increase in knee extension torque in early stance. Week 8 showed substantially more compensation, with the same Week 4 differences expanding out to cover larger percentages of stance and a new region of difference in hip adduction torque in mid-stance. Interestingly, the largest kinetic effects from the 20% VML injury were observed at Week 12. This timepoint showed significant increases in hip flexion moment, hip adduction moment, hip external rotation moment, and knee extension moment. The changes in hip adduction moment and knee extension moment were observed over a large percentage of the stance phase. In a similar fashion to the LGNR kinematics, there were no signs of improvement with the kinetics for these animals. Further, there was no indication that the animals had settled into any set compensation. This could be due to the fact that the gastrocnemius is a two-joint muscle. Because it acts on both the ankle and the knee, and is active throughout the gait cycle, the compensation and adaptation timelines are expected to be vastly different than what was observed with a TA VML injury. As mentioned in previous studies, it is this lack of a compensatory plateau that drives the need to expand experimental timepoints out to a minimum of 6 months.

The PTN group (**Figure 7-10**) showed a kinetic response that was much more in line with what would be expected as a result of injury. Differences were detected at all timepoints, and differences were detected in all evaluated metrics at Week 4 and Week 8. Contrary to the LGNR animals, the Week 12 kinetics were not dramatically worse than what was observed at the earlier timepoints. In fact, the differences observed at Week 4 and Week 8 were nearly exactly the same as those at Week 12. When these results are analyzed in combination with the kinematics, they are presenting two different pictures. The kinematics demonstrate that the joint angles being exhibited by the PTN animals are nearly normal, but the Week 12 kinetics clearly show that there is a

consistent increase in hip flexion torque, large increases in hip adduction torque and hip external rotation torque, and increases in both knee flexion and extension torque at different points in stance. The dichotomy of results presented by the kinematics and kinetics illustrate that despite the animals exhibiting near-normal movement patterns, their process by which they achieve this motion is still highly pathological. As expressed earlier, these pathological activation patterns and increased loads on muscles and joints that are unaccustomed to carrying such responsibility are what lead to secondary pathologies over time. Fortunately, our ability to perform kinetic analysis allows us to identify that these pathological processes are occurring despite the animal achieving near-normal motion.

This same trend of good kinematics and highly pathological kinetics continued when the curves for the LGPoly animals were evaluated (**Figure 7-11**). As discussed, the kinematics for the LGPoly animals looked the best of any group at every post-surgical timepoint. This was surprising for many reasons, but most significantly because this group received the most severe injury. However, the kinetic analysis presented results that were far more aligned with what was expected. There was an immediate, widespread kinetic impact from the 20% VML injury in combination with the partial tibial nerve laceration. Significant differences were detected at every timepoint and in every evaluated metric, and these differences did not improve or substantially decrease as the timepoints went on. This was very similar to what was observed in the PTN animals. The kinematics were trending towards normal movement patterns, but the kinetics were decidedly pathologic across the board.

The primary theory that emerged to explain the results of these groups arose out of the physiology of the posterior compartment. It is reasonable to theorize that there were not extreme kinetic changes in the LGNR animals at the early timepoints because the system was not acutely

aware of the problem. A VML injury to the TA (**Chapter 6**) demonstrated similar results, with little kinetic impact at Week 4 and increased impact at time passed. Because the gastrocnemius is a two-headed muscle (medial and lateral heads), the medial head might have attempted to take on the responsibilities of the injured lateral head at the early timepoints. As time passed and this compensation was ineffective, then it is possible that the entire posterior compartment muscular system was recruited to redistribute the load. The posterior compartment in rats is very complex (**Figure 7-12**⁶¹), containing at least 10 muscles (the major contributors are the biceps femoris, vastus lateralis, semitendinosus, tensor fasciae latae, caudofemoralis, semimembranosus, medial and lateral gastrocnemius, plantaris, and soleus) that share responsibility for actuating the knee and ankle. In theory, when carrying the entire gastrocnemius load became too much of a burden for the medial head to carry on its own, the rest of the muscles in the posterior compartment could have been recruited to contribute. In future studies, it would be beneficial to perform MRI to evaluate hypertrophy in the medial head at Week 4 and in other muscles at later timepoints in response to an LG VML injury to support this theory.

Further, it is theorized that the difference between the delayed onset of kinetic changes in the LGNR group versus the immediate and widespread changes seen in the PTN and LGPoly groups is due to one significant reason: the inclusion of the nerve injury. In the LGNR animals, only the lateral head of the gastrocnemius is injured and everything else in the compartment is left untouched. But when the nerve injury is incurred, the effects of that injury are spread wider throughout the compartment. Not only does the tibial nerve innervate the lateral gastrocnemius, it also feeds into the medial gastrocnemius, the soleus, the plantaris, the popliteus, and the sensory sural nerve for the foot⁶². This means that when the laceration injury is incurred, there is a massive accordion effect felt throughout the entire lower hindlimb. In response to this extent of injury, the physiological reaction of the animal would have to be swift and widespread in order to facilitate movement. We theorize that immediately after nerve injury, the animals compensated with a large-scale kinetic shift. They redistributed the load in the posterior compartment to the unaffected muscles, as demonstrated by the kinetic differences at the Week 4 timepoint, and they maintained these kinetic changes through the end of our observation period. The PTN and LGPoly animals were clearly successful with their compensation strategy based on the few kinematic differences observed at Week 12, but the cost of this compensation was continued widespread kinetic effects that would come with their own long-term detrimental impacts.

Future Work and Conclusions

The results of this study clearly demonstrate the need for further investigation of multi-joint, multi-muscle compartment injuries both on their own and in combination with nerve lacerations. While significant work has been completed on the TA, it only acts on the ankle and the compensation patterns are clear and predictable. Because rats walk utilizing a crouch gait

pattern and the LG acts on both the ankle and the knee in the posterior compartment, the muscle is under significant load throughout the gait cycle. An injury to the LG would cause a markedly different physiological response, but the complexity of the posterior compartment makes it difficult to directly identify what this response is. All of these facts together lead to a two key points: posterior compartment polytrauma injuries are extremely physiologically relevant and need to be investigated further with a combination of technologies (force testing, gait evaluation, MRI, modeling), and the inherent compensatory mechanisms within the posterior compartment need to be better understood before informed attempts at truly treating these injuries can begin in earnest. It would also be wise to extend the evaluation period of these injured animals out to a minimum of 6 months, or even further if that is what it takes to reach a compensatory plateau. The LGNR animals demonstrated that 3 months is not long enough, and because we saw no trend towards any kind of recovery it is difficult to make conclusions on the extent of injury or the recovery timeframe.

This study was the first to investigate polytrauma injuries to the LG and the posterior compartment, and the first to investigate the biomechanical impacts of LG injuries of any kind. As expected, there were numerous hurdles and we were met with unanticipated results, but this set of experiments has left us better informed than we have ever been before. The value of kinetic analysis was very clear in this study, revealing information about the inner workings of the posterior compartment that could not have been unveiled before. And as further experiments are conducted, we as investigators are better equipped to know which questions to ask, and how to more comprehensively evaluate our study animals to get to the root of the true impact of these catastrophic posterior compartment injuries.

References

1. Carlson, B. M. & Faulkner, J. A. The regeneration of skeletal muscle fibers following injury: a review. *Med. Sci. Sports Exerc.* **15**, 187–98 (1983).
2. Carlson, B. M. Regeneration of the completely excised gastrocnemius muscle in the frog and rat from minced muscle fragments. *J. Morphol.* **125**, 447–471 (1968).
3. Ciciliot, S. & Schiaffino, S. Regeneration of mammalian skeletal muscle. Basic mechanisms and clinical implications. *Curr. Pharm. Des.* **16**, 906–14 (2010).
4. Warren, G. L. *et al.* Mechanisms of skeletal muscle injury and repair revealed by gene expression studies in mouse models. *J. Physiol.* **582**, 825–41 (2007).
5. White, T. P. & Devor, S. T. Skeletal muscle regeneration and plasticity of grafts. *Exerc. Sport Sci. Rev.* **21**, 263–95 (1993).
6. Grogan, B. F. & Hsu, J. R. Volumetric muscle loss. *J. Am. Acad. Orthop. Surg.* **19 Suppl 1**, S35-7 (2011).
7. Holcomb, J. B., Stansbury, L. G., Champion, H. R., Wade, C. & Bellamy, R. F. Understanding Combat Casualty Care Statistics. *J. Trauma Inj. Infect. Crit. Care* **60**, 397–401 (2006).
8. Passipieri, J. A. *et al.* Keratin Hydrogel Enhances In Vivo Skeletal Muscle Function in a Rat Model of Volumetric Muscle Loss. *Tissue Eng. Part A* **23**, 556–571 (2017).
9. Corona, B. T. *et al.* The promotion of a functional fibrosis in skeletal muscle with volumetric muscle loss injury following the transplantation of muscle-ECM. *Biomaterials* **34**, 3324–3335 (2013).
10. Machingal, M. A. *et al.* A Tissue-Engineered Muscle Repair Construct for Functional Restoration of an Irrecoverable Muscle Injury in a Murine Model. *Tissue Eng. Part A* **17**, 2291–2303 (2011).
11. Corona, B. T. *et al.* Autologous minced muscle grafts: A tissue engineering therapy for the volumetric loss of skeletal muscle. *Am. J. Physiol. - Cell Physiol.* **305**, (2013).
12. Passipieri, J. A. *et al.* In Silico and In Vivo Studies Detect Functional Repair Mechanisms in a Volumetric Muscle Loss Injury. *Tissue Eng. Part A* ten.tea.2018.0280 (2019). doi:10.1089/ten.tea.2018.0280
13. Mintz, E. L., Passipieri, J. A., Lovell, D. Y. & Christ, G. J. Applications of In Vivo Functional Testing of the Rat Tibialis Anterior for Evaluating Tissue Engineered Skeletal Muscle Repair. *J Vis Exp* (2016).
14. Mintz, E. L. *et al.* Long-Term Evaluation of Functional Outcomes Following Rat Volumetric Muscle Loss Injury and Repair. *Tissue Eng. Part A* **26**, 140–156 (2020).
15. Dienes, J. A. *et al.* Analysis and Modeling of Rat Gait Biomechanical Deficits in Response to Volumetric Muscle Loss Injury. *Front. Bioeng. Biotechnol. - Biomech. Ahead of P*, (2019).

16. Merritt, E. K. *et al.* Functional assessment of skeletal muscle regeneration utilizing homologous extracellular matrix as scaffolding. *Tissue Eng. Part A* **16**, 1395–405 (2010).
17. Merritt, E. K. *et al.* Repair of traumatic skeletal muscle injury with bone-marrow-derived mesenchymal stem cells seeded on extracellular matrix. *Tissue Eng. Part A* **16**, 2871–81 (2010).
18. Menorca, R. M. G., Fussell, T. S. & Elfar, J. C. Nerve physiology: mechanisms of injury and recovery. *Hand Clin.* **29**, 317–30 (2013).
19. Höke, A. A (heat) shock to the system promotes peripheral nerve regeneration. *J. Clin. Invest.* **121**, 4231–4 (2011).
20. Grinsell, D. & Keating, C. P. Peripheral nerve reconstruction after injury: a review of clinical and experimental therapies. *Biomed Res. Int.* **2014**, 698256 (2014).
21. Corona, B. T., Ward, C. L., Baker, H. B., Walters, T. J. & Christ, G. J. Implantation of In Vitro Tissue Engineered Muscle Repair Constructs and Bladder Acellular Matrices Partially Restore In Vivo Skeletal Muscle Function in a Rat Model of Volumetric Muscle Loss Injury. *Tissue engineering. Part A* **20**, 705–15 (2014).
22. Pollot, B. E., Goldman, S. M., Wenke, J. C. & Corona, B. T. Decellularized extracellular matrix repair of volumetric muscle loss injury impairs adjacent bone healing in a rat model of complex musculoskeletal trauma. *J. Trauma Acute Care Surg.* **81**, S184–S190 (2016).
23. Goldman, S. M., Henderson, B. E. P., Walters, T. J. & Corona, B. T. Co-delivery of a laminin-111 supplemented hyaluronic acid based hydrogel with minced muscle graft in the treatment of volumetric muscle loss injury. *PLoS One* **13**, e0191245 (2018).
24. Pilia, M. *et al.* Transplantation and perfusion of microvascular fragments in a rodent model of volumetric muscle loss injury. *Eur. Cells Mater.* **28**, 11–24 (2014).
25. Kim, J. *et al.* Graft alignment impacts the regenerative response of skeletal muscle after volumetric muscle loss in a rat model. *Acta Biomater.* **105**, 191–202 (2020).
26. Vega-Soto, E. E., Rodriguez, B. L., Armstrong, R. E. & Larkin, L. M. A 30% Volumetric Muscle Loss Does Not Result in Sustained Functional Deficits After a 90-Day Recovery in Rats. *Regen. Eng. Transl. Med.* **6**, 62–68 (2020).
27. Huang, H. *et al.* Preferred M2 Polarization by ASC-Based Hydrogel Accelerated Angiogenesis and Myogenesis in Volumetric Muscle Loss Rats. *Stem Cells Int* **2017**, 2896874 (2017).
28. Hagiwara, K., Chen, G., Kawazoe, N., Tabata, Y. & Komuro, H. Promotion of muscle regeneration by myoblast transplantation combined with the controlled and sustained release of bFGFcp. *J. Tissue Eng. Regen. Med.* **10**, 325–333 (2016).
29. Qiu, X. *et al.* Mesenchymal stem cells and extracellular matrix scaffold promote muscle regeneration by synergistically regulating macrophage polarization toward the M2 phenotype. *Stem Cell Res. Ther.* **9**, 88 (2018).

30. Ju, Y. M., Atala, A., Yoo, J. J. & Lee, S. J. In situ regeneration of skeletal muscle tissue through host cell recruitment. *Acta Biomater.* **10**, 4332–4339 (2014).
31. Natsu, K. *et al.* Allogeneic bone marrow-derived mesenchymal stromal cells promote the regeneration of injured skeletal muscle without differentiation into myofibers. *Tissue Eng.* **10**, 1093–1112 (2004).
32. Dienes, J. A. *et al.* Analysis and Modeling of Rat Gait Biomechanical Deficits in Response to Volumetric Muscle Loss Injury. *Front. Bioeng. Biotechnol.* **7**, 146 (2019).
33. Aguilar, C. A. *et al.* Multiscale analysis of a regenerative therapy for treatment of volumetric muscle loss injury. *Cell Death Discov.* **4**, 1–11 (2018).
34. Greising, S. M. *et al.* Unwavering Pathobiology of Volumetric Muscle Loss Injury. *Sci. Rep.* **7**, 1–14 (2017).
35. Aurora, A., Roe, J. L., Corona, B. T. & Walters, T. J. An acellular biologic scaffold does not regenerate appreciable de novo muscle tissue in rat models of volumetric muscle loss injury. *Biomaterials* **67**, 393–407 (2015).
36. Corona, B. T. *et al.* Autologous minced muscle grafts: a tissue engineering therapy for the volumetric loss of skeletal muscle. *Am. J. Physiol. Physiol.* **305**, C761–C775 (2013).
37. Bennett, S. W., Lanovaz, J. L. & Muir, G. D. The biomechanics of locomotor compensation after peripheral nerve lesion in the rat. *Behav. Brain Res.* **229**, 391–400 (2012).
38. Jacobs, B. Y. *et al.* The Open Source GAITOR Suite for Rodent Gait Analysis. *Sci. Rep.* **8**, 1–14 (2018).
39. Howard, C. S., Blakeney, D. C., Medige, J., Moy, O. J. & Peimer, C. A. Functional assessment in the rat by ground reaction forces. *J. Biomech.* **33**, 751–7 (2000).
40. Schilling, B. K. *et al.* Adipose-derived stem cells delay muscle atrophy after peripheral nerve injury in the rodent model. *Muscle and Nerve* **59**, 603–610 (2019).
41. Passipieri, J. A. *et al.* Adipose Stem Cells Enhance Nerve Regeneration and Muscle Function in a Peroneal Nerve Ablation Model. *Tissue Eng. Part A* (2019). doi:10.1089/ten.TEA.2018.0244
42. Slater, L. V., Hart, J. M., Kelly, A. R. & Kuenze, C. M. Progressive Changes in Walking Kinematics and Kinetics After Anterior Cruciate Ligament Injury and Reconstruction: A Review and Meta-Analysis. *J. Athl. Train.* 1062-6050.52.6.06 (2017). doi:10.4085/1062-6050.52.6.06
43. Robbins, S. M. *et al.* Comparison of Gait Characteristics Between Patients With Nontraumatic and Posttraumatic Medial Knee Osteoarthritis. *Arthritis Care Res. (Hoboken)*. **68**, 1215–1223 (2016).
44. Ferrarin, M. *et al.* Gait pattern classification in children with Charcot-Marie-Tooth disease type 1A. *Gait Posture* **35**, 131–7 (2012).
45. Ijaz, A. *et al.* Analysis of knee joint kinematics during walking in patients with cerebral

- palsy through human motion capture and gait model-based measurement. in *2012 IEEE International Conference on Virtual Environments Human-Computer Interfaces and Measurement Systems (VECIMS) Proceedings* 196–199 (IEEE, 2012).
doi:10.1109/VECIMS.2012.6273181
46. Topp, R., Mikesky, A., Wigglesworth, J., Holt, W. & Edwards, J. E. The effect of a 12-week dynamic resistance strength training program on gait velocity and balance of older adults. *Gerontologist* **33**, 501–6 (1993).
 47. Damiano, D. L., Arnold, A. S., Steele, K. M. & Delp, S. L. Can strength training predictably improve gait kinematics? A pilot study on the effects of hip and knee extensor strengthening on lower-extremity alignment in cerebral palsy. *Phys. Ther.* **90**, 269–79 (2010).
 48. Damiano, D. L. & Abel, M. F. Functional outcomes of strength training in spastic cerebral palsy. *Arch. Phys. Med. Rehabil.* **79**, 119–25 (1998).
 49. Damiano, D. L., Prosser, L. A., Curatalo, L. A. & Alter, K. E. Muscle Plasticity and Ankle Control After Repetitive Use of a Functional Electrical Stimulation Device for Foot Drop in Cerebral Palsy. *Neurorehabil. Neural Repair* **27**, 200–207 (2013).
 50. Buchner, D. M. *et al.* The effect of strength and endurance training on gait, balance, fall risk, and health services use in community-living older adults. *J. Gerontol. A. Biol. Sci. Med. Sci.* **52**, M218-24 (1997).
 51. Bauman, J. M. & Chang, Y.-H. High-speed x-ray video demonstrates significant skin movement errors with standard optical kinematics during rat locomotion.
doi:10.1016/j.jneumeth.2009.10.017
 52. Garnier, C., Falempin, M. & Ene Canu, M.-H. A 3D analysis of fore-and hindlimb motion during locomotion: Comparison of overground and ladder walking in rats. *Behav. Brain Res.* **186**, 57–65 (2008).
 53. Canu, M.-H. & Garnier, C. A 3D analysis of fore- and hindlimb motion during overground and ladder walking: Comparison of control and unloaded rats. *Exp. Neurol.* **218**, 98–108 (2009).
 54. Roemhildt, M. L., Gardner-Morse, M., Rowell, C., Beynnon, B. D. & Badger, G. J. Gait alterations in rats following attachment of a device and application of altered knee loading. *J. Biomech.* **43**, 3227–31 (2010).
 55. Allen, K. D. *et al.* Kinematic and dynamic gait compensations resulting from knee instability in a rat model of osteoarthritis. *Arthritis Res. Ther.* **14**, R78 (2012).
 56. McClure, M. J. *et al.* Decellularized Muscle Supports New Muscle Fibers and Improves Function Following Volumetric Injury. *Tissue Eng. Part A* (2018).
doi:10.1089/ten.TEA.2017.0386
 57. Merritt, E. K. *et al.* Functional assessment of skeletal muscle regeneration utilizing homologous extracellular matrix as scaffolding. *Tissue Eng. Part A* **16**, 1395–405 (2010).
 58. Alluin, O. *et al.* Kinematic study of locomotor recovery after spinal cord clip compression

- injury in rats. *J. Neurotrauma* **28**, 1963–1981 (2011).
59. Pereira, J. E. *et al.* A comparison analysis of hindlimb kinematics during overground and treadmill locomotion in rats. *Behav. Brain Res.* **172**, 212–218 (2006).
 60. Canu, M. H. & Garnier, C. A 3D analysis of fore- and hindlimb motion during overground and ladder walking: Comparison of control and unloaded rats. *Exp. Neurol.* **218**, 98–108 (2009).
 61. Greene, E. C. The anatomy of the rat. *Trans. Am. Philos. Soc.* **27**, 8 (1935).
 62. Batt, J. A. E. & Bain, J. R. Tibial nerve transection - a standardized model for denervation-induced skeletal muscle atrophy in mice. *J. Vis. Exp.* (2013). doi:10.3791/50657

Chapter 8 – Conclusion

The ultimate goal of the work compiled in this dissertation was to refine and improve regenerative rehabilitation through the development of enhanced treatment technologies and evaluative methodologies. This work offers broad utility to the fields of regenerative therapeutics, rehabilitation, and muscular/neural regeneration, among others. Through this work, the value of full three-dimensional biomechanical analysis (including extensive joint-by-joint kinetic calculations) has been demonstrated to be an integral evaluative tool for complete understanding of the impact of injury and extent of recovery for pathologies modeled in the rat hindlimb.

In **Chapter 3**, I presented a one-off sequence of experiments where we showed the exceptional return of form and function to the TA muscle after VML injury and treatment with a proprietary hyaluronic acid hydrogel formulation. In **Chapter 4**, it was shown that small differences in 3-D rat treadmill gait kinematics could be detected using the same motion capture methodologies that are utilized in human subjects. In **Chapter 5**, those motion capture techniques were expanded to overground walking and a methodology was developed to calculate concurrent 3-D kinetics for the first time. This was a substantial step forward in the analysis of rat gait and provided extensive insight into the 3-D internal forces being experienced by the joints in the hindlimb during normal gait. In the first half of **Chapter 6**, it was demonstrated that treatment of a TA VML injury with the TEMR construct leads to significant improvements in both the kinematics and kinetics of gait when compared to untreated animals. These results further emphasized the utility of the TEMR construct as a viable regenerative therapeutic for the treatment of extremity VML injuries. In the second half of **Chapter 6** and in **Chapter 7**, full 3-D gait analysis was performed on novel injury groups in rat models. Untreated peripheral nerve injuries to both the peroneal nerve and tibial nerve, treated and untreated VML injuries to the lateral

gastrocnemius, and treated and untreated peripheral nerve-muscle VML polytraumas were fully evaluated to determine the impact of injury and the efficacy of treatment. Specifically in the cases of polytrauma and gastrocnemius VML injury, this was the first biomechanical investigation on record.

While the work presented here was extensive, it only lays the foundation for the work that must be completed moving forward. The utility of these methods and the translational potential of modeling pathologies in the rat hindlimb is clear, but in order to extract the maximum amount of information from these rat models there are clear next steps for future experiments. Now that we have the capability to visualize the internal loads being experienced by the joints in the hindlimb, adding muscles to the musculoskeletal models would lead to a better understanding of the loads being applied to the individual muscles in the system. Muscle loading will impact fiber regeneration, and as seen in **Chapter 7**, pathological loads can lead to extensive compensatory hypertrophy. If the loading can be identified and augmented with some form of orthotic, that could potentially mitigate the compensatory effects and expedite the return to healthy movement patterns. It would also be very useful to extend evaluation timepoints out as long as possible in order to definitively track when compensation plateaus or when rats complete their recovery timeline and return to healthy movement. This information would allow for more targeted treatment/rehabilitation approaches and would allow for more informed study design in order to maximize positive outcomes of treatment.

As also shown in **Chapter 7**, existing experimental approaches could be refined based on the information presented through these studies. The creation of the lateral gastrocnemius VML injury leads to extensive scar tissue formation and sticky effects between the muscles and skin in the system. When stimulating the muscles to extract information on force production ability, these

sticky effects could be additive or detrimental depending on how the target muscle is stuck to synergist or antagonist muscles. With this in mind, when stimulating the gastrocnemius it is imperative to clear all surrounding tissues from the target muscle and stimulate the muscle as proximal as possible to the insertion point of the tibial nerve. In polytrauma scenarios, it is also important to create as small of an incision as necessary to minimize the scar tissue and sticky effects of lacerating the biceps femoris in order to access the tibial nerve. And when creating this injury, again, it should be made as close to the insertion point in the gastrocnemius as the surgeon is capable of accessing. Another consideration when doing maximum force production evaluation, especially at early timepoints as in TA studies, would be to minimize the number of stimulations. There is extensive historical data showing that the maximum force production occurs at either 150hz, 175hz, or 200hz for the TA and between 50-80hz for the gastrocnemius. Each stimulation leads to a fatigue response in the muscle, and at the 4W timepoint for TA animals there is likely still extensive muscular damage from the surgery. Limiting the stimulations has the potential to elicit a more accurate maximal response, both from the angle of not burning out the fibers at lower stimulations and not causing additional muscle damage. Further, in the case of the gastrocnemius where the muscle is hanging in open air for the stimulations, minimizing the stimulations would lead to testing the muscle while it is still closer to natural physiological conditions.

Specifically with the gastrocnemius injury model, there are many challenges in isolating recovery to the target muscle and limiting compensatory effects that occur due to the other muscles in the posterior compartment. These challenges do provide opportunities though, opportunities to expand our understanding of how these compensation patterns are arriving and the physiological response to extreme neural/muscular trauma in a complex system. Rehabilitation and regeneration are multifaceted, it will never be as simple as “fix the muscle, fix the problem”. But by introducing

technologies such as MRI to the gastrocnemius studies in order to track the hypertrophy occurring in the other hindlimb muscles, or attempting to design and introduce orthotics to limit pathological movement in the hindlimb during walking, or adding rehabilitative treadmill walking/wheel running to the early phases of recovery after treatment for these muscle injuries, we are provided with significant opportunities to enhance the understanding of the internal response to injury. Further, this response is not limited to neural and muscular compensation, increased and pathological joint loading comes with eventual hindlimb osteoarthritic effects. If effective rehabilitative methods are developed that minimize compensation, I believe a long-term study into the impact of those methods on development of osteoarthritis in the hip and knee of injured and treated rats who do and do not receive rehab would provide extremely valuable information.

As with many pre-clinical animal studies, the broader implications of this work revolves around the translational impact on human patients. I strongly believe that the methodology established in this work, as well as the novel injury models being evaluated, will enhance studies into the efficacy of regenerative therapeutics for numerous pathologies. With so much more insight into the true biomechanical effects of therapeutics, and a more stringent definition of what it means to be “healthy”, identifying the treatments that truly make a difference could be extremely impactful. Further, by expanding these biomechanical methods into larger animal models with more direct muscular size/recovery translational potential, the identification of the most effective treatments for pathologies could again be massively improved. The reach of the methods developed here is clear, and I truly hope that their potential is reached. The impact of these methods on studies that benefit human patients struggling with VML injuries, nerve injuries, and any other leg injuries should not be ignored, and that is why it is so important for full biomechanical analysis to be a requisite evaluative tool for rat hindlimb studies moving forward.

As I wrap up, I would again like to express my appreciation. Thank you to Dr. George Christ, my primary advisor, for all the time and support you gave me over the years. I truly appreciate everything you did for me. Thank you to Dr. Shawn Russell, though my coding is still sloppy, I would not even be half as competent as I am now without your patience and guidance. Thank you to Dr. Silvia Blemker, my committee chair, for being there when I could not see the path forward and desperately needed guidance. And thank you to Dr. Steven Caliarì and Dr. Zhen Yan for their constructive feedback throughout all my presentations, it was remarkably useful to have voices from other circles of academia.

Lastly, a final thank you to my family, my fiancé, and my close friends. The support I felt throughout this program was unwavering, and I will never be able to properly put my appreciation into words.